Wideband Reconfigurable Vector Antenna for 3-D Direction Finding Application

Johan Duplouy

THÈSE

En vue de l'obtention du

DOCTORAT DE L'UNIVERSITÉ DE TOULOUSE

Délivré par : *l'Institut National Polytechnique de Toulouse (INP Toulouse)*

Présentée et soutenue le *14 janvier 2019* **par :**

JOHAN DUPLOUY

Wideband Reconfigurable Vector Antenna for 3-D Direction Finding Application

---

JURY

JEAN-YVES DAUVIGNAC	Professeur	Rapporteur
RAPHAËL GILLARD	Professeur	Rapporteur
HERVÉ AUBERT	Professeur	Directeur
LAURE HUITEMA	Maître de conférences	Examinatrice
THIERRY MONEDIÈRE	Professeur	Examinateur
CHRISTOPHE MORLAAS	Enseignant-chercheur	Co-directeur
PATRICK POTIER	Ingénieur	Examinateur
ANTHONY BELLION	Ingénieur	Invité
PHILIPPE POULIGUEN	Ingénieur HDR	Invité

École doctorale et spécialité :
GEET : Électromagnétisme et Systèmes Haute Fréquence
Unité de Recherche :
ENAC Lab (TELECOM) et LAAS-CNRS (MINC)
Directeur(s) de Thèse :
Hervé Aubert et *Christophe Morlaas*
Rapporteurs :
Jean-Yves Dauvignac et Raphaël Gillard

"Je crois qu'après avoir vu ça, on peut mourir tranquille. Enfin, le plus tard possible, mais on peut. Ah c'est super. Quel pied, ah quel pied ! Oh putain ! Olalala !"

– Thierry Roland, Finale de la coupe du monde 1998

Remerciements

"Ramenez la [thèse] à la maison...Allez [Johan], allez"

– Vegedream

Enfin, nous y voici ! Quelle aventure ... Une thèse est bien entendu un travail de longue haleine (oui, oui, on y croît), mais ce n'est pas une fin en soi, c'est un moment particulier dans la vie : un défi que l'on se donne à soi-même, il y aura eu un avant qui ne sera plus, et il y aura un après à construire. Au moment de franchir ce cap, je me rends compte que la thèse est loin d'être un travail solitaire et je ne peux pas ne pas penser à tous ceux qui, de près ou de loin, auront contribué à celle-ci grâce à leur bonne humeur, générosité, savoir et soutien. Allez, on dit merci qui ?

Je tiens tout d'abord à remercier la Direction Générale de l'Armement ainsi que la région Occitanie pour le financement de ces travaux de thèse. Ils ont été effectués au sein du laboratoire TELECOM de l'ENAC, dans l'équipe EMA. Je remercie donc chaleureusement MM. Christophe Macabiau et Alexandre Chabory (respectivement responsables de TELECOM et de EMA) pour m'avoir fait confiance et permis de réaliser ces trois années de doctorat au sein d'une équipe enthousiaste et passionnée !

Une thèse est un document jugé par des pairs. Toute ma reconnaissance va vers celle et ceux qui ont accepté d'évaluer ce travail, et notamment à MM. Jean-Yves Dauvignac (professeur à l'université de Nice Sophia Antipolis) et Raphaël Gillard (professeur à l'INSA de Rennes) qui ont accepté de rapporter ce manuscrit.

Mes remerciements les plus chaleureux vont à mes directeurs de thèse. Tout d'abord, M. Hervé Aubert (professeur à l'INP de Toulouse), pour la confiance et l'autonomie qu'il m'a accordées, pour ses précieux conseils lors de la réalisation de ces travaux de doctorat ainsi que pour les nombreuses heures qu'il a consacrées à la relecture de mes papiers. J'aimerais également lui dire à quel point j'ai apprécié nos discussions, et notamment celles sur la langue de Molière et sur l'art de l'écriture scientifique. Ensuite, s'il y a bien quelqu'un que je dois remercier, c'est M. Christophe Morlaas (enseignant-chercheur à l'ENAC), qui a eu la patience de me supporter et de m'épauler au quotidien. Il a eu la gentillesse de répondre de manière toujours claire et précise à mes nombreuses sollicitations durant ces trois années. Ses conseils et sa rigueur m'ont permis de mener à bien cette thèse dans un contexte agréable. C'est pour moi un grand honneur que d'avoir pu travailler avec eux.

Je tiens aussi à remercier M. Michel Paonessa (ingénieur au sein de l'ENAC) pour l'aide qu'il m'a apportée lors de la réalisation des antennes.

Pendant ces trois années de thèse a régné dans les couloirs et locaux du bâtiment F une ambiance chaleureuse, où il était agréable de travailler aux côtés des équipes EMA et SIGNAV.

Merci notamment aux permanents : la *fashion victim* Rémi D. (désolé mais les pantacourts et les chemisettes font partie du top Topito des vêtements à brûler d'urgence), la féministe Hélène (mais bon, on verra bien quand il faudra porter quelque chose de lourd), la supportrice marseillaise Anaïs (vous savez pourquoi la pelouse du stade Vélodrome est aussi verte et aussi belle ? car il y a 11 chèvres dessus), le gaffeur et blagueur Antoine (qui n'a pas peur de faire du politiquement incorrect, enfin quelqu'un de sensé !), le papa poule Paul (qui pourra revivre d'ici dix huit ans), la jeune Anne-Christine et ses bons plans (si jamais vous avez besoin d'un conseil pour acheter une poussette ou si vous avez envie de manger chinois, n'hésitez pas à la contacter), sans oublier le barcelonais Axel (à qui je ne parle plus depuis la remontada, la plus grosse escroquerie de l'histoire du football).

Je salue également les nombreux post-doctorants/doctorants et compagnons de route : le jusqu'au-boutiste enacien Jérémy (j'espère sincèrement que tu obtiendras un post de permanent, celui-ci est tant mérité), le détendu Quentin (qui va terminer sa thèse grâce à la volonté du "D"), la végan Capucine (qui veut bien éplucher le lapin, mais pas les carottes !), l'apprenti peintre et mystérieux Rémi C. (mais que fait-il de ses soirées pour arriver si tard l'après-midi ?), Anne-Marie dite Mercotte (qui nous empêche de poser notre lundi grâce à ses succulents gâteaux), sans oublier les expertes pâtisseries orientales Ikhlas et Sarah (cependant, j'attends toujours vos crêpes). Un merci particulier au parieur fou et homme d'honneur Seif qui a su prendre le temps de célébrer la victoire des Bleus à la coupe du monde malgré une charge de travail dantesque ! Par ailleurs, j'espère que tu auras de nouveau l'occasion de nous faire part de ton expertise en matière de sécurité sociale et d'impôt. Je tiens en outre à féliciter (malgré son amour pour le football business) Florian dit Ridaube, pour son expertise des normes OACI. L'harmonisation internationale sur la réglementation des drones repose sur ton travail exemplaire. J'espère qu'avec les années, il sortira de son bureau pour profiter de la vie car celle-ci ne se résume pas au travail. Il pourra alors assouvir son autre passion pour la météo avec Didier Labyt. Je tiens ensuite à remercier les fruits du laboratoire TELECOM: Thomas B. et Maxandre qui feraient mieux de sortir au lieu de jouer à Pokemon. La vie ne se résume pas à un monde virtuel. De plus, j'espère que les 10 commandements du thésard stakhanov que j'ai enseigné à Thomas V. aboutiront aux résultats escomptés. À dans cinq ans pour ta soutenance ! Enfin, je souhaite bon courage aux petits nouveaux: David et Uygar. Il y aurait aussi des crasses à dire sur eux mais je laisse ça aux suivants.

Je souhaite également une bonne continuation aux autres membres du laboratoire TELECOM : Carl, Enzo, Jade, Eugène, Heekwoon, Paul Verlaine, Junesol, Roberto, Auryn et Xiao. J'espère qu'on aura l'occasion de continuer nos longues discussions.

Je n'oublie pas non plus mes augustes prédécesseurs : miss Alizé et ses bons plans afterwork ainsi que le Zinédine de l'équipe TELECOM, JB. Je souhaite en outre adresser mes sincères remerciements à mon professeur d'italien Guiseppe, qui m'a permis de découvrir l'Italie dans toute sa splendeur (Da Michele, *il ragù di sua madre*, les négronis, sans oublier la chanson *"oh le le, oh la la..."*). Ce fut un réel plaisir de regarder avec toi les matchs de l'Italie lors de la coupe du monde de football 2018. J'ajouterai donc que cela a été un honneur pour moi de rencontrer Enik Shytermeja, ponte du GNSS, qui a décidé de continuer ses études malgré une carrière prometteuse en NBA. La communauté scientifique le remercie mais le monde du basket est en deuil. Officieusement, d'après les dernières révélations de Basket Leaks, il a été obligé d'arrêter sa carrière de basketteur suite à contrôle positif antidopage lors de la première phase du championnat d'Albanie.

L'occasion m'est donnée de faire part de toute ma gratitude à tous mes amis sur qui j'ai toujours

pu compter, qu'ils soient de Toulouse, de Paris, de Lille ou de Saint-O, sans oublier ceux du classement ATP. Un merci particulier à Phi-Nhan dite Hulk de l'apéro pour la relecture de ce manuscrit. Après, n'ayant pas envie d'en oublier, je préfère ne pas me lancer dans un listage car je sais qu'ils se reconnaîtront. Enfin, j'adresse mille mercis à mes parents, à mon frère, à l'ensemble de ma famille et à mon chien pour leur soutien permanent et leurs sacrifices à mon égard !

Un dernier merci à tous ceux qui ont partagé ce bout de chemin...

Vive la science,
Vive la France.

Contents

List of abbreviations

AUT	Antenna Under Test
CRB	Cramer-Rao lower Bound
DCS	Digital Cellular System
DF	Direction Finding
DoA	Direction of Arrival
EM	ElectroMagnetic
FIM	Fischer's Information Matrix
GSM	Global System for Mobile communications
HF	High Frequency
MUSIC	MUltiple SIgnal Classification
PNR	Power density to Noise Ratio
RMS	Root Mean Square
RP	Radiation Pattern
RPC	Radiation Patterns Combination
SNR	Signal to Noise Ratio
TSA	Tapered Slot Antenna
UHF	Ultra High Frequency
VA	Vector Antenna
VHF	Very High Frequency

VSWR	Voltage Standing Wave Ratio

General introduction

Context

The interest in estimating the direction-of-arrival (DoA) of incoming electromagnetic (EM) waves, also known as direction finding (DF), goes back to the very beginnings of wireless communications at the end of the twentieth century. Today, DF plays a crucial role in various civilian and military applications spanning across the terrestrial, airborne, naval and space sectors. DF applications include navigation, electronic warfare, object tracking, search and rescue, and radio astronomy [1].

In all the applications mentioned above, the objective is to estimate the DoA with the greatest range of detection and the highest accuracy as possible. Over the years, the detection and estimation capabilities of DF systems have steadily increased due to significant technological advances in electronics and array signal processing. However, all direction finders have a common architecture with a DF antenna as the first component. Therefore, any error introduced by the antenna will affect the rest of the DF system, so the antenna constitutes the key component of a direction finder. Moreover, the electrical characteristics of the DF antenna notably define the estimation accuracy along with the spatial and frequency coverages [2].

Traditionally, the azimuth angle of arrival has been considered sufficient to define the DoA of the incident EM-wave, but the estimation of the elevation angle may be necessary for some applications. Nevertheless, most of commercially available (see, e.g., [3–5]) or published (see, e.g., [6, 7]) DF antennas operate in the VHF or UHF band and offer a 2-D coverage (i.e., only the azimuth angle of the DoA can be estimated for a limited range of elevation angles of arrival). However, in all cases, the elevation angle of arrival of the impinging EM-wave will affect the performances of direction finders presenting a 2-D coverage, even if the estimation of the elevation angle is not needed [8]. Besides, significant degradation of the DF performances may be observed when single-polarized direction finders are used. Hence, it is of crucial importance that the direction finder is dual-polarized in order to overcome errors due to polarization mismatch [9]. Therefore, the ideal direction finder would be able to estimate the azimuth and elevation angles of arrival of the incident EM-waves over the 3-D space (i.e., 360° of azimuth and 180° of elevation) within a wide frequency range, and deal with all forms of polarization. In addition, DF nowadays requires smaller and more compact antennas to notably ensure increased mobility and discretion.

Over the years, many methods have been proposed to estimate the DoA of incoming EM-waves. On one hand, the standard technique is based on the spatial distribution of an antenna array [10]. However, the extension of this technique for wideband DF system targeting 3-D coverage is not straightforward, as the spatial and frequency coverages are limited by the spacing between antennas in the array. As a consequence, the design of a compact, low profile and wideband

DF antenna presenting a 3-D coverage is actually very challenging. On the other hand, an innovative technique was reported about twenty years ago and consists of deriving the DoA from the measurement of the six Cartesian components of the EM-wave through a so-called vector antenna (VA) [11]. VAs are multi-port antennas composed of three electric dipoles and three magnetic dipoles, all spatially co-located with orthogonal orientations. Hence, each component of the incident EM-wave is measured through the radiation pattern (RP) of the relevant dipole. They are gaining prominence nowadays since a single VA is sufficient to estimate the DoA of an incoming EM-wave over the 3-D space regardless of its polarization, and notably allows compactness by substituting a large antenna array.

Since their introduction into the signal processing domain in 1994, many VA designs have been proposed for the DoA estimation of incoming EM-waves. Nonetheless, there is no suitable VA for every DF application. Indeed, only few designs demonstrated the capability of covering the full 3-D space (or the upper hemisphere if the antenna is mounted over a metallic support in view of embedded applications). Moreover, the attention was mainly focused on the implementation of wideband and active VA structures [12,13]. In contrast, a passive and grounded VA that only estimates the DoA of incident vertically-polarized EM-waves in two separate narrow bandwidths was reported in [14]. Fully passive VAs do not suffer from the intrinsic and strong limitations of active antennas, but the wideband coverage is very challenging to be achieved. Up to now, no wideband and passive VA has been reported.

Objectives and originality

The main objective of this Ph.D. thesis is to study and design a passive and wideband VA for DF over the 3-D space with compactness and minimal complexity constraints. More precisely, the objective is to design a passive and compact VA that is able to estimate, with the highest accuracy and over the widest frequency range of operation, the DoA of impinging EM-waves over the 3-D space, regardless of their polarization. The scope of application covers both the civil and military domains.

In this thesis, three main research axes towards this objective are investigated:

I. The conception of a passive and wideband VA intended to estimate the DoA of vertically-polarized EM-waves in the upper hemisphere. Besides, the antenna is mounted over a metallic support in view of embedded applications.

II. The improvement of the DoA estimation process of VAs to enhance their DF performances in terms of estimation accuracy, frequency coverage, robustness to angular ambiguity and polarization mismatch.

III. The development of a passive and wideband VA intended to estimate the DoA of vertically- and horizontally-polarized EM-waves in the upper hemisphere to overcome the errors due to polarization mismatch.

The originality of this work resides in three distinct levels:

I. The wideband frequency coverage of VAs, which up to now has not yet been addressed from passive structures. Furthermore, an original antenna arrangement is proposed in order to synthesize the radiation patterns of magnetic and electric dipoles.

II. The improvement of the DF performances of VAs by adding new RP diversity to the one commonly used by standard VAs (i.e., the RP diversity that allows the measurement of the six components of an incident EM-wave) in the DoA estimation process. This additional RP diversity is enabled because VAs are multi-port antennas, and consequently, new RPs can be introduced. Moreover, a method based on the Cramer-Rao lower bound (CRB) in order to select efficiently and rapidly the additional RP diversity is also reported.

III. Two prototypes have been manufactured in order to experimentally validate the simulated results in terms of electrical characteristics and DF performances.

Outline

This dissertation is structured as follows.

Chapter 1 aims to detail the necessary background information on DF, in particular, the different techniques used to estimate the DoA of impinging EM-waves and the most recent DF antennas. This state of the art notably enables the identification of the challenges faced by current DF antennas so that the motivations of this Ph.D. work can be more precisely defined. The descriptors that will be used throughout this thesis for the DF performances evaluation are also specified.

Chapter 2 aims to design the first passive and wideband VA, referred to as the Two Season VA, which is intended to estimate the DoA of incident vertically-polarized EM-waves in the upper hemisphere. The first part of this chapter covers VAs in general and the techniques used in antenna design to obtain wideband impedance matching. Then, a feasibility study of a wideband antenna based of one of these techniques is realized, followed by a state of the art of the wideband electric and magnetic dipoles in order to identify the radiating elements that would be worthwhile to consider for designing the VA. The centerpiece of this chapter is the detailed description of the Two Season VA from the design of the constituting elements to the overall antenna. Finally, the electrical characteristics and DF performances are evaluated using full-wave EM-simulations. In particular, the theoretical and estimated DF performances are assessed using the realistic CRB (derived from the actual RPs of the antenna) and the popular estimation algorithm called multiple signal classification (MUSIC), respectively. Furthermore, a prototype has been manufactured to confront the measurement results with the prior simulations results.

Chapter 3 aims to enhance the DF performances of the Two Season VA. Three methods are presented to achieve the desired result. First, the DoA estimation process of the Two Season VA is improved by exploiting new RP diversity in addition to that employed to measure the electric and magnetic components of the incoming vertically-polarized EM-waves. A method for selecting efficiently and rapidly the additional RP diversity is proposed. Secondly, the frequency coverage is extended by a modification of the antenna feeding and the use of the new DoA estimation process. Thirdly, the topology of the Two Season VA is modified in order to estimate the DoA of incoming EM-waves in the upper hemisphere, regardless of their polarization. The electrical characteristics and DF performances of the prototype of this new VA, referred to as the Four Season VA, are assessed and confronted with the prior simulations results.

Finally, the **Conclusions** are drawn from the results obtained in this Ph.D. thesis, which includes recommendations for research work topics that could be addressed in the future.

A series of **Appendices** is also provided to ensure a more complete understanding of the research problem.

Chapter 1

State of the art

Contents

The purpose of this chapter is to review the literature on direction finding (DF). After providing general information about DF (Section 1.1), this chapter highlights the different DF techniques (Section 1.2) and the state-of-the-art DF antennas (Section 1.3). Finally, the motivations of this thesis work are drawn in order to overcome the challenges that current DF antennas face (Section 1.4).

1.1 Direction finding overview

1.1.1 Definition

"La mesure des angles dont il faisait une science à part sous le nom de goniométrie..."

– Bernard Le Bouyer de Fontenelle, *Éloge de M. de Lagny*

The mathematician Thomas Fantet de Lagny wrote for the first time the word goniometry in the 1734 memoirs in mathematics and physics of the French Royal Academy of Sciences [15]. Etymologically, it derives from the Greek terms *gonia* and *metron*, meaning angle and measurement, respectively. Hence, it serves to designate the science of measuring angles. Generally speaking, it also refers to the various techniques used to estimate the DoA of an acoustic, seismic, EM, or any other wave emitted by a source. Therefore, a radiogoniometer is a system that measures the DoA of an incoming EM-wave, and thus estimates the source direction. This process is more commonly referred to as radio DF (or just DF), and the instrument used to perform this task is thus named a radio direction finder (or simply a direction finder).

As illustrated in Fig. 1.1, the direction of propagation of an EM-wave is given by the direction of the wave vector $\boldsymbol{k}(\phi, \theta)$, where $\phi \in [0°; 360°]$ and $\theta \in [0°; 180°]$ denote the azimuth and elevation angles, respectively. The polarization of the impinging EM-wave is here described by the polarization vector $\boldsymbol{p}$ (referred to sometimes as the Jones vector) and is defined as the combination of vertical ($\hat{\boldsymbol{\theta}}$) and horizontal ($\hat{\boldsymbol{\phi}}$) polarizations as follows

$$\boldsymbol{p} = \sin(\gamma) e^{j\eta_f} \hat{\boldsymbol{\theta}} + \cos(\gamma) \hat{\boldsymbol{\phi}}, \tag{1.1}$$

where $\gamma \in [0°; 90°]$ and $\eta \in [-90°; 90°]$ refer to the auxiliary polarization angle and the polarization phase difference, respectively. Therefore, the parameters of the incoming EM-wave can be summarized by the parameter vector $\boldsymbol{\Omega} = [\theta \ \phi \ \eta \ \gamma]^{\mathrm{T}}$. The superscript $^{\mathrm{T}}$ refers to matrix transposition.

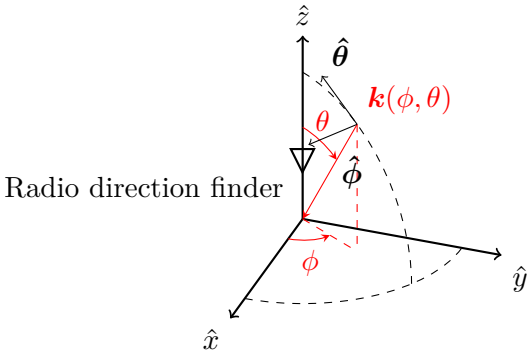

Figure 1.1: Definition of the azimuth ϕ and elevation θ angles of the DoA of the incident EM-wave in the Cartesian coordinate system

Direction finders are composed of an array of antennas, which enables the estimation of the DoA of an incident EM-wave by exploiting its propagation properties [16]. Unlike most radar systems, these devices perform a passive and inconspicuous measurement that the transmitter of the measured radio wave cannot detect.

1.1.2 History of direction finding

The beginning of DF is generally attributed to the discovery of EM-waves, and more particularly to Hertz's discovery in 1888 of the properties of directional antennas [17]. This discovery led to the development of the first DF system patented by Scheller in 1906. The earliest direction finders consisted of an electric or magnetic dipole mounted on a rotating support and oriented so that the dipole axis was brought to coincidence with the electric or magnetic component of the incident EM-wave. The direction of arrival (DoA) can be deduced from the measured direction of polarization. The rotating frame device remains the best-known direction finder at the time.

Bellini and Tosi filed in 1907 the patent for the first non-rotating DF system that exploits amplitude [18], which is represented in Fig. 1.2(a). Notwithstanding this useful invention, rotating-loop direction finders were commonly used during World War I, as shown in the photograph in Fig. 1.2(b). As the first DF systems operated in the high frequency (HF) band (3 MHz - 30 MHz), they exhibit considerable estimation inaccuracies, especially at night due to ionospheric effects at these frequencies [19]. In 1917, a new DF system was designed to overcome this issue. This design is depicted in Fig. 1.2(c) and consists of an array of four vertical dipoles which provides directional patterns that correspond to those of loop antennas. As the vertical dipoles do not pick up any interfering horizontally-polarized components, they can provide a good estimate of the DoA of incoming EM-waves even in the presence of sky-waves. This direction finder is known as the Adcock antenna array, named after its eponymous inventor and was patented in 1919 [20]. Although it was not used for practical applications until 1931, it is still used today.

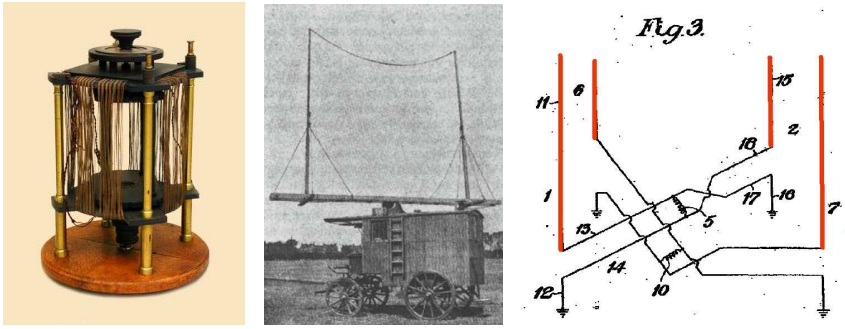

(a) (b) (c)

Figure 1.2: First direction finders: (a) Bellini-Tosi system [21], (b) rotating-loop used during WWI [17], and (c) Adcock antenna array [20]

In 1926, Sir Robert Watson-Watt, also known as one of the pioneers of radar development during World War II, improved the system introduced by Adcock. He proposed to use a fifth antenna in order to avoid the inherent angular ambiguity of the Adcock DF system [22]. Besides, a cathode ray oscilloscope is also added to the DF system to directly trace the DoA of the incoming EM-wave, allowing to operate the antenna array in a static configuration. English army ships were equipped with these devices from 1943 to locate German submarines during World War II.

At the same time, the German company Telefunken developed for military purposes a sizeable circular array known as the Wullenweber array to locate German submarines stationed in the

North Atlantic Ocean [10]. Fig. 1.3 is a photograph of one of these arrays.

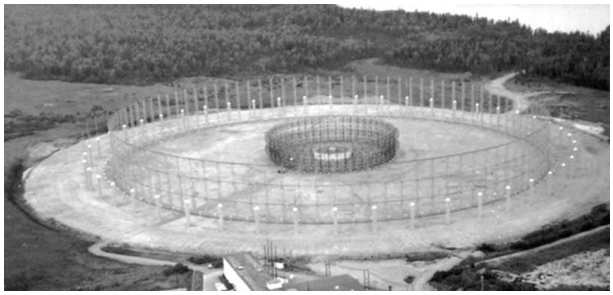

Figure 1.3: Wullenweber array [23]

The earliest HF direction finders based on the Doppler effect appeared in 1941. In 1943, following the radar development in Great Britain and given the need to cover higher frequencies, the first Doppler-based direction finder operating at 3 GHz was delivered [17]. After the Second World War, Doppler or pseudo-Doppler direction finders emerged and have been used for air traffic management at airports around the world since the 1950s.

After World War II, developments in electronics have extended the capabilities of DF systems. Moreover, since the end of the 1970s, digital signal processing has been introduced into DF, making direction finders more efficient thanks notably to the emergence of interferometry techniques and high-resolution methods.

1.1.3 Civil and military applications

As well in civil as military domains, DF has nowadays gained a significant position in a wide range of applications, related to either radionavigation or radiolocation.

Historically, DF was brought to bear for radionavigation purposes. However, this scope of applications is currently losing its importance because of the fast expansion of satellite navigation systems and their significant potential. One of the first applications related to radionavigation was homing, in which DF measurements were used to direct the user towards emission sources. At present, radionavigation provides a means of positioning and directing oneself by exploiting signals received from emission sources (e.g., radio beacons) whose positions are known. It is used in both the naval and aeronautical domains. For instance, various systems such as VHF omnidirectional radio range (VOR), instrument landing system (ILS) and marker beacons (MKR BCN) are currently in service in international civil and military aviation [24]. VOR system provides the aircraft with a bearing to the ground station location. During the landing approach, ILS assists aircraft pilots by giving an approach path for exact alignment and descent of the plane to a runway. It also enables a landing under Instrument Flight Rules (IFR) in case of poor visibility due to bad weather, a night landing, or a crosswind approach. Finally, MKR BCN provides aircraft pilots with a means of determining their position along the runway in lack of ILS facilities in certain airports.

At the same time, DF for radiolocation purposes has become more than ever a necessity in

various applications, especially in the military domain through the emergence of a new form of warfare named electronic warfare. Radiocommunications between the various army units or even the remote control of weapon systems have led to a military dependence on wireless communications. This dependence has grown steadily over the last few years and represents a real vulnerability that can be exploited. Hence, electronic warfare consists in exploiting the opponent's radio emissions and, conversely, in preventing him from doing the same. In particular, it enables the detection and location of enemy transmitters to evaluate their strength and position. Moreover, one of the essential components of electronic warfare is the monitoring of the electromagnetic spectrum to gain a good knowledge of the spectral occupancy and, identify and locate non-authorized transmitters, or even to search for sources of interference. This component is also common in the civil domain. Indeed, regulatory authorities such as the International Telecommunication Union (ITU) or International Radio Consultative Committee (IRC) also monitor the electromagnetic spectrum to ensure its proper use in accordance with the regulations in force. Other applications for radiolocation purposes can also be pointed out in the civil domain. For instance, during search and rescue (SAR) missions, the radiolocation of emergency transmitters enables faster assistance to people in distress who may be in areas with topographical difficulties. Finally, DF can be found in various scientific studies such as radio astronomy, Earth remote sensing or wildlife tracking.

The variety of DF applications cover almost the entire radio spectrum from the lowest frequencies (10 MHz) for locating the beacons of avalanche victims to higher frequencies (40 GHz) for radio astronomy. However, the majority of applications occur in the high frequency (HF from 3 MHz to 30 MHz), very high frequency (VHF from 30 MHz to 300 MHz) and ultra high frequency (UHF from 300 MHz to 3000 MHz) bands. Table 1 lists some operating frequency bands and highlights the main applications that are performed in each band [25].

1.1.4 Architecture overview of digital direction finders

Recent developments in the field of wireless communications have led to a renewed interest in DF, heightening at the same time the complexity and requirements of DF systems. Much progress has also been made on array signal processing, enabling a more accurate estimation of the DoA of the impinging EM-wave. However, all modern direction finders are based on the same structural diagram, as depicted in Fig. 1.4. Such system includes the following main parts:

- An antenna array consisting of a particular arrangement of several sensors that enables the sampling in amplitude and/or phase of the incident wavefront. After that, the samples can be processed through the following elements of the direction finder in order to derive the DoA of the incoming EM-wave. Design aspects of the antenna array such as the number, the choice of the radiating elements and their geometric arrangement are established with respect to the DF algorithm and the operating frequency band.
- A multiplexer may be used if the number of receiving channels differs from the number of antenna array output ports. Therefore, it simplifies the digital reception chain and reduces the hardware costs by connecting the output ports sequentially and selectively to the measurement channels.
- A receiver ensures the compliance between the measured signal and the specifications related to the processing unit through a series of analog signal processing operations that

preceded the digitization. Typical receiver architecture enables notably the following actions to precondition the radio frequency signal to efficient digitization: amplification, filtering and conversion to a suitable intermediate frequency if the analog/digital converter does not allow the processing at the frequency of the antenna signal. On another note, measurement characteristics (frequency of operation, bandwidth, amplification, etc.) are delivered to the receiver via command orders sent by the processing unit.

- A digital processing unit involves a DF algorithm implemented, for instance, on a field programmable gate array (FPGA). This unit also allows the control of the multiplexer if it is used. Moreover, a feedback loop is generally employed to improve the accuracy of the DoA estimation.

- A human-computer interface permits the operator to interact with the DF system through a user interface, which includes several features such as the display of the DoA and the control panel of the processing unit.

Frequency band	Uses
10 kHz - 10 MHz	Long-wave, medium-wave and short-wave broadcasting
10 MHz - 30 MHz	Avalanche beacon, navigational telex, maritime mobile, amateur radio
30 MHz - 88 MHz	Model control, radio microphones, military systems, professional mobile radio
88 MHz - 108 MHz	FM broadcasting
108 MHz - 144 MHz	Aeronautical communications, ILS/VOR
144 MHz - 400 MHz	Maritime communications, defense systems, radio broadcasting, professional mobile radio
400 MHz - 470 MHz	ARGOS beacon, COSPAS-SARTSAT beacon, amateur radio, TETRA and TETRAPOL cellular networks, professional mobile radio
470 MHz - 860 MHz	TV broadcasting, radio microphones
860 MHz - 890 MHz	Low power auxiliary (alarm, remote control), RFID sytems
890 MHz - 960 MHz	GSM (Global System for Mobile communications)
960 MHz - 1710 MHz	Aeronautical systems (DME, TACAN, IFF), Galileo, GPS, Glonass, Radars
1710 MHz - 1880 MHz	GSM
1880 MHz - 1900 MHz	Digital enhanced cordless telecommunications
1920 MHz - 2170 MHz	Universal mobile telecommunications system
2170 MHz - 2400 MHz	Telemetry, military systems
2400 MHz - 2500 MHz	Bluetooth, Wi-Fi networks
2500 MHz - 2700 MHz	Mobile communication services on board vessels
2700 MHz - 3400 MHz	Aeronautical navigation, radiolocation
>3400 MHz	Radar, radio astronomy, radiolocation

Table 1.1: Main applications in the HF, VHF and UHF bands

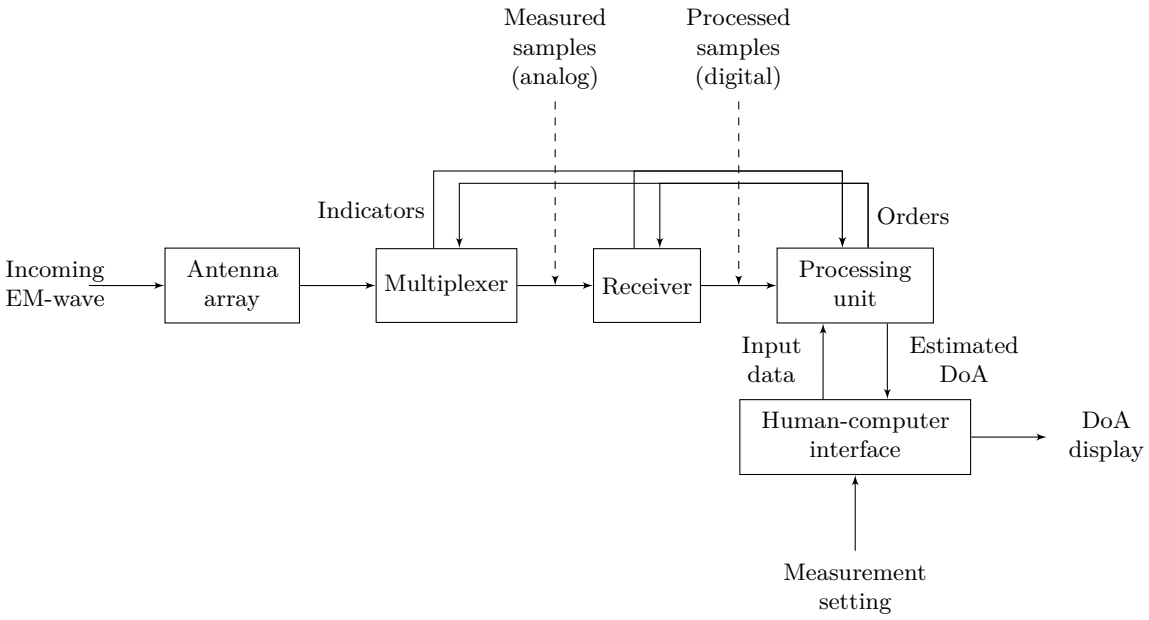

Figure 1.4: Functional architecture of a digital direction finder

1.1.5 Performance descriptors of direction finders

The DF performances of any direction finder are subject, on one hand, to the electrical characteristics of the constituting DF antenna, and on the other hand, to the applied DF technique. Therefore, practical aspects that regard both the design of a DF antenna and the choice of the DF technique should be made with the utmost care, taking into account the interdependence between them. These choices must also be made according to the foreseen application, which involves considering the economical aspect as well as managing several constraints (e.g., antenna size, weight, carrier, or even environmental conditions). This should lead to a trade-off between the expected performances and the operational situation. There are nevertheless some descriptors that can be used to significantly quantify the performances of a DF system.

1.1.5.1 Angular coverage

The angular coverage corresponds to an angular area in which a direction finder can estimate the DoA of an incident EM-wave in compliance with an accuracy specification. From the angular coverage aspect, it is possible to define three main categories of DF:

- DF with a 2-D angular coverage, meaning that the DoA of an incident EM-wave can be estimated only in azimuth or elevation;
- DF with a limited 3-D angular coverage, meaning that the DoA of an incident EM-wave can be estimated in azimuth and elevation in a restricted area of the three-dimensional space;
- DF with a 3-D angular coverage, meaning that the DoA of an incident EM-wave can be estimated in the overall three-dimensional space. If the DF antenna is mounted over a ground plane in view of embedded applications, this coverage is limited to the 3-D upper half-space.

The angular coverage is essentially subject to the radiation patterns (RPs) of the antenna elements constituting the direction finder.

1.1.5.2 Frequency coverage

In the same vein as the angular coverage, the frequency coverage specifies the frequency band in which a direction finder is able to estimate the DoA of an incident EM-wave in compliance with an accuracy specification. It also enables the identification of three categories of DF:

- Single-frequency DF which allows the estimation of the DoA of an incident EM-wave, as its name suggests, at only one frequency or over a small frequency range;
- Multi-frequency DF which allows the estimation of the DoA of an incident EM-wave at several frequencies or over small frequency ranges;
- Wideband DF which allows the estimation of the DoA of an incident EM-wave over a wide frequency range.

The frequency coverage depends essentially on the impedance matching and RPs of the antenna elements constituting the direction finder.

1.1.5.3 Theoritical limit, the Cramer-Rao lower bound

The Cramer-Rao lower bound (CRB) gives a lower bound on the variance of any unbiased estimators of a deterministic parameter. This bound was named in honor of H. Cramer and C. R. Rao who independently derived this limit in the 1940s [26, 27]. Special attention must be paid to P. Stoica [28] who established the CRB as one of the most utilized metrics for optimal DF accuracy. In this context, it allows to define the theoretical limit of the average precision that can be reached by a given direction finder regardless of the applied DF technique. It is important to note that the CRB is strongly dependent on the electrical characteristics of the DF antenna, especially its RPs. From a technical point of view, the CRB is related to the Fischer information (or equivalently, to the Fischer's information matrix (FIM), denotes $\mathbf{J}$, for a multi parameter problem) [29]. In mathematical statistics, this matrix provides a summary of the amount of information in the received data relative to the quantities of interest.

Consider that the n-th measurement of the received signal is $\boldsymbol{x}[t_n]$ at time t_n and that a stacked vector of N snapshots is $\boldsymbol{X} = [\boldsymbol{x}[t_1], \boldsymbol{x}[t_2], ..., \boldsymbol{x}[t_N]]$. Let us assume that the estimation of the unknown parameter vector $\boldsymbol{\Omega}$ through the observations $\boldsymbol{X}$ of a known probability density function (pdf) $f_{\boldsymbol{X}}(\boldsymbol{x}|\boldsymbol{\Omega})$ and likelihood function defined as follows

$$L(\boldsymbol{\Omega}|\boldsymbol{x}) = \prod_{n=1}^{N} f_{\boldsymbol{X}}(\boldsymbol{x}|\boldsymbol{\Omega}). \tag{1.2}$$

The likelihood function can be viewed as a function of the unknown parameter vector $\boldsymbol{\Omega}$ given the data $\boldsymbol{x}$. The natural logarithm of the likelihood function $l(\boldsymbol{\Omega}|\boldsymbol{x})$ given by

$$l(\boldsymbol{\Omega}|\boldsymbol{x}) = \sum_{n=1}^{N} \ln\left(f_{\boldsymbol{X}}(\boldsymbol{x}|\boldsymbol{\Omega})\right), \tag{1.3}$$

is generally used rather than the likelihood function to simplify the mathematical manipulations, which allows to work with a sum of pdfs instead of a product. The first derivative of the log-likelihood function is called Fisher's score. Since an unbiased estimator is an estimator having a mean that converges to the correct parameter vector as the number of snapshots tends towards infinity, the first moment of the score vanishes. The Fischer information corresponds to the second moment of the score. Mathematically, the elements in $\mathbf{J}$ are given by

$$\begin{aligned} J_{i,j} &= -E\left[\frac{\partial}{\partial\Omega_i} l(\boldsymbol{\Omega}|\boldsymbol{x}) \frac{\partial}{\partial\Omega_j} l(\boldsymbol{\Omega}|\boldsymbol{x})\right], \\ &= -E\left[\frac{\partial^2}{\partial\Omega_i \partial\Omega_j} l(\boldsymbol{\Omega}|\boldsymbol{x})\right]. \end{aligned} \tag{1.4}$$

The second derivatives specify how the likelihood function is peaked at the maximum point since the Fischer information measures the curvature of the log-likelihood. Higher is the curvature, easier is the estimation of the true value of the parameter $\boldsymbol{\Omega}$. This means, that there is a lot of information about $\boldsymbol{\Omega}$ from $\boldsymbol{X}$. According to the Cramer-Rao theorem, the variance of any unbiased estimate of $\boldsymbol{\Omega}$ is higher than the inverse of the Fischer information. Then,

$$\mathrm{C}(\hat{\boldsymbol{\Omega}}) \geqslant \mathrm{CRB}(\boldsymbol{\Omega}) = \boldsymbol{J}^{-1}, \tag{1.5}$$

where $\mathrm{C}(\hat{\boldsymbol{\Omega}}) = E\left[\left(\hat{\boldsymbol{\Omega}} - \boldsymbol{\Omega}\right)\left(\hat{\boldsymbol{\Omega}} - \boldsymbol{\Omega}\right)^{\mathrm{T}}\right]$ and $\mathrm{CRB}(\boldsymbol{\Omega})$ refer to the covariance matrix of the estimates and the CRB of the parameter $\boldsymbol{\Omega}$, respectively. It can be noted from Eq. 1.5 that the precision to which it is possible to estimate $\boldsymbol{\Omega}$ is limited by the Fisher information of the likelihood function. This makes sense, because the less information there is, the more difficult it is to accurately estimate $\boldsymbol{\Omega}$. This implies that the variance increases. The matrix inequality in Eq. 1.5 means that $\mathrm{C}(\hat{\boldsymbol{\Omega}}) - \boldsymbol{J}^{-1}$ is non-negative definite matrix. Therefore, the lower bound on the variance of any estimator of the parameter Ω_i is expressed as follows

$$\mathrm{Var}(\Omega_i) \geqslant [\boldsymbol{J}^{-1}]_{i,i}. \tag{1.6}$$

For 3-D DF purposes, the parameter vector $\boldsymbol{\Omega}$ contains the azimuth and elevation angles of the incoming EM-wave. It may also include the polarization parameters of the wave if they are to be estimated.

1.1.5.4 Estimation accuracy

The estimation accuracy is one of the most essential characteristics of a direction finder, if not the most important. This accuracy corresponds to the angular error between the estimated angles of arrival and the exact angles. In other words, it assesses the instrumental precision of the angular measurement, namely how far off is the measurement result from the true value of the DoA of the incoming EM-wave. In particular, this is subject to different matters such as the electrical characteristics of the DF antenna, the signal to noise ratio or even the propagation effects on the impinging EM-wave. Usually, the accuracy of the direction finder is characterized by the Root-Mean-Square (RMS) value of the angular error. Depending on the application, this accuracy may be given either as a function of the azimuth or elevation angles or as a function of the angular distance [30]. In the first case, it is defined by

$$E_{\mathrm{RMS}}(\Omega) = \sqrt{\frac{1}{L}\sum_{i=1}^{L} |\Omega - \hat{\Omega}|^2}, \tag{1.7}$$

where Ω is the true angle (azimuth angle ϕ or elevation angle θ), $\hat{\Omega}$ is the angle estimated by the direction finder and L denotes the number of Monte-Carlo trials. For the second one, it is given by

$$\Delta a_{\mathrm{RMS}}(\phi,\theta) = \sqrt{\frac{1}{L}\sum_{i=1}^{L} |\Delta a(\phi,\theta)|^2}, \tag{1.8}$$

where Δa is the minimal angular distance between the true (ϕ,θ) and estimated $(\hat{\phi},\hat{\theta})$ angles, as shown in Fig. 1.5. This angular distance is expressed as follows

$$\Delta a(\phi,\theta) = \cos^{-1}(\cos(\theta)\cos(\hat{\theta}) + \sin(\theta)\sin(\hat{\theta})\cos(\phi-\hat{\phi})). \tag{1.9}$$

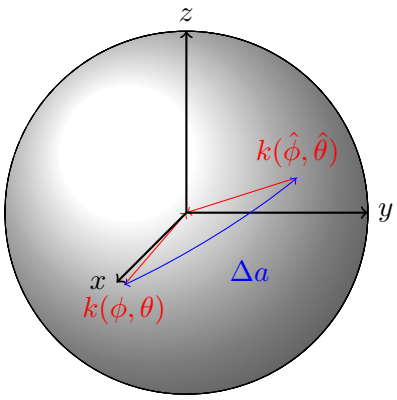

Figure 1.5: Definition of the angular distance Δa between the (ϕ,θ) and $(\hat{\phi},\hat{\theta})$ angles in the 3-D space

The estimation accuracy achieved by the DF antenna over a given angular coverage can be evaluated by analyzing either the maximum value or the 95th percentile of $\Delta a_{\mathrm{RMS}}(\phi,\theta)$ of all estimated DoAs. The latter corresponds to the error threshold for respectively 95% all simulated or measured DoAs in the 3-D upper half-space. Although the highest value of $\Delta a_{\mathrm{RMS}}(\phi,\theta)$ may be interesting in practice, it does not provide a good picture of the antenna performance when the accuracy is very good in the full 3-D half-space, except in few specific directions. In this case, the 95th percentile of $\Delta a_{\mathrm{RMS}}(\phi,\theta)$ offers a better descriptor as it is being less sensitive to the estimation errors in these directions. Looking at the 95th percentile is not restrictive in a sense that there is usually a notion of motion during DF measurements. For instance, either the DF antenna or the target (e.g., a missile in the military domain) can be mobile. It can also be interesting to look at the values of E_{RMS} for the azimuth and elevation angles as well as the corresponding 95th percentiles even if the direction finder is intended for 3-D DF. These values are an indication of whether the direction finder is more accurate in azimuth or elevation.

1.1.5.5 Sensitivity

The sensitivity designates the minimum power density P_{sensi}, expressed in dBW.m^{-2}, required to estimate the DoA of an incoming EM-wave with an error which does not exceed a prescribed threshold. It is also possible to express it as a function of the amplitude of the corresponding electric wave, that is in dBμV.m^{-1}. In other words, the sensitivity defines the required power

P_{ant} at the DF antenna output that ensures a minimum signal to noise ratio SNR for obtaining the desired accuracy. Mathematically, this implies that

$$P_{\text{ant}\,(\text{dBm})} \geqslant \text{SNR}_{(\text{dB})} + P_{n\,(\text{dBm})}, \tag{1.10}$$

where:

- P_n is the noise floor of the receiver, considered spatially invariant and defined by

$$P_{n\,(\text{W})} = k_B T_0 N_f \Delta f, \tag{1.11}$$

  or, expressed in decibel,

$$\begin{aligned} P_{n\,(\text{dBm})} &= 10\log(k_B T_0) + 30\text{dB} + 10\log(N_f) + 10\log(\Delta f), \\ P_{n\,(\text{dBm})} &= -174\text{dBm.Hz}^{-1} + N_{f\,(\text{dBm})} + 10\log(\Delta f), \end{aligned} \tag{1.12}$$

  with $k_B = 1,38.10^{-23}$ J/K the Boltzmann's constant, N_f the receiver noise factor, $T_0 = 300$ K the standard noise temperature in Kelvin, and Δf the receiver equivalent noise bandwidth expressed in Hz;

- SNR is the ratio between the measured signal power P_a and the noise floor of the receiver P_n, which is expressed as follows

$$\text{SNR} = 10\log\left(\frac{P_a}{P_n}\right). \tag{1.13}$$

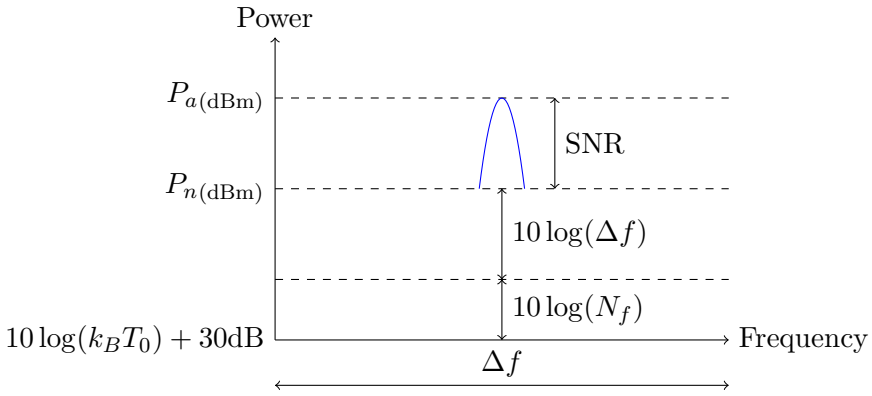

Figure 1.6: Principle of sensitivity determination

Fig. 1.6 illustrates the sensitivity determination principle. In this thesis, the 95th percentile of the Δa_{RMS} is used to specify the sensitivity of the DF antenna for a maximum error threshold of 5°.

Sensitivity is an essential characteristic of a DF system since it can be used to determine its theoretical range. In other words, it is possible to derive the maximum distance between the direction finder and the source of an EM-wave, whose DoA is estimated with a specified precision, knowing the transmission power and the sensitivity of the DF antenna. The theoretical range is established using the Friis transmission formula, which describes the free space transmission

between two spaced antennas (see Fig. 1.7). The received power at the DF antenna output P_{ant} is defined by

$$P_{\text{ant}}(\phi,\theta) = \underbrace{\frac{P_e G_e}{4\pi r^2}}_{P_s} \frac{G_r(\phi,\theta)\lambda^2}{4\pi}, \tag{1.14}$$

with P_e the power fed into the transmitting antenna input terminals, G_e the gain of the transmitting antenna, G_r the gain of the receiving antenna, r the distance between the antennas and λ the free space wavelength. This formulation assumes, on one hand, that the distance r is large enough to ensure a plane wavefront at the receiving antenna and sufficiently approximated by the Fraunhofer distance $\frac{2D^2}{\lambda}$ (where D is the is the largest linear dimension between the two antennas). On the other hand, this formula also presupposes that the polarization states of the antennas match and that there is no impedance mismatch. The range limit $r_{\max}$ is reached when the power density of the incident EM-wave P_s received by the DF antenna is equal to the sensitivity P_{sensi}, that is when

$$P_{\text{sensi}} = \frac{P_e G_e}{4\pi r_{\max}^2}. \tag{1.15}$$

Therefore, the theoretical range of a direction finder can be defined as follows

$$r_{\max} = \sqrt{\frac{P_e G_e}{4\pi P_{\text{sensi}}}}. \tag{1.16}$$

However, the theoretical range may be restricted by the radio horizon, which depends on the operational uses of the DF antenna.

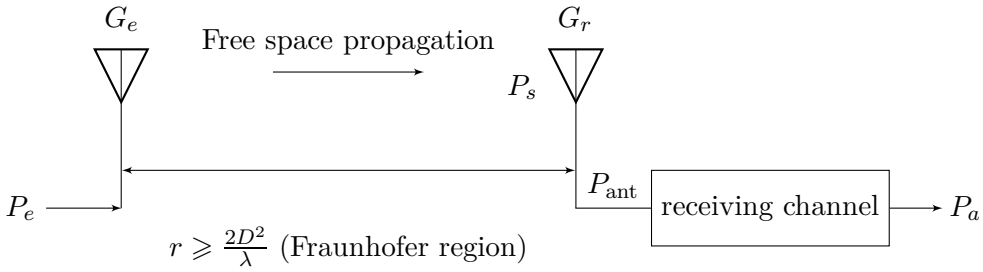

Figure 1.7: Friis transmission model

1.1.5.6 Robustness to angular ambiguity

For a given antenna array, the estimation accuracy of a direction finder can be degraded by the appearance of angular ambiguity. Generally speaking, two types of angular ambiguity can be distinguished.

The angular ambiguity of type I appears for a given DF antenna when two or more DoAs which are, sufficiently spaced apart with a relative phase-shift multiple of 2π and, present co-linear steering vectors [31, 32]. The occurrence of an angular ambiguity is related to the spatial distribution of the constitutive radiating elements of the DF antenna that enables the incident EM-wave sampling. The estimation becomes ambiguous if their relative position does not fulfill the Nyquist theorem on spatial sampling. Even if their relative position prevents sub-sampling

of the incident EM-wave, an angular ambiguity may appear due to other phenomena like the presence of inter-elements coupling or even near-field scattering. However, it is possible to evaluate the risk of angular ambiguity between two DoAs, sufficiently spaced apart, by verifying whether or not these directions provide two linearly dependent $\boldsymbol{d}(\phi_i, \theta_i)$ and $\boldsymbol{d}(\phi_j, \theta_j)$ steering vectors. This verification is performed by analyzing the value of angle $\alpha \in [0°; 90°]$ (mod 90°) between the two steering vectors [33], which is given by

$$\alpha(\phi_i, \theta_i, \phi_j, \theta_j) = \cos^{-1}\left(\frac{|\boldsymbol{d}^{\mathrm{H}}(\phi_i, \theta_i).\boldsymbol{d}(\phi_j, \theta_j)|}{\left\|\boldsymbol{d}^{\mathrm{H}}(\phi_i, \theta_i)\right\| . \|\boldsymbol{d}(\phi_j, \theta_j)\|}\right), \tag{1.17}$$

where $\boldsymbol{d}^{\mathrm{H}}(\phi_i, \theta_i)$ denotes the Hermitian conjugate (conjugate transpose) of the steering vector $\boldsymbol{d}(\phi_i, \theta_i)$. According to Eq. 1.17, two steering vectors are linearly dependent as long as

$$\alpha(\phi_1, \theta_1, \phi_2, \theta_2) = 0°, \tag{1.18}$$

and thus the risk of angular ambiguity is at its highest. Conversely, there is perfect orthogonality between them and therefore, no risk of angular ambiguity when

$$\alpha(\phi_1, \theta_1, \phi_2, \theta_2) = 90°. \tag{1.19}$$

In short, the smaller the angle α, the greater the risk of angular ambiguity. The risk of angular ambiguities in the 3-D space is usually evaluated from the 3-D spectrum of the minimum value of α between each pair of angles $(\phi_i, \theta_i, \phi_j, \theta_j)_{i \neq j}$ [14]. This method assumes that ambiguities appear for angles spaced apart by at least 15° to compute the minimum value of α. This assumption and method are retained in this thesis. Another method to assess the risk of angular ambiguities of type I in 3-D space was proposed in [34] but is more time consuming and the results analysis is less practical.

The angular ambiguity of type II occurs when several EM-waves are impinging the DF antenna with close DoA [35]. The latter is related to the separating power and, as its name indicates, corresponds to the property of detecting and separating these close EM-waves. The angular ambiguity of type II is not addressed in this Ph.D. work.

1.1.5.7 Robustness against polarization mismatch

Although dual-polarized DF systems are available, most DF systems are single-polarized. It is important to note that single-polarized direction finders are mainly vertically-polarized direction finders since most of the EM-waves emitted in the VHF and UHF bands are vertically-polarized. It is highly desired that single-polarized DF antennas present the same polarization of the incident EM-wave to avoid a polarization mismatch between them, which may degrade the DoA estimation accuracy. For instance, if a vertically-polarized DF system is employed for the estimation of the DoA of an incident horizontally-polarized EM-wave, the DF antenna will not be able to detect it, therefore, the DoA estimation will fail. This extreme situation illustrates that, depending on the polarization of the impinging EM-wave, significant degradation of the DF performances may be observed when single-polarized direction finders are used. Polarization mismatch is all the more detrimental when many obstacles surround the direction finder. Hence, it is evident that one of the greatest advantages of dual-polarized DF antennas is their capability to tackle polarization mismatch.

1.1.5.8 Robustness against multipath propagation

In operational conditions, the DF performances are degraded due to multipath propagation [36]. A phenomenon wherein the incoming EM-wave takes different paths towards the direction finder. Multipath propagation is commonly due to interactions like specular and diffuse reflection, scattering, and refraction from nearby objects such as obstacles, buildings or even trees. In a multipath scenario, the EM-wave impinging on the direction finder are a combination of multipath EM-waves that arrive from the same source through different paths, which undergo amplitude and phase alterations, and appear to be correlated as long as the excess multipath delay is lower than the inverse of the coherence bandwidth. Since DF techniques rely for instance on the hypothesis of an EM-wave presenting a plane and isophase wavefront, which is no longer necessarily the case in a multipath scenario, a degradation of the DF performance may arise. Hence, methods to mitigate these issues have been proposed. A notable example is the spatial smoothing, involving the use of a large linear array made up of multiple sub-arrays [37], which was later adapted by T. S. Shan to beamforming [38] and subspace decomposition [39] techniques.

1.2 Direction finding techniques

Several DF techniques can be implemented in the digital processing unit of the direction finder. All of them are based on the hypothesis that the incident EM-wave presents an isophase and plane wavefront. In general, the choice of one of these techniques is mainly related to the topology of the DF antenna. Furthermore, these DoA estimation techniques can be broadly classified into amplitude-based DF techniques, phase-based DF techniques, polarization-based DF techniques, maximum likelihood techniques as well as super- and high-resolution techniques.

1.2.1 Amplitude-based direction finding techniques

Amplitude-based direction finders estimate the DoA of an incident EM-wave by observing differences in amplitude at the DF antenna outputs. These direction finders rely principally on the RP of the DF antenna. Basically, amplitude-based techniques used on one of the following methods: detecting the minimum of amplitude, detecting the maximum of amplitude or comparing the amplitude between two antennas for which the RPs overlap.

- The amplitude-based DF technique that relies on detecting the minimum amplitude is the oldest approach and is based on the rotating frame designed by Bellini and Tosi. The rotating frame is used in conjunction with an electric dipole to form a “cardioid” (i.e., a heart-shaped RP, see Fig. 1.8(a)) by summing the received signals. By rotating the DF system, the null of the cardioid may be aligned with the incoming EM-wave to identify its DoA unambiguously. Considering that the pattern minimum represents a DoA indicator, this method can also be operated using a pair of rotating directional antennas. Fig. 1.8(b) gives a representation of this approach. Since the amplitude diversity is significant for directions close to the one of the minimum, the estimation accuracy of the DoA is improved.

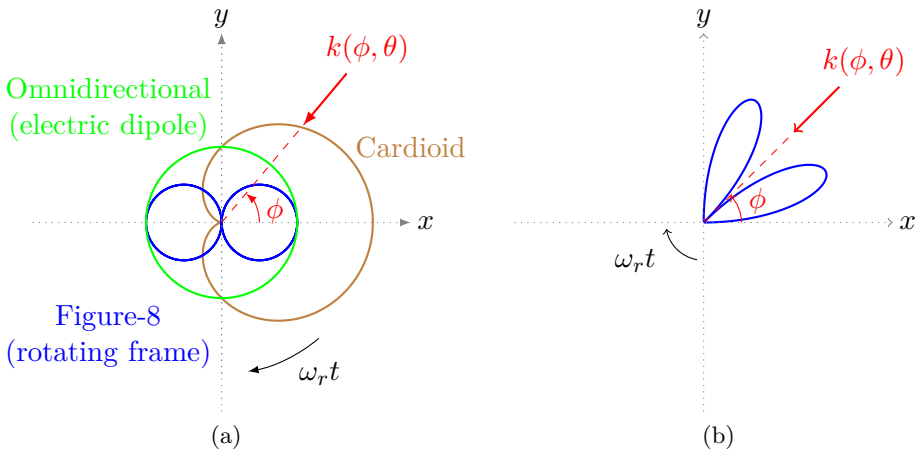

Figure 1.8: Minimum amplitude-based DF technique with: (a) the Bellini and Tosi system, (b) a pair of rotating directional antennas

- The amplitude-based DF technique that relies on detecting the maximum amplitude can be implemented effortlessly since it only required a directional antenna mounted on a rotating support. Fig. 1.9 gives an illustration of this technique. When the orientation of the antenna coincides with the DoA of the incident EM-wave, the amplitude of the output signal passes through a maximum. Nevertheless, the DoA estimation accuracy obtained from this technique is lower than the one achieved from the minimum amplitude-based approach. Indeed, there is not a wide diversity of amplitude for directions close to the one where the gain is at its maximum.

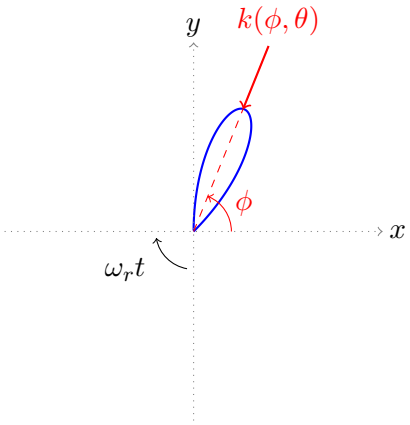

Figure 1.9: Maximum amplitude-based DF technique

- Another amplitude-based DF technique that relies on detecting the maximum amplitude is called beamforming. The principle of this technique is to use a P-port antenna array to steer or form a beam in one direction at a time and measure the power level received from this direction (or equivalently the steering angles), which reaches its maximum for the direction that coincides with the DoA of the incoming EM-wave. This steering operation towards a given direction is achieved by introducing phase shifts on the received signal at the antenna array outputs through a complex set of weightings $\boldsymbol{w}(\phi,\theta) \in \mathbb{C}^{P,1}$ (which acts like a spatial

filter) as shown in Fig. 1.10. The output signal $b(t, \phi, \theta)$ measured at time t is a weighted-sum of the signals received simultaneously at the antenna array outputs $\boldsymbol{x}(t) \in \mathbb{C}^{P,1}$, expressed as follows

$$b(t, \theta, \phi) = \boldsymbol{w}(\phi, \theta)^{\mathrm{H}} \boldsymbol{x}(t). \tag{1.20}$$

As previously stated, the objective of a beamformer is to find the direction for which the output power is maximum, or equivalently, find the maximum of the power spectrum $P_{\text{beamforming}}$ defined by

$$\begin{aligned} P_{\text{beamforming}}(\boldsymbol{w}(\phi, \theta)) &= \frac{1}{N} \sum_{n=1}^{N} |b[t_n]|^2 , \\ &= \frac{1}{N} \sum_{n=1}^{N} \boldsymbol{w}(\phi, \theta)^{\mathrm{H}} \boldsymbol{x}[t_n] \boldsymbol{x}^{\mathrm{H}}[t_n] \boldsymbol{w}(\phi, \theta), \\ &= \boldsymbol{w}(\phi, \theta)^{\mathrm{H}} \left(\frac{1}{N} \sum_{n=1}^{N} \boldsymbol{x}[t_n] \boldsymbol{x}^{\mathrm{H}}[t_n] \right) \boldsymbol{w}(\phi, \theta), \\ &= \boldsymbol{w}(\phi, \theta)^{\mathrm{H}} \hat{\mathbf{R}_{\boldsymbol{X}}} \boldsymbol{w}(\phi, \theta), \end{aligned} \tag{1.21}$$

where $\hat{\mathbf{R}_{\boldsymbol{X}}}$ denotes the estimate of the spatial covariance matrix of $\boldsymbol{x}[t_n]$ over N snapshots. The weighting coefficients of the conventional beamformer, also called Bartlett beamformer, are given by

$$w_{\text{Bartlett}}(\phi, \theta) = \frac{\boldsymbol{d}(\phi, \theta)}{\sqrt{\boldsymbol{d}^{\mathrm{H}}(\phi, \theta) \boldsymbol{d}(\phi, \theta)}}. \tag{1.22}$$

By substituting the weight vector of Eq. 1.22 into Eq. 1.21, the conventional power spectrum is expressed as

$$P_{\text{Bartlett}}(\phi, \theta) = \frac{\boldsymbol{d}^{\mathrm{H}}(\phi, \theta) \hat{\mathbf{R}_{\boldsymbol{X}}} \boldsymbol{d}(\phi, \theta)}{\boldsymbol{d}^{\mathrm{H}}(\phi, \theta) \boldsymbol{d}(\phi, \theta)}. \tag{1.23}$$

The implementation of this method is reasonably straightforward. However, to obtain a sufficiently fine antenna beam and therefore a good DoA estimation accuracy, a large number of antenna elements is required. Originally, beamforming was achieved through fixed delays prearranged in the antenna array design coupled with mechanical steering, while modern beamformers are steered electronically.

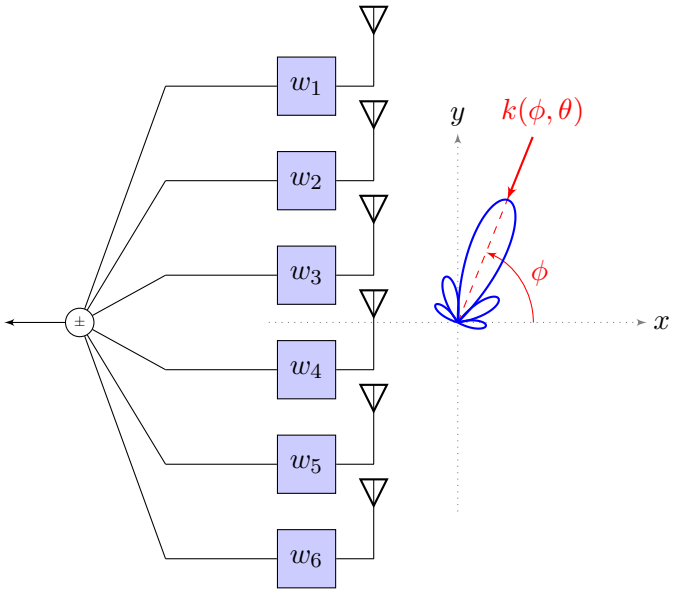

Figure 1.10: Beamforming principle using a 6-port antenna array

- Another amplitude-based DF method is the so-called Watson-Watt DF technique, named after its eponymous inventor. It is one of the oldest DoA estimation methods since it was invented in the 1920s. It enables the spatial sampling of an incident EM wave using two orthogonal antennas whose RPs present a sine-shaped and a cosine-shaped, respectively. The amplitude ratio between the two antenna outputs $V_{\sin}$ and $V_{\cos}$ is $\tan(\phi)$ and, therefore, the relation

$$\phi = \arctan\left(\frac{V_{\sin}}{V_{\cos}}\right) \pm \pi, \tag{1.24}$$

  permits the estimation of the azimuth angle ϕ. However, this estimation is ambiguous since the tangent function is π-periodic. An unambiguous DoA estimation is obtained if an omni-directional antenna is additionally positioned at the geometric center of the array to supply a phase reference.

  The first directions finders using this method consisted of two orthogonal loop antennas. Although this is one of the oldest DF techniques, it is still being employed through Adcock arrays composed of four or eight elements. Fig. 1.11 gives an illustration of these arrays. More specifically, the Adcock array is a circular array of diameter d composed of 4 or 8 equidistant vertical dipoles (or monopoles) from which it is possible to synthesize the outputs $V_{\cos}$ and $V_{\sin}$ (which correspond to the RPs in cosine-shaped and sinus-shaped, respectively) by combining the antenna outputs. For the 4-element Adcock array, the outputs $V_{\cos}$ and $V_{\sin}$ are defined by

$$\begin{aligned} V_{\cos} &= 2jA\,\mathrm{e}^{-j\pi\frac{d}{\lambda}} \sin\left(2\pi\frac{d}{\lambda}\cos(\phi)\right), \\ V_{\sin} &= 2jA\,\mathrm{e}^{-j\pi\frac{d}{\lambda}} \sin\left(2\pi\frac{d}{\lambda}\sin(\phi)\right), \end{aligned} \tag{1.25}$$

  where A is the amplitude of the received signal, λ is the free-space wavelength corresponding

to the operating frequency. For the 8-element Adcock array, they are defined as follows

$$\begin{aligned} V_{\cos} &= A \sin\left(\pi \frac{d}{\lambda} \cos(\theta)\cos(\phi)\cos\left(\frac{\gamma}{2}\right)\right) \cos\left(\pi \frac{d}{\lambda} \cos(\theta)\sin(\phi)\sin\left(\frac{\gamma}{2}\right)\right), \\ V_{\sin} &= A \sin\left(\pi \frac{d}{\lambda} \cos(\theta)\sin(\phi)\cos\left(\frac{\gamma}{2}\right)\right) \cos\left(\pi \frac{d}{\lambda} \cos(\theta)\cos(\phi)\sin\left(\frac{\gamma}{2}\right)\right), \end{aligned} \tag{1.26}$$

with γ the half-angle between two elements constituting the array. Assuming $d \ll \lambda$, Eq. 1.25 and Eq. 1.26 can be simplified to

$$\begin{aligned} |V_{\cos}| &= 4\pi A \frac{d}{\lambda} |\cos(\phi)|, \\ |V_{\sin}| &= 4\pi A \frac{d}{\lambda} |\sin(\phi)|, \end{aligned} \tag{1.27}$$

as part of the 4-element Adcock array and by

$$\begin{aligned} |V_{\cos}| &= A\pi \frac{d}{\lambda} \left|\cos(\theta)\cos(\phi)\cos\left(\frac{\gamma}{2}\right)\right|, \\ |V_{\sin}| &= A\pi \frac{d}{\lambda} \left|\cos(\theta)\sin(\phi)\cos\left(\frac{\gamma}{2}\right)\right|, \end{aligned} \tag{1.28}$$

as part of the 8-element Adcock array. Hence, it is possible to retrieve the azimuth angle of the incoming EM-wave using Eq. 1.24.

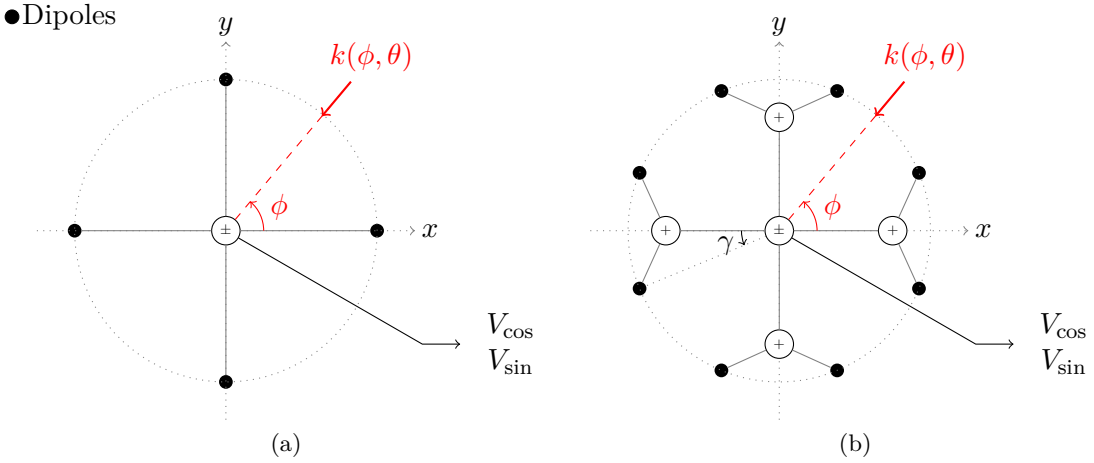

Figure 1.11: Watson-Watt technique with (a) 4-element and (b) 8-element Adcock arrays

This method presents a significant drawback since it involves small-aperture[1] direction finders causing estimation errors in the presence of multipath propagation.

[1]Classical Watson-Watt direction finder with crossed loop antenna is considered as a small-aperture system since $\frac{D}{\lambda} \leqslant 0.2$. However, wider aperture direction finders can be implemented to overcome this issue (e.g., 8-element Adcock array with $\frac{D}{\lambda} \leqslant 1$).

1.2.2 Phase-based direction finding techniques

Generally, the phase-based DF techniques achieve a better DoA estimation accuracy than amplitude-based techniques if the incoming EM-wave comes from the same angular area and is measured using the same number of sensors. However, amplitude-based direction finders are still widely employed due to their lower complexity and cost. Two main phase-based direction finders are explained hereinafter.

1.2.2.1 Doppler direction finder

Doppler direction finders appeared in the 1940s. This kind of direction finders is based, as its name indicated, on a phenomenon called the Doppler effect. This latter is also named after the physicist C. Doppler who discovered the frequency change whenever the source of a wave is moving with respect to an observer in 1842. As illustrated in Fig. 1.12, original Doppler direction finders estimate the DoA by measuring the Doppler shift induced on the signal that is received by one antenna physically rotated around a reference antenna [40]. Indeed, as the rotated antenna moves toward the source, the received frequency increases, and as it moves away, it decreases. Let us assume that an omnidirectionnal antenna which rotates on a circle of radius R is sensing an incident EM-wave. The received signal $x_{\text{rot}}(t)$ with carrier frequency f_0 is frequency-modulated with the rotational frequency w_r of the antenna and can be described as follows

$$x_{\text{rot}}(t) = A\cos\left(2\pi f_0 t + \varphi + m(t)\right), \tag{1.29}$$

with A the amplitude of the received signal, φ the phase of the signal and

$$m(t) = \frac{2\pi R}{\lambda_0}\cos\left(\theta\right)\cos\left(w_r t - \phi\right). \tag{1.30}$$

It can be noted that the modulating signal $m(t)$ contains the azimuth ϕ as a simple phase shift, thus comparing it after demodulation with the signal received by the reference antenna

$$x_{\text{ref}}(t) = A\cos\left(2\pi f_0 t + \varphi\right), \tag{1.31}$$

enables the derivation of the DoA for small elevation angles θ. In practical systems, the rotating motion of the antenna can be replaced by a circular array of several antennas (usually four, eight, or sixteen) that are sequentially switched into the receiver. The sequential switching of the antenna array avoids the rotation of the antenna, which is not always mechanically possible (a sufficiently high rotational frequency is often required) or desirable. Direction finders using this technique are referred to as pseudo-Doppler direction finders.

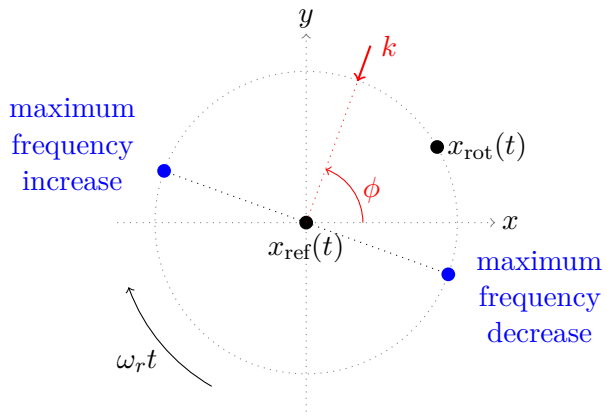

Figure 1.12: Principle of Doppler direction finder

1.2.2.2 Interferometer

Interferometers are DF systems based on interferometry. This DF technique can be considered as the most efficient among those previously described [41]. Unlike the aforementioned techniques, the DoA estimation is not entirely analog and requires digital processing, more or less complicated, depending on the antenna array configuration. This technique could therefore only be implemented once microprocessors had arrived in the early 1980s. The DoA estimation of an incoming EM-wave is derived from the propagation phase delay between two or more spatially separated antennas.

For the sake of simplicity, let us consider the antenna array, depicted in Fig. 1.13(a), which includes only two dipoles separated by a distance d. Interferometry consists of measuring the phase of a received signal at each antenna and deriving the DoA from the difference between them. Mathematically, the phase difference $\delta\varphi$ between dipoles A and B, is expressed as follows

$$\delta\varphi = \frac{2\pi d}{\lambda_0}\sin(\phi)\sin(\theta) \pmod{2\pi}. \tag{1.32}$$

The benefit of interferometry is its applicability to different antenna array topologies, some examples are illustrated in Fig. 1.13(b). However, an unambiguous estimate of the DoA requires a minimum of 3 antenna elements. These elements must not be all located on the same plane and the distance between the elements must be less than $\frac{\lambda_0}{2}$. Moreover, the topology, spacing, and number of array elements condition the protection from angular ambiguity as well as the DoA estimation accuracy.

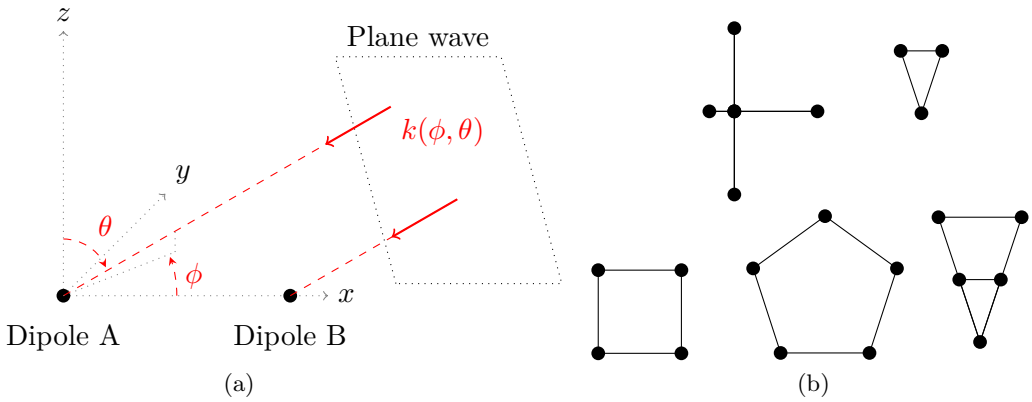

Figure 1.13: Interferometry: (a) principle and (b) examples of commonly used interferometers

1.2.3 Polarization-based techniques

The previously-cited DF standard techniques are based on the spatial distribution of an antenna array and are generally used for DF with a 2-D angular coverage. Such antenna array is commonly referred to as a uniformly polarized array or scalar array. However, the extension of the spatial diversity technique for DF with a 3-D coverage is not straightforward. The antenna design becomes too complex and cumbersome to estimate the DoA in the entire space.

Another main DF technique consists of deriving the DoA from the measurement of the six components of the EM-wave through a Vector Antenna (VA). This technique is therefore based on polarization diversity. Typical VAs are composed of three electric dipoles and three magnetic dipoles, all spatially colocated with orthogonal orientations (see Section 2.1 for further details on VAs). Since all the components are measured, one of the main advantages of VAs is their ability to estimate the DoA of any incoming EM-wave across the whole 3-D space, regardless of its polarization.

By measuring the incoming EM-wave in terms of its six individual EM components, the VA physically gathers the full data necessary to estimate the Poynting-vector, via a simple vector cross-product between the electric-field vector $\boldsymbol{E}$ and the magnetic-field vector $\boldsymbol{H}$. This estimated Poynting-vector $\mathbf{p}$, when normalized gives the direction-cosines of the incoming EM-wave and therefore the elevation and azimuth angles can be deduced.

For an incoming unit-power EM-wave, the electric-field vector $\boldsymbol{E}$ and magnetic-field vector $\boldsymbol{H}$ can be described in the spherical coordinate system as follows [42]

$$\begin{aligned} \boldsymbol{E} &= \sin(\gamma)e^{j\eta}\hat{\theta} + \cos(\gamma)\hat{\phi}, \\ \boldsymbol{H} &= \frac{1}{\zeta}\left(-\cos(\gamma)\hat{\theta} + \sin(\gamma)e^{j\eta}\hat{\theta}\right), \end{aligned} \tag{1.33}$$

where ζ is the intrinsic impedance of the medium. In the Cartesian coordinate system (refer to

Fig. 1.1 for its definition) and after normalization, it can be expressed as

$$\begin{aligned} \boldsymbol{e} = & \left(\cos(\phi)\cos(\theta)\sin(\gamma)e^{j\eta} - \sin(\phi)\cos(\gamma)\right)\hat{x} \\ & + \left(\sin(\phi)\cos(\theta)\sin(\gamma)e^{j\eta} + \cos(\phi)\cos(\gamma)\right)\hat{y} \\ & - \sin(\theta)\sin(\gamma)e^{j\eta}\hat{z}, \\ \boldsymbol{h} = & -\left(\sin(\phi)\sin(\gamma)e^{j\eta} + \cos(\phi)\cos(\theta)\cos(\gamma)\right)\hat{x} \\ & + \left(\cos(\phi)\sin(\gamma)e^{j\eta} - \sin(\phi)\cos(\theta)\cos(\gamma)\right)\hat{y} \\ & + \sin(\theta)\cos(\gamma)\hat{z}. \end{aligned} \tag{1.34}$$

Hence, the normalized Poynting vector is expressed as follows

$$\begin{aligned} \mathbf{p} &= \boldsymbol{e} \times \boldsymbol{h}^*, \\ &= \begin{bmatrix} u \\ v \\ w \end{bmatrix} = \begin{bmatrix} \sin(\theta)\cos(\phi) \\ \sin(\theta)\sin(\phi) \\ \cos(\theta) \end{bmatrix}, \end{aligned} \tag{1.35}$$

where the superscript * and $\times$ denote the complex conjugation and the vector cross-product operator. In Eq. 1.35, u, v and w are the direction-cosines of the incident EM-wave along the $\hat{x}$-axis, the $\hat{y}$-axis, and the $\hat{y}$-axis, respectively. After deriving the DoA of the incoming EM-wave, the polarization state (γ,η) could also be estimated.

1.2.4 Super- and high-resolution techniques

Super- and high-resolution methods include all the DF methods that achieve better accuracy for DoA estimation compared to those mentioned above such as Watson-Watt technique, interferometry, or even classical beamforming. Furthermore, super- and high-resolution methods enable to estimate the DoA of several EM-waves impinging the DF antenna. This ability depends substantially on the number of elements in the antenna array, the angular spacing between the sources, and on the signal and noise characteristics.

1.2.4.1 Capon's minimum variance distortionless response method

The best-known super-resolution method is the Capon beamforming technique which was originally developed in the late 1960s to analyze seismic data [43]. Capon beamformer is similar to the conventional Bartlett beamformer (described in Section 1.2.1) but exhibits a better capability to separate two EM-waves presenting nearby DoA. Capon's method consists of minimizing the power contributed by the noise or any interferences coming from other directions than the one observed. This is done through the formation of nulls in these directions while maintaining a unitary gain in the steering direction. Mathematically, this problem is posed as

$$\min_{\boldsymbol{w}(\phi,\theta)} P_{\text{beamforming}}(\boldsymbol{w}(\phi,\theta)) \text{ subject to } \boldsymbol{w}(\phi,\theta)^{\text{H}}\boldsymbol{d}(\phi,\theta) = 1. \tag{1.36}$$

The solution to this optimization problem is given by

$$w_{\text{Capon}}(\phi,\theta) = \frac{\hat{\mathbf{R}_{\boldsymbol{X}}}^{-1}\boldsymbol{d}(\phi,\theta)}{\boldsymbol{d}^{\text{H}}(\phi,\theta)\hat{\mathbf{R}_{\boldsymbol{X}}}^{-1}\boldsymbol{d}(\phi,\theta)}. \tag{1.37}$$

By substituting the weight vector of Eq. 1.37 into Eq. 1.21, the Capon power spectrum is expressed as

$$P_{\text{Capon}}(\phi,\theta) = \frac{1}{\boldsymbol{d}^{\text{H}}(\phi,\theta)\hat{\mathbf{R}_{\boldsymbol{X}}}^{-1}\boldsymbol{d}(\phi,\theta)}. \tag{1.38}$$

Furthermore, this weight vector is often referred to as the minimum variance distortionless response (MVDR), which is the other name of the Capon's method. Indeed, for the direction of interest, it minimizes the variance (i.e., the average power) of the array while normalizing the beam pattern in the steered direction. Therefore, Capon beamformers can be seen as spatial filters with narrow bandpass. Finally, they are designed using a large number of antennas since the number of available nulls is related to this number.

1.2.4.2 Subspace decomposition method

Subspace-based DoA estimation algorithms are high-resolution techniques based on the concept of signal and noise subspaces. These subspace-based DoA estimators have gained a significant attention since their introduction in the early 1980s as they are more efficient, offer higher resolutions, and were shown to be consistent[2]. One of the most popular subspace-based methods is the multiple signal classification (MUSIC) algorithm proposed by R. Schmidt in 1986 [31], which is detailed in Appendix A. Another subspace-based DOA estimation algorithms providing a significantly improved DF performance as compared to the MUSIC algorithm have been reported. Among them are the estimation of signal parameters via rotational invariance technique (ESPRIT) [44] as well as the root-MUSIC [45, 46] algorithm.

1.2.5 Maximum likelihood techniques

The last category of DoA estimators is the Maximum Likelihood (ML) techniques, which exploit the statistical properties of received signals [47,48]. Notwithstanding ML techniques are superior to other estimators in terms of performance (especially at low SNR conditions), they are less popular than other techniques since they are computationally intensive. ML techniques estimate the DoA of incident EM-waves from a given set of observations by maximizing the likelihood function (or equivalently the log-likelihood function) of the received data $\boldsymbol{x}(t)$, which means in essence, choosing the parameter vector that makes the data actually observed as likely as possible. Mathematically, the ML estimator is the value $\hat{\boldsymbol{\Omega}}$ such that

$$l(\boldsymbol{x},\hat{\boldsymbol{\Omega}}) \geqslant l(\boldsymbol{x},\boldsymbol{\Omega}) \text{ for all } \boldsymbol{\Omega}. \tag{1.39}$$

Furthermore, the ML estimator is asymptotically unbiased and efficient, which means that the performance of the ML processor is very close to the CRB.

[2]In statistics, a consistent estimator is an estimator that converges to the actual value of the estimated parameter when the number of measured data increases indefinitely

1.3 Direction finding antennas

Recently, there has been a surge of interest in designing DF antennas as they are the key element of a DF system. This section provides a state of the art of the DF antennas available on the industrial market and in the literature. The purpose of this survey is to identify the variety of DF antennas in terms of angular coverage, frequency coverage, polarization, and overall dimensions. Moreover, this census can best be treated under three headings: DF antennas with 2-D angular coverage, DF antennas with limited 3-D angular coverage and DF antennas with 3-D angular converage.

1.3.1 Direction finding antennas with 2-D angular coverage

DF antennas with 2-D angular coverage are the most widespread. Among them, it is possible to draw a distinction between stationary and mobile DF antennas. Table 1.2 and Table 1.3 show a sample of these. For the first case, the DF antenna is installed at a fixed site (e.g., a mast) or can be used as a part of a ground deployed array. For the second case, the DF antenna is directly mounted on carriers (e.g., on the roof of a car, fuselage of an aircraft or a helicopter). Closer inspection of the electrical size of the antennas reported in Table 1.2 and Table 1.3 shows that mobile DF antennas are generally smaller than stationary in order to facilitate their integration on carriers. Active antennas are generally used on these antennas for maintaining the DF antenna compact while covering the lowest frequencies. However, active antennas exhibit strong limitations (see Section 1.3.3.2). Some DF antennas, whether stationary or mobile, are divided into sub-antenna systems to achieve wideband coverage, each system covering a part of the frequency range. A number of mobile DF antennas are designed using both techniques. In addition to providing wideband coverage, this enables the design of DF antennas presenting diameters less than $\lambda/10$. For higher operating frequencies, the compactness constraint may be loosened given the small size of the antennas. On another note, vertically-polarized EM-waves carry the majority of the transmitted signals of relevant communications emitted in the HF, VHF and UHF bands. As a result, each of these direction finders is at least able to estimate the DoA of incoming vertically-polarized EM-waves. However, most current DF antennas are dual-polarized to meet the growing demand that appeared a few years ago to estimate the DoA of horizontally-, even circularly- or elliptically-polarized EM-waves [49]. As the polarization of the transmitter is in general not known, dual-polarized DF antennas ensure adaptability to all situations and applications.

Stationary DF antennas			
Constructor / Reference	Frequency coverage	Polarization	Dimensions[a]
ALARIS / DF-A0031 [50]			
	20 MHz - 300 MHz (Band 1) 300 MHz - 1000 MHz (Band 2) 1000 MHz - 3600 MHz (Band 3)	Vertical	D = 2.5 m (λ/5.9) H = 3.8 m (λ/3.9)
ALARIS / DF-A0049 [51]			
	1 MHz - 30 MHz	Vertical LHCP RHCP [b]	D = 1.9 m (λ/157.8) [c] H = 2.25 m (λ/133.2)

Table 1.2: Examples of stationary DF antennas presenting a 2-D angular coverage

[a] D (diameter) and H (height) are given in terms of free-space wavelength at the lowest operating frequency

[b] LHCP and RHCP (left and right hand circular polarization)

[c] This DF antenna needs to be deployed as part of either a linear or circular array. Therefore, the overall diameter will be increased.

Mobile DF antennas			
Constructor / Reference	Frequency coverage	Polarization	Dimensions
R&S / ADD253 [3]			
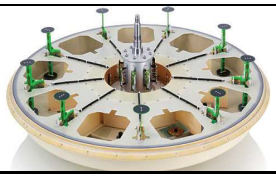	20 MHz - 1300 MHz (Band 1) 1300 MHz - 3000 MHz (Band 2)	Vertical	D = 1.1 m (λ/13.6) H = 0.45 m (λ/33.3)
R&S / ADD170 [52]			
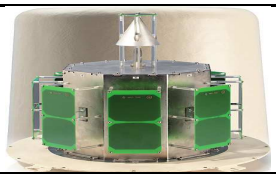	800 MHz - 2000 MHz	Vertical	D = 0.45 m (λ/0.8) H = 0.39 m (λ)
THALES / ANT-184 [49]			
	20 MHz - 700 MHz 700 MHz - 3000 MHz	Vertical	D = 1.1 m (λ/13.6) H = 0.38 m (λ/39.4)
PhD works in collaboration with THALES / enhancement of ANT-184 [49]			
	30 MHz - 500 MHz 500 MHz - 3000 MHz	Vertical Horizontal	D = 1.1 m (λ/9.1) H = 0.38 m (λ/26.3)
PhD works in collaboration with THALES [49]			
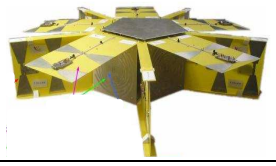	30 MHz - 500 MHz 500 MHz - 3000 MHz	Vertical Horizontal	D = 1.2 m (λ/8.3) H = 0.38 m (λ/26.3)
PhD works in collaboration with THALES [53]			
	500 MHz - 3000 MHz	Vertical Horizontal	D = 0.26 m (λ/2.3) H = 0.15 m (λ/4)
TCI / Model 643 [5]			
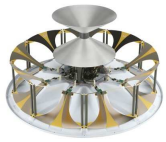	20 MHz - 3000 MHz (Band 1) 40 MHz - 2400 MHz (Band 2)	Vertical (Band 1) Horizontal (Band 2)	D = 1.3 m (λ/11.5 at 20 MHz) H = 0.7 m (λ/21.4 at 20 MHz)
CRFS / RFeye Array 300 [4]			
	300 MHz - 8000 MHz	Vertical Horizontal	D = 1.1 m (λ/0.9) H = 0.8 m (λ/1.3)

Table 1.3: Examples of mobile DF antennas presenting a 2-D angular coverage

1.3.2 A word on solutions that slightly improve the angular coverage

There are a tremendous number of dual-polarized DF antennas whose purpose is to estimate the DoA of incoming EM-waves only on a 2-D angular coverage, meaning that only the azimuth or elevation angle can be measured according to the DF antenna position (see Section 1.3.1). For the sake of simplicity, let us consider one of these DF antennas installed to estimate the azimuth angle of incoming EM-waves. Looking at Fig. 1.14, the DoA of an incoming EM-wave can be evaluated with ease if the radiating source is located in the same plane of the DF antenna. However, when this is not the case, the DoA can rarely be estimated. Indeed, as it can be observed, there is a blind zone in which the DoA of incoming EM-waves cannot be measured since the DF antenna presents a 2-D angular coverage (i.e., usually the antenna exhibits a RP which is omnidirectional in the azimuth plane and null at low elevation angles).

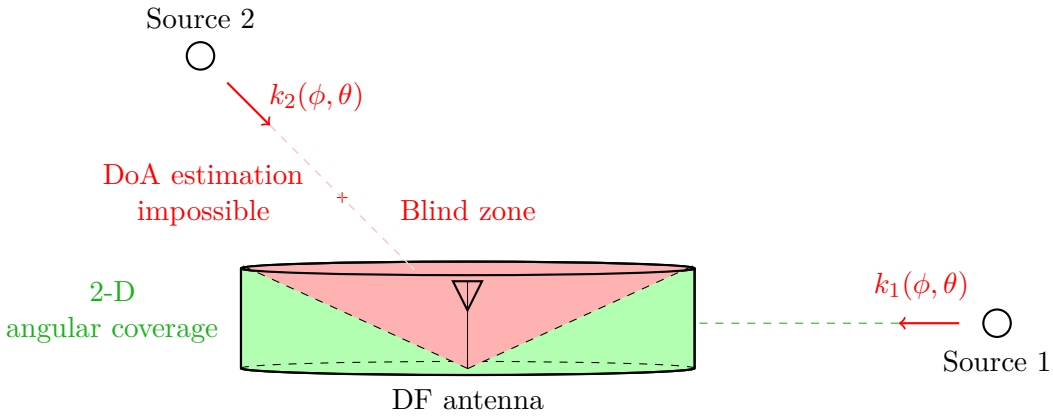

Figure 1.14: Blind zone of a DF antenna presenting a 2-D angular coverage

In the last few years, some DF antennas offering a wider angular coverage have appeared, such as the ones set out in Table 1.4. For instance, the DF antenna developed for the LUTECE project (*Localisation d'Urgence de Téléphone Cellulaire*) consists of a circular array of five dual-band patch antennas covering the uplink bands for GSM (Global System for Mobile Communications) and DCS (Digital Cellular System) standards. This antenna can be mounted on the fuselage of a helicopter [54]. As its name suggests, this DF antenna is dedicated to the emergency localization of cellular phones of persons in distress. The DF antenna designed under the STARRS (Sensor for Terrestrial and Airborne Radio-transmitter Rescue Search) project was conceived in the same vein and for the same application purpose [55]. Unlike the two previous multiband DF antennas, the third antenna depicted in Table 1.4 operates over a wider frequency range using a spiral antenna with four modulated arms [56]. These antennas are intended to be mounted on a carrier and exhibit directive RPs pointing towards $\theta = 0°$. It can be seen from Fig. 1.15 that the blind zone for DF antenna with limited 3-D angular coverage is therefore located for elevation angles close to 90°.

Research project	Frequency coverage	Polarization	Angular coverage	Dimensions[a]
LUTECE project [54]				
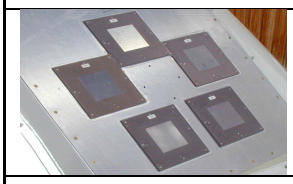	890 MHz - 915 MHz (Band 1) 1710 MHz - 1785 MHz (Band 2)	N/A [b]	$\theta \in [-60°; 60°]$ $\phi \in [-60°; 60°]$	L= 0.8 m (λ/0.42) W = 0.8 m (λ/0.42)
STARRS project [55]				
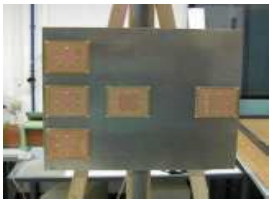	890 MHz - 915 MHz (Band 1) 1710 MHz - 1785 MHz (Band 2) 1920 MHz - 1980 MHz (Band 3)	N/A	$\theta \in [-60°; 60°]$ $\phi \in [-60°; 60°]$	L = 0.8 m (λ/0.42) W = 0.8 m (λ/0.42)
PhD works [56]				
	1200 MHz - 5500 MHz	Vertical Horizontal	$\theta \in [-30°; 30°]$ $\phi \in [0°; 360°]$	D = 0.095 m (λ/2.63)

Table 1.4: Examples of DF antennas presenting a limited 3-D angular coverage

[a] L (length) and W (width)
[b] Not Available

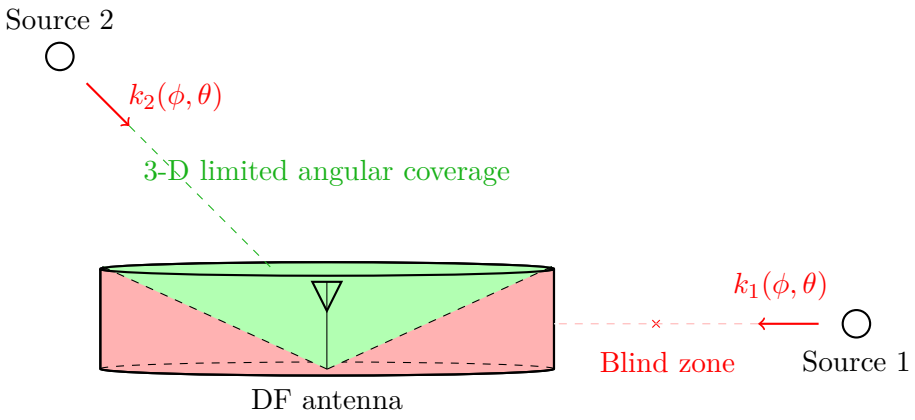

Figure 1.15: Blind zone of a DF antenna presenting a limited 3-D angular coverage

1.3.3 Solution to the 3-D angular coverage deficiency, the vector antenna

DF antennas with 3-D angular coverage can estimate the DoA of incident EM-waves across the entire 3-D space (or the upper hemisphere if the antenna is mounted on carrier). Hence, they overcome blind zones in which the DoA cannot be estimated (see Fig. 1.16). Over the years, only a few DF antennas offering a 3-D angular coverage have appeared, such as the ones set out in Table 1.5. In the 1960s, the University of Michigan demonstrated the feasibility to develop a wideband DF antenna with a complete hemisphere coverage employing sixteen

circularly polarized radiating elements (log conical or spiral antennas) mounted on a spherical surface [57, 58]. However, the main drawback of this DF antenna is its bulky structure. Most recently, the German company Aaronia has put on the market a 3-D DF antenna [59] in 2016, named IsoLOG 3D, covering a wide frequency band from 680 MHz to 20 GHz and designed from a customizable array of vertically- and horizontally-polarized directional log-periodic antennas. Additionally, eight or sixteen active low-frequency antennas can be added to extend the frequency range down to 20 MHz, which can bring the total up to sixty-four independent antennas. This antenna is very interesting from its compactness and vast operating bandwidth. Nevertheless, it only enables sectoral 3-D DF, which means that the DoA of an incoming EM-wave is estimated in one of the angular sectors used for the 3-D angular sectoring.

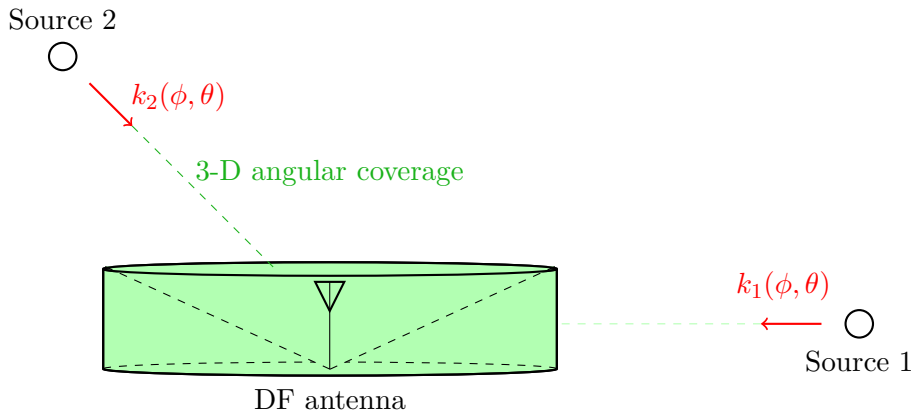

Figure 1.16: Removal of blind zone with a DF antenna presenting a 3-D angular coverage

Reference	Frequency coverage	Polarization	Dimensions
Michigan university project [57, 58]			
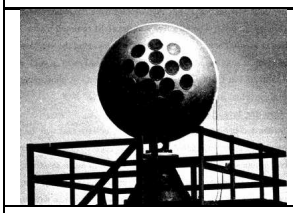	600 MHz - 3000 MHz	Circular	D = 1.8 m (λ/0.28) H = 0.9 m (λ/0.55)
IsoLOG 3D [59]			
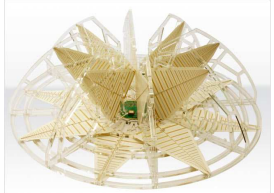	680 MHz - 20000 MHz	Vertical Horizontal	L = 0.96 m (λ/0.49) W = 0.96 m (λ/0.49) H=0.38m (λ/1.16)

Table 1.5: Examples of DF antennas presenting a 3-D coverage

Previous DF antenna designs are based on a tremendous number of radiating elements, resulting in direction finders being complex, bulky and difficult to design. Another approach for developing DF antennas that provide 3-D coverage was proposed in the early 1990s. This approach is based on using a VA, which consists of spatially colocated polarization-sensitive radiating elements (see Section 1.2.3 and Section 2.1 for more information). One of the significant assets of VAs is the colocation of the radiating elements that yields to compact direction finders. A commercially

available example of VA is the SuperCART array, manufactured by Flam and Russell [60] and patented in 1994 [61]. A photograph of the SuperCART array is given Fig. 1.17.

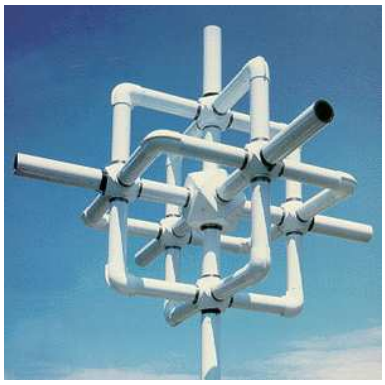

Figure 1.17: SuperCART VA

1.3.3.1 Existing vector antenna designs

Since 1994, many VA designs were reported for estimating the DoA of impinging EM-waves (see, e.g., [12–14, 62–66]). However, only few designs demonstrated the capability of covering the full 3-D space (or the upper hemisphere if the antenna is mounted on carrier) [12–14, 65, 66] which are set out Table 1.6. The first VA [12, 65] is manufactured by the ELTA subsidiary of IAI (Israel Aerospace Industries) and was patented in 2013. It consists of a remarkably compact active solution, composed of three electric dipoles nested in three magnetic sensors (made by slot antennas), and aimed at covering frequencies below 30 MHz. However, considering the applications in this part of the EM spectrum (see Table 1.1), it can be noted that only a small part of the existing applications is covered by this DF antenna. The second VA [13] is another interesting active solution combining three small loops. These loops can operate either as an electric dipole or as a magnetic dipole from excitation control. There is no concrete information on its bandwidth except that it is intended to cover the VHF band. The third VA [66] is a passive solution operating at 2.8 GHz, which combines two half-loops and one monopole. The fourth VA [14] is another passive solution designed using dual-band folded-monopoles and loaded half-loops in order to operate in two separate narrow bandwidths for GSM and DCS standards. The two previously described passive VAs are mounted on a metallic plate in view of embedded applications, therefore all the components of incoming EM-waves cannot be measured. However, measuring fewer than six components (only three with these antenna topologies) is sufficient to estimate the DoA of vertically-polarized EM-waves [14, 66].

Reference	Frequency coverage	Polarization	Dimensions
IAI / ELK-7065 [12, 65]			
	2 MHz - 30 MHz	Linear	L = 0.5 m (λ/300) W = 0.3 m (λ/500)
Research works [13]			
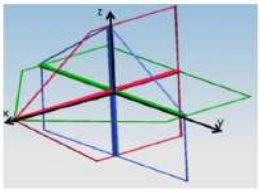	N/A	Linear	L = 0.35 m W = 0.35 m H = 0.35 m
PhD works in collaboration with Rockwell Collins [66]			
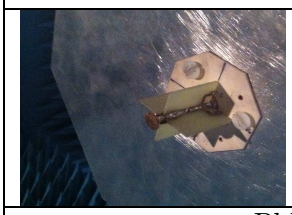	2800 MHz	Vertical	D = 0.025 m (λ/4.28) H = 0.037 m (λ/2.89) [a]
PhD works in collaboration with Rockwell Collins [14]			
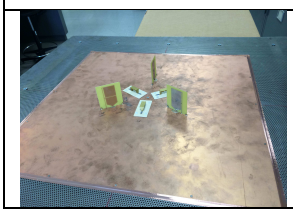	890 MHz - 965 MHz (Band 1) 1710 MHz - 1880 MHz (Band 2)	Vertical	D = 0.17 m (λ/1.98) H = 0.06 m (λ/5.61) [b]

Table 1.6: VAs presenting a 3-D angular coverage

[a] VA mounted on an octagonal ground plane with a circumcicle diameter of 0.32 m (λ/0.34)
[b] VA mounted on a square ground plane of side 0.8 m (λ/0.42)

1.3.3.2 Active versus passive direction finding antennas

Looking at Table 1.6, it is apparent that the attention is mainly focused on the implementation of active structures when designing VAs with 3-D angular coverage. The reasons for this are obvious since active structures permit wideband capabilities while keeping small dimensions, which are generally essential requirements. By definition, an active antenna is a radiating element connected to an active device or circuitry that is located directly at the radiator. This active part of the antenna system is primarily used for impedance matching. Consequently, the bandwidth of the antenna is increased thanks to the impedance transformation capability of the active device. In contrast, a passive antenna is a radiating element with or without a passive matching network to match the cable and receiver impedance.

Further benefits of active antennas are reasonable sensitivity with respect to the physical size and the environmental noise, and the fact that the RP is almost constant over the operating frequency range. Moreover, due to the generally short dimensions of the radiating element and

the fact that it is not resonant, an active antenna shows less EM coupling to the immediate surroundings. Therefore, it is possible to have closer spacing with other antenna structures, resulting in a more compact system. However, there are also certain drawbacks. Active antennas can only be used for reception. Although this is not a constraint for designing a DF antenna, it is for a wide range of other applications. Indeed, they are not reciprocal since they always need a power supply device and contain non-linear components which might lead to linearity problems (intermodulation products, harmonics generation, signal distortion, etc.). These phenomena occur since the filtering prior to the active device is usually not possible, which most often results in a reduction of the dynamic range. Finally, much effort needs to be devoted to the design of the active circuitry to prevent these linearity problems [67,68]. These circuits are tuned to a given frequency band and are not easily adaptable to other bands. On the contrary, fully passive VAs do not suffer from these limitations, but the wideband coverage is very challenging to achieve. The advantages of active antennas are the disadvantage of passive antennas and vice-versa. Table 1.7 summarizes the benefits and drawbacks of these antennas.

	Benefits	Drawbacks
Active antennas	• Wideband coverage • Significant size reduction • Reasonable sensitivity • Constant RP • Less EM Coupling	• Only suitable for reception applications • Active device required • Tricky circuit design • Linearity problem • Poor adaptability
Passive antennas	• Highest sensitivity • Reciprocal • Good adaptability • No active circuit required	• Wideband coverage is hard to obtain • Large size • Frequency-dependent RP

Table 1.7: Benefits and drawbacks of active and passive antennas

1.3.3.3 Multiband versus wideband direction finding antennas

Looking at Table 1.1, it can be seen that DF applications are spread over a large part of the EM spectrum. Through this exhaustive use of the EM spectrum, a great interest for direction finders that cover simultaneously two or more frequency bands have been triggered (see Table 1.2 to Table 1.6). These direction finders are designed either using a multiband or wideband topology. Conventional passive and compact antennas, that can be used to design a direction finder, limit the DoA estimation over a very small part of the EM spectrum. Indeed, they are intrinsically narrow-band due to their often resonant nature. Moreover, their behavior strongly depends on the physical size to wavelength ratio. The slightest deviation from the operating frequency affects considerably their electrical performances in terms of impedance matching, RP, and gain (refer to Appendix B for the definition of these parameters).

By definition, a multiband DF antenna is an antenna which operates in two or more separate frequency bands with relatively similar electrical performances in these bands. It can be designed using several radiating elements operating on different frequency bands. A wideband DF antenna is an antenna which exhibits a relatively frequency independent radiating characteristics over a large frequency range (typically, a fractional bandwidth [3] of at least 20%). According to the number of frequency bands to be addressed for the DoA estimation of incoming EM-waves, one of the two antenna topologies is generally more suitable, although theoretically both can be used. For example, if there is a significant frequency gap between the first and last bands, it is easier to design the DF antenna using a multiband topology since wideband radiating elements still exhibit limited bandwidth. However, for small frequency gap, the number of bands has to be considered. Indeed, the more frequency bands to operate on, the more difficult or even impossible it is to design the DF antenna with a multiband topology. Finally, if the gap between two successive bands is small, it is not easy to develop a multiband DF antenna with relatively close frequency bands [69].

Further benefits and drawbacks can be assigned to these two antenna topologies. As is often the case, the advantage of one is the disadvantage of the other. Multiband antennas exhibit a significant and inherent selectivity since they operate only on the frequency bands of interest by acting as a frequency filter. Depending on the application, a rejector circuit may be necessary for wideband antennas for filtering the frequency bands of interest. They can also be adaptable since they can modify their radiating characteristics from one band to another by using different radiating elements for each band. In contrast, wideband antennas are well-known for exhibiting a higher directivity than multiband antennas, which can be an asset when designing DF antennas. Finally, it can be difficult to achieve wide bandwidth while maintaining a compact antenna size (refer to Section 2.3.1 for further information). Table 1.8 highlights the benefits and drawbacks of multiband and wideband antennas.

	Benefits	Drawbacks
Multiband antennas	• Frequency selectivity • Adaptability	• Limited number of frequency bands • Tricky design according to frequency band specifications
Wideband antennas	• Wide range of applications due to wideband coverage • High-directivity	• Large size • No frequency selectivity

Table 1.8: Benefits and drawbacks of multibands and wideband antennas

[3] $\mathrm{BW}(\%) = 200\frac{f_{\max}-f_{\min}}{f_{\max}+f_{\min}}$, where $f_{\max}$ and $f_{\min}$ correspond to the upper and lower frequencies of operation, respectively.

1.4 Thesis motivations

The design of **DF antennas** that offer a **3-D angular coverage** has become very appealing to fulfill the growing demand for a broad scope of applications, in either civil or military domains, which can benefit from their use. Many methods can be applied to estimate the DoA of an incident EM-wave. As previously stated in Section 1.2, standard techniques are generally based on the spatial distribution of an antenna array. However, as far as 3-D coverage is concerned, the extension of these techniques are not straightforward and required volumetric antenna array. Moreover, the spacing between the radiating elements of the array also limits the frequency coverage. Designing a compact DF antenna with a 3-D angular coverage is actually very challenging. As was pointed out in Section 1.3.3, **VAs** are gaining prominence as they are an excellent technical solution to overcome this significant stake. Among the various VA structures, there is no **passive** and **wideband** design. Such configuration does not suffer from the limitations of active antennas but achieving the wideband coverage while retaining a **compact** structure is also a tremendous challenge. Although, the DoA estimation of incoming vertically-polarized EM-waves is the dominant feature of a DF antenna, there has been a huge amount of innovative scientific inquiry on **multi-polarized** DF antennas due to their capability to tackle polarization mismatch. The design of such structure, characterized by the words shown in bold print, will constitute the centerpiece of this thesis. Last but not least, part of the thesis work was also devoted to the improvement of the DF processing of VAs for enhancing their DF performances (e.g., estimation accuracy, frequency coverage, robustness to angular ambiguity and polarization mismatch).

Chapter 2

Design and evaluation of the grounded Two Season vector antenna

Contents

Various efforts have been made in the past to realize compact DF antennas in order to fulfill the growing demand of a broad scope of applications. However, as seen in Section 1.3.3, only a few VAs enable the estimatation of the DoA of incident EM-waves within the 3-D space. The purpose of this chapter is to design the first passive and wideband VA, which is referred to as the "Two Season VA" in the remainder of this thesis. The Two Season VA is intended to estimate the DoA of vertically-polarized EM-waves in the upper hemisphere through the measurement of the three components E_z, H_x and H_y. Moreover, this VA is mounted over a ground plane in view of embedded applications. This chapter begins with an overview of VAs (Section 2.1). Since DF antennas generally operate over a wide frequency range to cover as many applications as possible, the specific principles that enable the design of wideband antennas are then presented (Section 2.2). Besides, a feasibility study concerning the design of a compact and wideband antenna from small resonant antennas is realized (Section 2.3). In response to this study, a state of the art of wideband dipoles is provided to identify the radiating elements that would be worthwhile to consider for designing the VA (Section 2.4). This chapter ends with a detailed description of the Two Season VA design (Section 2.5), followed by a review of its electrical characteristics (Section 2.6) and DF performances (Section 2.7).

This chapter corresponds to the content of Duplouy *et al.* [I1, I2, J1, J2, N1, N2].

2.1 Overview of vector antennas

Before proceeding to the design of the proper Two Season VA, it is essential to highlight the theoretical concepts of VAs. After briefly reviewing the historical development of VAs, this section describes the six-element VA, its advantages as well as the observation models used for the DF estimation.

2.1.1 Historical development

The problem of DoA estimation has received considerable attention through the years. Initial work has focused on uniformly polarized arrays, in other words scalar DF antennas, which enable the measurement of only one component of the incoming EM-wave. Subsequent research has led to the development of DF antennas that provide the measurement of two or more components. Special cases are the dipole-pair, the dipole-triad, or the loop-triad. Diversely polarized antenna arrays offer a significant advantage over uniformly polarized arrays such as the capability to distinguish two closely spaced EM-waves from their polarization characteristics [70, 71]. In general, this added information improves the DoA estimation accuracy. More recently, Nehorai and Paldi have introduced VAs that measure the six components of incoming EM-waves [11].

2.1.2 The six-element vector antenna

Conceptually, a VA is a multi-element antenna aiming at measuring different components of any incoming EM-wave. In its "complete and traditional" shape, the VA comprises three identical and orthogonally oriented short electric dipoles, plus three identical short and orthogonally oriented magnetic dipoles, all spatially located in a point-like geometry [11]. Thus, these six dipoles enable the measurement of all six components of any incoming EM-wave at the VA location, said E_x, E_y, E_z, H_x, H_y and H_z in the Cartesian coordinate system (refer to Fig. 2.1 for its definition).

In this well-known approach, every EM-wave component is derived from the signal received by a specific constitutive dipole. Indeed, the measurement of a given electric or magnetic component of the EM-wave is associated with the radiation pattern (RP) of an electric or magnetic dipole. For instance, the component E_x is derived from the output signal of an electric dipole oriented along the $\hat{x}$-axis, which is obtained thanks to the RP of this specific dipole. Commonly, all three magnetic components of the incident EM-wave are measured through small electric loops (whose maximum dimension is less than a tenth of a wavelength) [72]. For example, the output of the loop with its normal parallel to the $\hat{x}$-axis enables the measurement of the component H_x. The usual topology of a VA is depicted in Fig. 2.1. Furthermore, the theoretical observation model used for the DoA estimation with this VA topology is described in Section 2.1.4.1.

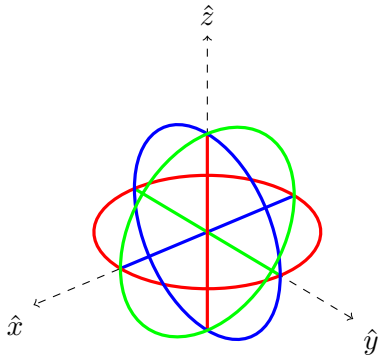

Figure 2.1: Topology of a VA that enables the measurement of all six Cartesian components of any incoming EM-wave

Another approach can be considered for designing a VA, which involves using radiating elements other than electric or magnetic dipoles (see, e.g., the second VA [13] depicted in Table 1.6). In this approach, every EM-wave component is derived from the appropriate combination or weighted summation of signals simultaneously received by the relevant constitutive radiating elements. This is valid as long as the weighting coefficients assigned to the received signals allow the synthesis of the RPs of three electric dipoles and three magnetic dipoles. Hence, the VA can be viewed as a RP reconfigurable VA. In practice, the set of weighting coefficients assigned to the received signals for measuring every EM-wave component can be obtained from either passive circuits or signal post-processing. The observation model used for the DoA estimation with this VA topology is described in Section 2.1.4.2.

Once all the components of the incoming EM-wave are obtained, it is possible to estimate both its azimuth/elevation arrival angles (ϕ, θ) and polarization parameters (η, γ) as follows:

- Use the polarization-based DF method described in Section 1.2.3, which is based on the computation of the Poynting vector;
- Exploit another method also based on the computation of the Poynting vector, which consists in reconstructing the incident EM-wave using an expansion in spherical harmonics of the RPs of the VA [73]. Interested readers may refer to the well-detailed study in [74].
- Apply one of the high-resolution techniques, such as the MUSIC algorithm [31] detailed in Appendix A. This method was adopted throughout this Ph.D. work.

During the past two decades, many VAs were reported for estimating the DoA of incoming EM-waves using one of two previously-cited design approaches (see, e.g., [12–14, 62–66]). However,

as mentioned earlier in Section 1.3.3.1, only the VAs set out in Table 1.6 have demonstrated their ability to cover the 3-D space (or only the upper hemisphere if the VA is mounted on carrier) [12–14, 65, 66]. The particular VAs that incorporate a ground plane are not able to measure the six components of the incoming EM-wave but only three: E_z , H_x and H_y (see, e.g, the third and fourth VAs shown in Table 1.6 [14,66]). However, the measurement of these three components are sufficient to estimate the DoA of incoming vertically-polarized EM-waves. The Two Season VA to be designed in this chapter is a grounded VA which allows the measurement of these three components.

Furthermore, a minimum of three diversely polarized antennas (i.e., a triad of orthogonally oriented dipole(s) and/or loop(s)) is required to estimate the vector parameter $\mathbf{\Omega} = [\theta\ \phi\ \eta\ \gamma]^{\mathrm{T}}$ of the incoming EM-wave thanks to several closed-form formulas given in [75]. However, prior information concerning the EM-wave is generally needed to avoid an ambiguous estimation. Moreover, among the twenty possible triad configurations, four do not lead to closed-form formulas. These correspond to compositions that do not include either an electric or magnetic dipole oriented along $\hat{z}$. Finally, since the measurement of all the components of an incident EM-wave is not necessarily required to estimate the azimuth/elevation arrival angles, it is nevertheless preferable to take full advantage of the benefits offered by VAs, which are described thereafter.

Besides, there are various figures-of-merit defined in Appendix B that describe the electrical characteristics of a VA.

2.1.3 Advantages of vector antennas

Since their introduction into array signal processing by Nehorai and Paldi in 1994 [11], VAs are gaining prominence. The main advantage of VAs is their ability to make use of all available EM information since they are sensitive to both DoA and polarization of the incoming EM-waves. Hence, they outperform scalar sensor arrays in terms of DoA estimation accuracy. Further explanations can be meaningfully used to interpret the eminence of using a single VA for DoA estimation:

- It is sufficient to estimate the DoA over the 3-D space;
- As it may replace a large antenna array, VA enables high mobility thanks to its compactness;
- It provide an isotropic response;
- Ability to estimate the DoA of any incoming EM-wave, regardless of its polarization, since all components are measured;
- The discrimination of two close directions of incoming EM-waves (even coincident) can be performed from polarization difference [76];
- Ability to process wideband signals in the same way as narrow-band signals [77];
- Location calibration and time synchronization are not needed among the different VA elements [77];

Most of these capabilities result from the fact that there is no phase delays between the VA elements since they are all spatially located in a point-like geometry. Conversely, 3-D DF from a scalar rather than vectorial approach requires a volumetric antenna array, an accurate location

calibration and time synchronization, and a high computational cost to process wideband signals [77].

On another side, spatial diversity can also complement the DF approach based on polarization diversity by exploiting the spatial phase delays across the displaced dipoles of a VA. This technique is commonly applied to improve the accuracy of the DoA estimation (see, e.g., [14,62,76,78–80]). However, as shown in [14], angular ambiguity may occur if the electrical spacing between the VA elements is too large.

2.1.4 Observation models of vector antennas

As was pointed out in Section 2.1.2, there are two main approaches to design a VA, namely the six-element VA or the RP reconfigurable VA. Specifically, all six components of the incoming EM-wave can be measured either directly through six short dipoles or by an appropriate combination (or equivalently, weighted summation) of signals simultaneously received by relevant constitutive radiating elements. The observation models used for the DoA and/or polarization estimation(s) through these two VA designs are set out in the following section.

2.1.4.1 Observation model of the six-element vector antenna

In the case of a VA composed of short dipoles, it is possible to simply explicit a theoretical observation model. After a brief description of the constitutive short electric and magnetic dipoles, this section presents the spatial response of the VA and the resulting observation model.

The short electric and magnetic dipoles

The short electric dipole, also known as the Hertzian electric dipole, is an infinitesimal linear wire of length l substantially less than the wavelength. Let us consider that the short electric dipole is positioned at the origin of the Cartesian coordinate system and oriented along the $\hat{z}$-axis, as illustrated in Fig. 2.2. The electric current flowing through the dipole is assumed to be constant and is denoted I_0.

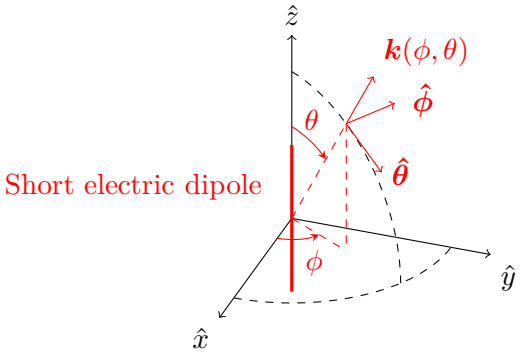

Figure 2.2: Short electric dipole oriented along the $\hat{z}$-axis

The EM-field radiated from the short electric dipole in the far-field region, which is valid only

for an observation distance $r \gg \lambda$ is defined as follows [81]

$$\begin{aligned} \boldsymbol{E} &= jk\zeta I_0 l \sin(\theta)\frac{e^{-jkr}}{4\pi r}\hat{\boldsymbol{\theta}}, \\ \boldsymbol{H} &= jkI_0 l \sin(\theta)\frac{e^{-jkr}}{4\pi r}\hat{\boldsymbol{\phi}}, \end{aligned} \tag{2.1}$$

where ζ is the intrinsic impedance of the medium. It can be observed from Eq. 2.1 that only the components E_θ and H_ϕ are nonzero in the far-field region. Moreover, the electric and magnetic components of the EM-field are in-phase and perpendicular to one another. Besides, the variations in r of these components are separable from those in θ and ϕ. The electric and magnetic components of the EM-field are also transverse to the direction of propagation $\boldsymbol{k}$ and their magnitudes are related by the intrinsic impedance of the medium ζ since

$$H_\phi = \frac{E_\theta}{\zeta}. \tag{2.2}$$

Furthermore, a short electric dipole is vertically-polarized according to Eq. 2.1. Using Eq. B.4, the normalized far-field pattern of the short electric dipole is given by

$$f(\phi, \theta) = \sin(\theta), \tag{2.3}$$

as displayed in Fig. 2.3. It can be seen from Fig. 2.3(a) that any plane containing the $\hat{z}$-axis has the same RP because there is no variation in ϕ in the electric field. A plane taken from one of these planes is called the E-plane since it contains the electric field vector. Besides, as shown in Fig. 2.3(b), the RP taken in the plane perpendicular to the E-plane is omnidirectional. In the same manner, this plane is called the H-plane as it contains the magnetic field vector. Furthermore, the maximum directivity of a short electric dipole can be obtained from Eq. B.6 and is of 1.5 in natural, namely 1.76 in dBi.

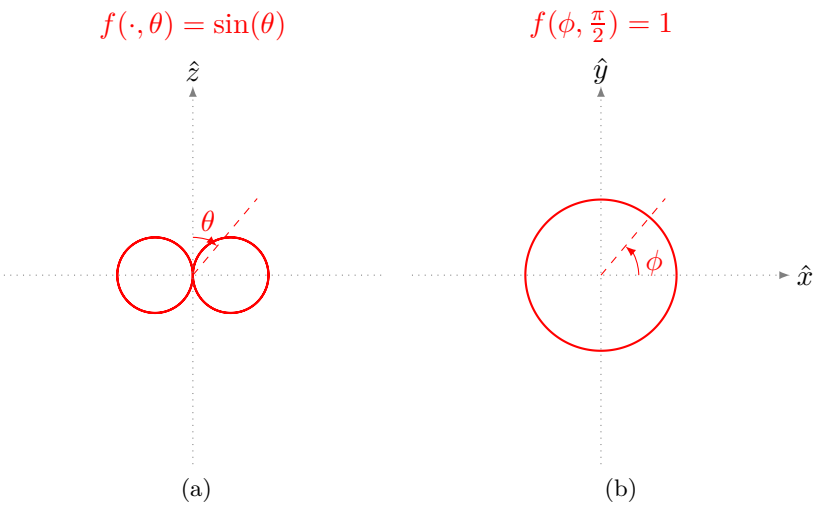

Figure 2.3: Normalized far-field pattern $f(\phi, \theta)$ of a short electric dipole in the: (a) E-plane, and (b) H-plane

Let us now consider a short magnetic dipole, positioned at the origin of the Cartesian coordinate system and oriented along the $\hat{z}$-axis, which is the same configuration as that depicted in Fig. 2.2

except that this time the short dipole carries a constant magnetic current denoted I_m. The radiated field can be found by duality [82], which yields to

$$\begin{aligned} \boldsymbol{E} &= -jkI_m l \sin(\theta)\frac{e^{-jkr}}{4\pi r}\hat{\boldsymbol{\phi}}, \\ \boldsymbol{H} &= jk\frac{I_m l}{\zeta}\sin(\theta)\frac{e^{-jkr}}{4\pi r}\hat{\boldsymbol{\theta}}. \end{aligned} \tag{2.4}$$

According to Eq. 2.4, a short magnetic dipole is horizontally-polarized. Moreover, the radiation patterns of a short magnetic dipole are identical to those of an short electric dipole, except that Fig. 2.3(a) and Fig. 2.3(b) correspond to the H-plane and E-plane, respectively.

Spatial response of the six-element vector antenna

Since each element of the VA is a short electric or magnetic dipole, the output voltage $\{e_i\}_{i=x,y,z}$ or $\{h_i\}_{i=x,y,z}$ from each dipole is proportional to the electric field or magnetic field component along the dipole. According to Eq. 1.34, it is possible to define the steering vector $\boldsymbol{d}$ of the six-element VA, or equivalently its spatial response to an incoming EM-wave, as follows

$$\boldsymbol{d}(\phi,\theta,\gamma,\eta) = \begin{bmatrix} e_x \\ e_y \\ e_z \\ h_x \\ h_y \\ h_z \end{bmatrix} = \underbrace{\begin{bmatrix} \cos(\phi)\cos(\theta) & -\sin(\phi) \\ \sin(\phi)\cos(\theta) & \cos(\phi) \\ -\sin(\theta) & 0 \\ -\sin(\phi) & -\cos(\phi)\cos(\theta) \\ \cos(\phi) & -\sin(\phi)\cos(\theta) \\ 0 & \sin(\theta) \end{bmatrix}}_{\boldsymbol{f}(\phi,\theta)} \underbrace{\begin{bmatrix} \sin\gamma e^{j\eta} \\ \cos(\gamma) \end{bmatrix}}_{\boldsymbol{p}(\gamma,\eta)}, \tag{2.5}$$

which depends on the azimuth/elevation angles of arrival of the incident EM-wave via $\boldsymbol{f}(\phi,\theta)$ and on its polarization parameters through $\boldsymbol{p}(\gamma,\eta)$. Specifically, the columns of the matrix $\boldsymbol{f} \in \mathbb{R}^{6,2}$ denote the normalized spatial transfer functions for both polarization components in the Cartesian coordinate system (refer to Fig. 2.1 for its definition), and $\boldsymbol{p} \in \mathbb{C}^{2,1}$ is the polarization vector of the incident EM-wave (see Section 1.1.1). It can be noted that the steering vector $\boldsymbol{d}$ described in Eq. 2.5 assumes that there is no mutual coupling between the VA elements. This property is essential and must be remembered when designing a VA in order to maintain this mathematical model.

Resulting observation model

Consider V narrow-band EM-waves traveling in an isotropic, homogeneous and lossless medium and incident upon the VA placed at the origin of the Cartesian coordinate system. The observation model used here corresponds to the one usually used in signal processing. In presence of V incoming EM-waves, the output voltage $\boldsymbol{x} \in \mathbb{C}^{6,1}$ received at time t can be written as follows

$$\boldsymbol{x}(t) = \boldsymbol{D}(\boldsymbol{\Omega}).\boldsymbol{s}(t) + \boldsymbol{n}(t), \tag{2.6}$$

where $\boldsymbol{D}(\boldsymbol{\Omega}) = [\boldsymbol{d}(\boldsymbol{\Omega}_1)\ldots\boldsymbol{d}(\boldsymbol{\Omega}_v)\ldots\boldsymbol{d}(\boldsymbol{\Omega}_V)] \in \mathbb{C}^{6,V}$ is the VA response to the V incident EM-waves characterized by $\boldsymbol{\Omega}_v = [\theta_v\ \phi_v\ \eta_v\ \gamma_v]^{\mathrm{T}}$. In Eq. 2.6, $\boldsymbol{s} \in \mathbb{C}^{V,1}$ designates the signal vector associated with these incoming EM-waves (i.e., the amplitude and phase of each signal) and

$\boldsymbol{n} \in \mathbb{C}^{6,1}$ denotes the additive white Gaussian noise. It is assumed here that this noise is spatially invariant with zero-mean and covariance matrix $\mathbf{R}_{\boldsymbol{n}} = \sigma_n^2 \boldsymbol{I} \in \mathbb{C}^{6,6}$. Usually, a set of N snapshots is used for the DoA and/or polarization estimation(s) and thereby, the stacked observation model can be written as $\boldsymbol{X} = [\boldsymbol{x}[t_1], \boldsymbol{x}[t_2], ..., \boldsymbol{x}[t_N]] \in \mathbb{C}^{6,N}$.

The observation model of an ideal VA that enables only the measurement of the components E_z, H_x and H_y of incoming EM-waves is described in Appendix C.

2.1.4.2 Observation model of a RP reconfigurable vector antenna

Moving now on the observation model description of the other main VA design, which is the RP reconfigurable VA. The measurement of the components of an incident EM-wave is obtained with such VA thanks to an appropriate combination (or equivalently, weighted summation) of the signals simultaneously received by relevant radiating elements.

Let us consider a VA composed of several radiating elements and comprising a total of P output ports. It is also assumed here that M different sets of weighting coefficients that will be assigned to the P received signals can be obtained from a passive circuit or signal post-processing. Therefore, M different RPs including those allowing the measurement of the components of the incoming EM-waves are available.

For V EM-waves incident upon the VA, the output voltage $\boldsymbol{x}$ received at time t and at the P ports of the VA can be written as in Eq. 2.6, except that this time $\boldsymbol{x} \in \mathbb{C}^{P,1}$, and $\boldsymbol{D}(\boldsymbol{\Omega}) = [\boldsymbol{d}(\boldsymbol{\Omega}_1) \dots \boldsymbol{d}(\boldsymbol{\Omega}_v) \dots \boldsymbol{d}(\boldsymbol{\Omega}_V)] \in \mathbb{C}^{P,V}$ where $\boldsymbol{d} \in \mathbb{C}^{P,1}$ is the spatial response of the P-port radiating elements. The combined data model $\boldsymbol{x_c} \in \mathbb{C}^{M,1}$ at time t is then derived from a weighted summation of the received signals $\boldsymbol{x} \in \mathbb{C}^{P,1}$ at the outputs of the radiating elements. The $m-$th component of $\boldsymbol{x_c}$ associated with the m-th set of weightings can be written as follows

$$x_c^m(t) = \boldsymbol{w}^m . \boldsymbol{x}(t), \tag{2.7}$$

where $\boldsymbol{w}^m = [w_1^m \dots \ w_p^m \dots \ w_P^m] \in \mathbb{C}^{1,P}$ denotes the complex weighting coefficients applied at the P ports of the VA (and corresponds to the m-th RP). The stacked observation model can be written as $\boldsymbol{X_c} = [\boldsymbol{x_c}[t_1], \boldsymbol{x_c}[t_2], ..., \boldsymbol{x_c}[t_N]] \in \mathbb{C}^{M,N}$ for N snapshots.

It can be noted that $\boldsymbol{x_c} = \boldsymbol{x}$ if the radiating elements that constitute the VA are in fact already short electric and magnetic dipoles.

Finally, the observation model written in Eq. 2.7 is used throughout this thesis assuming that only one incoming EM-wave is incident upon the VA ($V = 1$), notably under three aspects:

- The DF performances of the 4-port "Two Season VA", whose design is described in Section 2.5, are evaluated in Section 2.7 using three sets of weightings that enable the measurement of three components of the incoming EM-wave, which are E_z, H_x and H_y. In that respect, $M = 3$ and $P = 4$.
- The DF performances of the 8-port "Four Season VA", a new VA whose design is described in Section 3.3.1, are evaluated in Section 3.3.3.1 using six sets of weightings to enable the measurement of all six components of the incoming EM-wave, namely E_x, E_y, E_z,H_x, H_y and H_z. In that respect, $M = 6$ and $P = 8$;
- The DF performances of Two Season and Four Season VAs are re-evaluated in Section 3.1.2 and Section 3.3.3.2 using additional RPs (or accordingly, more sets of weightings assigned to

each received signal) than those used to measure the components of the incoming EM-wave (i.e., $M > 3$ and $M > 6$, respectively). Besides, an improved version of the Two Season VA was also designed during this Ph.D. and its DF performances using additional RP are assessed in Section 3.2.3.2. Moreover, a method for selecting rapidly and efficiently the new RPs is proposed in Section 3.1.1.1.

2.2 Basic principles of wideband antennas

It can be noted from Table 1.3 to Table 1.6 that particular attention was devoted to the design of wideband and mobile direction finders in order to cover a maximum of DF applications, which are spread out over the EM spectrum (see also Table 1.1). There exists a vast number of principles in the literature to achieve wideband impedance matching with a passive antenna structure. Many of these antennas radiate over a wide frequency range by combining two or more of the principles that are set out below.

2.2.1 Self-complementary antennas

Self-complementary antennas are introduced by Mushiake in 1948 [83] and derived from Babinet's principle, which was introduced in optics and stated that a perturbation in wave propagation caused by a small aperture is entirely compensated by the disturbance caused by its complementary structure. An extension of this principle was introduced into antenna theory by Booker in 1946 [84]. He notably discovered that the impedance Z_1 of a dipole antenna and the impedance Z_2 of the complementary slot antenna are related through the relation

$$Z_1 Z_2 = \frac{\zeta_0^2}{4}, \tag{2.8}$$

where ζ_0 is the free-space impedance of 377 (approximately 120π) Ω. Fig. 2.4 shows an example of these complementary antennas.

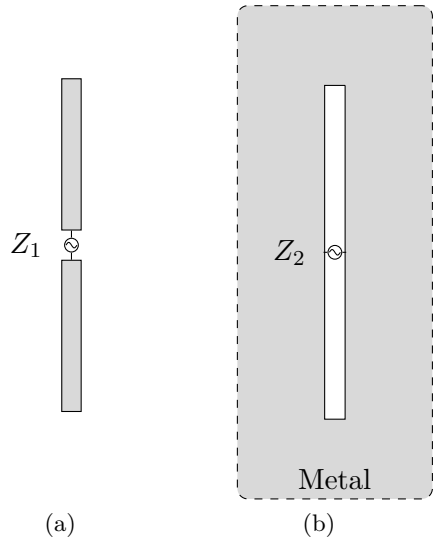

Figure 2.4: Complementary (a) dipole and (b) slot antennas

This relation was also independently derived by Mushiake and further exploited to identify the concept of self-complementary antennas. These are characterized, whatever the form of their geometry, by a self-complementary metalization. According to Eq. 2.8, a self-complementary antenna presents an input impedance Z which is theoretically constant at any frequency and given by

$$Z = \frac{\zeta_0}{2}. \tag{2.9}$$

The impedance of a self-complementary antenna is therefore frequency independent. Fig. 2.5 presents typical examples of self-complementary antennas. It can be noted that many frequency independent antennas (described hereafter) exploit the self-complementarity principle to achieve a wideband bandwidth. A typical example is the four-arm log-periodic spiral antenna, depicted in Fig. 2.5(c), which exhibits a wideband behavior due to its log-periodic and self-complementarity structure.

(a) (b) (c)

Figure 2.5: Examples of self-complementary antennas: (a) two-arm spiral antenna [82], (b) four-arm sinuous spiral antenna [82], and (c) four-arm log-periodic spiral antenna [82]

2.2.2 Frequency independent antennas

Rumsey has stated the concept of frequency independent antennas in the mid-1950s, known as the "equiangular" antennas theory. Before his work, it had been noticed that the RP and impedance matching of an antenna vary only with the geometry as described in wavelengths. Therefore, modifying the operating frequency of an antenna is equivalent to scaling its geometry. This is commonly referred to as the scaling principle and can be applied to any antenna made of perfect conductors and dielectrics. As a consequence, Rumsey's principle suggests that if the dimensions of a lossless antenna are specified entirely by angles such that they remain constant in terms of wavelength, this antenna can be considered as a frequency independent antenna. As a result, it can theoretically operate over an infinite bandwidth and exhibit RP properties that will be frequency independent. In practice, the physical truncation of the antenna structure limits the lowest frequency of operation, and the antenna feed structure dictates the upper frequency of operation. A frequency independent antenna has an electrically active region that is a subdivision of the antenna structure. This active region moves as a function of frequency to other parts of the antenna structure. The currents on the antenna structure tend to decay rapidly away from the center of the structure, especially beyond the active region. Therefore, the performance of a frequency independent antenna is not affected if its structure is truncated beyond the active region where the currents are relatively low. Any lossless antenna design that

can be entirely specified by angles, and thus be considered as a frequency independent antenna, fulfills in spherical coordinates an equation of the form

$$r = \mathrm{e}^{a\phi}\, f(\theta), \tag{2.10}$$

where $f(\theta)$ is an arbitrary function and $a = \frac{1}{K}\frac{dK}{dC}$ is a parameter, in which the rotation angle C depends on K but neither depends on θ and ϕ. For instance, the equiangular spiral and conical spiral antennas as well as the biconical antenna are typical structures that exploit this concept (see Fig. 2.6).

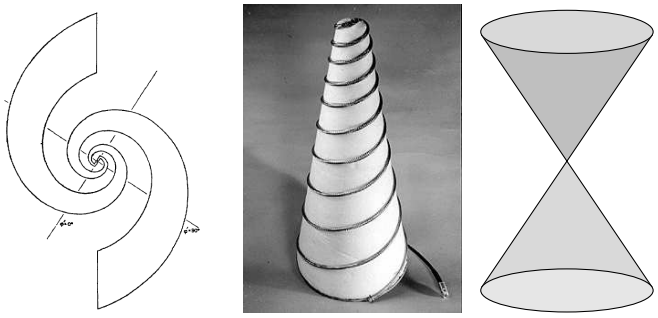

(a) (b) (c)

Figure 2.6: Examples of frequency independent antennas: (a) equiangular spiral antenna [85], (b) conical log-spiral antenna [86], and (c) biconical antenna

Furthermore, log-periodic structures were introduced by DuHamel and Isbell [87] in 1957 and exhibit an operating principle similar to that of frequency-independent antennas, with the difference that their geometries cannot be specified entirely by angles. Therefore, they do not exactly answer their definitions. They are incredibly wideband as they present an electrical periodicity that is a logarithm of frequency.

2.2.3 Multiple resonance antennas

Multiple resonance antennas consist of a combination of several narrow-band radiating elements. Each element, usually a dipole, covers a limited bandwidth of the overall bandwidth but the overlapping of these narrow bandwidths leads to a wide operating frequency range. DuHamel and Isbell initiate these antennas in 1957 through their work on log-periodic structure [87], which also falls within this category. A typical example is illustrated in Fig. 2.7(a) and consists in a log-periodic dipole antenna array where each dipole covers 20% of the overall bandwidth [88,89]. Another example is the fractal antenna [90,91], like the Minkowski island loop antenna depicted in Fig. 2.7(b).

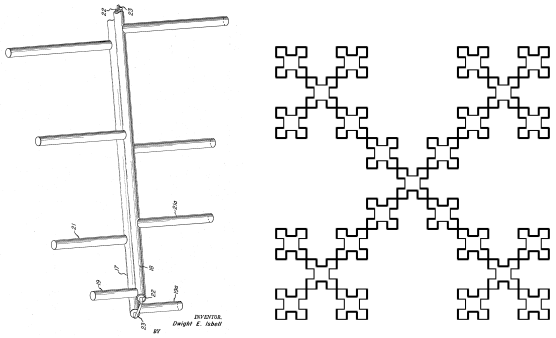

(a) (b)

Figure 2.7: Examples of multiple resonance antennas: (a) log-periodic dipole array [88], and (b) Minkowski island loop antenna [92]

2.2.4 Traveling-wave antennas

Resonant antennas present a wave traveling outward from the feed point to the end of the antenna and being reflected, setting up a standing-wave type current distribution [72]. On the contrary, if an antenna does not strongly present standing-waves, it can be referred to as a traveling-wave antenna. Hence, traveling-wave antennas act as their name indicated as a guiding structure for traveling waves. They behave ideally like a matched transmission line [82]. There are two methods to design a traveling-wave antenna [81]. The first is to properly terminate the antenna for eliminating the reflections or at least minimizing them. The second is to use a very long antenna to ensure that most of the power is radiated in order to limit the presence of reflected waves. Moreover, a traveling-wave antenna exhibits a directional RP since it supports a wave traveling in a single direction. Last but not least, the input impedance of a traveling-wave antenna is mostly real since there is no standing-wave, enabling the antenna to operate over a wide frequency range. Fig. 2.8 gives some typical examples of traveling-wave antennas such as the helical wire antenna, the horn antenna, and the tapered slot antenna (TSA).

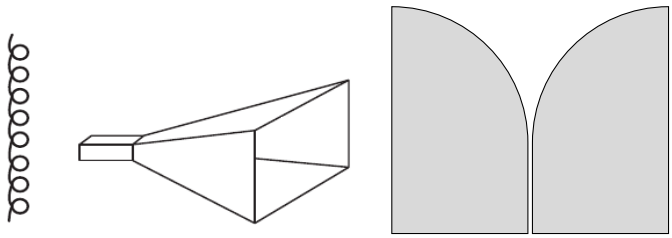

(a) (b) (c)

Figure 2.8: Examples of traveling-wave antennas: (a) helical wire, (b) pyramidal horn, and (c) exponentially tapered slot

2.3 Feasibility study of a compact and wideband antenna

One of the principal considerations in designing a wideband VA is the choice of the constituting radiating elements. Since a passive VA is traditionally composed of typical electric and magnetic

dipoles, the bandwidth is very small since these dipoles are resonant-type structures. For years, the wish to design small DF antennas has grown steadily. However, it is well-known that the radiation efficiency and bandwidth of small antennas are dramatically reduced as their size decreases. This section is intended to provide a feasibility study of a compact and wideband antenna presenting optimal radiation performance, and designed from several resonant antennas. This investigation is based on the small antennas theory, which has been extensively studied in the literature and is briefly reported below.

2.3.1 Theory of small antennas, the Chu limit

An antenna is considered as small when its size is very small compared to the wavelength at the operational frequency. Although there are no strictly physical criteria associated, this subjective notion is often represented by the length introduced by Wheeler in 1947 [93]. He defined an electrically small antenna as an antenna whose maximum dimension is less than $\lambda/2\pi$, which is commonly referred to as the "radianlength". This definition is equivalent to saying that an antenna is electrically small if it satisfies the condition

$$ka < 0.5, \tag{2.11}$$

where a is the radius of the minimum size sphere that encloses the antenna. This sphere is usually known as the "Chu sphere" and is depicted in Fig. 2.9.

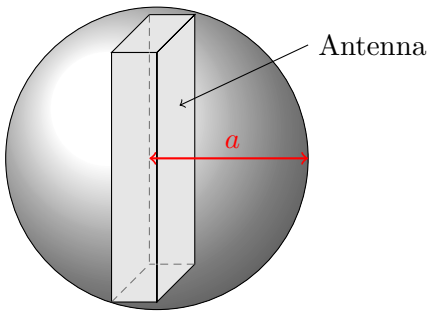

Figure 2.9: Chu sphere enclosing an electrically small antenna

Another widely accepted condition for an antenna to be considered as electrically small is

$$ka < 1, \tag{2.12}$$

which was established by Hansen in 1981 [94]. An electrically small antenna can be seen through Eq. 2.12 as an antenna enclosed in a sphere of radius equals to one radianlength. Such sphere is commonly referred to as a "radiansphere" [95], and defines the region where the reactive power density is greater than the radiated power density. It represents the boundary of the transition between the near- and far-field region.

Wheeler highlighted the significant influence of the electrical size ka and the volume of an antenna on its radiation performance, which led him to a fundamental remark on the design of small antennas: the optimization of the radiation performance of an antenna is directly related to the filling of the spherical volume occupied by the antenna. In other words, an antenna that fully utilizes the volume that circumscribes its maximum size will provide the lowest quality factor Q compared to other antenna topologies within the same volume.

Small antennas theory is currently the subject of numerous discussions. Among them, several studies have led to the establishment of the minimum value of the quality factor $Q_{\min}$ of a resonant antenna given its electrical size. For a linearly-polarized electrically small antenna radiating only the TM_{10} or TE_{10} modes, McLean's formula of $Q_{\min}$ was demonstrated using two approaches (fields and circuits) [96] and is expressed by

$$Q_{\min} = \frac{1}{(ka)^3} + \frac{1}{ka}. \tag{2.13}$$

It is commonly stated that the fractional bandwidth BW is inversely proportional to the quality factor Q. However, this formulation

$$\mathrm{BW} \approx \frac{1}{Q} \tag{2.14}$$

is not extremely useful by itself since the impedance matching of the antenna is not taken into account. Hence, Eq. 2.14 may be rewritten as follows [97]

$$\mathrm{BW} = \frac{\mathrm{VSWR} - 1}{Q\sqrt{\mathrm{VSWR}}}. \tag{2.15}$$

In 2006, Best generalized McLean's formula in Eq. 2.13 and provided an upper bound for the matched VSWR fractional bandwidth , which is

$$\mathrm{BW} = \frac{1}{\eta_r} \frac{(ka)^3}{1 + (ka)^2} \frac{\mathrm{VSWR} - 1}{\sqrt{\mathrm{VSWR}}}. \tag{2.16}$$

This formulation also includes the radiation efficiency η_r (defined in Appendix B.3) of the electrically small antenna.

2.3.2 Radiation efficiency of electrically small antennas

The radiation efficiency η_r of an electrically small antenna is evaluated using Eq. 2.16. This study assumes the Utopian case where the operating bandwidth of the antenna is of r_{ref}:1 $\in \{2, 2.5, 3\}$ and presumes a VSWR of 2. Furthermore, the RP of the antenna would fulfill the specifications on the same frequency band r_{ref}:1. Fig. 2.10 presents the radiation efficiency achieved for the different operating bandwidth. It can be observed that as the frequency range of operation increases, the radiation efficiency of the antenna decreases strongly with ka. Besides, it is possible to get an idea of the gain of such antennas using Eq. B.10 and assuming the directivity of a short dipole (i.e., $D = 1.5$). As depicted in Fig. 2.11, the gain is extremely weak for the smaller antennas since they do not radiate efficiently. It should be noted that these curves represent a theoretical limit, which can hardly be reached for real antennas, especially for low values of ka. The loss of radiation efficiency caused by the miniaturization of the DF antenna is incompatible with DF. Indeed, the sensitivity and the theoretical range of a direction finder are notably subject to it (see Section 1.1.5.5). Therefore, the idea is to use several resonant antennas in order to cover the intended bandwidth using the overlapping technique presented in Section 2.2.3.

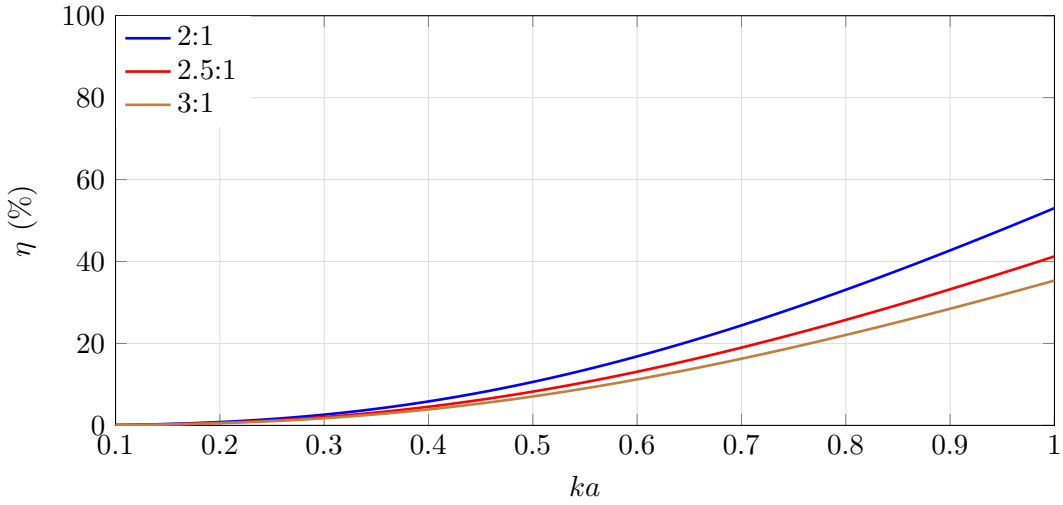

Figure 2.10: Radiation efficiency η_r of an electrically small antenna having a bandwidth of r_{ref}:1 $\in \{2, 2.5, 3\}$ in function of its electrical size ka for a VSWR=2

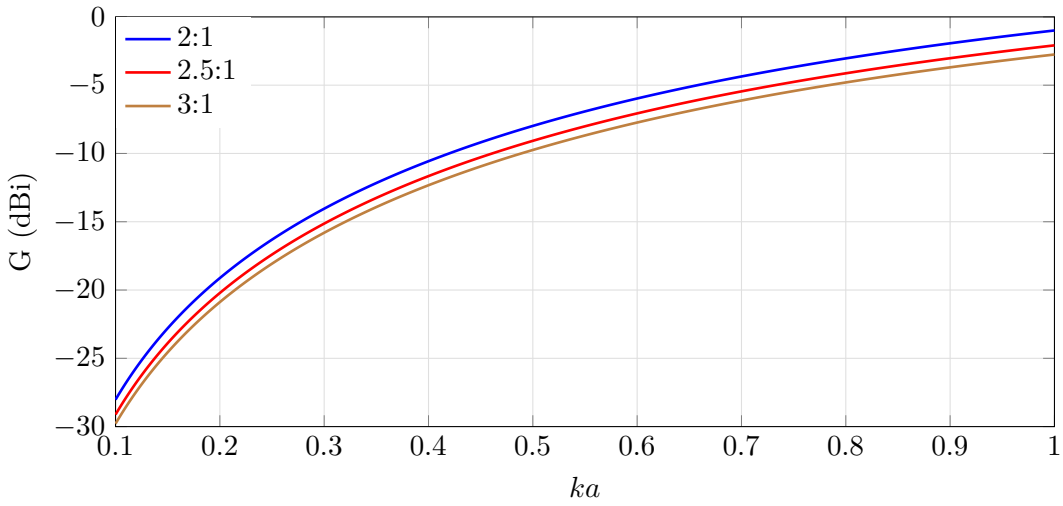

Figure 2.11: Gain G of an electrically small antenna having a bandwidth of r_{ref}:1 $\in \{2, 2.5, 3\}$ in function of its electrical size ka for VSWR=2 and $D = 1.5$

2.3.3 Bandwidth of electrically small antennas

In the same vein of the previous study, the maximum theoretical bandwidth of an electrically small antenna is evaluated using Eq. 2.16 for different radiation efficiency $\eta_r \in \{25\%, 50\%, 100\%\}$ in function of its electrical size is shown in Fig. 2.12. These values of efficiency correspond to an antenna gain (relative to a short dipole) of 1.76 dBi, -1.22 dBi and -4.26 dBi, respectively. This study also assumes a VSWR of 2. It can be observed that the maximal bandwidth decreases significantly if the electrical size of the antenna is diminished. For a given antenna size, the antenna efficiency has to be reduced in order to increase the bandwidth, which is also not suitable for the intended application. As a consequence, it seems difficult to design a compact antenna that radiates efficiently over a wide frequency range.

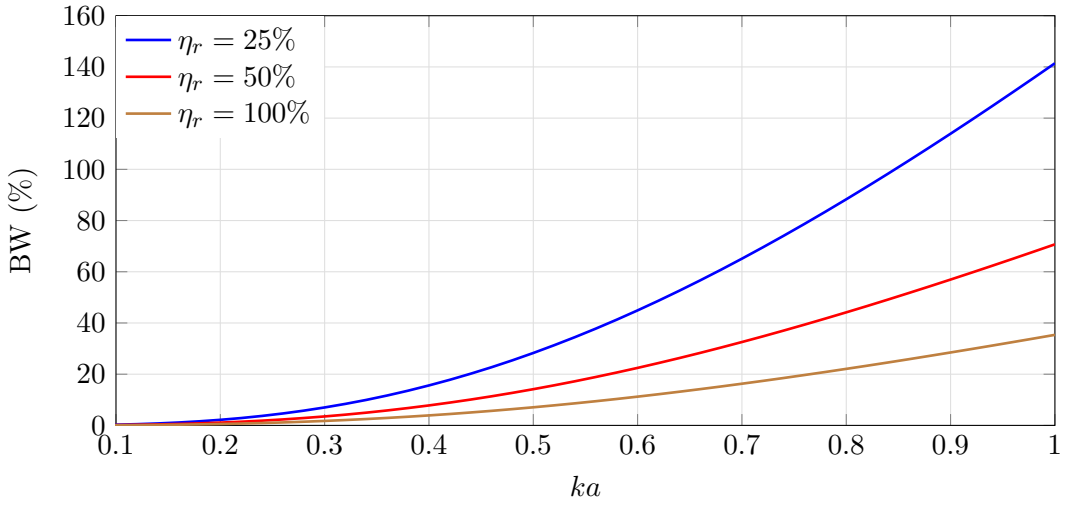

Figure 2.12: Maximal theoretical bandwidth BW of an electrically small antenna having a radiation efficiency $\eta_r \in \{25\%, 50\%, 100\%\}$ in function of its electrical size ka for a VSWR=2

2.3.4 Number of elements required to cover a wide bandwidth

The goal of this study is to determine the number of antennas required to cover a wide frequency band of BW:1 knowing that each antenna presents a reference operating band of r_{ref}:1 using the overlapping bandwidths technique described in Section 2.2.3 to obtain the large frequency range of operation. Indeed, the bandwidth of a resonant antenna (e.g., electric or magnetic dipoles) rarely exceeds 20%. The study assumes also the ideal case where the antenna has a RP that fulfills the specifications on the same frequency band r_{ref}:1.

Fig. 2.13 presents the results of this study for BW:1 $\in \{2, 2.5, 3\}$. As expected, it appears that the number of antennas required to cover a wide frequency range rapidly becomes large if the reference antenna bandwidth is limited. According to Fig. 2.12 and Fig. 2.13, six antennas are required to cover a bandwidth of 3:1 if the reference antenna exhibits a radiating efficiency η_r of 50%, an electrical size ka of 0.5, and a reference operating band of 1.22:1 (i.e., 20%). The number of antennas is reduced to five or four if the requiered bandwidth is only of 2.5:1 or 2:1, respectively.

This is all the more problematic when designing a wideband VA, which requires multiplying this number of antennas by six if the six components of an incoming EM-wave are intended to be measured. Moreover, all antennas are normally spatially in a point-like geometry, which appears difficult considering the large number involved to achieve a wide frequency range of operation. The use of the overlapping bandwidths technique is therefore not really suited for designing a wideband and compact antenna from resonant dipoles antennas. *A fortiori*, it is even more difficult to design a VA.

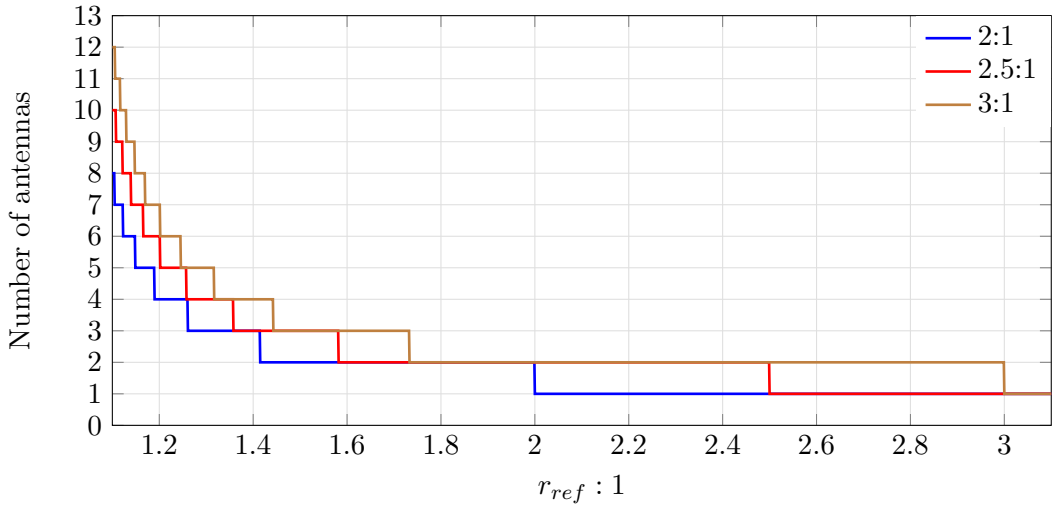

Figure 2.13: Number of antennas having a fractional bandwidth of r_{ref}:1 required to cover a frequency band of BW:1 using the overlapping bandwidths technique

2.3.5 Conclusion

This preliminary study shows the feasibility limits regarding the radiation efficiency, the bandwidth and the compactness achievable with one or more passive resonant antennas. Such antennas are not suited for designing a passive, wideband and compact antenna. As a consequence, it is all the more problematic to design a VA from the resonant antennas using the overlapping bandwidths technique. Hence, a state of the art of wideband dipole antennas is provided hereunder to study possible design solutions.

2.4 State of the art of wideband dipole antennas

The section that follows consists in a brief state of the art of wideband electric and magnetic dipoles/monopoles recently reported in the literature, which can be taken into consideration when designing a wideband VA. Radiating structures which show dipole-like characteristics over a large frequency range will also be discussed. Additionally, in DF applications, antennas are required to radiate efficiently and exhibit constant radiation characteristics (polarization and RP) over the entire band of operation. Throughout this state of the art, λ refers to the lowest operating frequency.

2.4.1 An unimaginable number of wideband electric dipoles

The electric dipole and monopole are undoubtedly the most basic types of antennas available on the industrial market but are probably the most studied in the literature.

Widening the impedance bandwidth of these antennas was tried early in the history of antennas. Indeed, the first work began with O. Lodge who built the first biconical antenna [98] in 1898 (see Fig. 2.6(c) for an illustration of this antenna structure). This antenna generally achieves a 2:1 impedance bandwidth ratio if the heights of the cones are at least $\lambda/4$ [72]. As previously

stated in Section 2.2.2, a wide impedance bandwidth is achievable with this structure since it exploits the principle of frequency independent antennas. For small cone angles, the RP of a finite biconical antenna is similar to the RP of an electric dipole of the same length. The equivalent of the electric monopole for the finite biconical antenna is the discone antenna if one of the cones is replaced by a disc-shaped ground plane. This antenna is represented in Fig. 2.14(a). The bow-tie and triangular antennas are simpler alternatives to the finite biconical and discone antennas, respectively. Due to their planar structures, they are lighter, easier to build, and naturally less bulky. Hence, it is less complicated to spatially locate in a point-like geometry and orthogonally orient the VA elements during the design process.

It is now well established that the thicker is the dipole, the wider is its bandwidth [92]. However, early works began with G. Dubost and S. Zisler who proposed to increase the bandwidth of the conventional wire monopole by widening the surface area of the antenna in 1976 [99]. They replaced the wire structure with a square planar structure. In this manner, other variations of the planar monopole as the one shown in Fig. 2.14(b) have recently been studied. Among them are notably the rectangular, elliptical, hexagonal and circular shapes. In [100], Agrawall performed a bandwidth comparison of several planar monopoles, and the results show that the circular and elliptical monopoles achieve a wider bandwidth than the others. Both obtain an impedance bandwidth ratio exceeding 10:1 but suffer from RP degradation at the upper-end of their impedance bandwidth. Although the impedance bandwidth ratio of the square planar monopole does not exceed 2:1, its RP is less degraded within the impedance bandwidth compared to other forms of planar monopoles [101]. However, modified versions of the circular and elliptical monopoles have been introduced to solve this problem [102]. An example is given in Fig. 2.14(c), which achieves a 10:1 impedance bandwidth ratio and radiates an omnidirectional RP over a 7:1 bandwidth. Nevertheless, the height of these planar monopole antennas is about $\lambda/4$.

At the expense of the ease of fabrication, another approach can be considered to increase the bandwidth of an antenna structure with monopole-like radiation characteristics if the antenna height is a primary design consideration. This approach is notably based on the old technique which consists of top-loading a monopole to be self-resonant at a given frequency with a reduced height. Specifically, this approach involves a monopole-like radiating structure with a top hat and several vertical impedance-matching elements (e.g., short pins or series inductors) within the body of the antenna [103, 104]. The oldest example is the Goubau antenna [103] shown in Fig. 2.14(d), which exhibits an omnidirectional RP over a 2:1 impedance bandwidth ratio for an antenna height of 0.09λ and a radius of 0.07λ. However, the bandwidth of these antenna structures are limited to one octave. Far more recently, an antenna demonstrating monopole-like radiation characteristics over a 4:1 bandwidth using two diamond-shaped loops and capacitive loading from a rectangular hat was published [105]. The 0.033λ height of this antenna is extremely small but this comes at the expense of a large lateral dimension of 0.22λ. In 2017, the antenna presented in Fig. 2.14(e) which combines two volumetric loops, two parasitic small loops and a circular top hat was reported [106]. This antenna is the same size as the Goubau antenna and presents omnidirectional radiation characteristics over a bandwidth of two octaves. These latter electric monopole-like antennas are very interesting in terms of their electrical performances (bandwidth and radiation characteristics) and size. Nevertheless, it can be difficult to incorporate them into a VA design since they are volumetric.

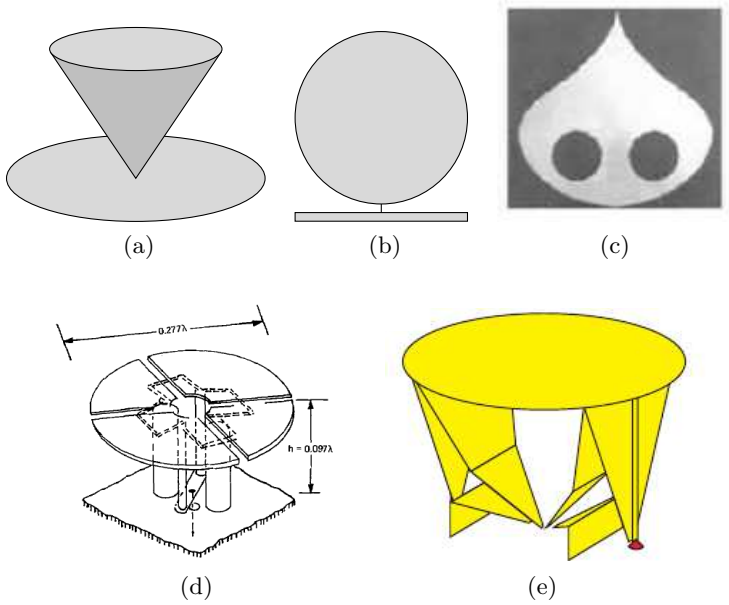

Figure 2.14: Wideband electric monopoles: (a) discone antenna, (b) circular and planar antenna, (c) planar inverted cone antenna [101], (d) Goubau antenna [104], and (e) top-loaded antenna proposed in [106]

2.4.2 The few wideband magnetic dipoles

Lot of studies with different approaches in designing wideband electric dipoles with good electrical performances have been documented for years. It could be eventually worthwhile to consider those for designing a wideband VA. At the same time and compared to the tremendous number of wideband electric dipoles, only a few wideband magnetic dipoles have been reported in the literature since they are more difficult to design [107].

As stated in Section 2.1.2, a small electric loop antenna (with dimension lower than a tenth of wavelength) which carries a uniform and in-phase current distribution is traditionally used for designing a magnetic dipole [72]. Unfortunately, impedance matching is very difficult to achieve with such antenna due to its naturally large input reactance. Meanwhile large loop antennas can achieve better impedance matching, nonuniform current distributions will occur. Hence, it is difficult to obtain omnidirectional RP with such structures. The Alford loop antenna was investigated to obtain better omnidirectional RP but this design suffer also from narrow bandwidth (typically less than 10%) [108, 109].

Another technique for designing a magnetic dipole in addition to the small electric loop is to use a narrow slot antenna at its first resonant frequency [81]. The main limitation of slot antennas is their bi-directional RP, which can be a drawback in various applications, where the antenna is mounted on a metallic surface. A cavity is placed behind the slot to suppress the backward radiation and overcome this problem. Notwithstanding several attempts have been made in the last decade to reduce the cavity dimensions, these designs are either bulky or have narrow bandwidths as well [110–112].

Very recently, several studies have been carried out to widen the bandwidth of antenna structures with magnetic dipole-like radiation characteristics. In 2012, the loop antenna of radius

0.17λ shown in Fig. 2.15(a) uses periodical capacitive loading to remain the current in phase and uniform over a 1.36:1 impedance bandwidth ratio was reported [107]. Nevertheless, the gain variation (maximum to minimum) in the horizontal plane is as large as 5 dB at high frequencies. The next year, a double-layered planar antenna which contains four pairs of flag-shaped dipoles and parasitic strips (see Fig. 2.15(b)) was published [113]. Compared to the aforementioned antenna, this structure exhibits a 1.52:1 impedance bandwidth ratio at the expense of increasing the antenna dimension, the radius being here of 0.29λ. Also, the gain variation in the horizontal plane also increases with the operating frequency. The antenna structure represented in Fig. 2.15(c) which is made up of twelve tightly coupled dipoles that are arranged on a double-layered circular substrate was reported in 2015 [114]. This antenna of radius 0.43λ achieves a good omnidirectional RP over a 2.1:1 impedance bandwidth ratio. In 2017, the antenna structure of radius 0.32λ shown in Fig. 2.15(d) was published [115]. It also uses four flag-shaped dipoles with etched slots, parasitic strips, and director elements to achieves an omnidirectional RP with less than 2.2 dB gain variation over a 2.55:1 impedance bandwidth ratio.

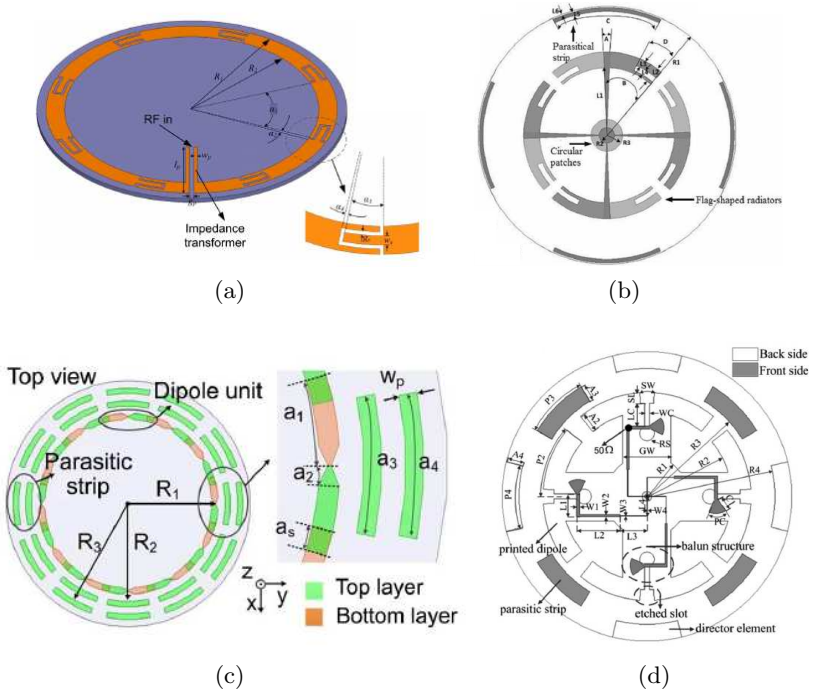

(a) (b)

(c) (d)

Figure 2.15: Wideband magnetic dipoles from (a) [107], (b) [113], (c) [114], and (d) [115]

Furthermore, looking at the topology of these magnetic dipoles, it seems difficult to easily exploit and adapt such antenna structures for designing a grounded wideband VA. The conception of the proposed VA, called the "Two Season VA", is all the more arduous because it requires both x- and y-oriented magnetic dipoles and a z-oriented electric monopole.

2.4.3 Conclusion

Through the brief state of the art of wideband electric and magnetic dipoles, it can be found that designing a wideband and passive VA is very difficult, especially a grounded VA. Although there are several electric dipoles/monopoles that can be interesting to consider for designing

a wideband VA, only a few wideband magnetic dipoles/monopoles have been published before the start of this Ph.D. work in October 2015. From this survey, it also becomes clear how challenging it is to design a magnetic dipole that simultaneously has a large operating bandwidth, an omnidirectional RP with a minimal gain variation, and a small size. That is why the first step in designing a wideband grounded VA is to design the wideband magnetic dipoles.

2.5 The Two Season vector antenna design

The following section highlights the concepts used for designing a passive and wideband grounded VA, which is referred to as the "Two Season VA" in the remainder of this work. As explained above, the first step consists in designing the wideband magnetic dipoles, which is covered in the first part of this section. The next part will be devoted to the conception of the strictly speaking Two Season VA, which enables as a typical grounded VA the measurement of the components H_x, H_y and E_z of an incoming EM-wave in the upper hemisphere.

2.5.1 Design of the magnetic dipoles

Before proceeding to the design of the Two Season VA, let us start with the design of its constitutive magnetic dipoles.

2.5.1.1 Design principle and methodology

The underlying design principle of a wideband magnetic dipole is to synthesize an omnidirectional RP in the E-plane over a large frequency range. In order to meet this criterion, a study was carried out on the basis of the preliminary work published by Chu in 1959 concerning the use of a circular array composed of identical elements to obtain an omnidirectional RP [116]. Specifically, he analyzed the relationship between the number of radiating elements and the gain variation as the radius of the circular array varies. The following presents the design procedure of circular arrays with omnidirectional RP.

Let us consider the array configuration depicted in Fig. 2.16 and assume that each element is identical, equally-spaced on the circle, fed in phase and radiate a symmetrical RP.

The RP of a single radiating element can be expressed as a finite Fourier cosine series as follows

$$F(\phi') = \sum_{n=1}^{N} A_n \cos(\phi')^n, \tag{2.17}$$

with A_n the Fourier cosine series coefficients, and ϕ' the modified azimuth centered on the s_i-th element of the array (i.e., $\phi' = 0$ at $\phi = s_i \frac{2\pi}{S}$ with $s_i \in [\![1; S]\!]$). Therefore, by applying the superposition theorem and after some manipulations, the total far-field pattern TF in the plane of the array (i.e., $\theta = 90°$) is approximately [116]

$$TF(\phi) \approx S \sum_{n=1}^{N} A_n (-j)^n \frac{\mathrm{d}^n}{\mathrm{d}Z^n} \left[J_0(Z) + 2j^S J_S(Z) \cos(S\phi) \right], \tag{2.18}$$

where $Z = \frac{2\pi}{\lambda} a$ is the circumference of the array expressed in wavelengths, and J_α is the ordinary Bessel function of the first kind for the integer orders α equal to 0 or S.

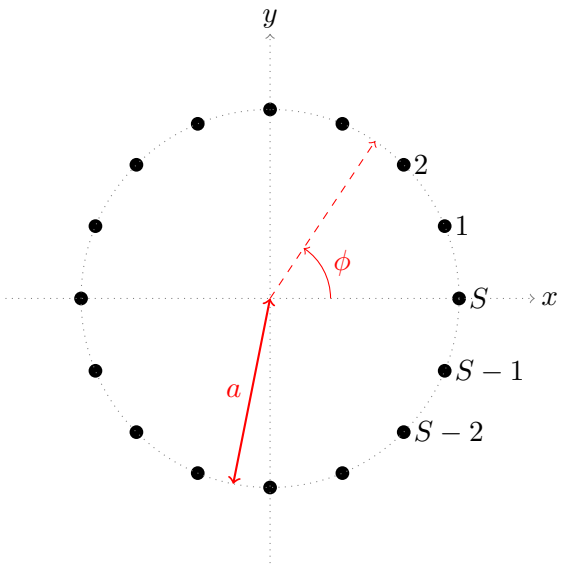

Figure 2.16: Geometry of a circular array with radius a and S equally-spaced radiating elements

Furthermore, it can be noted from Eq. 2.17 and Eq. 2.18 that the use of elements which radiate already an omnidirectional pattern (i.e., elements such as $F(\phi') = A_0$) is not really suited. Indeed, for specific values of Z, the fluctuations[1] in the total far-field pattern approach to infinity. This occurs independently of S when $J_0(Z)$ tends to zero. Hence, the minimum number of terms required to express a RP from Eq. 2.17 is two, which can be expressed as

$$F(\phi') = A_0 + A_1 \cos(\phi'). \tag{2.19}$$

This type of RP expression corresponds to that of a vast number of directional antennas. In this case, Eq. 2.18 can be re-written as follows

$$TF(\phi) \approx S\left(A_0\left[J_0(Z) + 2j^S J_S(Z)\cos(S\phi)\right] - jA_1\frac{\mathrm{d}}{\mathrm{d}Z}\left[J_0(Z) + 2j^S J_S(Z)\cos(S\phi)\right]\right). \tag{2.20}$$

For radiating elements having a pattern of the form $1+\cos(\phi)$ or $1+\frac{1}{2}\cos(\phi)$, the fluctuations in the omnidirectional plane are plotted as a function of Z and S in Fig. 2.17. As it could be so expected, the fluctuations are sensitive to the pattern of the single radiating element. However, it can be seen that the two sets of curves are close for small fluctuations (typically less than 2 dB). Therefore, without knowing the pattern of the radiating element that will be used for designing the circular array, these curves can be used as they are to obtain a fast and reasonable approximation when the objective is to obtain an omnidirectional RP with small fluctuations. Besides, increasing the number of radiating elements improves the omnidirectionality at the expense of a more complex feeding network for a given array radius. Moreover, if the array is to be operated over a large frequency range, the radius should be designed accordingly to the maximal fluctuation acceptable at the highest frequency. Indeed, for a given circular array (i.e., a and S fixed), the fluctuations increase with the frequency. This assumes that the RP of the radiating element remains nearly unchanged in the frequency band of interest.

[1]They are the deviation from omnidirectional RP and are defined as the ratio of the maximum to minimum total far-field pattern, so expressed in dB, is $20\log\frac{|TF_{\max}|}{|TF_{\min}|}$

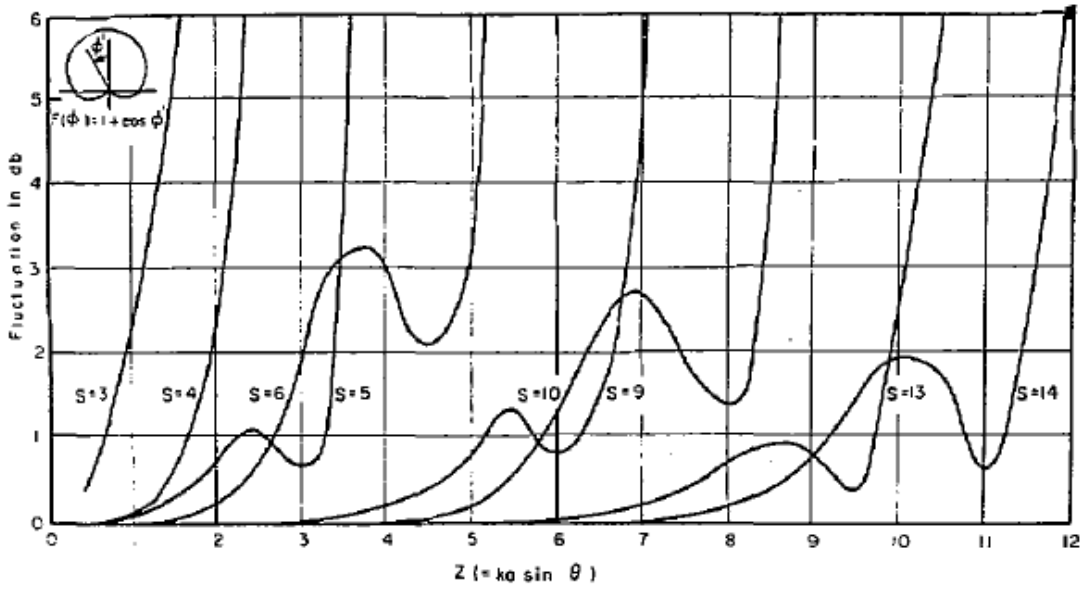

(a)

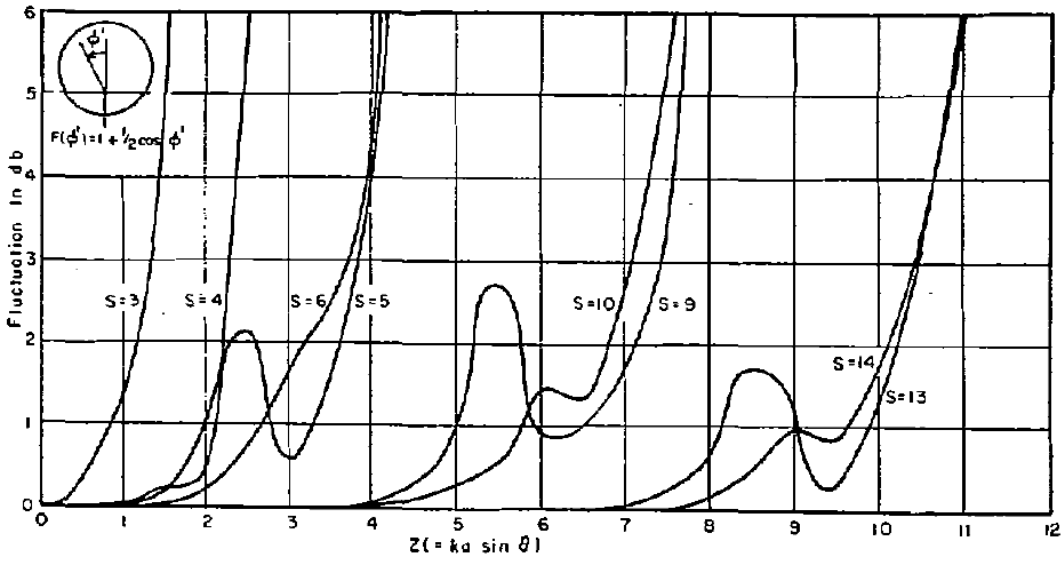

(b)

Figure 2.17: Fluctuations in the omnidirectional RP of a uniform circular array composed of S radiating elements having a RP of the form: (a) $1+\cos(\phi)$ [116] and (b) $1+\frac{1}{2}\cos(\phi)$ [116]

Using Fig. 2.17, a circular array of radius 76.5 mm composed by eight wideband directional radiating elements is expected to achieve a nearly omnidirectional RP at 3.4 GHz with some fluctuations lower than 2 dB. This upper frequency of operation was chosen arbitrarily allows in particular to cover the radiolocation service that is allocated in the band 2.7 GHz – 3.4 GHz (see Table 1.1). The choice of eight elements is a good trade-off between omnidirectionality and feeding-network complexity. All that remains to synthesize an omnidirectional RP in the E-plane over a large frequency range, and consequently design a wideband magnetic dipole, is to choose the proper wideband radiating element that provides the correct polarization in the plane of the array and a RP that remains constant over the frequency range of interest.

2.5.1.2 Choice of the array element, the Vivaldi antenna

As stated in Section 2.2.4, the TSA is one of the conventional traveling-wave antennas, which is well-known for exhibiting a directive radiation pattern with a moderate gain over a wide bandwidth [72]. This antenna consists of etching a tapered slot into a thin layer of metal without or with a dielectric substrate holding it. The first TSA was introduced in 1974 by Lewis *et al.* [117]. Shortly afterward, Gibson designed an exponentially tapered slot, also referred as Vivaldi antenna, which provides a constant beamwidth in the E-plane over the frequency range of operation [118]. As illustrated in Fig. 2.18, the exponential taper profile (1) is commonly defined as follows

$$x = c_1 e^{\mathrm{R}z} + c_2, \tag{2.21}$$

with

$$c_1 = \frac{x_2 - x_1}{e^{\mathrm{R}z_2} - e^{\mathrm{R}z_1}},$$

and

$$c_2 = \frac{x_1 e^{\mathrm{R}z_2} - x_2 e^{\mathrm{R}z_1}}{e^{\mathrm{R}z_2} - e^{\mathrm{R}z_1}},$$

where R is the opening rate, $\mathrm{P}_1(x_1, z_1)$ and $\mathrm{P}_2(x_2, z_2)$ indicate the start and end points of the slotline, respectively. Several configurations of TSAs, which include in particular the linearly tapered slot antenna (LTSA, see Fig. 2.19(a)), the constant width slot antenna (CWSA, see Fig. 2.19(b)) and the Vivaldi antenna have been analyzed in [119]. The shape of the taper profile of the antenna has a significant impact upon the beamwidth, as well as on the sidelobe level. In practice, the widest beamwidth and the lowest sidelobes are achieved through a Vivaldi antenna, followed by a LTSA and then a CWSA when compared with the same length and aperture width on a given substrate. Moreover, TSAs radiate a linearly polarized electric field parallel to the plane of the antenna and towards the tapered opening transition axis (denoted in Fig. 2.18 by $\hat{x}$). Other noticeable advantages of any TSAs are their planar structure, low-profile, light-weight, simple construction and low-cost characteristics.

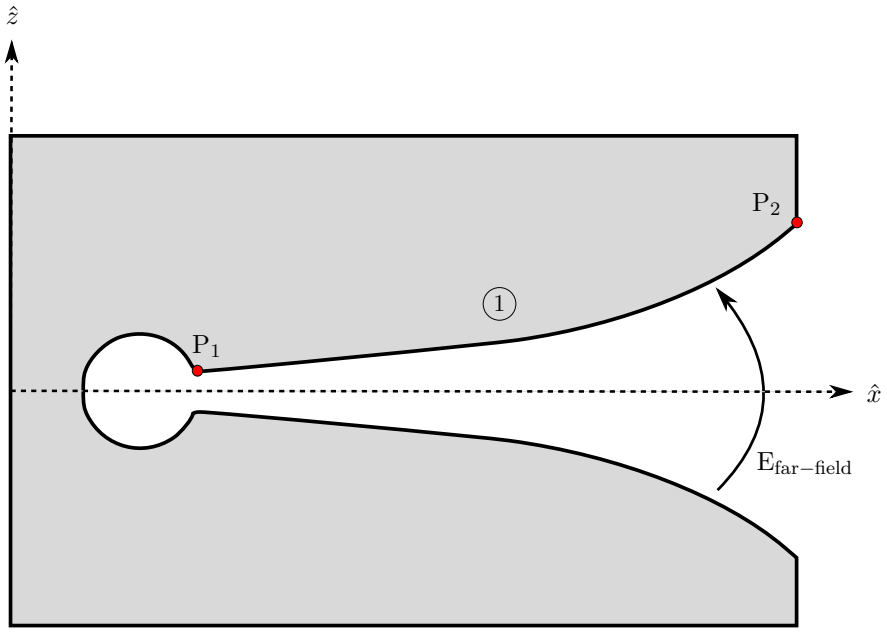

Figure 2.18: Topology of a Vivaldi antenna

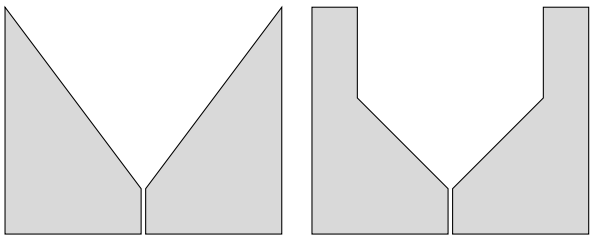

Figure 2.19: Examples of TSAs: (a) LTSA and (b) CWSA

For the aforementioned reasons, the Vivaldi antenna is a good candidate for designing a wideband magnetic dipole from a circular array in order to achieve an omnidirectional RP in the E-plane (corresponding to the longitudinal plane of the array) over a wide frequency range. Simultaneously with this Ph.D. work, a circular array composed of eight Vivaldi antennas (see Fig. 2.20(a)) and exhibiting a nearly omnidirectional RP in the E-plane but with some undesirable ripples (up to 4 dB) in the LTE (Long Term Evolution) band ranging from 1.9 GHz to 2.7 GHz was reported by See *et al.* in 2015 [120]. Another example was published by Liu *et al.* in 2017 [121] and this time consists of sixteen Vivaldi antennas arranged in a circular array (see Fig. 2.20(b)) . This array provides an omnidirectional RP (with gain variations below 3 dB from 1.28 GHz to 8 GHz) and an impedance bandwidth from 1.28 GHz to 11.51 GHz. It can be noted that no detailed design methodology was provided in [120, 121]. Only the impedance bandwidth of the circular array was studied through parametric studies in [121] as a function of the number of elements and the electrical connection or not of the elements of the array. Overall, the analysis in this study finds that the lower cutoff frequency is mainly determined by the radius of the size of the array under the condition that enough connected elements are arranged in the array. These antennas are illustrative examples to validate the underlying design principle described in Section 2.5.1.1.

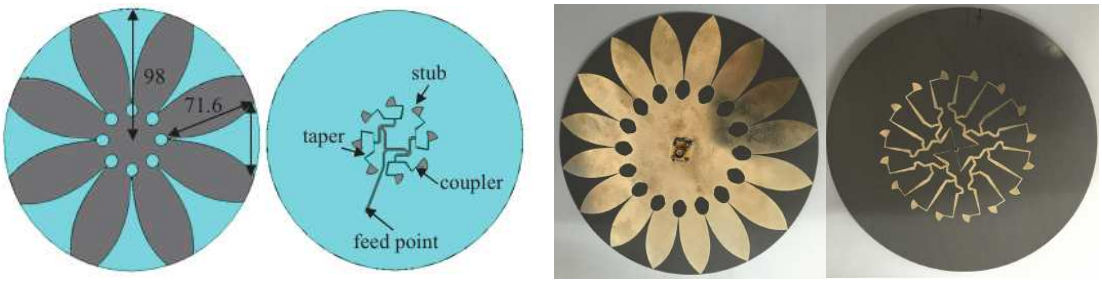

(a) (b)

Figure 2.20: Top and back views of wideband magnetic dipoles designed from a circular array of Vivaldi antennas: (a) [120], and (b) [121]

2.5.1.3 Topology of the magnetic dipoles

The geometry of the magnetic dipoles investigated in this thesis is shown in Fig. 2.21. Each dipole consists of a semi-circular array of four Vivaldi antennas mounted over a ground plane. According to the well-documented image theory, the RP of the grounded array of four Vivaldi antennas is equivalent in the upper half-space to the RP of the array of eight Vivaldi antennas.

Parametric studies on l_1, w_1 and the opening rate R (defined in Eq. 2.21) have been carried out to simultaneously: maximize the bandwidth, minimize the lower frequency of operation f_L, and limit the mid-band amplitude of the VSWR. The higher operating frequency is determined by the undesirable emergence of grating lobes resulting in omnidirectionality defects. The results of these parametric studies are given in Appendix D.1.

Each 50 Ω input port is connected to the 1:2 microstrip line power splitter fabricated using the T-junction. This junction is followed by the impedance transition line to connect the 65 Ω characteristic impedance line to the Vivaldi input port. The slotlines associated with each Vivaldi antenna are electromagnetically coupled through the microstrip-to-slot transition that features the circular cavity and the 80° radial stub in order to broaden the bandwidth [122]. Using $r_c = r_s$, a parametric study has been performed to minimize the lower operating frequency f_L (see also Appendix D.1). According to the geometry of the two ports feeding-section, a 180° phase differential has to be applied to obtain the RP of the magnetic dipole.

The Vivaldi antennas present an opening rate R of 0.11 mm^{-1} and are printed on a low-cost 0.8 mm thick FR4 substrate (dielectric constant of 4.3 and loss tangent of 0.025). The array is mounted over an octagonal ground plane of side length e. Its dimensions are specified in Table 2.1.

Parameter	W_t	H_t	w_1	w_2	l_1	l_2	l_3
Value (in mm)	153	76.5	43.8	14.4	50.5	15	26.7
Parameter	g	r_c	r_s	w_3	w_4	w_5	e
Value (in mm)	0.6	5.5	5.5	6.1	1	1.6	125

Table 2.1: Dimensions of the semi-circular arrays used for designing the Two Season VA

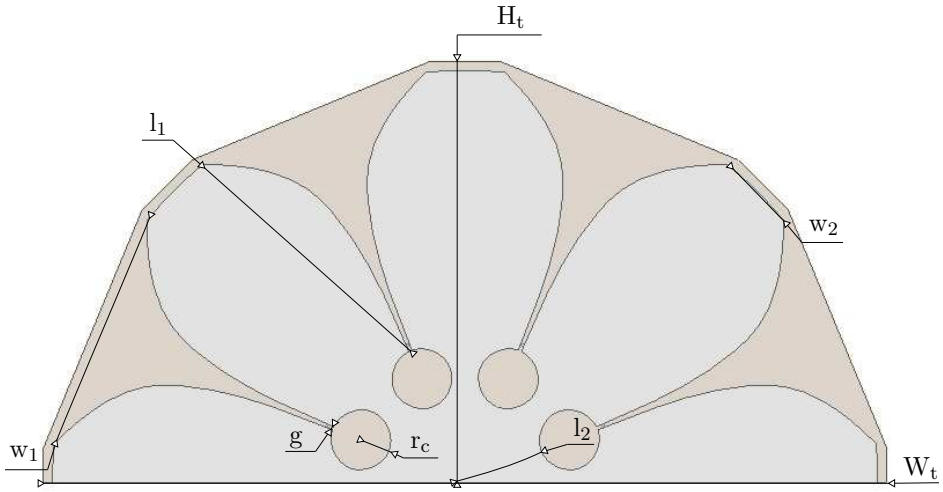

(a)

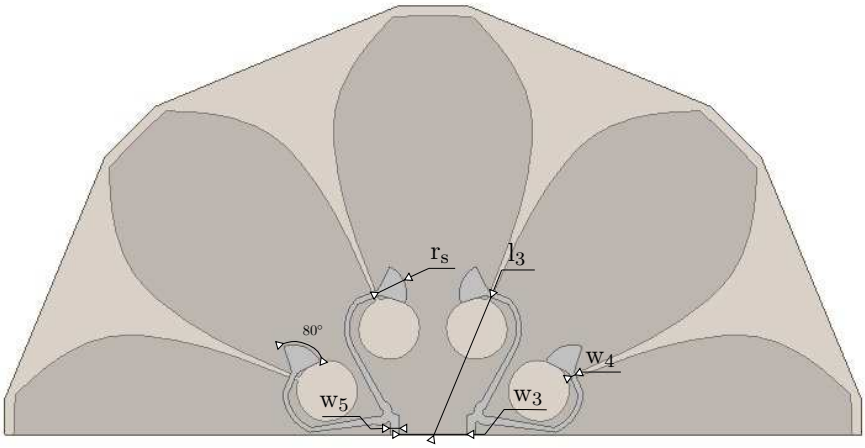

(b)

Figure 2.21: Topology of the semi-circular used for designing the Two Season VA mounted over a ground plane (not depicted in these figures): (a) Radiating surface and (b) Feeding-section.

The electrical performances regarding the impedance matching and radiation properties of this semi-circular array mounted over an infinite ground plane and used as a magnetic dipole (i.e., a 180° phase differential is applied to its feeding ports) are given in Appendix D.2.

2.5.2 The reconfigurable Two Season vector antenna

Having discussed how to construct a wideband magnetic dipole, the final part of this section addresses the design of the grounded VA whose topology is depicted Fig. 2.22. The Two Season VA is intended to estimate the DoA of vertically-polarized EM-waves in the upper hemisphere through the measurement of the components H_x, H_y and E_z. As a reminder, the measurement of these components is associated with RPs of two magnetic dipoles oriented along the $\hat{x}$-axis and $\hat{y}$-axis and one electric monopole oriented the $\hat{z}$-axis. It can be observed from Fig. 2.22 that the

Two Season VA consists of two orthogonal and colocated semi-circular arrays of Vivaldi antennas, which have been previously described during the conception of a wideband magnetic dipole. This VA is mounted over a metallic and octagonal surface in view of embedded applications.

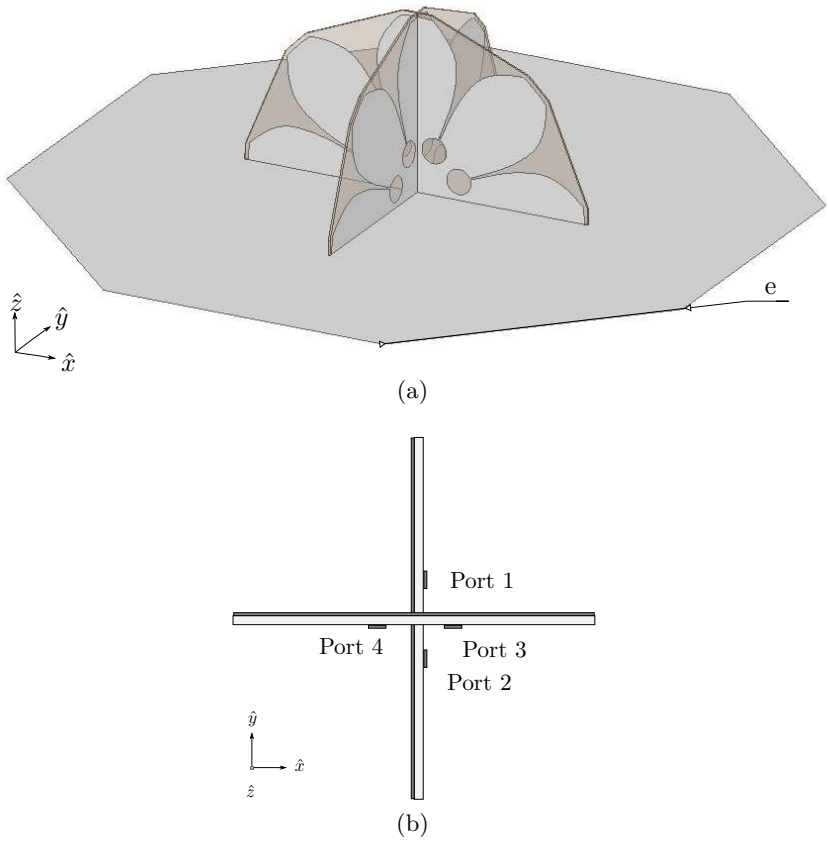

Figure 2.22: Topology of the Two Season VA: (a) 3-D view and (b) Top view

It can also be observed that the Two Season VA is a 4-port VA. In practice, the amplitude and phase of the received signal are sequentially measured at each port, while the other ports are impedance matched. Next, each EM-wave component is derived from the combination or summation of signals that are simultaneously received at the four ports of the VA, after assigning to every signal an appropriate weighting. According to the Two Season VA topology, it is clear that this antenna enables the measurement of the x-component and y-component of the magnetic field using the arrays positioned along the y-axis (Ports 1 and 2) and the x-axis (Ports 3 and 4), respectively. Meanwhile, the z-component of the electric field is measured by recombining all the output ports in phase [123]. Indeed, the Two Season VA can act as a virtual electric monopole oriented along the $\hat{z}$-axis (see the RPs in Section 2.6.2). The three sets of weighting coefficients assigned to the received signals at the antenna ports for deriving the three components E_z, H_x, and H_y of the incoming EM-wave are summarized in Table 2.2. Throughout this Ph.D. thesis, these three sets of weighting coefficients are denoted by the acronym RPC 0, which means Radiation Patterns Combination. Finally, in accordance with the approach used to measure these EM-wave components, the Two Season VA can be viewed as a RP reconfigurable VA.

RPC	Measured Component	Port 1	Port 2	Port 3	Port 4
0	H_x	1	-1	0	0
	H_y	0	0	1	-1
	E_z	1	1	1	1

Table 2.2: Sets of weighting coefficients assigned to the signals received at the four ports of the Two Season VA for measuring the three EM-wave components H_x, H_y and E_z

2.6 Electrical performances of the Two Season vector antenna

So far this chapter has focused on the design of the reconfigurable Two Season VA. As mentioned in the previous chapter, the estimation performances of any direction finders are notably subject to the electrical characteristics of the constituting DF antenna. The following section will assess the electrical performances in terms of impedance matching and radiation properties of this antenna. As shown in Fig. 2.23, a prototype has been manufactured according to the parameters given in Table 2.1. Hence, the electrical performances are appraised not only through full-wave EM simulations with Ansys HFSS but also from measurements performed in the LAAS-CNRS anechoic chamber (refer to Appendix E for more information regarding this anechoic chamber). Comparisons between simulation and measurement results are also carried out in order to experimentally validate the electrical performances.

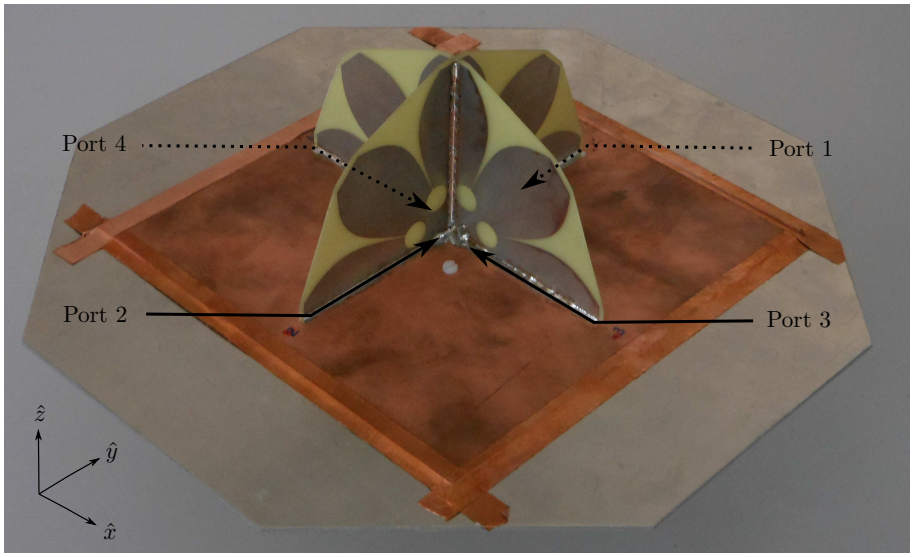

Figure 2.23: Photograph of the Two Season VA and ports numbering description

2.6.1 Impedance matching and mutual coupling

As indicated previously in Section 1.1.5, one of the performance descriptors of a direction finder is the frequency coverage. The latter depends in particular on the impedance matching of the DF antenna.

The simulated and measured VSWR of the Two Season VA are displayed in Fig. 2.24. According to the method used for measuring the components of an incoming EM-wave through the RP reconfigurability of the VA (see Section 2.5.2), only the VSWR at port i ($i \in [\![1, 4]\!]$) has to be considered here employing the classical S-parameters definition. Furthermore, only the simulated VSWR at port 1 is plotted for symmetry reasons. The simulated and measured impedance bandwidths (for a VSWR smaller than 2.3) are of 1.71:1 from 2.08 GHz to 3.56 GHz and of 1.69:1 from 2.10 GHz to 3.55 GHz, respectively. Using Eq. B.3, this VSWR value corresponds to a power loss of less than 16% at the antenna terminals due to impedance mismatch.

Overall, a good agreement is obtained between the simulated and measured results. The slightly discrepancy between the measured VSWR can be attributed to manufacturing imperfections. Moreover, the redesign of the feeding section (T-junctions and impedance transition lines) in Section 3.2.1 will improve the VSWR at 2.8 GHz and even increase the operating bandwidth. The VA is included in a half-sphere within a $0.52\lambda_0$ radius and mounted on a finite metallic and octagonal support with a circumcircle radius of $1.14\lambda_0$, where λ_0 is the free space wavelength at 2.10 GHz.

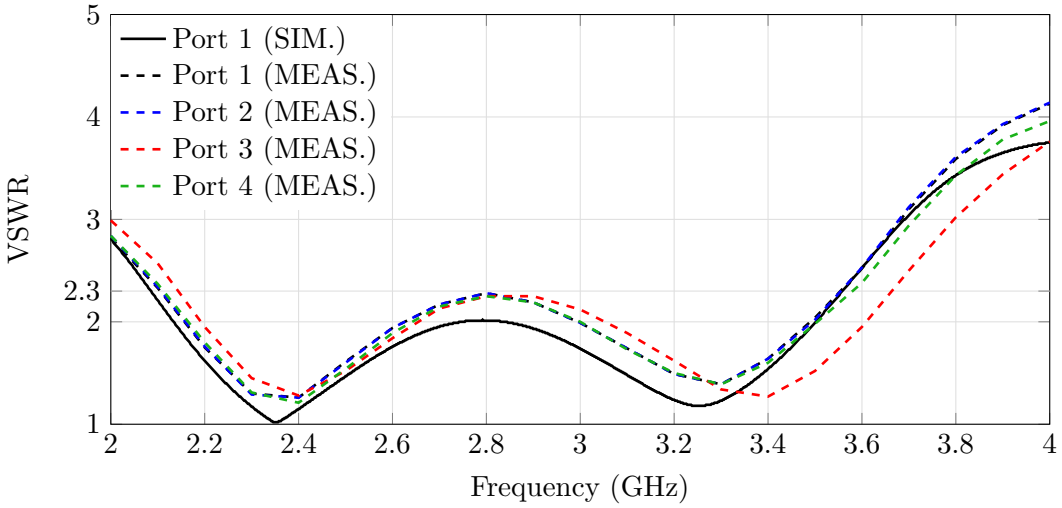

Figure 2.24: Simulated and measured VSWR of the Two Season VA

Fig. 2.25 shows the measured isolation between port 1 and the three other ports of the Two Season VA. The measured isolation S_{1j} ($j \in [\![2, 4]\!]$) corresponds to the standard case where the ports 1 and j are connected to the vector network analyzer while the other ports are impedance matched. It can be observed that the mutual coupling between the port 1 and the other ports does not exceed -23 dB over the operating bandwidth. Furthermore, the same level of isolation is obtained at the other ports. This good isolation between the Two Season VA ports is essential for estimating the DoA of an incoming EM-wave from a vectorial approach.

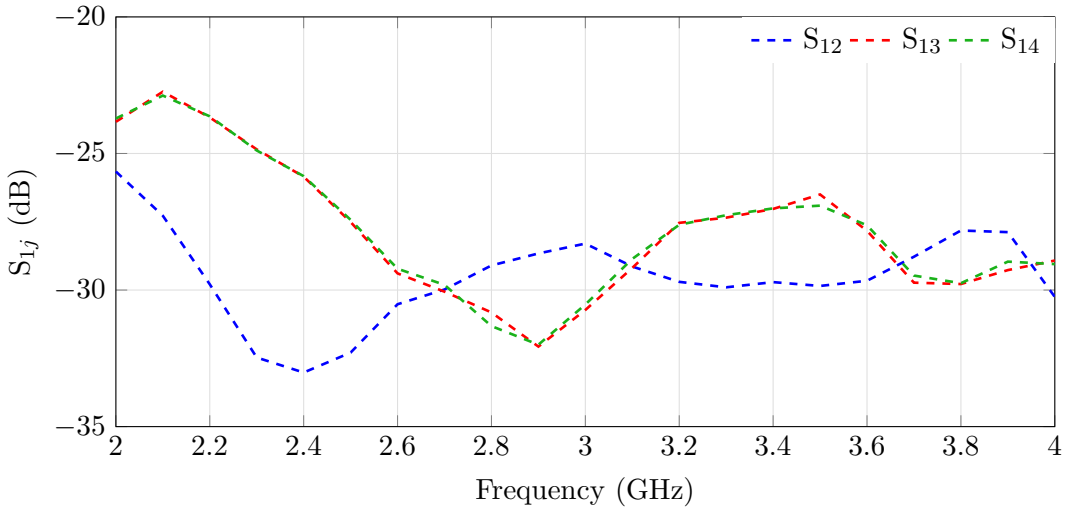

Figure 2.25: Measured isolation at port 1 of the Two Season VA

2.6.2 Radiation patterns

Most of the performance descriptors of a DF antenna is substantially related to its RPs. Examples are the angular and frequency coverages as well as the estimation accuracy. In this section, the measured RPs of the reconfigurable Two Season VA are analyzed and compared with simulation results at three frequencies in the VA bandwidth, which are 2.2 GHz, 2.8 GHz and 3.4 GHz. These frequencies approximatively correspond to the lower, center and upper frequencies of the bandwidth. It can be noted that the measurement of the RPs of the wideband magnetic dipoles and electric monopole incorporated in the VA were performed from post-processing, as follows:

- Each port of the antenna was successively fed while the other ports were impedance matched, and four RPs (one pattern per port) were measured over the entire VA frequency band.
- Since the antenna topology has a rotation symmetry, the radiation is characterized only for $\phi \in [0°; 90°]$ and $[180°; 270°]$ with a 5° step in azimuth and for $\theta \in [0°; 90°]$ with a 2° step in elevation. RPs of each VA port are then reconstructed over the 3-D upper half-space from their symmetrical counterparts. Some of these measured RPs are provided in Appendix F.2.
- The RPs of the magnetic dipoles and electric monopole were derived from the appropriate combinations of these four patterns (that is, by using the magnitude/phase specified in Table 2.2 to be impressed at the four ports of the VA).

Besides, the same octagonal ground plane was used for both EM simulations and measurements. Moreover, simulation results with an infinite ground plane are also given here and in Appendix F.1 in order to analyze the impact of the finite ground plane on the radiation characteristics.

Fig. 2.26 and Fig. 2.29(a) present the realized gain of the Two Season VA in the $\hat{y}\hat{z}$-plane and $\hat{x}\hat{z}$-plane when the amplitude/phase for measuring the component H_x (see Table 2.2) are impressed at the four ports of the antenna at the three frequencies of interest, respectively. Looking at these figures, it is apparent that the combined RPs are similar to the ones of a magnetic dipole

oriented along the $\hat{x}$-axis in its E-plane (i.e., omnidirectional RP) and H-plane (i.e., 8-shape RP). Closer inspection of Fig. 2.26 shows that the RP of this magnetic dipole is quasi-omnidirectional with some undesirable ripples, which can be attributed to the effect of the finite size of the ground plane. Indeed, an omnidirectional RP in the E-plane is achieved with the infinite ground plane. However, even with this ground plane configuration and in accordance with Chu's theory (see Section 2.5.1.1), some ripples occur when the frequency increases, but these are less than 2 dB over the entire bandwidth. As a reminder, this level of fluctuation was retained during the design process. By the way, it can be noted that the presence of the second semi-circular array oriented along the $\hat{x}$-axis and constituting the Two Season VA does not disrupt the RP required to measure the component H_x of an incoming EM-wave. Indeed, no significant differences were found between the RPs given in Fig. 2.26 and the ones displayed in Fig. D.8 where only one semi-circular array is considered. For obvious symmetry reasons, the RPs of the Two Season VA associated with the measurement of the component H_y (see Table 2.2) are not presented here.

Fig. 2.27 and Fig. 2.28 set out the realized gain of the Two Season VA in two vertical planes when the amplitude/phase for measuring the component E_z (see Table 2.2) are impressed at the four ports of the antenna at the three frequencies of interest and, respectively. These planes correspond to those defined by $\phi = 45°$ and $\phi = 90°$ (i.e., the $\hat{y}z$-plane). As for Fig. 2.29(b), the gain is displayed in the $\hat{x}y$-plane. The RPs identified in these figures are the ones of an electric monopole oriented along the $\hat{z}$-axis in its E-plane (i.e., 8-shape RP) and H-plane (i.e., omnidirectional RP). As the frequency increases, it can be observed from Fig. 2.27 and Fig. 2.28 that undesirable blind directions appear in the RP when then VA is mounted over an infinite ground plane (θ close to 70° for $\phi = 0° \pmod{90°}$).

As shown from Fig. 2.26 to Fig. 2.28, a relatively good correlation between the simulated and measured results is obtained. Finally, these RPs clearly indicate the Two Season VA can measure the components H_x, H_y and E_z of an incoming EM-wave thanks to its RP reconfigurability through the three sets of weightings denoted by RPC 0.

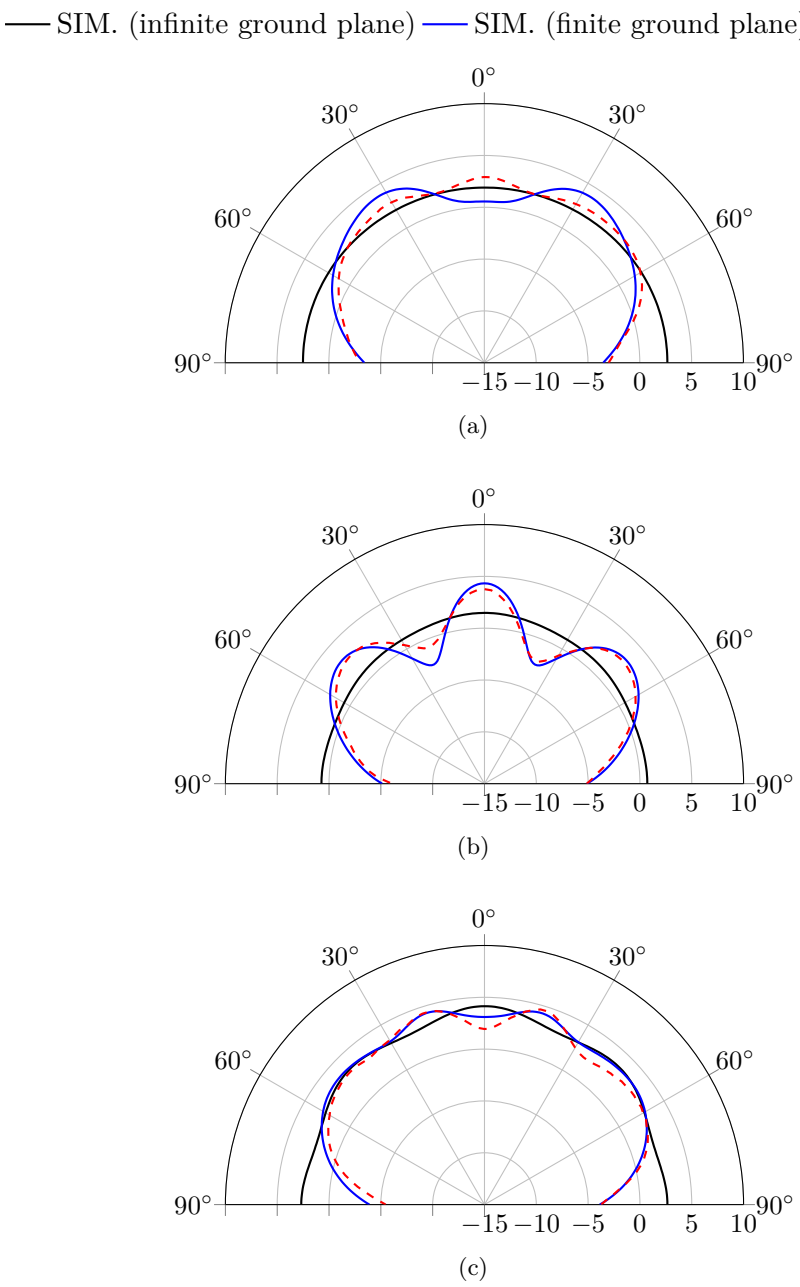

Figure 2.26: Simulated and measured realized gain of the Two Season VA in θ-polarization and in the $\hat{yz}$-plane associated with the amplitude/phase impressed at the four ports of the antenna for measuring the component H_x (specified in Table 2.2) at: (a) 2.2 GHz, (b) 2.8 GHz, and (c) 3.4 GHz

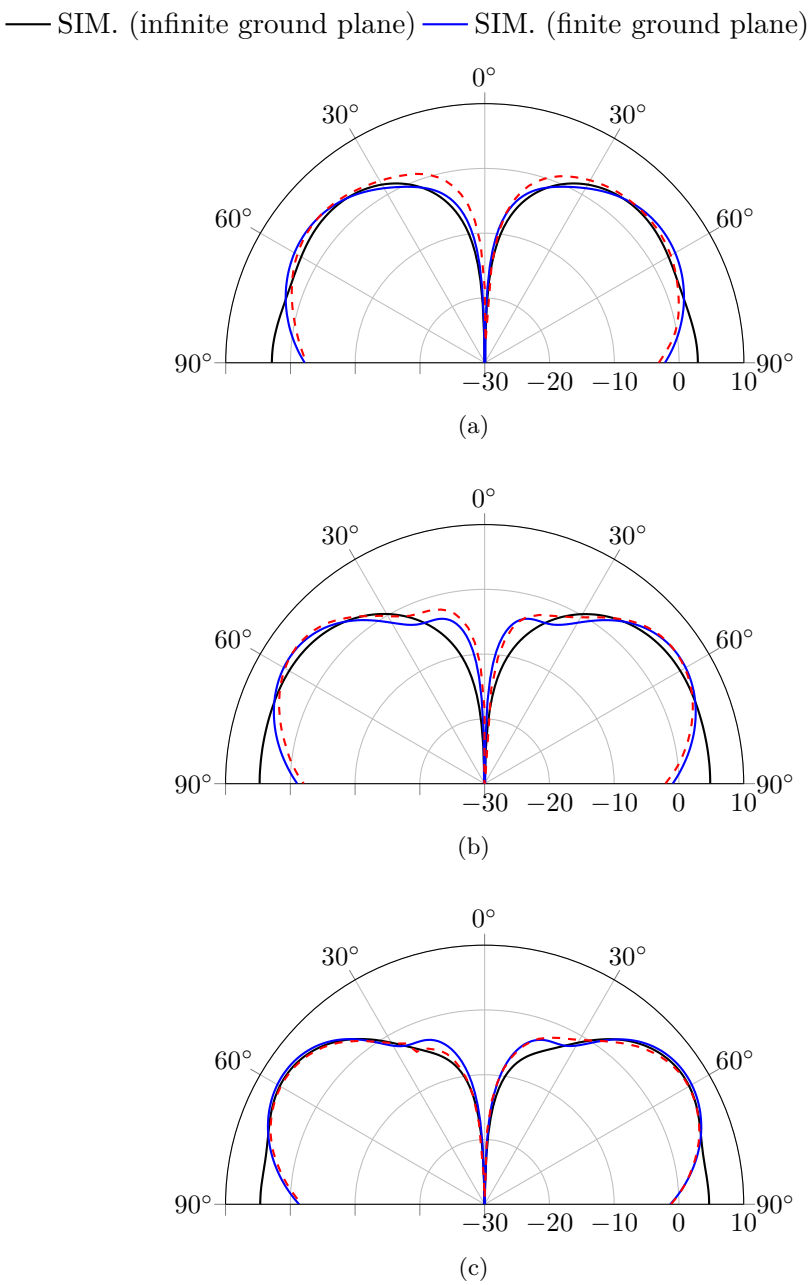

Figure 2.27: Simulated and measured realized gain of the Two Season VA in θ-polarization and in the $\phi = 45°$ vertical plane associated with the amplitude/phase impressed at the four ports of the antenna for measuring the component E_z (specified in Table 2.2) at: (a) 2.2 GHz, (b) 2.8 GHz, and (c) 3.4 GHz

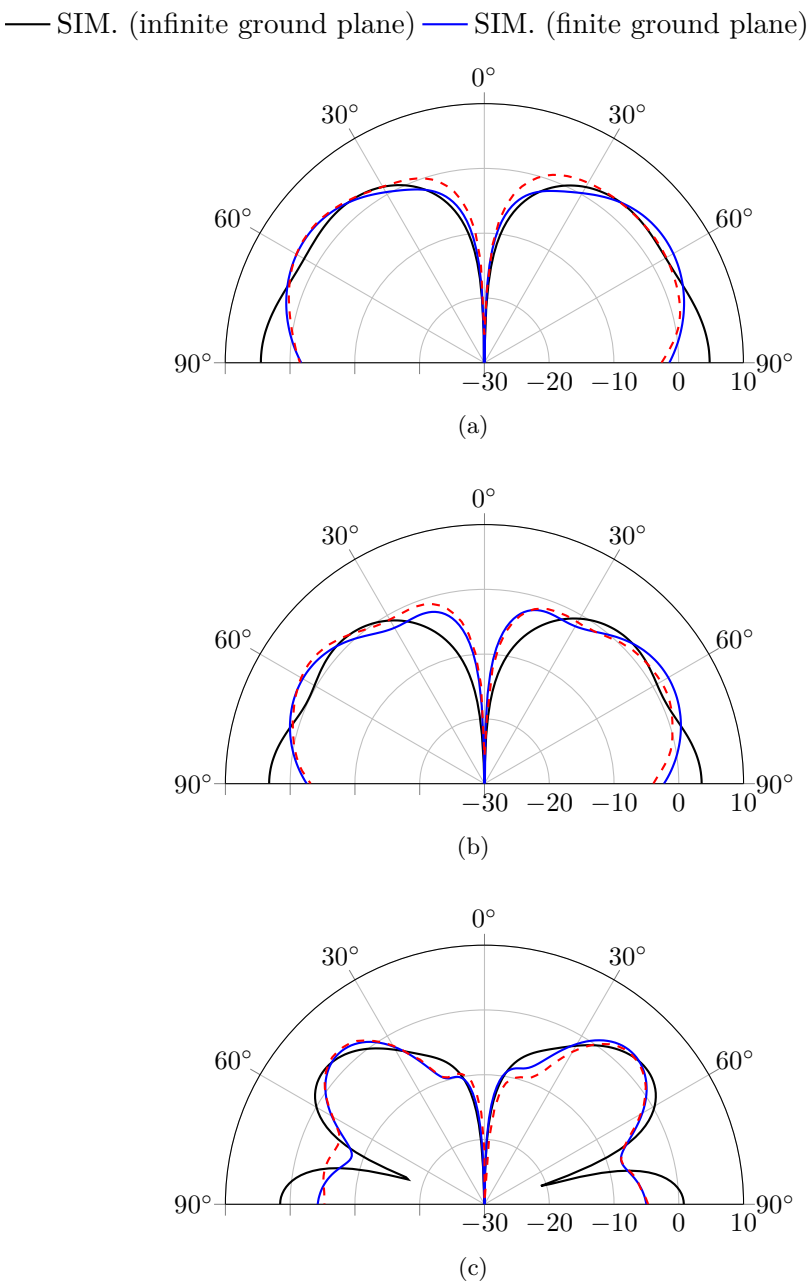

Figure 2.28: Simulated and measured realized gain of the Two Season VA in θ-polarization and in the $\hat{yz}$-plane associated with the amplitude/phase impressed at the four ports of the antenna for measuring the component E_z (specified in Table 2.2) at: (a) 2.2 GHz, (b) 2.8 GHz, and (c) 3.4 GHz

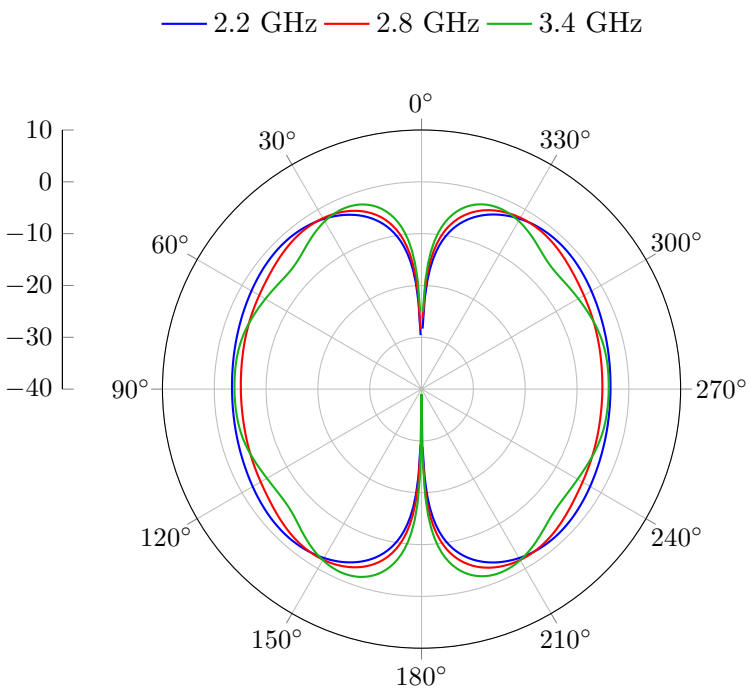

(a)

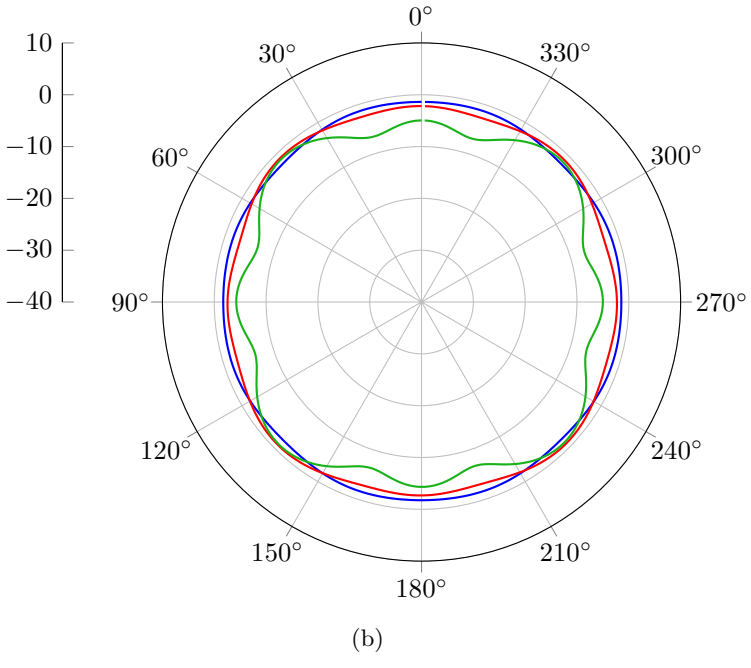

(b)

Figure 2.29: Simulated realized gain in θ-polarization and in the $\hat{xz}$-plane of the Two Season VA (mounted on the octagonal metallic support) at several frequencies in the bandwidth when the amplitude/phase specified in Table 2.2 are impressed at the four ports of the antenna for measuring the component: (a) H_x and (b) E_z

2.6.3 Efficiency

The simulated total efficiency (defined in Eq. B.12) of the Two Season VA is depicted in Fig. 2.30, when the antenna is mounted over the octagonal ground plane. Specifically, the total efficiency corresponds to the ratio of radiated to input power of the VA considering any occurring reflections at the feeding location. According to method used for measuring the three component H_x, H_y and E_z of an incoming EM-wave, only the efficiency at port i ($i \in [\![1,4]\!]$) has to be considered. Besides, only the total efficiency at port 1 is displayed in Fig. 2.30 for symmetry reasons. The total efficiency is evaluated from 2 GHz to 4 GHz with a frequency step of 0.1 GHz in order to cover the Two Season VA bandwidth. It can be observed that the simulated total efficiency exceed 80% over the entire bandwidth and consequently, good 3-D DF performances may be expected.

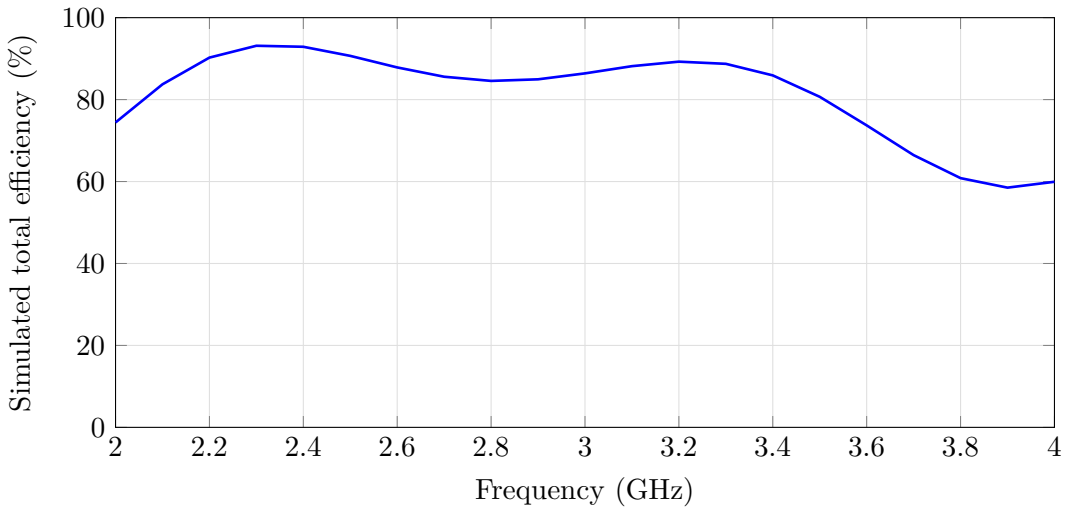

Figure 2.30: Simulated total efficiency of the Two Season VA (mounted on the octagonal ground plane)

2.7 Direction finding performances of the Two Season vector antenna

After discussing the electrical characteristics of the Two Season VA that are seemingly well suited for 3-D DF over a wide frequency range, it is now time to evaluate and compare its simulated and measured DF performances. As a reminder, the reconfigurable Two Season VA is intended to estimate the DoA of vertically-polarized EM-waves in the upper hemisphere through the measurement of the components E_z, H_x and H_y. In this section, the DF performances are assessed using several descriptors described in Section 1.1.5. An analysis of the simulated ambiguity risk and CRB is first provided. Then, the simulated and measured estimation accuracies are evaluated as well as the sensitivity of the prototype.

2.7.1 Scenario used for the direction finding performances evaluation

Before assessing the DF performances of the Two Season VA, it is first necessary to define a scenario for this evaluation. Let us consider an incoming vertically-polarized EM-wave ($\gamma = \pi/2$ and $\eta = 0$) in the 3-D upper half-space (along the $+\hat{z}$ axis, i.e. $\phi \in [0°; 360°]$ and $\theta \in [0°; 90°]$) that presents a power density P_s of -105 dBW.m^{-2} at the VA location. To obtain a good view of the DF performances across the VA bandwidth, the evaluation is assessed at the three following frequencies: 2.2 GHz, 2.8 GHz and 3.4 GHz. Moreover, only the three sets of weighting coefficients (RPC 0) reported in Table 2.2 are assigned to the signals received at the four ports of the Two Season for measuring the incoming EM-wave components H_x, H_y and E_z. These three sets are sufficient, at least in principle, to estimate the DoA of the incoming vertically-polarized EM-wave. The DoAs are computed from the MUSIC algorithm (described in Appendix A) and full-wave EM simulations (Ansys HFSS) or measurement data. Besides, the noise floor power level P_n at the receiver output is of -111 dBm (see Appendix G.2) and consequently, the ratio of the power density of the incoming EM-wave to noise power[2] (PNR) defined by Eq. G.1 is of 36 dB.m^{-2}. Furthermore, following [14], the analysis is carried out for $N = 100$ snapshots per DoA estimation, and the number L of Monte Carlo trials is set to 20. Finally and yet importantly, as some amplitude and phase distortions may eventually occur at the VA outputs, a calibration process (see, e.g., [1, 2]) is used as it is generally applied in practice. The calibration technique applied here is based on the computation of the combined steering vector $\boldsymbol{d}$ from the simulated or measured RPs of the antenna VA radiating elements as described in [14]. All estimation parameters are summarized in Table 2.3.

DoA Algorithm	MUSIC
Number of incoming EM-waves	1
Polarization of the incoming EM-wave	Vertical
Angular coverage	$\phi \in [0° ; 90°]$ and $\theta \in [0° ; 90°]$
Angular resolution	$\Delta\phi = 5°$ and $\Delta\theta = 2°$
Incoming EM-wave power density	-105 dBW.m^{-2}
Noise power level	-111 dBm
PNR	36 dB.m^{-2}
Snapshots per DoA estimation	100
Number of estimations per DoA	20
Frequencies of interest	2.2 GHz, 2.8 GHz, and 3.4 GHz

Table 2.3: Parameters used for evaluating the DF performances

[2]The use of SNR is not suited for the evaluation of the DF performances with a VA, that is why the incoming EM-wave power density to noise ratio (PNR) is introduced to describe the operational situation (refer to Appendix G.1 for further information)

2.7.2 Angular ambiguity risk

The problem of angular ambiguity is in practice related both to the geometry of the DF antenna and to the RP of each antenna element. Conducting an analysis of the angular ambiguity risk is an important step prior to the evaluation of the actual DoA estimation accuracy. Indeed, potential issues associated with the estimation of the DoA in certain angular areas can be uncovered through this analysis.

It may be interesting to begin this study with an analysis of the angular ambiguity spectrum of an ideal VA consisting of three colocated dipoles and measuring the three components E_z, H_x and H_y of an incident vertically-polarized EM-wave in order to establish a reference. Fig. 2.31 displays the ambiguity spectrum of this ideal VA that has been computed analytically using Eq. 1.17. It can be observed that the risk of angular ambiguity is at its highest (i.e., $\alpha_{\min}$=0°) for low elevation angles, that is for θ around 0°. Especially at $\theta = 0°$, there is a singularity attached to the estimation of the azimuth angle ϕ. However, the risk of angular ambiguity can be disregarded in this angular region since the azimuth angle is not really significant. However, no angular ambiguity risk is observed in the rest of the 3-D upper space since $\alpha_{\min}$ values are relatively high.

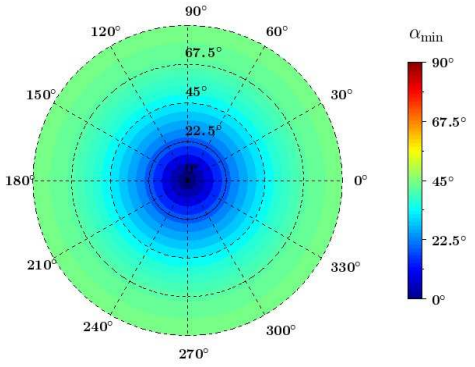

Figure 2.31: 3-D ambiguity spectrum $\alpha_{\min}$ of an ideal VA consisting of three colocated dipoles and measuring the three components E_z, H_x and H_y of an incident vertically-polarized EM-wave. Elevation angles θ are given on the radial axis and azimuth angles ϕ are given on the angular axis.

Fig. 2.32 presents the 3-D ambiguity spectrum of the Two Season VA either mounted on the infinite or octagonal metallic support at the three frequencies of interest when only RPC 0 is used for the estimation of the DoA of the incoming EM-wave. The angular ambiguity was also computed using Eq. 1.17, where $\boldsymbol{d}$ was replaced by the combined steering vector $\boldsymbol{d_c}$ since the Two Season VA is a RP reconfigurable VA. Moreover, the $m-$th component of $\boldsymbol{d_c}$ associated with the m-th set of weightings can be written as follows

$$d_c^m = \boldsymbol{w}^m . \boldsymbol{d}. \tag{2.22}$$

First, it can be noted that the risk of angular ambiguity is at its highest for low elevation angles as might be expected. In addition, the comparison between Fig. 2.31 and Fig. 2.32 helps to analyze the impact of a realistic antenna on the risk of ambiguity. Indeed, unlike the ideal VA, the Two Season VA has a risk of angular ambiguity that increases with the frequency. This can be explained by the fact that the RPs of the Two Season VA exhibit some ripples that increase with the frequency (see Section 2.6.2) and thus, are not similar to the ideal RPs of a VA. Furthermore, it can be pointed out that the the risk of angular ambiguity is higher if the Two Season VA is mounted on a finite size metallic support, especially at 2.2 GHz and 2.8 GHz. In fact, this can be explained by the same reason since the RPs are subject to more fluctuations when the Two Season VA is not mounted on an infinite metallic support. For both ground plane configurations, the risk of angular ambiguity is quite high in the angular zones around $\phi = 0°$ (mod 90°) at 3.4 GHz. It will unfortunately be confirmed subsequently in the analysis of the accuracy of the DoA estimation provided in Section 2.7.4.

2.7.3 Cramer-Rao lower bound

Before evaluating the actual accuracy of the estimation of the DoA of an incoming vertically-polarized EM-wave using the Two Season VA, it may be interesting to begin with the analysis of the estimation performance using the CRB. As a reminder, the CRB corresponds to the theoretical limit of the average precision that can be reached regardless of the applied DF technique (in particular within the framework of this Ph.D. thesis, the MUSIC algorithm). From a technical point of view, the CRLB is given by the inverse of the Fischer information matrix $\mathbf{J}$ (see Eq. 1.5). In this Ph.D., the polarization of the incoming EM-wave is assumed to be known, and the Gaussian noise is spatially invariant with zero-mean. According to these assumptions and the observation model described in Section 2.1.4, the Fischer information matrix $\mathbf{J}$ for estimating the vector parameter $\mathbf{\Omega} = [\theta \ \phi]^{\mathrm{T}}$ can be expressed as follows [124]

$$\mathbf{J} = \begin{bmatrix} J_{\theta,\theta} & J_{\theta,\phi} \\ J_{\phi,\theta} & J_{\phi,\phi} \end{bmatrix}, \tag{2.23}$$

with

$$J_{\mathbf{\Omega}_i,\mathbf{\Omega}_j} = \frac{2N}{\sigma_n^2} \mathfrak{Re} \left\{ \frac{\partial \boldsymbol{d_c}^*}{\partial \mathbf{\Omega}_i} \frac{\partial \boldsymbol{d_c}}{\partial \mathbf{\Omega}_j} \right\}. \tag{2.24}$$

In the same vein, as the work carried out on the risk of angular ambiguity, this study also begins with an analysis of the CRB of an ideal VA[3] consisting of three colocated dipoles and measuring the three components E_z, H_x and H_y of an incident vertically-polarized EM-wave.

[3] $\boldsymbol{d_c} = \boldsymbol{d}$ for an ideal VA composed of short electric and magnetic dipoles

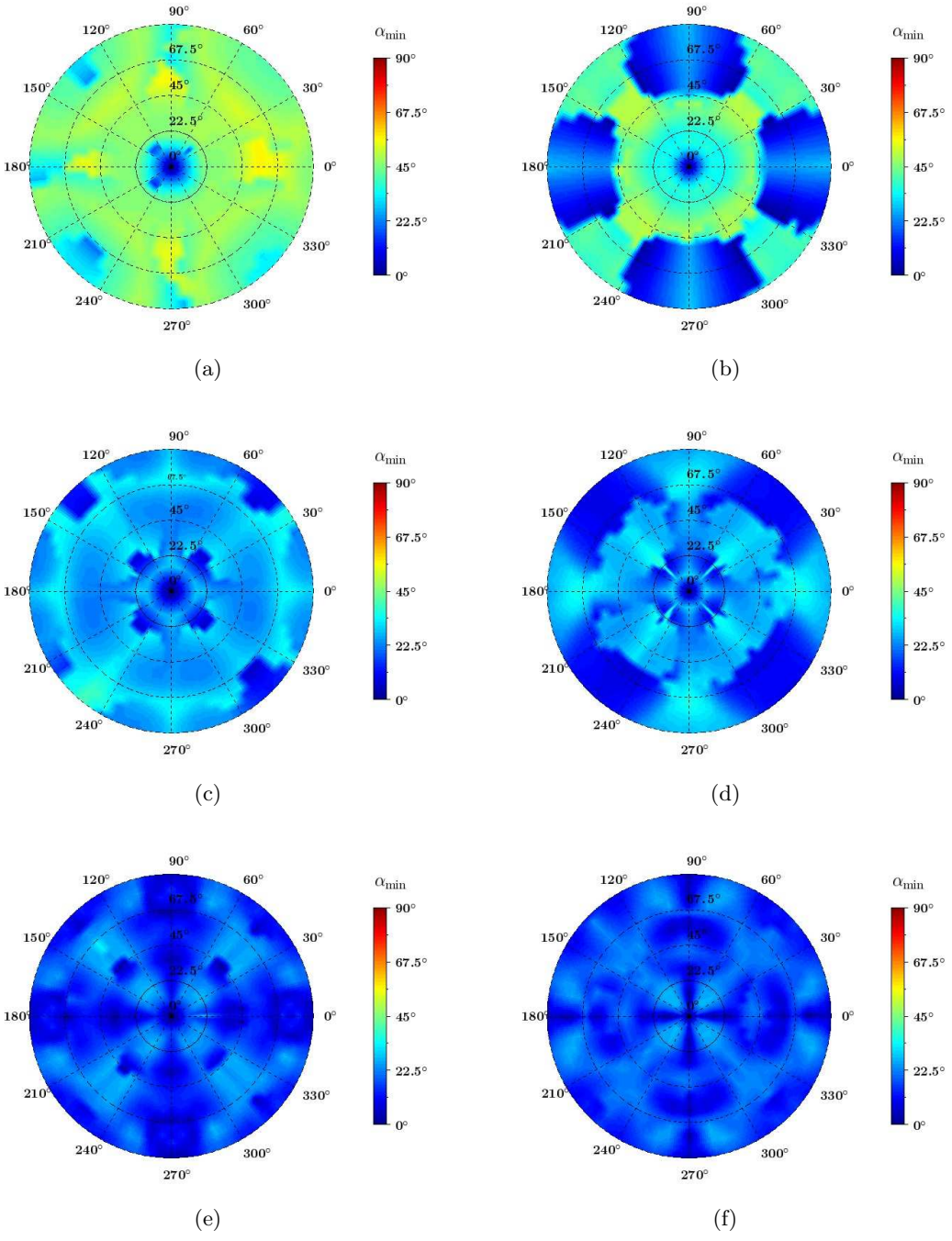

Figure 2.32: Simulated 3-D ambiguity spectrum $\alpha_{\min}$ of the Two Season VA from using RPC 0 only, at the following frequencies: (a) & (b) 2.2 GHz, (c) & (d) 2.8 GHz, and (e) & (f) 3.4 GHz. The antenna is either mounted on an infinite ground plane (left figures) or the finite octagonal ground plane (right figures). Elevation angles θ are given on the radial axis and azimuth angles ϕ are given on the angular axis.

Fig. 2.33 shows the CRB associated with the θ and ϕ estimate of this ideal VA that has been computed analytically under the scenario conditions defined in Table 2.4. The parameters are similar to those used for the DoA estimation using the MUSIC summarized in Table 2.3. The CRB is here computed over the entire 3-D upper half-space, except at $\theta = 90°$ due to a singularity of the CRB [74]. It can be observed that the CRB_θ increases with θ, resulting from the small variation in θ of the steering vector $\boldsymbol{d}$ (defined by Eq. C.3) when θ approaches 90°. Indeed, as stated in Section C.2, the estimation of the elevation angle θ is derived exclusively from the E_z component measurement of the incoming EM-wave realized through an electric monopole oriented along the $\hat{z}$-axis and whose output power varies in $\sin(\theta)^2$. As a consequence, the estimation is more sensitive to amplitude variations caused by the noise at elevation angles close to 90° than at lower elevation angles. Besides, the CRB_ϕ is constant and does not depend on θ. Furthermore, the azimuth angle ϕ estimate is globally more accurate than the one for the elevation angle θ.

Number of incoming EM-waves	1
Polarization of the incoming EM-wave	Vertical
Angular coverage	$\phi \in [0° \ ; \ 90°]$ $\theta \in [0° \ ; \ 360°]$
Angular resolution	$\Delta\phi = 1°$ $\Delta\theta = 1°$
Incoming EM-wave power density	-105 dBW.m^{-2}
Noise power level	-111 dBm
PNR	36 dB.m^{-2}
Snapshots per DoA estimation	100
Frequencies of interest	2.2 GHz 2.8 GHz 3.4 GHz

Table 2.4: Parameters used for the CRB analysis

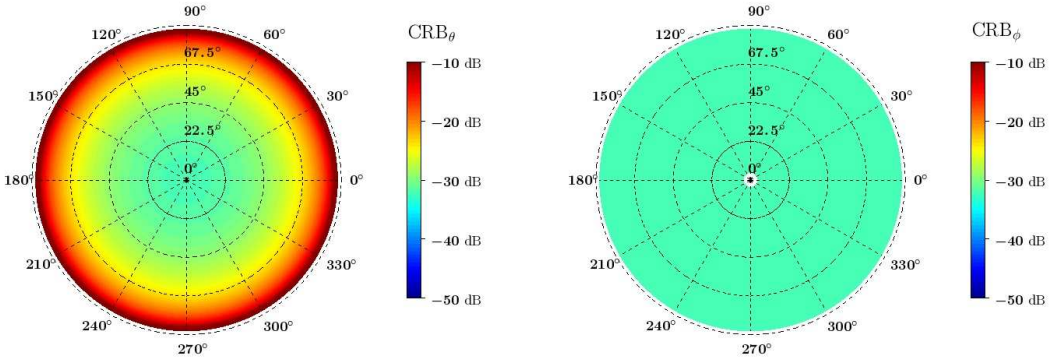

(a) (b)

Figure 2.33: Simulated (a) CRB$_\theta$ and (b) CRB$_\phi$ of an ideal VA consisting of three colocated dipoles and measuring the three components E_z, H_x and H_y of an incident vertically-polarized EM-wave. Elevation angles θ are given on the radial axis and azimuth angles ϕ are given on the angular axis.

Fig. 2.34 and Fig. 2.35 show the CRB$_\theta$ and CRB$_\phi$ of the Two Season VA either mounted on the infinite or octagonal metallic support at the three frequencies of interest when only RPC 0 is used for the estimation of the DoA of the incoming vertically-polarized EM-wave. Several observations can be inferred from these figures as well as through their comparison with Fig. 2.33. First, it can be seen that CRB$_\theta$ of the Two Season VA mounted on the infinite ground plane have roughly the same aspect as that of the ideal VA, namely it increases when θ is near 90°. However, the CRB$_\theta$ variation in θ is not quite linear as for the ideal VA given the emergence of higher values near $\theta = 45°$, resulting from the imperfect 8-shape RP of the electric monopole. Besides, the CRB$_\theta$ of the Two Season VA mounted on finite metallic support does not have its highest values for elevation angles close to 90°. This can be explained by the dynamic introduced on the RP of the electric monopole if the antenna is mounted on this support. Secondly, unlike the ideal VA, the CRB$_\phi$ of the Two Season VA presents a dependence in θ for both ground plane configurations. More generally, it can be noted that highest values of CRB$_\theta$ and CRB$_\phi$ of the Two Season VA are found in specific directions depending on the operating frequency and the configuration (infinite or finite ground plane). Finally, these CRBs are generally lower than those of the ideal grounded VA. This is due to the fact that the dipoles constituting the Two Season VA exhibit a higher gain than 1.76 dBi, which corresponds to the gain of the elementary dipoles constituting the ideal VA.

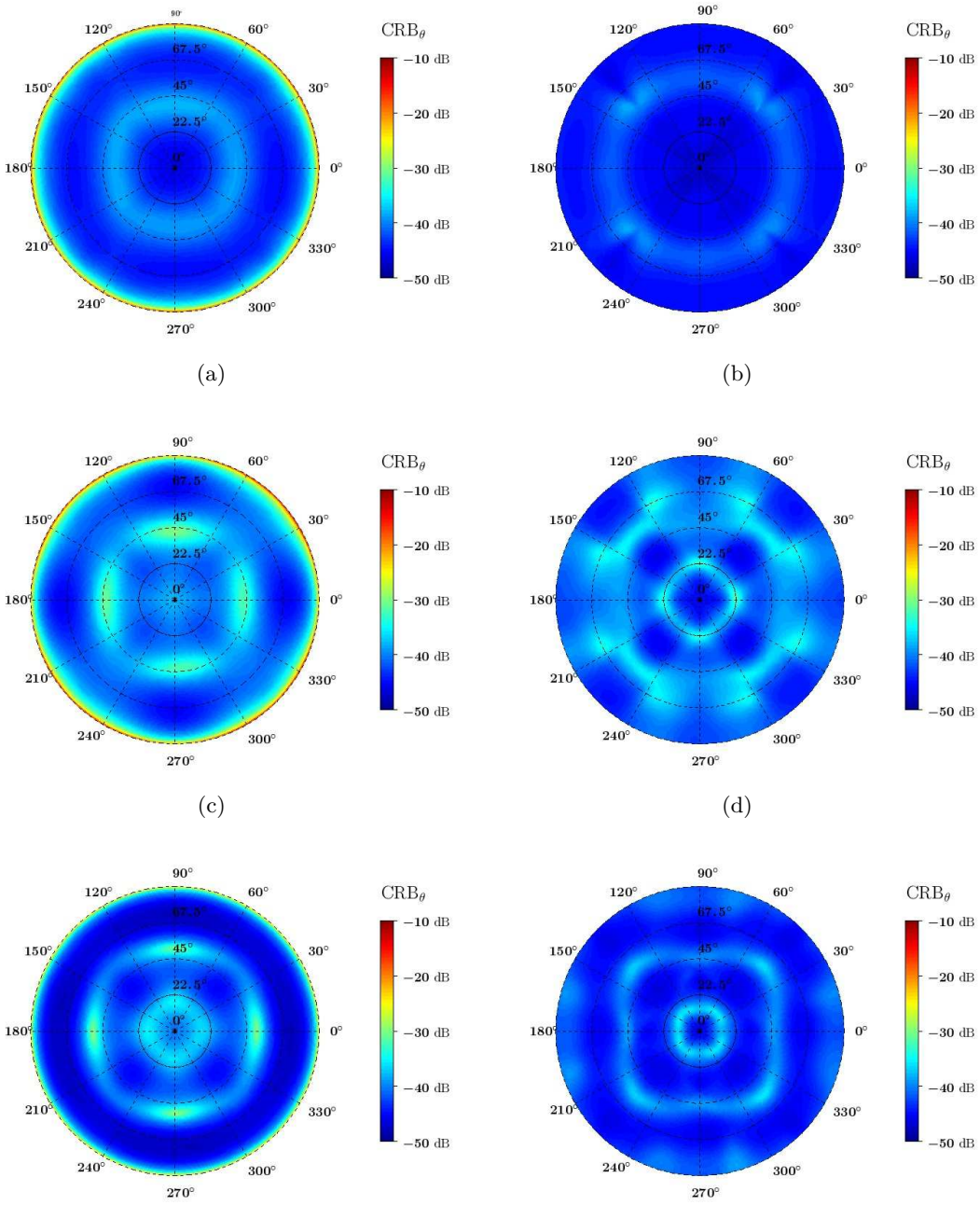

Figure 2.34: Simulated CRB$_\theta$ of the Two Season VA from using RPC 0 only, and under the scenario conditions defined in Table 2.3 at the following frequencies: (a) & (b) 2.2 GHz, (c) & (d) 2.8 GHz, and (e) & (f) 3.4 GHz. The antenna is either mounted on an infinite ground plane (left figures) or the finite octagonal ground plane (right figures). Elevation angles θ are given on the radial axis and azimuth angles ϕ are given on the angular axis.

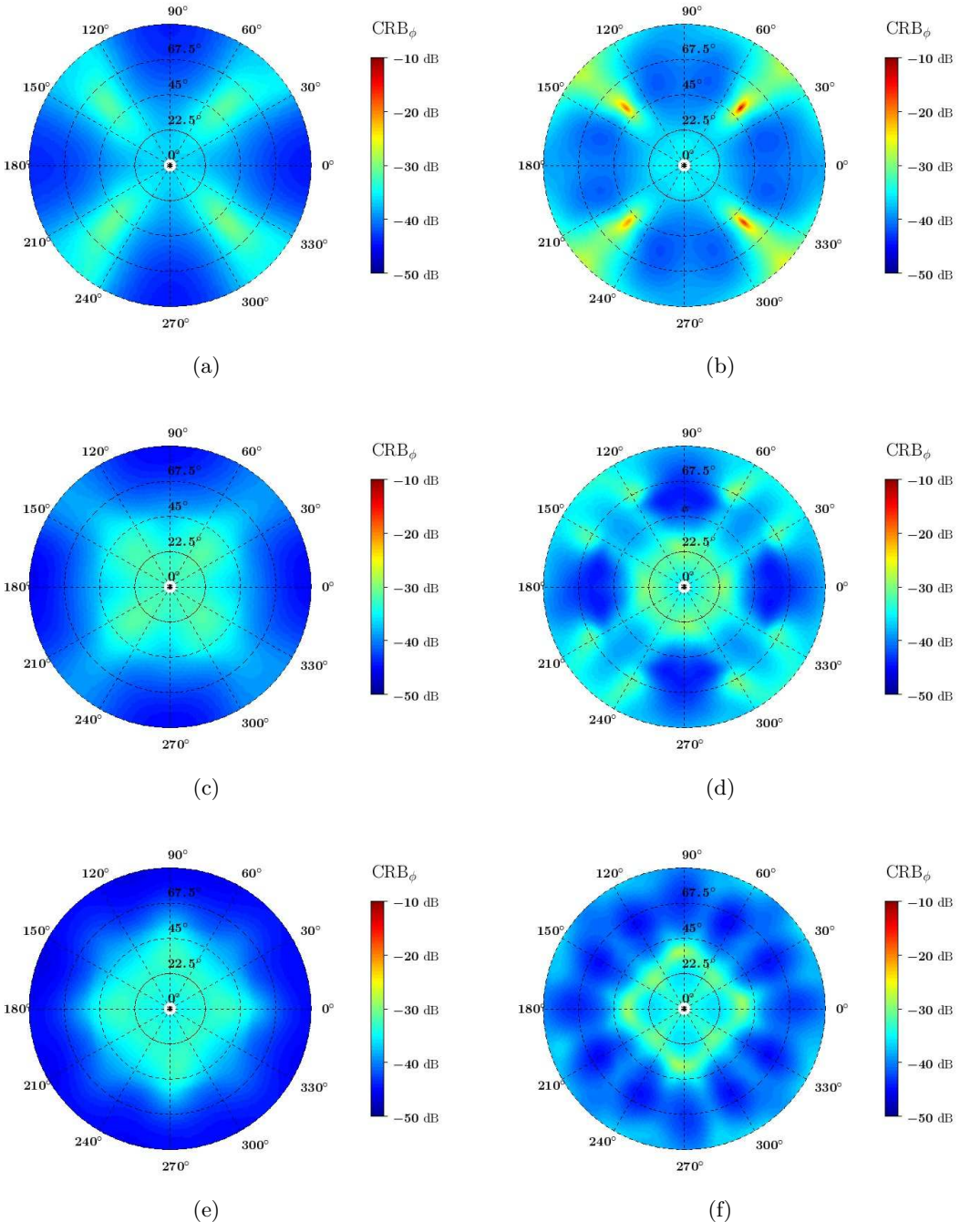

Figure 2.35: Simulated CRB$_\phi$ of the Two Season VA from using RPC 0 only, and under the scenario conditions defined in Table 2.3 at the following frequencies: (a) & (b) 2.2 GHz, (c) & (d) 2.8 GHz, and (e) & (f) 3.4 GHz. The antenna is either mounted on an infinite ground plane (left figures) or the finite octagonal ground plane (right figures). Elevation angles θ are given on the radial axis and azimuth angles ϕ are given on the angular axis.

2.7.4 Direction-of-arrival estimation accuracy

After analyzing the risk of angular ambiguity and the CRB of the Two Season VA, the actual DF performances in terms of estimation accuracy achievable using the MUSIC algorithm is now evaluated. This evaluation is done under the scenario reported in Table 2.3 and based only on the measurement of three components H_x, H_y and E_z (RPC 0) which is derived from the RP reconfigurability of the VA. Comparisons between simulation and measurement results are also carried out to experimentally validate the DF performances.

Fig. 2.36 displays the simulated and measured angular distance Δa_{RMS} (defined by Eq. 1.8) at the three frequencies of interest. Simulation results when the Two Season VA is mounted over an infinite ground plane are also provided. Several observations can be highlighted.

First, it can be observed that the Δa_{RMS} does not exceed 5° in almost every direction in the 3-D upper half-space within the VA bandwidth for both ground plane configurations.

Secondly, highest values of Δa_{RMS} are found in specific directions depending on the operating frequency and the size of the metallic support. However, it can be observed that the use of the finite ground plane does not significantly degrade the estimation performances. As shown in Fig. 2.37 and Fig. 2.38, the highest values of Δa_{RMS} originate either from an inaccuracy in the estimation of the azimuth angle ϕ or the elevation angle θ. This is consistent with the analysis conducted in Section 2.7.3 on the CRB since highest values of Δa_{RMS} are reached in the same directions in which the highest values of CRB_θ and CRB_ϕ are found. For example, the highest value of Δa_{RMS} at 2.2 GHz is reached for $(\phi, \theta) = (45°, 45°)$ when the VA is mounted on the finite octagonal metallic support (see Fig. 2.36(b)), which corresponds to a maximum error in the ϕ estimate (see also Fig. 2.38(b) and Fig. 2.37(b)) and had been foretold in the CRB study (see also Fig. 2.35(b) and Fig. 2.34(b)). In addition, as stated in Section 2.7.2, the risk of angular ambiguity was quite high in the angular zones around $\phi = 0° \pmod{90°}$ at 3.4 GHz, resulting in significant estimation error in these areas as notably shown in Fig. 2.36(g-h-i).

Thirdly, measurement and simulation results are in good agreement. Closer comparison between the measured and simulated results is illustrated in Fig. 2.39 to Fig. 2.41, where the RMS estimation errors are displayed in three specific ϕ-planes and for the poorest accuracy of the DoA estimation. Again, a good agreement between the simulated and measured results is obtained. However, the measured estimation accuracy is slightly degraded since errors appear for elevation angles close to 0°. These estimation errors are not apparent in the simulation results and originate from the inaccurate gears in the positioning system.

Finally, the maximum RMS error as well as the 95th percentile of the Δa_{RMS} (defined in Section 1.1.5.4) are reported in Table 2.5. As above-discussed, a discrepancy between the simulated and measured maximum values of Δa_{RMS} is observable. However, at the three frequencies of interest, the simulated and measured 95th percentile of the Δa_{RMS} is lower than 2.0° and 3.1°, respectively. Details on the maximum RMS error as well as the 95th percentile of the $E^{\theta}_{\mathrm{RMS}}$ and E^{ϕ}_{RMS} (defined by Eq. 1.7) that may be relevant depending on the intended application are provided for interested readers in Table 2.7 and Table 2.6, respectively. In brief, the estimation accuracy measured under the scenario reported in Table 2.3 from the first passive and wideband VA are very encouraging using only the measurement of the three components E_z, H_x and H_y of the incoming EM-wave, and they allow to experimentally validate the simulated DF performances.

Frequency	Simulated		Measured	
	max Δa_{RMS}	95th percentile of Δa_{RMS}	max Δa_{RMS}	95th percentile of Δa_{RMS}
2.2 GHz	4.2°	1.7°	20.9°	2.4°
2.8 GHz	3.8°	2.0°	43.9°	3.0°
3.4 GHz	142.5°	1.6°	109.9°	3.1°

Table 2.5: Simulated and measured $\Delta a_{\mathrm{RMS}}(\phi, \theta)$ obtained with the Two Season VA (mounted on the octagonal metallic support) using RPC 0 only, and under the scenario conditions defined in Table 2.3

Frequency	Simulated		Measured	
	max $E^{\theta}_{\mathrm{RMS}}$	95th percentile of $E^{\theta}_{\mathrm{RMS}}$	max $E^{\theta}_{\mathrm{RMS}}$	95th percentile of $E^{\theta}_{\mathrm{RMS}}$
2.2 GHz	2.0°	1.3°	20.9°	2.3°
2.8 GHz	2.3°	1.4°	41.4°	2.6°
3.4 GHz	41.6°	1.5°	33.7°	2.7°

Table 2.6: Simulated and measured $E^{\theta}_{\mathrm{RMS}}$ obtained with the Two Season VA (mounted on the octagonal metallic support) using RPC 0 only, and under the scenario conditions defined in Table 2.3

Frequency	Simulated		Measured	
	max E^{ϕ}_{RMS}	95th percentile of E^{ϕ}_{RMS}	max E^{ϕ}_{RMS}	95th percentile of E^{ϕ}_{RMS}
2.2 GHz	5.3°	1.3°	25.5°	1.5°
2.8 GHz	3.0°	2.0°	42.7°	1.8°
3.4 GHz	175.4°	1.3°	140.3°	4.2°

Table 2.7: Simulated and measured E^{ϕ}_{RMS} obtained with the Two Season VA (mounted on the octagonal metallic support) using RPC 0 only, and under the scenario conditions defined in Table 2.3

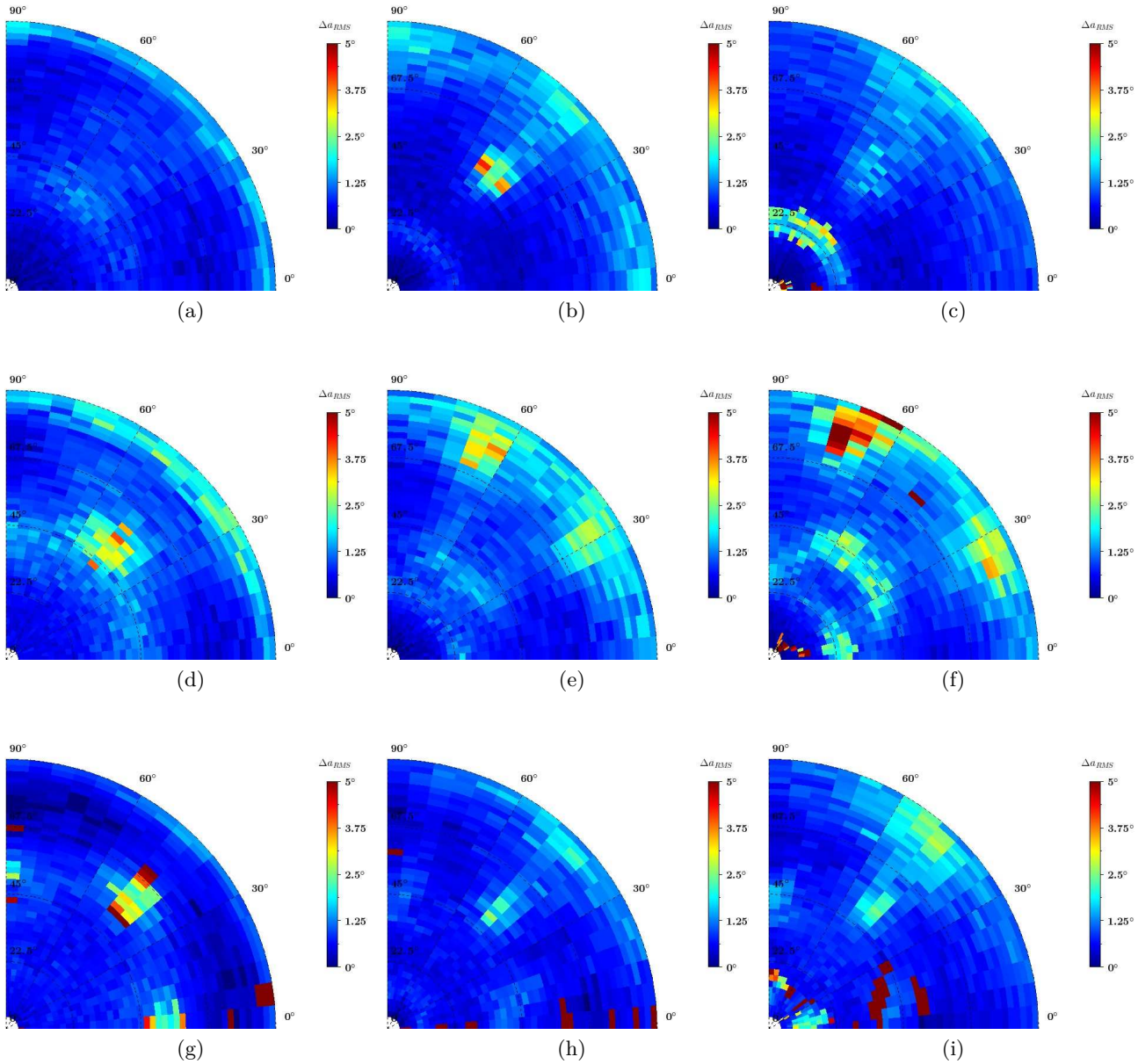

Figure 2.36: Simulated (left and middle figures) and measured (right figures) $\Delta a_{\mathrm{RMS}}(\phi, \theta)$ obtained with the Two Season VA from using RPC 0 only, and under the scenario conditions defined in Table 2.3 at the following frequencies: (a) to (c) 2.2 GHz, (d) to (f) 2.8 GHz, and (g) to (i) 3.4 GHz. The VA is either mounted on an infinite ground plane (left figures) or on the finite octagonal ground plane (middle and right figures). Elevation angles θ are given on the radial axis and azimuth angles ϕ are given on the angular axis.

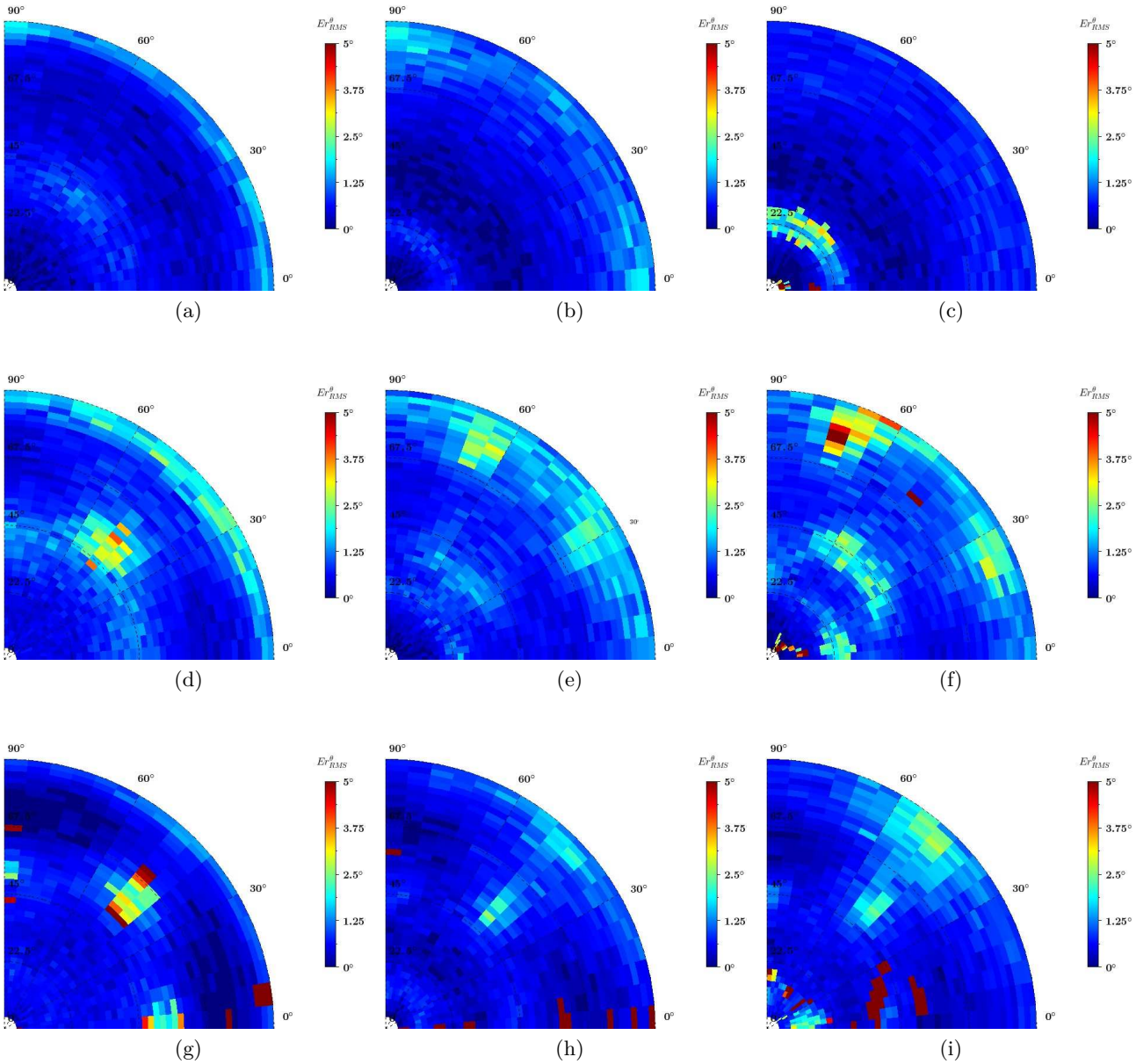

Figure 2.37: Simulated (left and middle figures) and measured (right figures) $E^{\theta}_{\mathrm{RMS}}$ obtained with the Two Season VA from using RPC 0 only, and under the scenario conditions defined in Table 2.3 at the following frequencies: (a) to (c) 2.2 GHz, (d) to (f) 2.8 GHz, and (g) to (i) 3.4 GHz. The VA is either mounted on an infinite ground plane (left figures) or on the finite octagonal ground plane (middle and right figures). Elevation angles θ are given on the radial axis and azimuth angles ϕ are given on the angular axis.

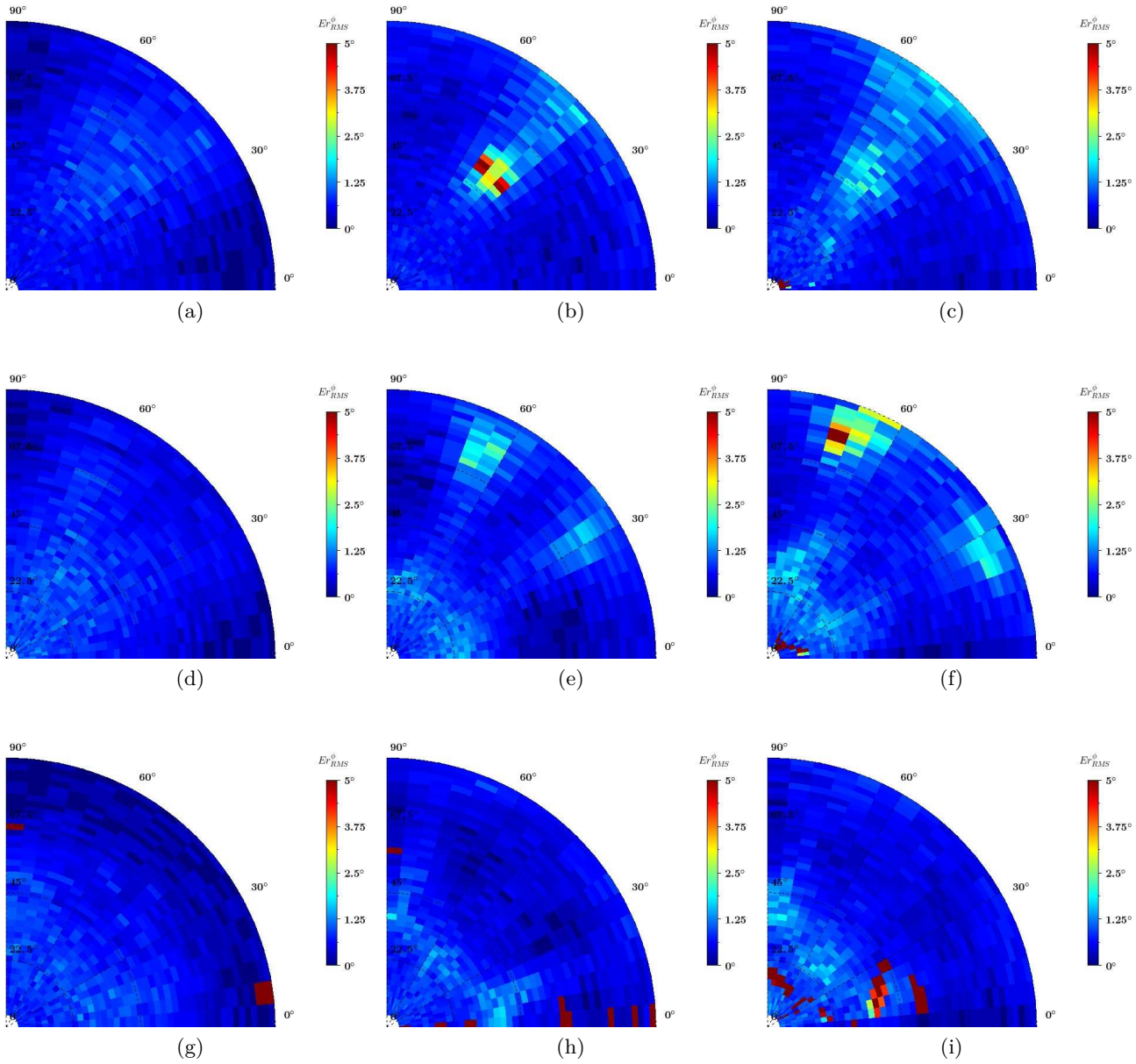

Figure 2.38: Simulated (left and middle figures) and measured (right figures) E^{ϕ}_{RMS} obtained with the Two Season VA from using RPC 0 only, and under the scenario conditions defined in Table 2.3 at the following frequencies: (a) to (c) 2.2 GHz, (d) to (f) 2.8 GHz, and (g) to (i) 3.4 GHz. The VA is either mounted on an infinite ground plane (left figures) or on the finite octagonal ground plane (middle and right figures). Elevation angles θ are given on the radial axis and azimuth angles ϕ are given on the angular axis.

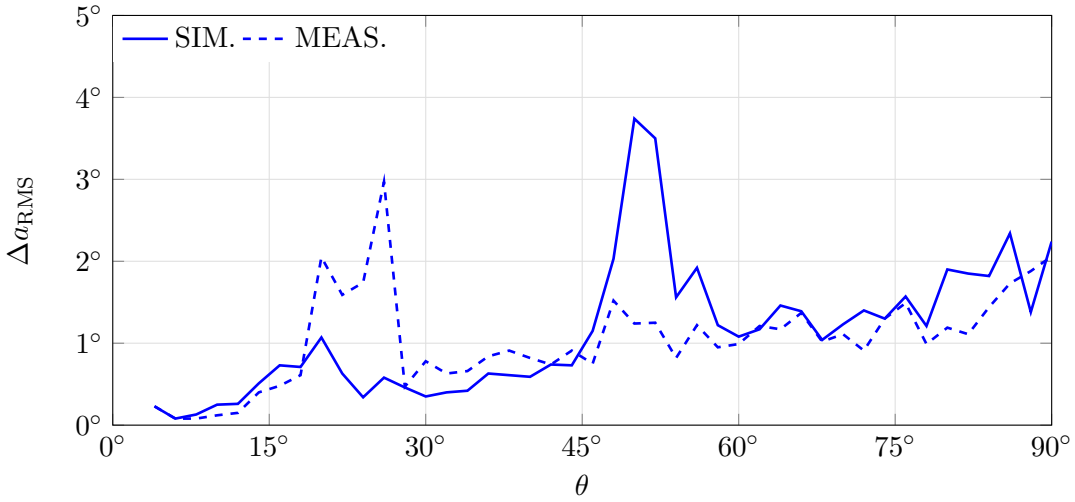

Figure 2.39: Simulated and measured $\Delta a_{\mathrm{RMS}}(\phi, \theta)$ obtained with the Two Season VA (mounted on the octagonal metallic support) using RPC 0 only, and under the scenario conditions defined in Table 2.3 at 2.2 GHz in the cut plane $\phi = 40°$.

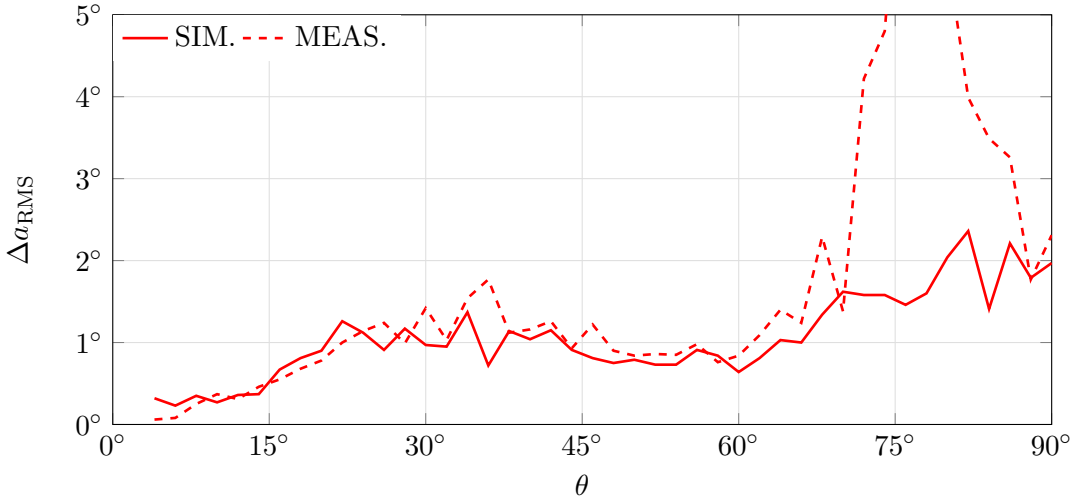

Figure 2.40: Simulated and measured $\Delta a_{\mathrm{RMS}}(\phi, \theta)$ obtained with the Two Season VA (mounted on the octagonal metallic support) using RPC 0 only, and under the scenario conditions defined in Table 2.3 at 2.8 GHz in the cut plane $\phi = 70°$.

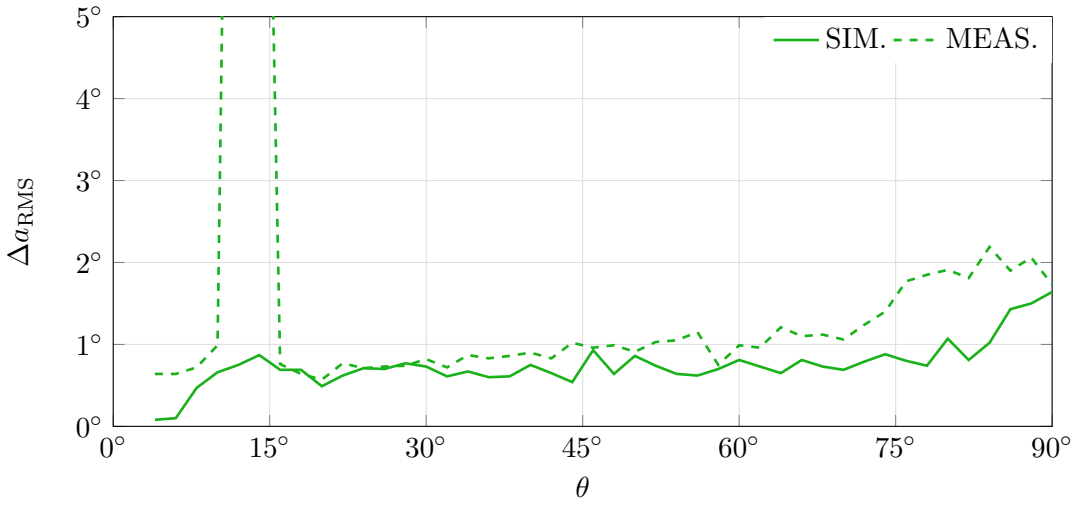

Figure 2.41: Simulated and measured $\Delta a_{\mathrm{RMS}}(\phi, \theta)$ obtained with the Two Season VA (mounted on the octagonal metallic support) using RPC 0 only, and under the scenario conditions defined in Table 2.3 at 3.4 GHz in the cut plane $\phi = 55°$.

2.7.5 Sensitivity of the prototype

Let us now examine an essential characteristic of the prototype of the Two Season VA which is its sensitivity. As mentioned in Section 1.1.5.5, the theoretical range of the DF antenna can be derived from this characteristic. The theoretical range corresponds to the maximum distance at which an estimate of the DoA of the incoming EM-wave can be obtained with an error less than a specified threshold. As a reminder, the 95th percentile of the Δa_{RMS} is used in this thesis to specify the sensitivity of the DF antenna for a maximum error threshold of 5°.

Fig. 2.42 displays the 95th percentile of Δa_{RMS} obtained thanks to the measurement of three components H_x, H_y and E_z (RPC 0) of an incoming vertically-polarized EM-wave with the Two Season VA at the three frequencies of interest and for different PNRs, ranging from 18 dB.m^{-2} to 36 dB.m^{-2} (with a step of 3 dB). Equally, these PNRs correspond to an EM-wave impinging the Two Season VA with a power density P_s ranging from -123 dBW.m^{-2} to -105 dBW.m^{-2}. It can be noted that the measured 95th percentile of Δa_{RMS} increases with the frequency, which means that the sensitivity of the Two Season VA is degraded. The sensitivity P_{sensi} of the Two Season VA using only RPC 0 for the DoA estimation of an incident vertically-polarized EM-wave is of -111 dBW.m^{-2} at 2.2 GHz (PNR $\approx$ 30 dB.m^{-2}), -108 dBW.m^{-2} at 2.8 GHz (PNR $\approx$ 33 dB.m^{-2}) and -106 dBW.m^{-2} at 3.4 GHz (PNR $\approx$ 35 dB.m^{-2}).

The theoretical range $r_{\max}$ can be evaluated knowing the gain G_e and the emitted power P_e of the transmitter using Eq. 1.16. For example, let us consider an isotropic antenna which emits a power of 1 W. The theoretical range of the Two Season VA using only RPC 0 for the DoA estimation is therefore of 100 km at 2.2 GHz, 71 km at 2.8 GHz and 56 km at 3.4 GHz.

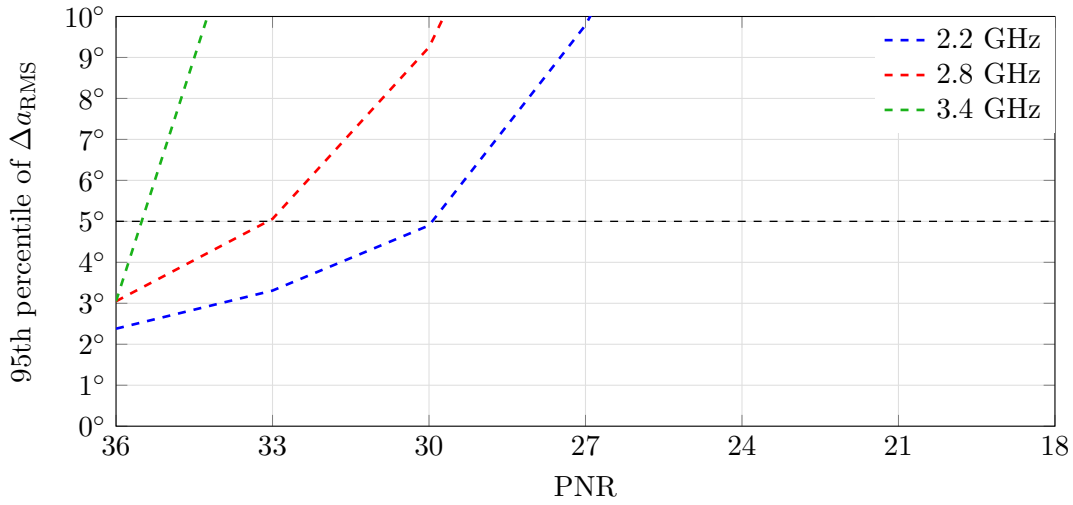

Figure 2.42: Measured 95th percentile of Δa_{RMS} for different PNRs using only RPC 0 for the DoA estimation of an incident vertically-polarized EM-wave at 2.2 GHz, 2.8 GHz and 3.4 GHz

2.8 Conclusion

In this chapter, the first passive and wideband VA referred to as the Two Season VA has been presented. The Two Season VA is mounted over a ground plane in view of embedded applications and is intended to estimate the DoA of vertically-polarized EM-waves in the upper hemisphere through the measurement of the three components E_z, H_x and H_y thanks to the RPs of two magnetic dipoles and one electric monopole.

After providing a general overview of VAs, this chapter started with a feasibility study of a compact and wideband VA from small resonant antennas. Based on small antennas theory, this study demonstrated that such design is not suited for designing the Two Season VA regarding the radiation efficiency, bandwidth and compactness that can be achieved.

Secondly, a state of the art of wideband dipoles was provided to identify the radiating elements that would be worthwhile to consider for designing the Two Season VA. This survey showed that the literature is full of electric dipoles that can be interesting to investigate. In contrast, only a few magnetic dipoles were published before the start of this Ph.D. work in October 2015 and consequently, the first step in designing the Two Season VA was to design the wideband magnetic dipoles. Furthermore, this state of the art also pointed out the tremendous difficulties associated with the design of a compact magnetic dipole offering wide impedance bandwidth and omnidirectional RP with a minimal gain variation.

The central part of this chapter was the actual design of the Two Season VA, followed by the evaluation of its electrical characteristics and DF performances. To begin with, a study has been carried out to design a wideband magnetic dipole according to Chu's theory of using a circular array to obtain an omnidirectional RP. This study has led to the use of a semi-circular array of Vivaldi antennas mounted over a ground plane so that the requirements associated with the design of a wideband magnetic dipole could be met. Then, the Two Season VA has been introduced. This VA consists of only two orthogonal and colocated dual-port semi-circular arrays of Vivaldi antennas. The RP reconfigurability of the proposed VA enables the measurement of the three components E_z, H_x and H_y of an incoming EM-wave over a 1.69:1 bandwidth from

2.1 GHz to 3.55 GHz thanks to three sets of weighting coefficients (RPC 0). A prototype of this VA was manufactured and experimentally characterized. Besides, the Two Season VA presents good isolation between its ports (lower than -23 dB) and good radiation efficiency (higher than 80%). The prototype is included in a half-sphere within a $0.52\lambda_0$ radius and mounted on a finite metallic and octagonal support with a circumcircle radius of $1.14\lambda_0$, where λ_0 is the free space wavelength at the lowest operating frequency. Finally, an accurate DoA estimation of an incoming vertically-polarized EM-wave has been measured across the overall the bandwidth and the 3-D upper hemisphere using only RPC 0 and the MUSIC algorithm, as shown in Table 2.8. An accuracy of 5° (95th percentile of Δa_{RMS}) is obtained for a PNR of 35 dB.m^{-2} at the upper frequency band (3.4 GHz). Above this frequency, the presence of ripples in the RPs degrades the DF performances. Overall, a good agreement between the experimental results and the simulation results has been obtained for both electrical characteristics and DF performances.

Frequency	P_{sensi}	PNR	$r_{\max}$ † (P_e, G_e)
2.2 GHz	-111 dBW.m^{-2}	30 dB.m^{-2}	100 km † (1 W, 0 dBi)
2.8 GHz	-108 dBW.m^{-2}	33 dB.m^{-2}	71 km † (1 W, 0 dBi)
3.4 GHz	-106 dBW.m^{-2}	35 dB.m^{-2}	56 km † (1 W, 0 dBi)

Table 2.8: Sensitivity and theoretical range of the Two Season VA prototype using only RPC 0 for the DoA estimation of an incident vertically-polarized EM-wave

In the following chapter, several improvements of the Two Season are tackled.

Chapter 3

Improvements of the Two Season vector antenna

Contents

Previously, a VA referred to as the Two Season VA was designed. This VA has shown good DF performances to estimate the DoA of an incoming vertically-polarized EM-wave in the upper hemisphere and over an impedance bandwidth of 1.69:1 from 2.1 GHz to 3.55 GHz. The DoA estimation is realized through the measurement of the three components E_z, H_x and H_y (RPC 0). The purpose of this chapter is to improve the DF performances of the Two Season VA. Three methods are provided to achieve the desired result. The first method consists in enhancing the DoA estimation process of the Two Season VA by making greater use of its RP reconfigurability (Section 3.1). Specifically, new RPs are employed for the DoA estimation in addition to the ones that enable the measurement of the components of the incoming EM-wave. Furthermore, a method based on the CRB is proposed to select efficiently and rapidly the additional RP diversity to be included. The second method entails extending the frequency coverage of the Two Season

through a modification of the antenna feeding and the use of the new DoA estimation technique (Section 3.2). This modified version of the Two Season VA is referred to as the improved version of the Two Season VA in the reminder of this thesis. Its simulated electrical characteristics and DF performances are reported. The third method involves modifying the topology of the improved version of Two Season VA in order to estimate the DoA of incoming EM-waves in the upper hemisphere regardless of their polarization (Section 3.3). The electrical characteristics and DF performances of a prototype of this new VA, referred to as the Four Season VA, are also assessed.

The first section of this chapter corresponds to the content of Duplouy *et al.* [J1].

3.1 Enhancement of the direction finding performances using additional radiation pattern diversity

The aim of this section is to enhance the DF performances of RP reconfigurable VAs by adding new RPs to those commonly employed to estimate the DoA of an incoming EM-wave (i.e., the RPs associated to the measurement of its components). The use of additional RPs results from the conjunction of two main considerations:

- The desire of improving the DF performances under the following constraint: how to make the most of existing RP reconfigurable VAs?
- Advances in both technology and on-board computing can be easily applied to slightly more complex DoA estimation algorithms.

Although the addition of new RPs is explored here through the re-evaluation of the simulated and measured DF performances of the Two Season VA[1], it can be applied to any RP reconfigurable VAs. The question that arises at this stage is how to quickly and efficiently select the RPs to add to the DoA estimation process.

In the same vein, some research work is currently emerging and has been published very recently on the use of multi-mode antennas for DF [125, 126]. These multi-mode antennas[2] are another interesting substitute to large antenna arrays.

3.1.1 A Cramer-Rao lower bound based criterion for selecting the radiation patterns

3.1.1.1 Methodology

In the following, an original method based on the CRB is proposed in order to select the RP diversity that enhances the accuracy of the DoA estimation across the VA operating bandwidth. Since this method is based on the CRB, it provides results that do not depend on the technique used for the DoA estimation (e.g., MUSIC in this Ph.D. work). This independence constitutes the main advantage of this CRB-based criterion.

[1] The Two Season VA is mounted on the finite and octagonal metallic surface throughout this section and to the end of the manuscript.

[2] A multi-mode antenna is defined as a multi-port antenna that allows independent excitation of different characteristics modes, and therefore different RPs.

As indicated in Table 2.2, the RP reconfigurability of the Two Season VA enables the measurement of the three components E_z, H_x, and H_y through three sets[3] of weighting coefficients (or equivalently, three RPs denoted by RPC 0) assigned to the signals received at the four antenna ports. These three sets were used for the previous evaluation of the DF performances in Section 2.7. By assigning random weighting coefficients to the signals received at the VA ports, a large number of sets may be added to the three initial ones.

Let 1, 0 and -1 be the possible values for the weighting coefficients (complex coefficients could be used). As a result, 81 sets of weighting coefficients could *a priori* be assigned to the signals received at the four ports of the Two Season VA. Some of these allow the measurement of the three components E_z, H_x and H_y of an incoming EM-wave. Since they are already included in the DoA estimation process through RPC 0, these sets can be disregarded. Moreover, some sets of weighting coefficients (such as, e.g., the set $[1, 1, \text{-}1, 1]$ and the set $[\text{-}1, \text{-}1, 1, \text{-}1]$) provide identical RPs when used as excitation laws for feeding the 4-port Two Season VA. In these cases, only one set is kept while the others are discarded. Finally, it remains 37 different RPs and consequently, there are[4]

$$\sum_{k=1}^{37} \binom{37}{k} = 2^{37} - 1 \tag{3.1}$$

available RPCs that can be added to RPC 0 to improve the DF performances. From there, the challenge is to select the RPCs that maximize the DoA estimation accuracy.

In order to avoid a long processing time for detecting the RPCs that improve the DF performances, 11 RPCs are pre-selected. Each of these RPCs is added to RPC 0 in the DoA estimation process, and consists of a set of different weighting coefficients that provide the same RP with a rotation of 90° in the azimuth plane in order to ensure the same DF performances across the 3-D upper half-space. Besides, the 11 RPCs (that regroup the 37 available RPs) and their associated sets of weighting coefficients are summarized in Table 3.1. For illustrative purposes, the RPs corresponding to RPC 4 are displayed at 3.4 GHz in Fig. 3.1 (see Appendix F.3 for the RPs associated with the other RPCs). Finally, the computation of the CRB enables the selection among them of the RPC that achieves the highest DoA estimation accuracy in the 3-D upper hemisphere.

[3] A set is defined as $[w_1, w_2, w_3, w_4]$, where $w_i \in [\![1; 4]\!]$ designates the weighting at port i

[4] As a reminder, the acronym RPC means Radiation Patterns Combination and represents a group of RPs. In Eq. 3.1, the left side sums the number of RPCs of sizes $k = \{1, 2, \ldots, 37\}$ (or equivalently, the left side sums number of RPCs comprising k different RPs). The order of selection of the RPs constituting the RPC does not matter.

	RPC 1				RPC 2				RPC 3			
Port 1	1	0	0	0	1	1	1	0	1	0		
Port 2	0	0	1	0	1	0	1	1	1	0		
Port 3	0	0	0	1	1	1	0	1	0	1		
Port 4	0	1	0	0	0	1	1	1	0	1		

	RPC 4				RPC 5				RPC 6			
Port 1	1	1	1	-1	1	0	1	-1	1	1	0	0
Port 2	1	-1	1	1	1	-1	1	0	0	0	1	1
Port 3	1	1	-1	1	0	1	-1	1	1	0	0	1
Port 4	-1	1	1	1	-1	1	0	1	0	1	1	0

	RPC 7				RPC 8				RPC 9			
Port 1	1				1	0	0	-1	1	1		
Port 2	1				0	-1	1	0	-1	-1		
Port 3	-1				0	0	-1	1	1	-1		
Port 4	-1				-1	1	0	0	-1	1		

	RPC 10				RPC 11			
Port 1	1	1	0	-1	1	1	0	-1
Port 2	0	-1	1	1	0	-1	1	1
Port 3	1	0	-1	1	-1	1	1	0
Port 4	-1	1	1	0	1	0	-1	1

Table 3.1: RPCs and corresponding weighting coefficients assigned to the signals received by the 4-port Two Season VA

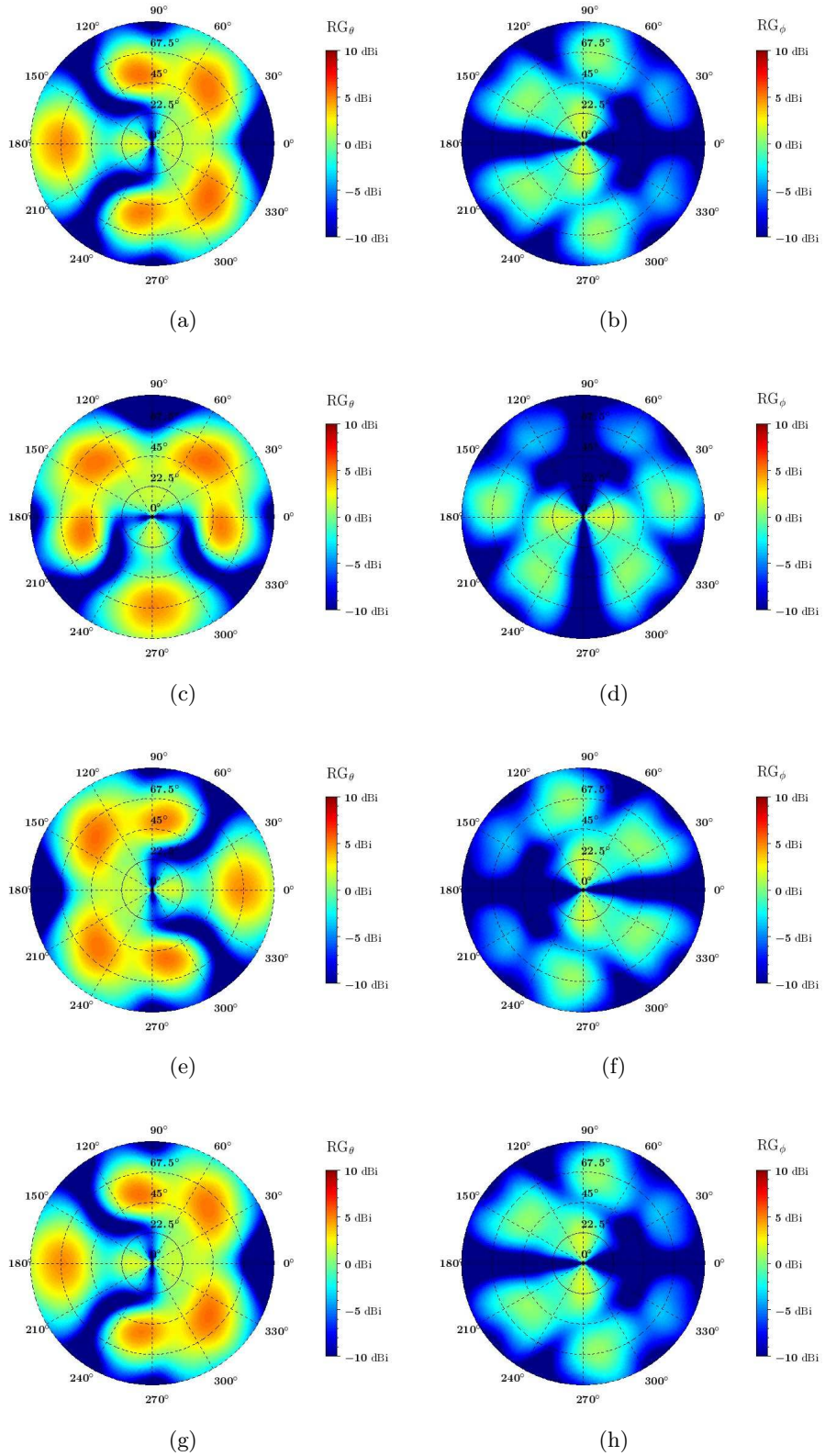

Figure 3.1: Simulated realized gain associated to RPC 4 in the θ-polarization (left figures) and ϕ-polarization (right figures) of the Two Season VA at 3.4 GHz. The RPs correspond to the following sets of weighting coefficients: (a) & (b) [1, 1, 1, -1], (c) & (d) [1, -1, 1, 1], (e) & (f) [1, -1, 1, 1] , and (g) & (f) [-1, 1, 1, 1]. Elevation angles θ are given on the radial axis and azimuth angles ϕ are given on the angular axis.

3.1.1.2 Selection of the radiation patterns combination

For each RPC, the CRB on θ and ϕ is computed from the parameters displayed in Table 3.2 and using the simulated RPs at 2.2 GHz, 2.8 GHz and 3.4 GHz, which are roughly the lower, center and upper operating frequencies of the Two Season VA. The optimal RPC is defined as RPC i ($i \in [\![1;11]\!]$) that added to RPC 0 obtains the smallest value of CRB on θ and ϕ. It can be noted that the parameters used here are similar to those reported in Table 2.4, except that the power density of the incoming EM-wave is set to -117 dBW.m^{-2} (PNR = 24 dB.m^{-2}) in order to highlight the benefits of adding RPs diversity. As a matter of fact, this scenario corresponds to a decrease of 12 dB of the PNR used in Section 2.7.

Fig. 3.2 and Fig. 3.3 present the results of the CRB analysis on θ and ϕ, respectively. It can be observed that the different RPCs are more or less effective in improving the accuracy of the DoA estimation in azimuth or elevation. Interestingly, RPC 4 achieves practically the highest accuracy for the estimation of the azimuth and elevation angles at the three frequencies of interest. Among the RPCs used to complete RPC 0, only RPC 2 presents a CRB on θ lower that the one achieved by RPC 4 at 3.4 GHz. There is no significant difference between the two as the CRB on θ are -26.81 dB and -26.57 dB, respectively. However, RPC 4 offers the best overall performances, and most particularly at 2.8 GHz.

Fig. 3.4 and Fig. 3.5 display CRB_θ and CRB_ϕ which have been computed with or without adding RPC 4 to RPC 0 at the three frequencies of interest. These figures are quite revealing in several ways. First, the CRB_θ and CRB_ϕ obtained using only RPC 0 are consistent with those shown in Fig. 2.34(b-d-f) and Fig. 2.35(b-d-f). As might be expected, the same trend is observed with an apparent increase in values since the PNR is diminished. Secondly, it can be clearly seen that the addition of RPC 4 to RPC 0 improves the DoA estimation over the entire bandwidth since CRB_θ and CRB_ϕ are significantly lowered. Finally, by looking at the new CRB values achieved in specific directions corresponding to the peaks of CRB_θ and CRB_ϕ when only RPC 0 was used (depending on the frequency), it can be stated that the use of RP diversity enables the resolution of the estimation problems in these angular areas. For instance, a clear benefit of adding RPC 4 to RPC 0 can be identified by looking at the CRB_ϕ in the direction $(\phi, \theta) = (45°, 45°)$ at 2.2 GHz (see Fig. 3.5(a) and Fig. 3.5(b)). In this direction, the previously maximal CRB_ϕ is now minimal.

Number of incoming EM-waves	1
Polarization of the incoming EM-wave	Vertical
Angular coverage	$\phi \in [0° ; 360°]$ and $\theta \in [0° ; 90°]$
Incoming EM-wave power density	-117 dBW.m^{-2}
Noise power level	-111 dBm
PNR	24 dB.m^{-2}
Snapshots per DoA estimation	100
Frequencies of interest	2.2 GHz, 2.8 GHz, and 3.4 GHz

Table 3.2: Parameters used for the CRB analysis

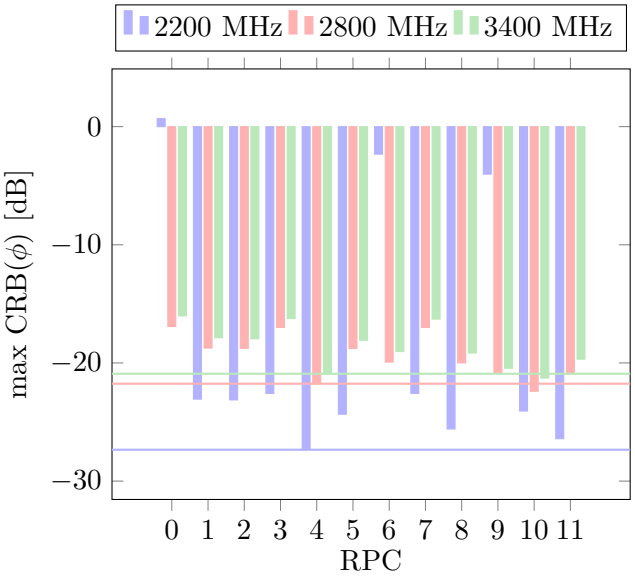

Figure 3.2: Highest simulated CRB(ϕ) using different RPCs [1 to 11] added to the RPC 0, and under the scenario conditions defined in Table 3.2 at 2.2 GHz, 2.8 GHz and 3.4 GHz. The horizontal lines correspond to the lowest CRB.

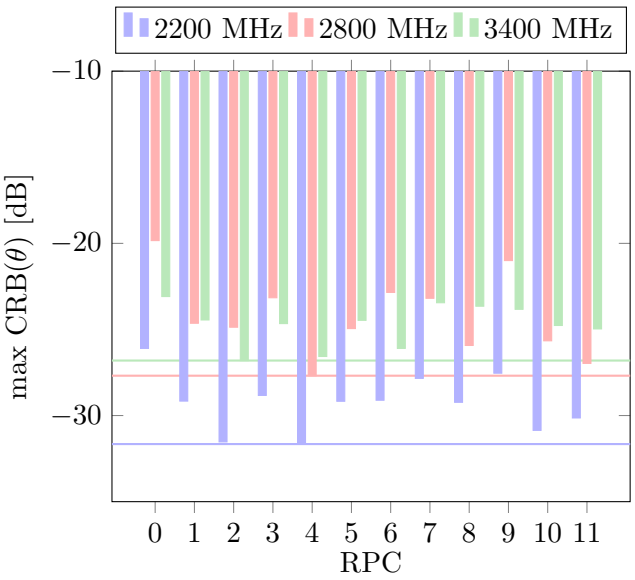

Figure 3.3: Highest simulated CRB(θ) using different RPCs [1 to 11] added to the RPC 0, and under the scenario conditions defined in Table 3.2 at 2.2 GHz, 2.8 GHz and 3.4 GHz. The horizontal lines correspond to the lowest CRB.

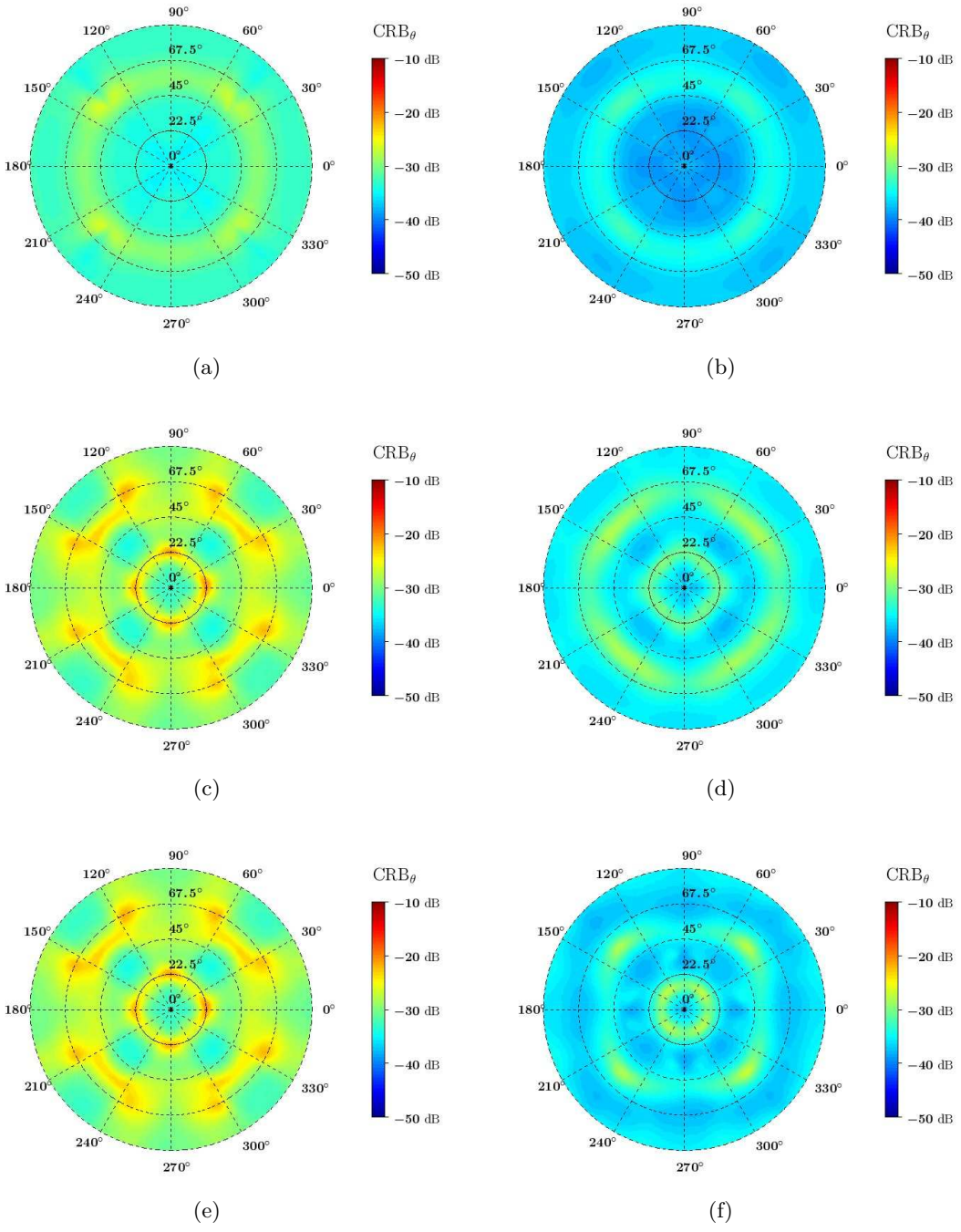

Figure 3.4: Simulated CRB$_\theta$ obtained from the Two Season VA using RPC 0 only (left figures) or adding RPC 4 to RPC 0 (right figures), and under the scenario conditions defined in Table 3.2 at the following frequencies: (a) & (b) 2.2 GHz, (c) & (d) 2.8 GHz, and (e) & (f) 3.4 GHz. Elevation angles θ are given on the radial axis and azimuth angles ϕ are given on the angular axis.

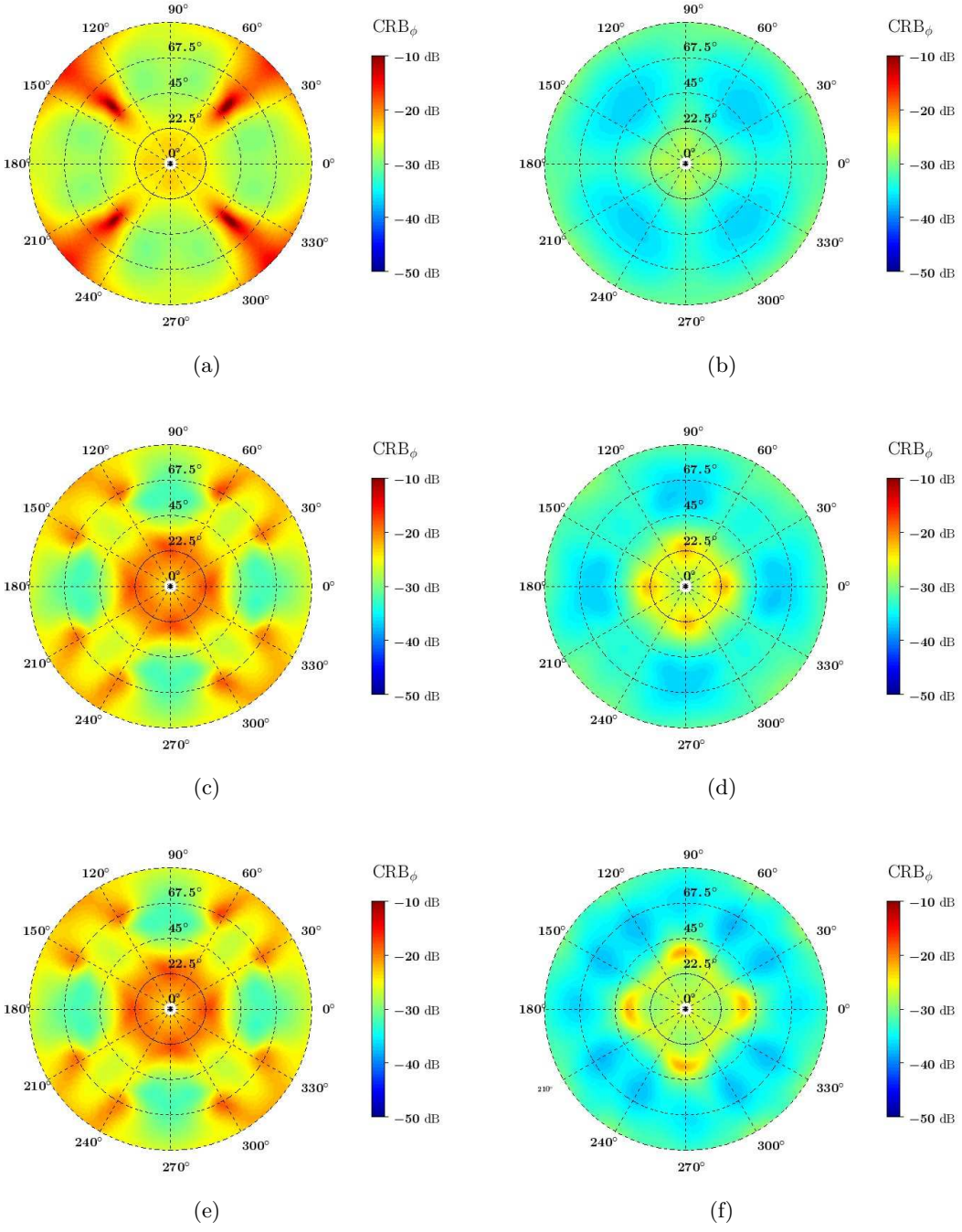

Figure 3.5: Simulated CRB$_\phi$ obtained from the Two Season VA using RPC 0 only (left figures) or adding RPC 4 to RPC 0 (right figures), and under the scenario conditions defined in Table 3.2 at the following frequencies: (a) & (b) 2.2 GHz, (c) & (d) 2.8 GHz, and (e) & (f) 3.4 GHz. Elevation angles θ are given on the radial axis and azimuth angles ϕ are given on the angular axis.

3.1.1.3 Validation

In order to validate the CRB-based selection of the RPC, the DoA estimation accuracy of the Two Season VA is evaluated here using the MUSIC algorithm and the simulated RPs. The parameters used for this evaluation are set out in Table 3.3. They are similar to those reported in Table 2.3, except the power density of incoming EM-wave which is set to -117 dBW.m^{-2} (PNR = 24 dB.m^{-2}) as in the CRB analysis performed in Section 3.1.1.2. As previously said, this PNR value highlights the benefits of adding RP diversity in the DoA estimation process. For comparison purposes, Table 3.4 gives the maximum RMS error as well as the 95th percentile of Δa_{RMS} obtained from RPC 0 only at PNR = 24 dB.m^{-2} and recalls those achieved at PNR = 36 dB.m^{-2}. As expected, since the PNR is significantly lower, the DF performances of the Two Season VA based only on the measurement of the three components E_z, H_x and H_y of an incoming EM-wave (RPC 0) are significantly degraded.

DoA Algorithm	MUSIC
Number of incoming EM-waves	1
Polarization of the incoming EM-wave	Vertical
Angular coverage	$\phi \in [0° ; 90°]$ $\theta \in [0° ; 90°]$
Angular resolution	$\Delta\phi = 5°$ $\Delta\theta = 2°$
Incoming EM-wave power density	-117 dBW.m^{-2}
Noise power level	-111 dBm
PNR	24 dB.m^{-2}
Snapshots per DoA estimation	100
Number of estimations per DoA	20
Frequencies of interest	2.2 GHz 2.8 GHz 3.4 GHz

Table 3.3: Parameters used for evaluating the DF performances

Frequency	PNR=36 dB.m^{-2}		PNR=24 dB.m^{-2}	
	max Δa_{RMS}	95th percentile of Δa_{RMS}	max Δa_{RMS}	95th percentile of Δa_{RMS}
2.2 GHz	4.2°	1.7°	15.1°	8.2°
2.8 GHz	3.8°	2.0°	33.5°	15.0°
3.4 GHz	142.5°	1.6°	140.3°	74.6°

Table 3.4: Simulated $\Delta a_{\mathrm{RMS}}(\phi, \theta)$ obtained from the Two Season VA using RPC 0 only, and under the scenarios defined in Table 2.3 and Table 3.3.

Fig. 3.6 presents the simulated 95th percentile of Δa_{RMS} when the different RPCs are added to RPC 0 in the DoA estimation process. Comparing the results of Table 3.4 with this chart shows that the DoA estimation accuracy is clearly improved. Furthermore, as predicted from the CRB analysis (see Section 3.1.1.2), the addition of RPC 4 to RPC 0 achieves the highest level of accuracy over the Two Season VA bandwidth. The 95th percentile of Δa_{RMS} is thus reduced by a factor 2.5 at 2.2 GHz, 2.8 at 2.8 GHz and 20 at 3.4 GHz.

To sum up, the MUSIC analysis strengthens the idea that the CRB-based method allows to quickly and efficiently choose the RPC to be added to RPC 0 in the DoA estimation process of a RP reconfigurable VA in order to improve its DF performances.

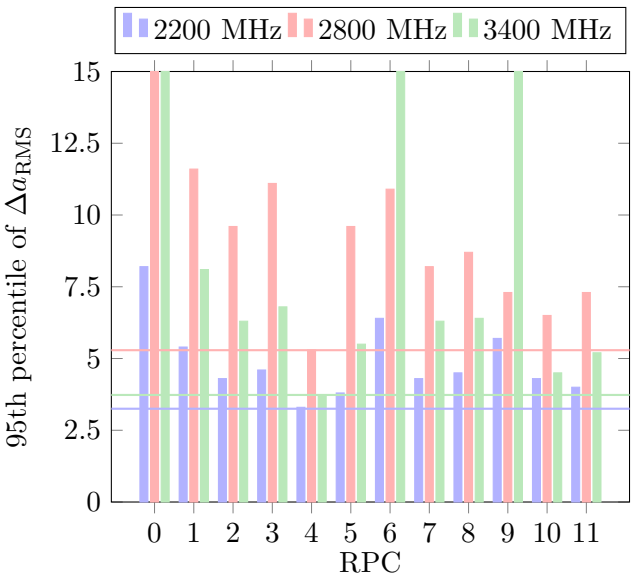

Figure 3.6: Simulated 95th percentile of Δa_{RMS} obtained from the Two Season VA adding different RPCs [1 to 11] to RPC 0 at 2.2 GHz, 2.8 GHz and 3.4 GHz, and under the scenario conditions defined in Table 3.3. The horizontal lines correspond to the lowest 95th percentile of Δa_{RMS}.

3.1.1.4 A word on the use of multiple radiation patterns combinations

After studying the DF performances of the Two Season VA when only one RPC is added to RPC 0, a relevant question here is whether, and to what extent, the estimation performances might be further improved by adding the other RPCs. In order to do so, the simulated DF performances of the Two Season VA are evaluated in terms of estimation accuracy using the MUSIC algorithm when all the RPCs [1 to 11] are added to RPC 0 in the DoA estimation process. Hence, the 37 available RPs in Section 3.1.1.2 are employed for the DoA estimation. The parameters used for this investigation are those reported in Table 3.3. By comparing the 95th percentile of Δa_{RMS} set out in Table 3.5, it can be noted that the addition of all RPCs to RPC 0 yields globally to similar results than those achieved when only RPC 4 and RPC 0 are used. It is therefore not necessary to add other RPCs (other than RPC 4) to RPC 0 for enhancing the DoA estimation accuracy achievable with Two Season VA. The addition of all RPCs will make the DoA estimation process more cumbersome and time-consuming, which is not necessary considering the achievable DF performances.

Frequency	95th percentile of Δa_{RMS}	
	RPC 4 + RPC 0	All RPC [1 to 11] + RPC 0
2.2 GHz	3.25°	3.34°
2.8 GHz	5.29°	7.86°
3.4 GHz	3.73°	3.64°

Table 3.5: Simulated 95th percentile of Δa_{RMS} obtained from the Two Season VA adding only RPC 4 or all RPCs [1 to 11] to RPC 0, and under the scenario conditions defined Table 3.3

3.1.1.5 A word on the risk of angular ambiguity

As stated in Section 2.7.2, the problem of angular ambiguity is related both to the geometry of the DF antenna and its RPs. Since the geometry of the Two Season VA is already fixed, the question that arises is whether the addition of a RPC reduces the risk of angular ambiguity. Fig. 3.7 displays at the three frequencies of interest the ambiguity spectrum in the 3-D half-space of the Two Season VA when RPC 4 or RPC 6 is added to RPC 0. The results obtained in Section 2.7.2 from using only RPC 0 are also recalled for comparison purposes. It can be noted that depending on the RPC added to RPC 0, its effectiveness in reducing the risk of angular ambiguity varies. However, the angular ambiguity risk is significantly reduced across the overall VA bandwidth when RPC 4 is added. For instance, this is especially true at 3.4 GHz in the direction $\phi = 0°$ (mod 90°) where the estimation error was maximum (see Fig. 2.36(h)). In contrast, no significant reduction of the risk of angular ambiguity is obtained when RPC 6 is used in addition to RPC 0. This is consistent with the results reported in Fig. 3.6, which indicate that adding RPC 6 does not improve the overall DF performances. This leads to the conclusion that the addition of a RPC can significantly alleviate the problem of angular ambiguity.

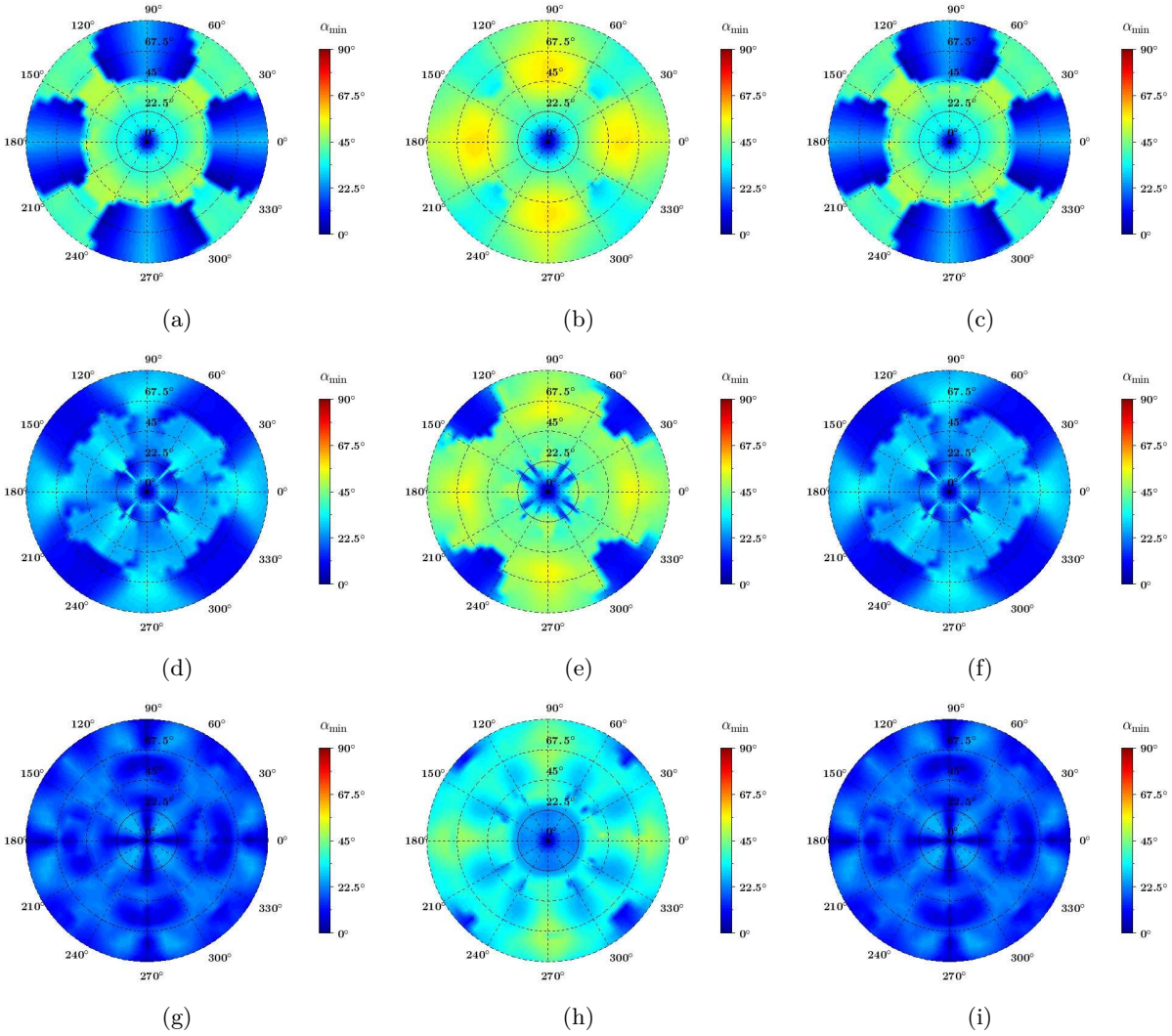

Figure 3.7: Simulated 3-D ambiguity spectrum $\alpha_{\min}$ of the Two Season VA from using RPC 0 only (left figures) or adding RPC 4 (central figures) or RPC 6 (right figures) to RPC 0 at the following frequencies: (a-c) 2.2 GHz, (d-f) 2.8 GHz, and (g-i) 3.4 GHz. Elevation angles θ are given on the radial axis and azimuth angles ϕ are given on the angular axis.

3.1.2 Re-evaluation of the direction finding performances of the Two Season vector antenna

In the previous section, a CRB-based method was provided to improve the DF performances of a reconfigurable VA by exploiting additional RP diversity. It has been pointed out that RPC 4 is the most likely to improve the DF performances of the Two Season VA. It is now time to briefly re-evaluate the DoA estimation accuracy (in simulation and measurement) as well as the sensitivity of the prototype using RPC 4. These new performances are compared to those achieved in Section 2.7, which were based only on the measurement of the three components E_z, H_x and H_y (RPC 0) of an incoming vertically-polarized EM-wave.

3.1.2.1 Direction-of-arrival estimation accuracy

In this section, the simulated and measured DoA estimation accuracy achievable using the Two Season VA and the MUSIC algorithm are re-evaluated under the scenario reported in Table 2.3. This re-evaluation is based on the measurement of the components E_z, H_x and H_y (RPC 0) of an incoming vertically-polarized EM-wave combined with additional RP diversity (RPC 4). As a reminder, this is made possible by the RP reconfigurability of the Two Season VA using different sets of weighting coefficients assigned to the signals received at its ports (see Table 2.2 and Table 3.1). Fig. 3.8 displays the simulated and measured angular distance Δa_{RMS} at the three frequencies of interest. The measured results previously reported in Section 2.7.4 and obtained under the same scenario from using RPC 0 only are also recalled for comparison purposes. It can be seen that the accuracy is clearly improved thanks to the addition of RPC 4 to RPC 0 in the DoA estimation process. Moreover, Δa_{RMS} does not exceed 5° for every direction in the 3-D upper half-space within the VA bandwidth. In fact, this additional RP diversity enables the correction of the estimation errors in the angular areas where the accuracy of the DoA estimation was the lowest, especially at 3.4 GHz for directions in the angular zones around $\phi = 0°$ (mod 90°). This is due to the significant reduction of the risk of angular ambiguity in these angular areas by adding RPC 4 to RPC 0 (see Fig. 3.7(g) and Fig. 3.7(h)). Besides, adding RPC 4 eliminates estimation errors in the measurement results for θ close to 0°. Furthermore, the results of the measurements and simulations are in good agreement, which is also confirmed by the values of the maximum Δa_{RMS} and 95th percentile of Δa_{RMS} set out in Table 3.6. The simulated and measured maximum Δa_{RMS} is lower than 1.4° and 2.4° across the Two Season VA bandwidth, respectively. Therefore, using RPC 4 in addition to RPC 0 clearly reduces the measured maximum error of Δa_{RMS} by a factor 8.7 at 2.2 GHz, 27.4 at 2.8 GHz and 57.8 at 3.4 GHz (in comparison with the values specified in Table 2.5). As for the measured 95th percentile of Δa_{RMS}, it is lowered by a factor 3.4 at 2.2 GHz, 3 at 2.8 GHz and 3.4 at 3.4 GHz. Moreover, details on the estimation errors $E^{\theta}_{\mathrm{RMS}}$ and E^{ϕ}_{RMS} that may be relevant for some applications are provided for interested readers in Appendix F.4.

Frequency	Simulated		Measured	
	max Δa_{RMS}	95th percentile of Δa_{RMS}	max Δa_{RMS}	95th percentile of Δa_{RMS}
2.2 GHz	1.2°	0.8°	2.4°	0.7°
2.8 GHz	1.4°	1.1°	1.6°	1.0°
3.4 GHz	1.4°	0.8°	1.9°	0.9°

Table 3.6: Simulated and measured $\Delta a_{\mathrm{RMS}}(\phi, \theta)$ obtained from the Two Season VA using both RPC 0 and RPC 4, and under the scenario conditions defined in Table 2.3

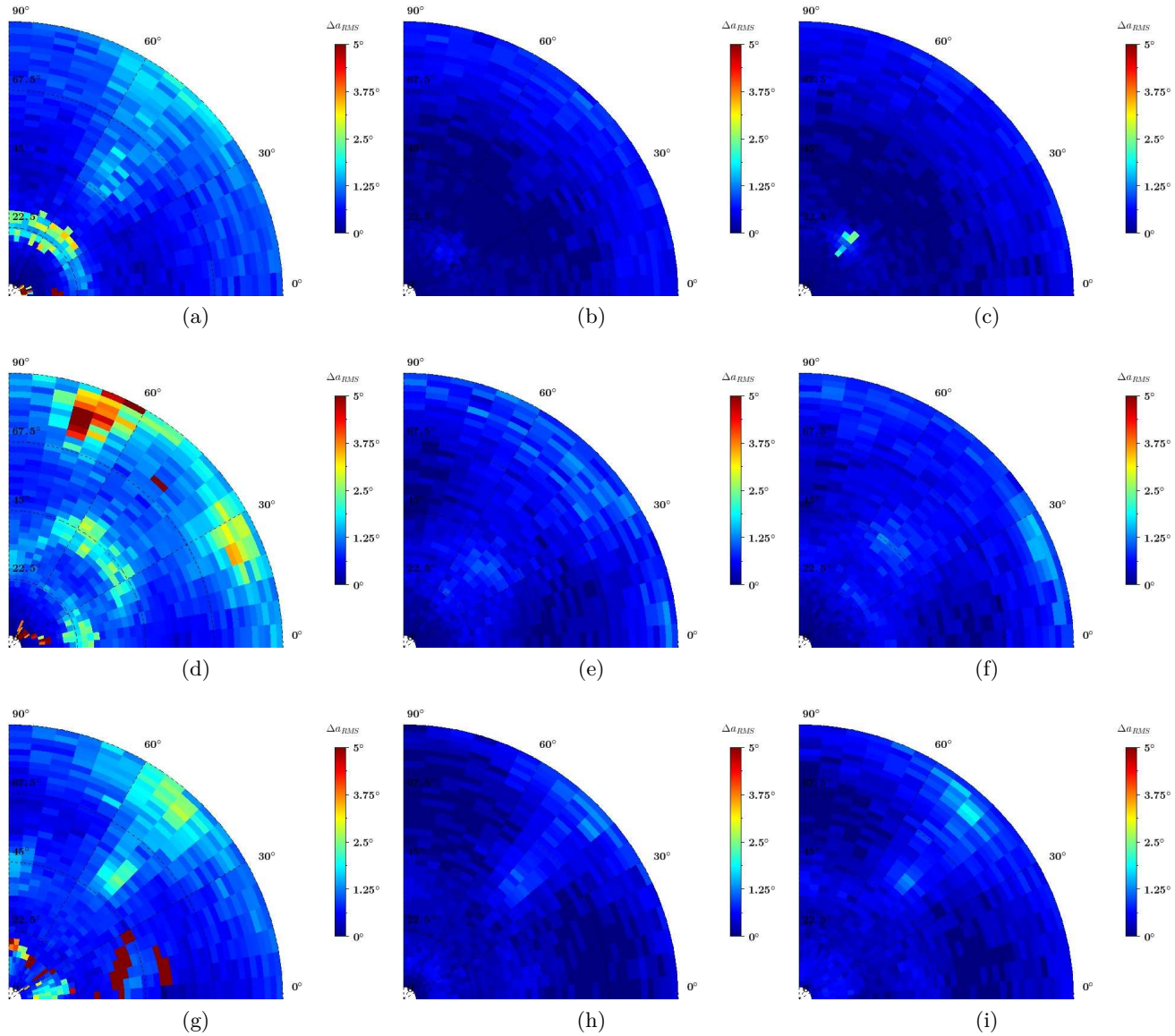

Figure 3.8: Simulated (central figures) and measured (right and left figures) $\Delta a_{\mathrm{RMS}}(\phi, \theta)$ obtained from the Two Season VA using RPC 0 only (left figures) or both RPC 0 and RPC 4 (central and right figures), and under the scenario conditions defined in Table 2.3 at the following frequencies: (a-c) 2.2 GHz, (d-f) 2.8 GHz, and (e-i) 3.4 GHz. Elevation angles θ are given on the radial axis and azimuth angles ϕ are given on the angular axis.

3.1.2.2 Sensitivity of the prototype

Let us now re-evaluate the sensitivity of the Two Season VA prototype when RPC 4 is used in addition to RPC 0 in the DoA estimation process of an incoming vertically-polarized EM-wave. As a reminder, the 95th percentile of Δa_{RMS} is used in this thesis to specify the sensitivity for a maximum error threshold of 5°. It is displayed in Fig. 3.9 to Fig. 3.11 at the three frequencies of interest and for different PNRs, ranging from 18 dB.m^{-2} to 36 dB.m^{-2} (with a step of 3 dB). The results obtained in Section 2.7.5 from using RPC 0 only are also recalled on the graphs. It can be observed that thanks to the addition of RPC 4 to RPC 0, the sensitivity of the Two Season VA is globally improved and also remains stable in the upper bandwidth. Hence, the sensitivity of the Two Season VA using RPC 0 and RPC 4 for the DoA estimation of an incident vertically-polarized EM-wave is of -121 dBW.m^{-2} at 2.2 GHz (PNR $\approx$ 20 dB.m^{-2}), -115 dBW.m^{-2} at 2.8 GHz (PNR $\approx$ 26 dB.m^{-2}) and -115 dBW.m^{-2} at 3.4 GHz (PNR $\approx$ 26 dB.m^{-2}). Indeed, as derived in Section 3.1.1.5, the addition of RPC 4 to RPC 0 in the DoA estimation process reduces the ambiguity risk (which increases with frequency). As a consequence, the sensitivity is unchanged as the frequency increases. The theoretical range $r_{\max}$ can also be re-evaluated taking into account the same emitter as before (i.e., an isotropic antenna and an emitting power of 1 W). The theoretical range of the Two Season VA using RPC 0 and RPC 4 for the DoA estimation is now of 317 km at 2.2 GHz, and 159 km at 2.8 GHz and 3.4 GHz. This corresponds to an extension of the range, which is multiplied by the factors 3.2 to 2.2 GHz, 2.2 to 2.8 GHz and 2.8 to 3.4 GHz.

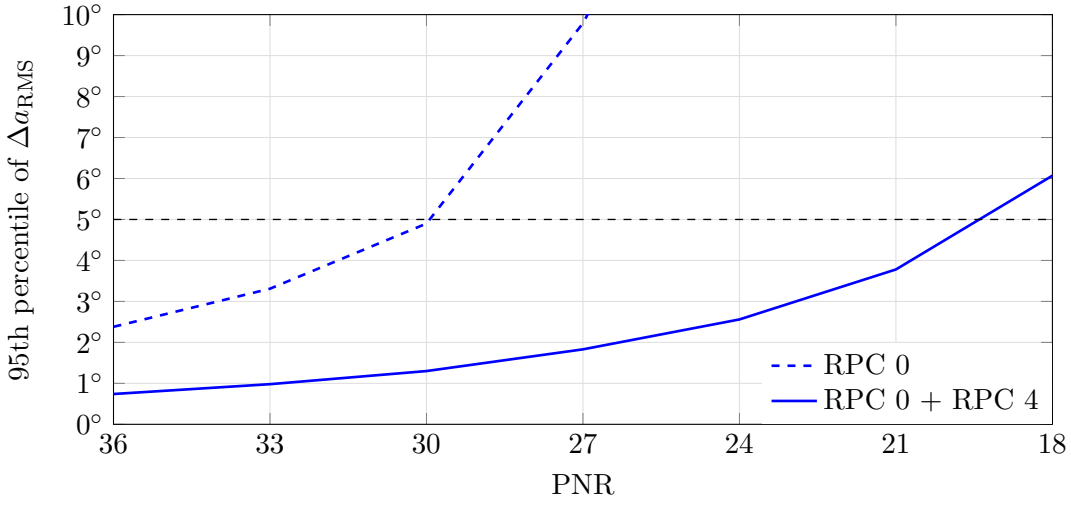

Figure 3.9: Measured 95th percentile of Δa_{RMS} at 2.2 GHz using both RPC 0 and RPC 4 for the DoA estimation of an incident vertically-polarized EM-wave

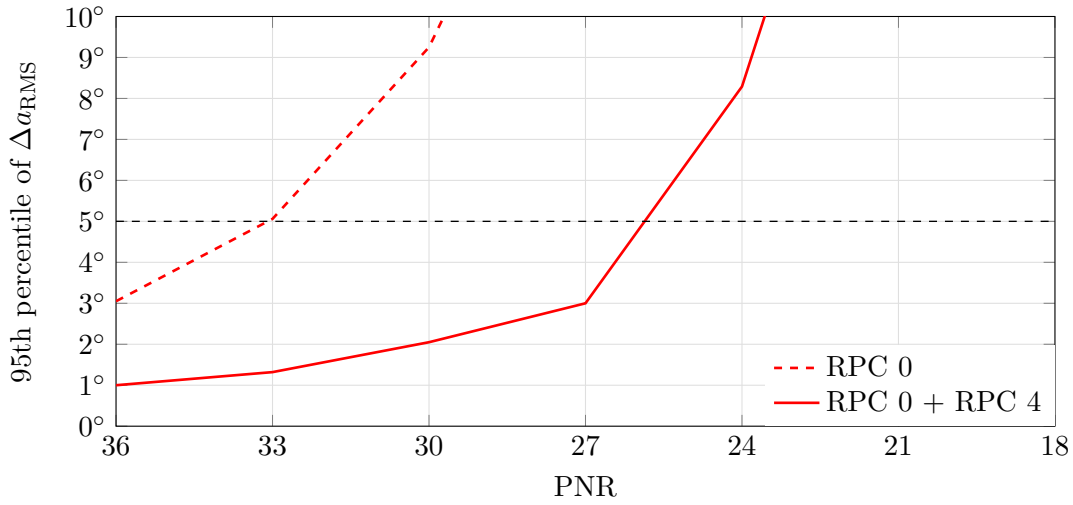

Figure 3.10: Measured 95th percentile of Δa_{RMS} at 2.8 GHz using both RPC 0 and RPC 4 for the DoA estimation of an incident vertically-polarized EM-wave

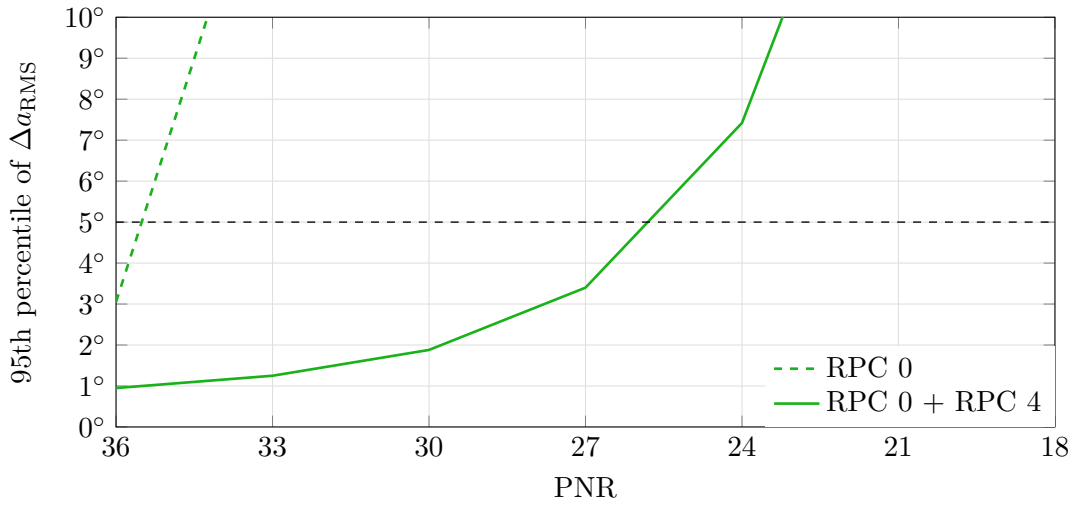

Figure 3.11: Measured 95th percentile of Δa_{RMS} at 3.4 GHz using both RPC 0 and RPC 4 for the DoA estimation of an incident vertically-polarized EM-wave

3.1.3 Conclusion

The first section of this chapter was dedicated to the enhancement of the DF performances of the Two Season VA by further exploiting its RP reconfigurability. Specifically, the RP reconfigurability was leveraged by adding new RPs to those associated to the measurement of the components of the incoming EM-waves in the DoA estimation process. First, an original method based on the CRB was proposed in order to rapidly select the RP diversity that maximizes the accuracy of the estimate across the overall bandwidth. It can be noted that this method is not subject to the DoA estimation technique used for evaluating the DF performances of the VA. Then, it was shown that the selection of additional RP diversity minimizes the risk of angular ambiguity. Finally, simulated and measured DF performances were re-evaluated using additional RP diver-

sity and the MUSIC algorithm. It was demonstrated that such RP diversity allows a significant improvement of the DF performances in terms of DoA estimation accuracy and sensitivity, as shown in Table 3.7 (see Table 2.42 for prior performances).

Frequency	P_{sensi}	PNR	$r_{\max}$ † (P_e, G_e)
2.2 GHz	-121 dBW.m^{-2}	20 dB.m^{-2}	317 km † (1 W, 0 dBi)
2.8 GHz	-115 dBW.m^{-2}	26 dB.m^{-2}	159 km † (1 W, 0 dBi)
3.4 GHz	-115 dBW.m^{-2}	26 dB.m^{-2}	159 km † (1 W, 0 dBi)

Table 3.7: Sensitivity and theoretical range of the Two Season VA prototype using RPC 0 and RPC 4 for the DoA estimation of an incident vertically-polarized EM-wave

Although the addition of new RPs was explored here through the re-evaluation of the simulated and measured DF performances of the Two Season VA, it can be applied to any RP reconfigurable VAs.

3.2 Enhancement of the frequency coverage: an improved version of the Two Season vector antenna

The aim of this section is to enhance the frequency coverage of the Two Season VA thanks to a modification of its feeding-profile as well as the deployment of the previously-cited RP diversity technique. This led to a "new version" of this VA, referred to as the improved version of the Two Season VA in the remainder of this thesis. In this section,the electrical characteristics and DF performances are only assessed through full-EM simulations.

3.2.1 Topology of the improved version of the Two Season vector antenna

The improved version of Two Season VA still consists of two orthogonal and colocated semi-circular arrays of Vivaldi antennas. Furthermore, the same port-numbering is used (see Fig. 2.22). The geometry of the semi-circular arrays constituting this new version is depicted in Fig. 3.12 and their dimensions are specified in Table 3.8. Besides, they are again printed on the 0.8 mm thick FR4 substrate (dielectric constant of 4.3 and loss tangent of 0.025) and mounted over the octagonal metallic surface of side length e. Only the feeding-profile is modified in order to design this new version of the Two Season VA. The slotlines associated with each Vivaldi antenna are still electromagnetically coupled through the microstrip-to-slot transition that features a circular cavity of 5.5 mm radius (r_c) and an 80° radial stub of radius $r_s = r_c$ in order to broaden the bandwidth. In contrast to that mentioned in the Section 2.5.1.3, the input impedance of the Vivaldi antennas is around 100 Ω and not 65 Ω. Therefore, the 1:2 microstrip line power splitter, which was previously fabricated using the T-junction and impedance transition lines, can simply be replaced by two 100 Ω parallel microstrip lines connected to the 50 Ω input port. Indeed, as two 100 Ω microstrip lines are connected in parallel, a 50 Ω microstrip line can be used to provide power with equal magnitude across a wide frequency range.

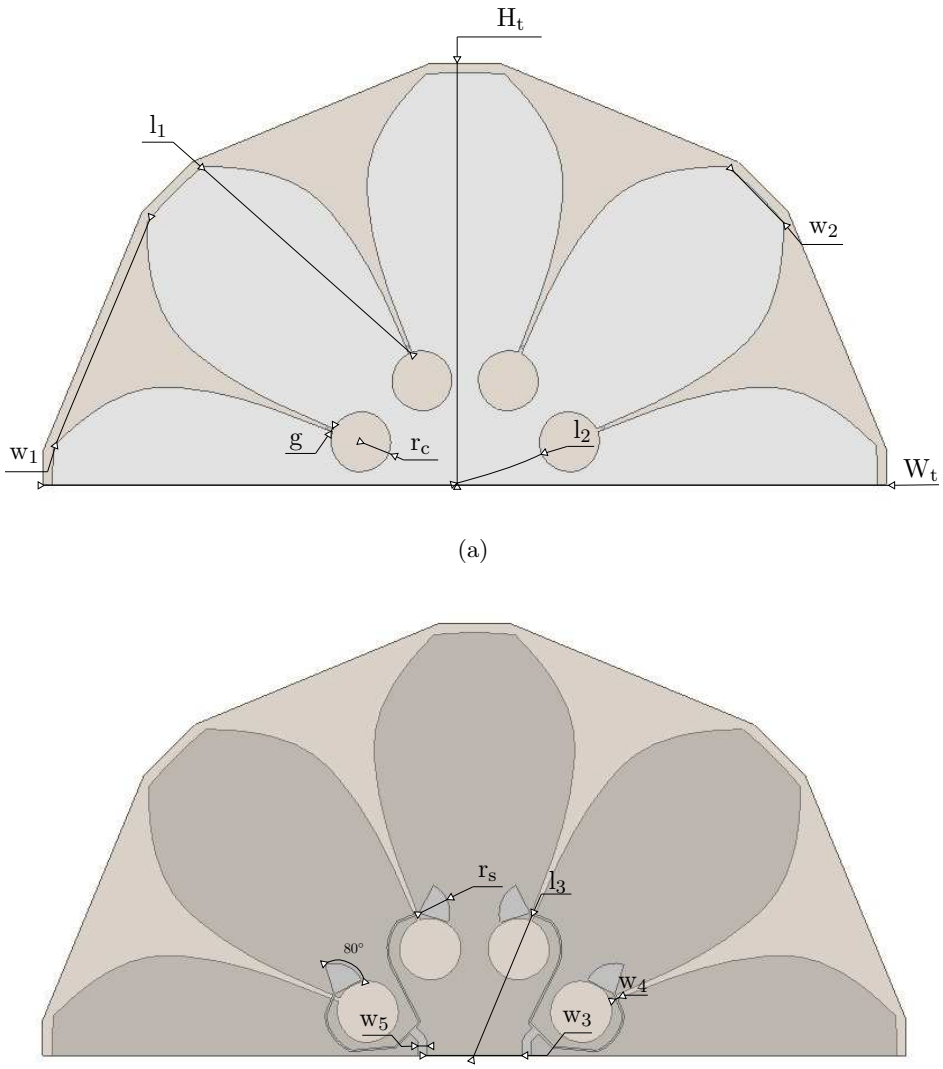

Figure 3.12: Topology of the semi-circular arrays constituting the improved version of the Two Season VA mounted over a ground plane (not depicted in these figures): (a) radiating- and (b) feeding-profiles.

Parameter	W_t	H_t	w_1	w_2	l_1	l_2	l_3
Value (in mm)	153	76.5	43.8	14.4	50.5	15	26.7
Parameter	g	r_c	r_s	w_3	w_4	w_5	e
Value (in mm)	0.6	5.5	5.5	16.9	0.36	1.58	125

Table 3.8: Dimensions of the semi-circular arrays used for designing the improved version of the Two Season VA

3.2.2 Electrical performances of the improved version of the Two Season vector antenna

So far this section has presented the topology of the new version of the Two Season VA, the electrical performances in terms of impedance matching and radiation properties are now re-evaluated through full-wave EM simulations with Ansys HFSS.

3.2.2.1 Impedance matching and mutual coupling

Fig. 3.13 shows the simulated VSWR of the improved version of the Two Season VA. Besides, only the port 1 is considered according to the reasons previously-mentioned in Section 2.6.1. Considering also a VSWR smaller than 2.3, the simulated impedance bandwidth is of 8.72:1 from 1.31 GHz to 11.42 GHz. Hence, the redesign of the feeding profile in Section 3.2.1 enables the global improvement of the VSWR and the widening of the simulated bandwidth, which was previously of 1.71:1 from 2.08 GHz to 3.56 GHz. The electrical size of the improved version of the Two Season VA is therefore diminished by a factor of 1.59. The VA is now included in a half-sphere within a $0.33\lambda_0$ radius and mounted on a finite metallic and octagonal support with a circumcircle radius of $0.71\lambda_0$, where λ_0 is the free space wavelength at 1.31 GHz.

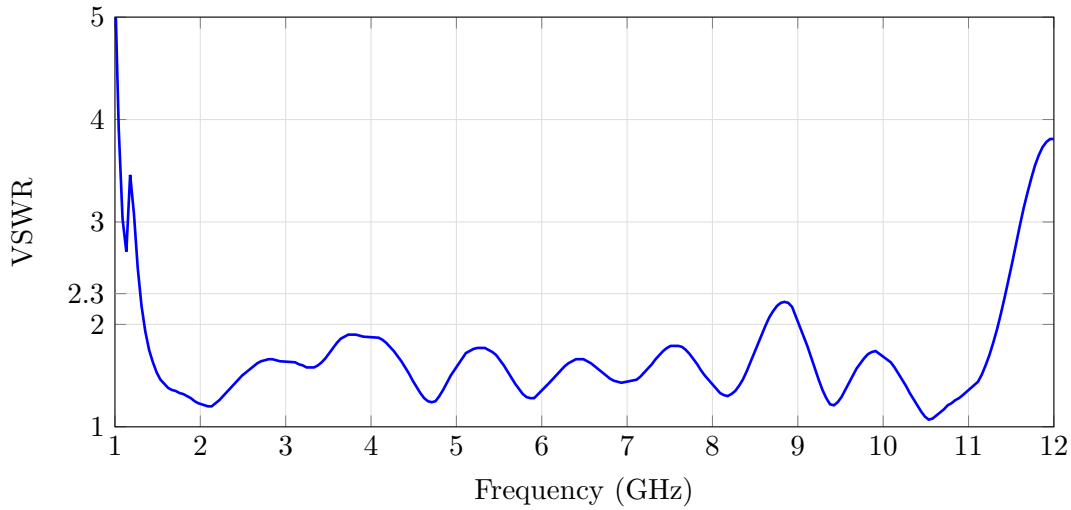

Figure 3.13: Simulated VSWR of the improved version of the Two Season VA

Fig. 3.14 displays the simulated isolation between port 1 and the three other ports of the improved version of Two Season VA. It can be observed that the mutual coupling between the port 1 and the other ports does not exceed -20 dB from 1.9 GHz to 12 GHz. However, the isolation is slightly poorer at lower frequencies since the mutual coupling is only below -10 dB. Moreover, the same level of isolation is obtained at the other ports. But anyway, it can be stated that a good isolation is achieved across the overall operating bandwidth.

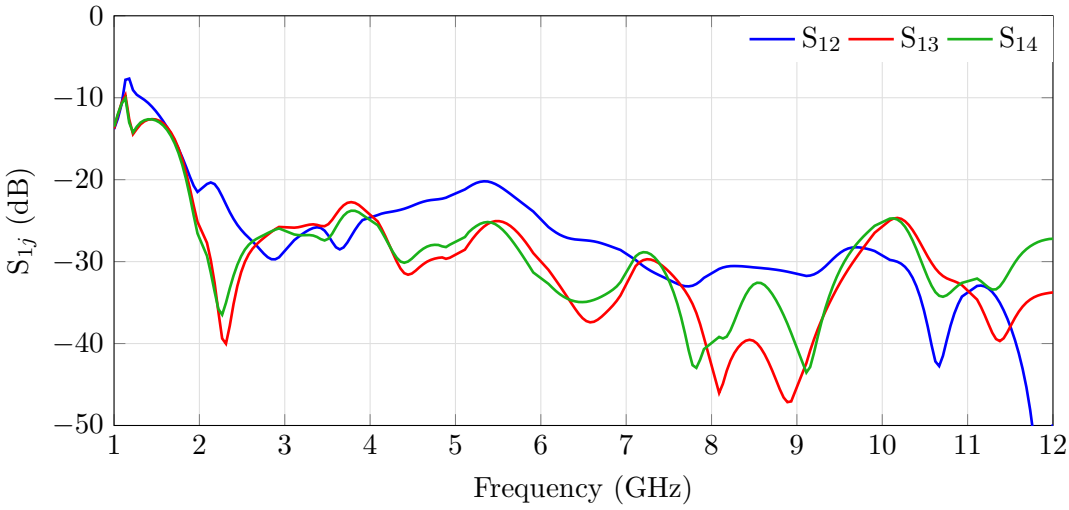

Figure 3.14: Simulated isolation at port 1 of the improved version of the Two Season VA

3.2.2.2 Radiation patterns

The RPs of the improved version of the Two Season VA associated with the measurement of the components E_z and H_x of an incoming EM-wave are depicted in Fig. 3.16 and Fig. 3.15, respectively. These RPs are represented in four frequencies: 1.4 GHz, 5 GHz, 8.6 GHz, and 11 GHz in order to provide an overview across the impedance bandwidth. Besides, the RPs associated with the measurement of the component H_y are not shown for symmetry reasons. In addition, it is worth mentioning that the RPs at 2.2 GHz, 2.8 GHz, and 3.4 GHz are similar to those of the previous Two Season VA reported in Fig. F.5 to Fig. F.6 but are not displayed here for brevity reasons. Several observations can be highlighted. Firstly, it can be observed that some ripples appear in the E-plane of the magnetic dipole as the frequency increases, yielding to omnidirectionality defects. Indeed, these fluctuations occur from 3.4 GHz in accordance with Chu's theory, as explained in Section 2.6.2. As for the electric monopole, it can be seen that a few blind directions appear at higher frequencies. These directions depend on the operating frequency. Secondly, the level of cross-polarization[5] of the electric monopole increases with the frequency (see Fig. 3.16(a-c)), which may lead to DoA estimation errors. Based on these observations, the improved version of the Two Season VA is likely to provide good DF performances in the frequency range 1.31 GHz to 3.55 GHz. Indeed, the RPs differ from those of ideal magnetic dipoles and electric monopole beyond 3.6 GHz.

[5]The RPs in θ-polarization and ϕ-polarization correspond to the ones in co-polarization and cross-polarization for an electric dipole oriented along the $\hat{z}$-axis.

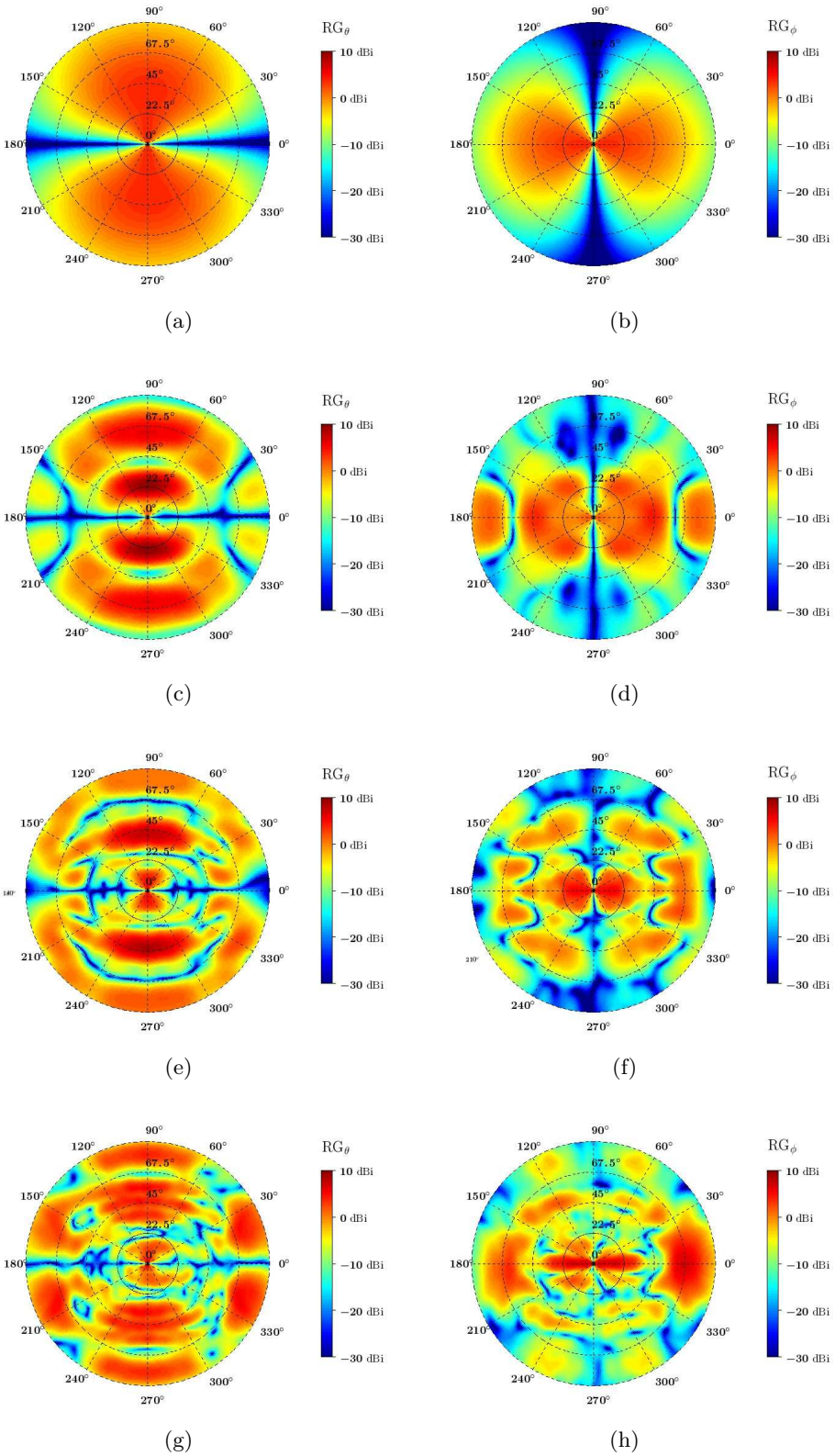

Figure 3.15: Simulated realized gain in the θ-polarization (left figures) and ϕ-polarization (right figures) of the improved Two Season VA (mounted on the octagonal metallic support) used for measuring the component H_x of the incoming EM-wave at: (a) & (b) 1.4 GHz, (c) & (d) 5 GHz, (e) & (f) 8 GHz, and (g) & (h) 11 GHz.

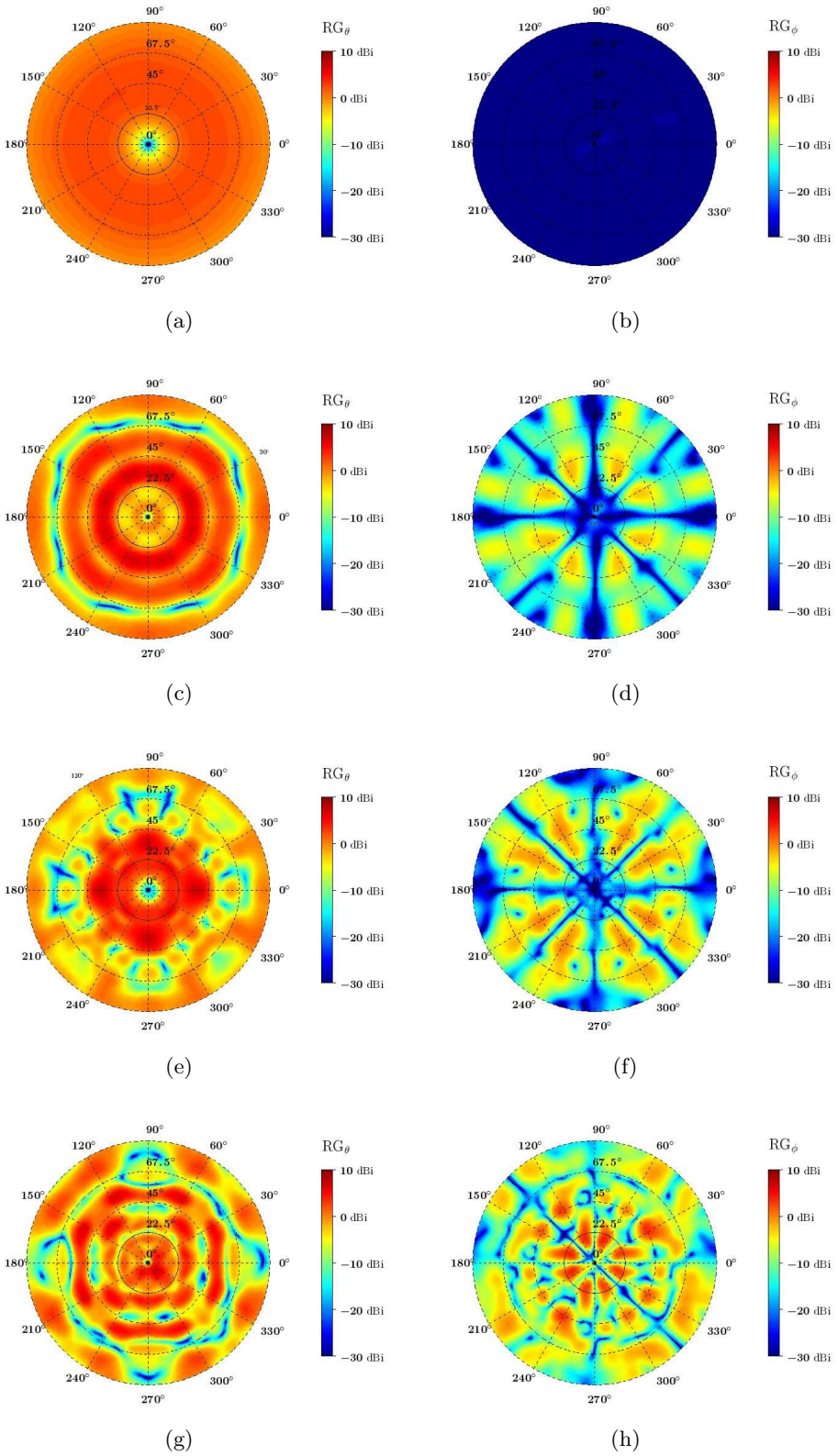

Figure 3.16: Simulated realized gain in the θ-polarization (left figures) and ϕ-polarization (right figures) of the improved Two Season VA (mounted on the octagonal metallic support) used for measuring the component E_z of the incoming EM-wave at: (a) & (b) 1.4 GHz, (c) & (d) 5 GHz, (e) & (f) 8 GHz, and (g) & (h) 11 GHz.

3.2.2.3 Efficiency

The simulated total efficiency of the improved version of the Two Season VA is represented in Fig. 3.17 between 1.3 GHz and 11.5 GHz, which corresponds to the impedance bandwidth of the VA. The frequency step used for the efficiency evaluation is of 0.1 GHz. As indicated in Section 2.6.3, only the efficiency at port 1 has to be considered. It can be observed that the total efficiency decreases with the frequency but exceeds 80% between 1.3 GHz and 8.4 GHz. Furthermore, it is still higher than 70% at higher frequencies (up to 11 GHz). Therefore, good DF performances may be expected.

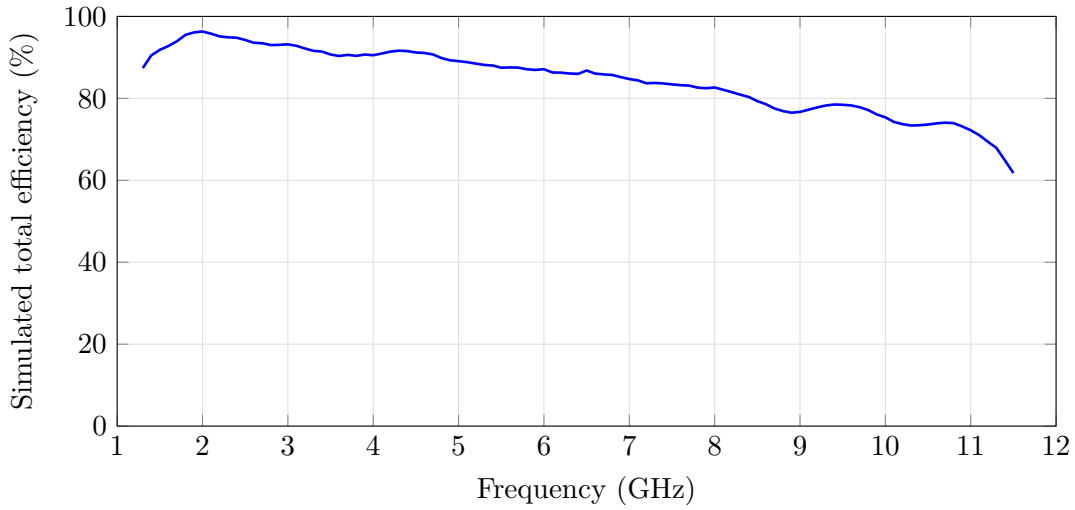

Figure 3.17: Simulated total efficiency of the improved version of the Two Season VA

3.2.3 Direction finding performances of the improved version of the Two Season vector antenna

The Two Season VA is intended to estimate the DoA of vertically-polarized EM-waves in the upper hemisphere through the measurement of the components E_z, H_x and H_y (RPC 0). The DF performances of the prior Two Season VA have been evaluated between 2.2 GHz to 3.4 GHz from using RPC 0 only (see Section 2.7) and from adding the previously-introduced RP diversity technique (see Section 3.1). The overall DF performances were improved using this technique, in particular at 3.4 GHz where the accuracy of the DoA estimation was the poorest. In the sections that follow, the simulated DF performances of the improved version of the Two Season VA are briefly re-evaluated across the new impedance bandwidth from 1.31 GHz to 11.42 GHz with or without using the RP diversity technique.

3.2.3.1 Direction finding performances without using additional radiation pattern diversity

The evaluation of the DoA estimation accuracy of an incoming vertically-polarized EM-wave using the improved version of the Two Season VA is done under the scenario reported in Table 2.3. However, the frequencies of interest now range from 1.4 GHz to 7.8 GHz with a step of 0.4 GHz.

Moreover, this evaluation is based solely on the measurement of three components E_z, H_x, and H_y which is derived through RPC 0.

Fig. 3.18 shows the simulated 95th percentile of the angular distance Δa_{RMS} as a function of the frequency. It can be observed that the 95th percentile of Δa_{RMS} is lower than 5° up to 3.4 GHz and is only equal to 5.9° at 3.8 GHz. However, it is more than 30° for higher frequencies, which means that the improved version of the Two Season VA is not suited for 3-D DF at these frequencies (if only RPC 0 is used for the DoA estimation). This can be explained by the fact that the RPs that permit the measurement of the components E_z, H_x, and H_y are not as similar as those of ideal dipoles, as they are at lower frequencies (see Section 3.2.2.2). It can be noted the DF performances between 2.2 GHz and 3.4 GHz are consistent with the ones achieved with the prior Two Season VA reported in Section 2.7.4. Besides, in view of the results obtained between 3.8 GHz and 7.8 GHz, the DF performances evaluation was not performed in the frequency range from 7.8 GHz to 11.4 GHz (i.e., in the upper-end of the impedance bandwidth).

Fig. 3.19 presents the simulated Δa_{RMS} at four frequencies: 1.4 GHz, 2.2 GHz, 3 GHz, and 3.8 GHz. It can be seen that Δa_{RMS} does not exceed 5° in almost every direction in the 3-D upper half-space over this frequency range. As stated in Section 2.7.4, these specific directions depend on the operating frequency.

Hence, the frequency coverage of the improved version of the Two Season VA is enhanced. Indeed, this VA can estimate accurately the DoA of an incoming vertically-polarized EM-wave across the 3-D upper half-space and over a 2.9:1 bandwidth between 1.31 GHz to 3.8 GHz from using only the measurement of the three components E_z, H_x, and H_y. As a reminder, the former prototype Two Season VA reached the same level of DF performances over a 1.69:1 bandwidth from 2.1 GHz to 3.55 GHz.

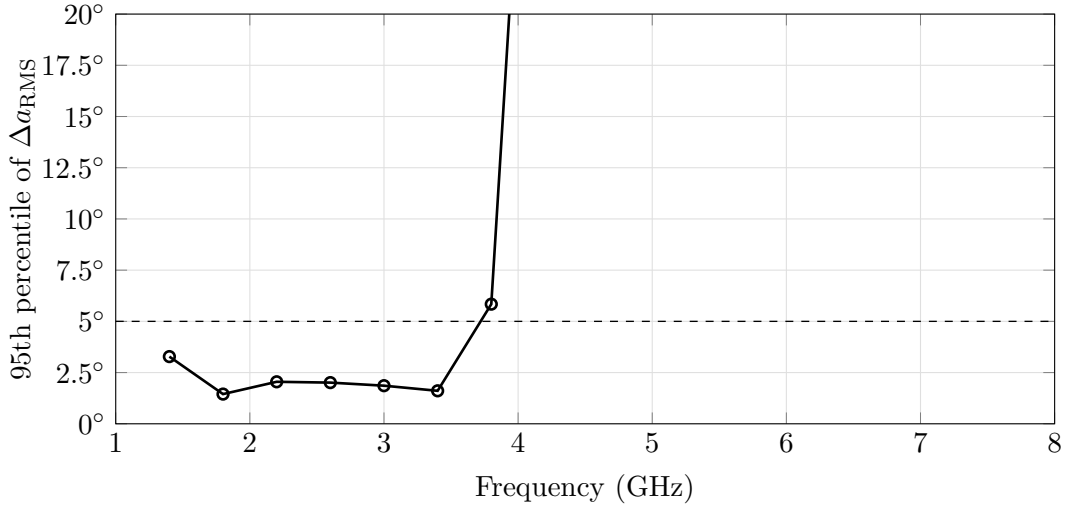

Figure 3.18: Simulated 95th percentile of Δa_{RMS} obtained from the improved version of the Two Season VA using RPC 0 only, and under the scenario conditions defined in Table 2.3

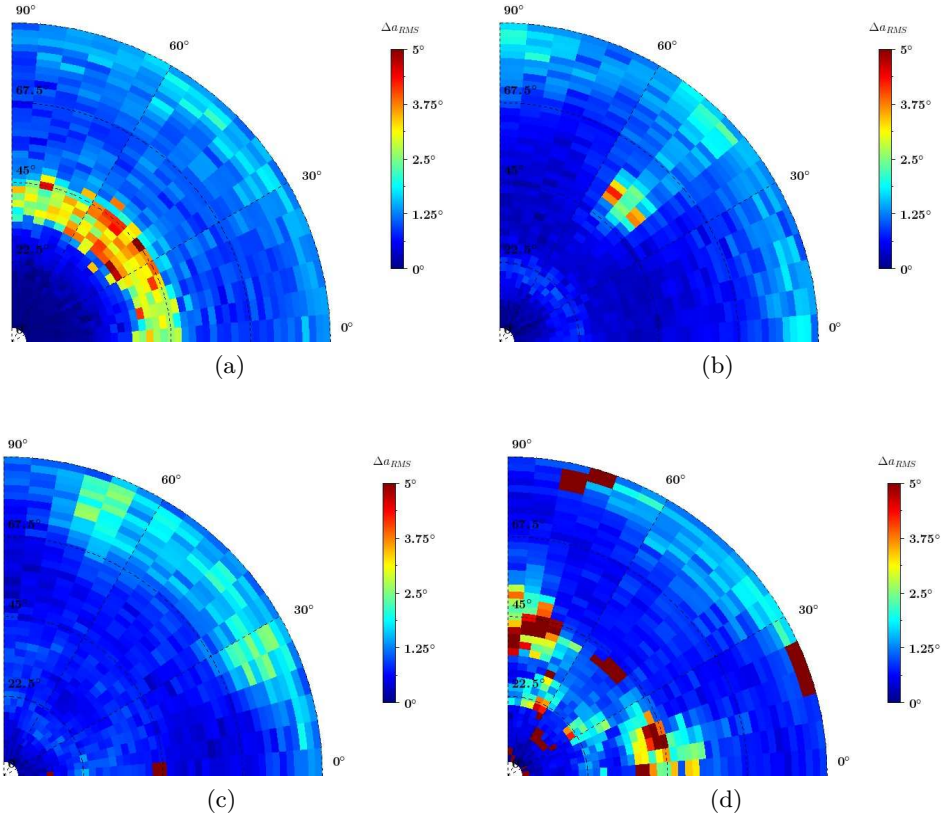

Figure 3.19: Simulated $\Delta a_{\mathrm{RMS}}(\phi, \theta)$ obtained with the improved version of Two Season VA from using RPC 0 only, and under the scenario conditions defined in Table 2.3 at the following frequencies: (a) 1.4 GHz, (b) 2.2 GHz, (c) 3.0 GHz, and (d) 3.8 GHz. Elevation angles θ are given on the radial axis and azimuth angles ϕ are given on the angular axis.

3.2.3.2 Direction finding performances using additional radiation pattern diversity

The DF performances of the improved version of the Two Season VA are now re-evaluated using the additional RP diversity technique introduced in Section 3.1.

Selection of the RPC

The first step consists in choosing the RPC to add to RPC 0 in the DoA estimation process among the 11 available RPCs summarized in Table 3.1. For each RPC, the CRB on θ and ϕ is computed from the parameters displayed in Table 3.2 and between 1.3 GHz to 8.9 GHz with a 0.1 GHz step. The CRB_ϕ and CRB_θ are shown in Fig. 3.20 and Fig. 3.21, respectively. The results achieved from using only RPC 0 are also set out for comparison purposes. First, it can be noted that the improvement of the DoA estimation accuracy is more or less effective in ϕ and θ as a function of the RPC as well as the frequency. Secondly, RPC 4 achieves practically the highest accuracy for estimating θ over the studied frequency range. As for estimating ϕ, it is basically the case up to 3.8 GHz. At higher frequencies, RPC 4 is globally the most effective RPC for enhancing the DoA estimation accuracy both in azimuth and elevation. Therefore, RPC 4 is

chosen to be added to RPC 0 over the entire bandwidth without inhibition as it already greatly improves the DF performances. It can be noted that a more complicated DoA estimation process could eventually be implemented by choosing the most favorable RPC at each frequency.

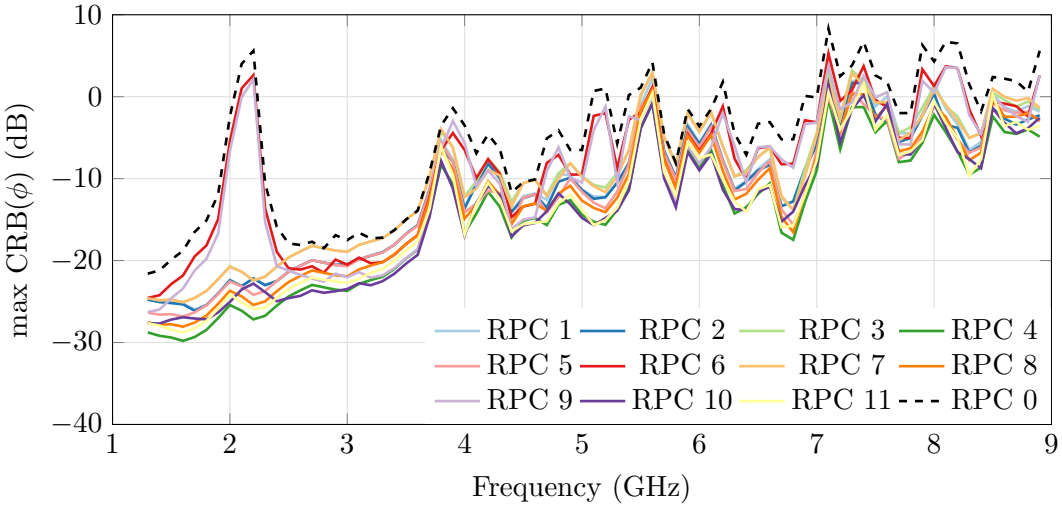

Figure 3.20: Highest simulated CRB(ϕ) of the improved version of the Two Season VA using different RPCs [1 to 11] added to RPC 0, and under the scenario conditions defined in Table 3.2

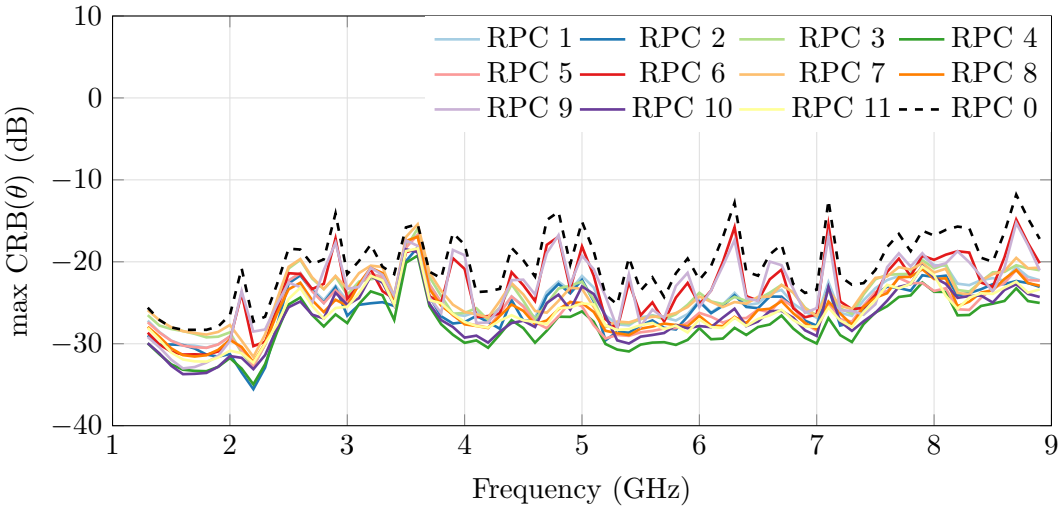

Figure 3.21: Highest simulated CRB(θ) of the improved version of the Two Season VA using different RPCs [1 to 11] added to RPC 0, and under the scenario conditions defined in Table 3.2

DoA estimation accuracy

The simulated estimation accuracy of the DoA of an incoming vertically-polarized EM-wave achievable using the improved version of the Two Season VA and the MUSIC algorithm are evaluated under the scenario conditions specified in Table 2.3 between 1.4 GHz to 9.8 GHz (with a 0.2 GHz step). In this evaluation, RPC 4 is employed in the DoA estimation process in

addition to the measurement of the three components E_z, H_x and H_y of the incident EM-wave (RPC 0).

Fig. 3.22 displays the simulated maximum value and 95th percentile of the angular distance Δa_{RMS} achieved under these conditions. For comparison purposes, the results obtained in Section 3.2.3.1 are also reported in these charts. Several observations can be highlighted. Firstly, it can be clearly seen that the addition of RPC 4 to RPC 0 improves the accuracy of the DoA estimation. Secondly, estimation errors increase with frequency whether or not RPC 4 is used, which is consistent with the CRB curves depicted in Fig. 3.20 and Fig. 3.21. However, the 95th percentile of Δa_{RMS} is now lower than 5° up to 8.6 GHz thanks to the addition of RPC 4, compared to 3.4 GHz beforehand. The frequency coverage is therefore extended.

In particular, the angular distance Δa_{RMS} is set out at four frequencies (that are 1.4 GHz, 3.8 GHz, 5 GHz, and 8.6 GHz) when RPC 4 is added to RPC 0 in Fig. 3.23 in order to provide an overview of the DF performances. It can be observed that Δa_{RMS} does not exceed 5° in almost every direction in the upper hemisphere. As previously-stated, the accuracy of the DoA estimation decreases as the frequencies increases. However, the addition of RPC 4 improves the overall DF performances (see, e.g., the accuracy achieved at 1.4 GHz and 3.8 GHz in Fig. 3.19(a & d) and Fig. 3.23(a & b)) and independently of the frequency.

In a nutshell, the improved version of the Two Season VA can estimate the DoA of an incoming vertically-polarized EM-wave across the 3-D upper half-space and over a 6.56:1 bandwidth between 1.31 GHz to 8.6 GHz with a good accuracy if the RP diversity technique is added to the measurement of the three components E_z, H_x, and H_y in the estimation process. This technique not only improves the accuracy of the DoA estimation, but also enables the extension of the frequency coverage. The same RPC (RPC 4) is used across the overall bandwidth, which is interesting in order to simplify the DoA estimation process.

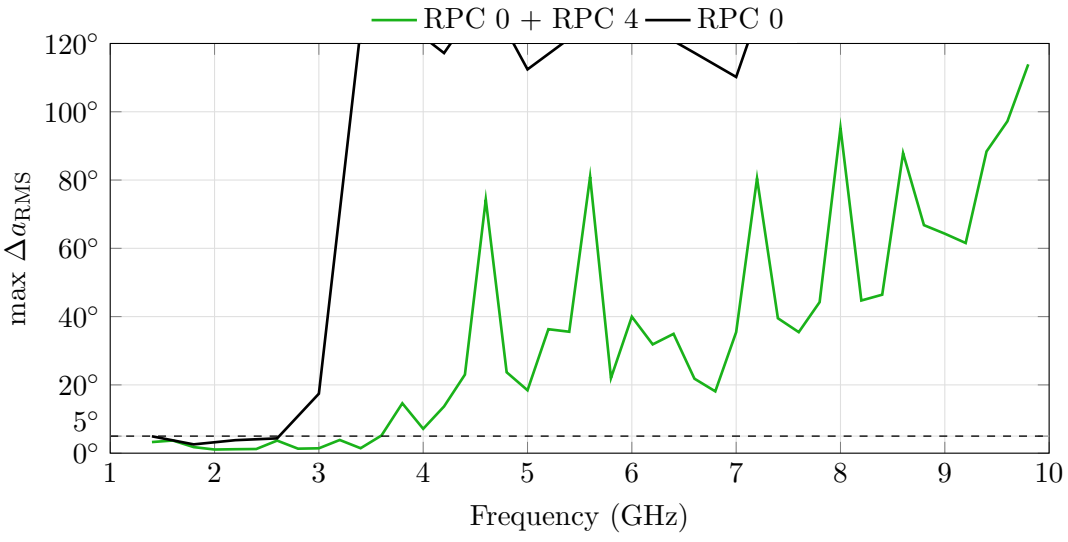

(a)

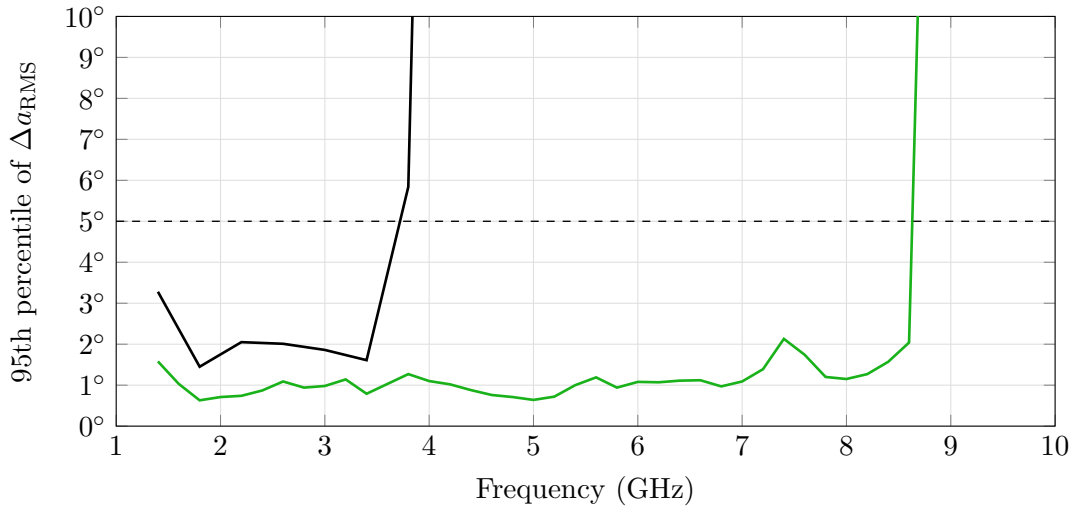

(b)

Figure 3.22: Simulated (a) max Δa_{RMS} and (b) 95th percentile of Δa_{RMS} obtained with the improved version of the Two Season VA from adding RPC 4 to RPC 0, and under the scenario conditions defined in Table 2.3

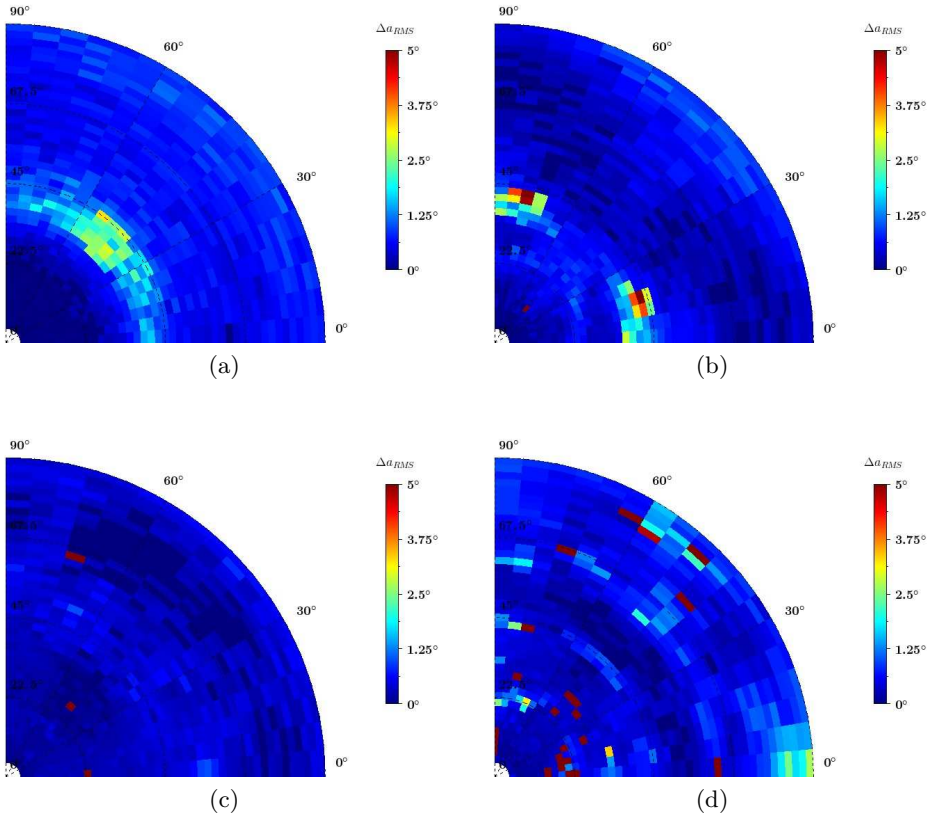

(a) (b)

(c) (d)

Figure 3.23: Simulated $\Delta a_{\mathrm{RMS}}(\phi, \theta)$ obtained with the improved version of Two Season VA from adding RPC 4 to RPC 0, and under the scenario conditions defined in Table 2.3 at the following frequencies: (a) 1.4 GHz, (b) 3.8 GHz, (c) 5 GHz, and (d) 8.6 GHz. Elevation angles θ are given on the radial axis and azimuth angles ϕ are given on the angular axis.

Simulated sensitivity

The simulated sensitivity of the improved version of the Two Season VA is now re-evaluated at 1.4 GHz, 5 GHz and 8.6 GHz when RPC 4 is added to RPC 0 for the estimation of the DoA of an incident vertically-polarized EM-wave. These frequencies correspond approximately to the lower, central and upper frequencies of the VA bandwidth within which the 95th percentile of Δa_{RMS} was below 5° (under the scenario conditions summarized in Table 2.3). This figure-of-merit is shown in Fig. 3.24 at the three frequencies of interest and for different PNRs, ranging from 18 dB.m^{-2} to 36 dB.m^{-2} (with a step of 3 dB). The sensitivity of the improved Two Season VA is degraded as the frequency increases since the 95th percentile of Δa_{RMS} also rises (see Fig. 3.22). From Fig. 3.24, it can be stated that P_{sensi} is approximately of -115 dBW.m^{-2} at 1.4 GHz (PNR $\approx$ 26 dB.m^{-2}), -109 dBW.m^{-2} at 5 GHz (PNR $\approx$ 32 dB.m^{-2}) and -106 dBW.m^{-2} at 8.6 GHz (PNR $\approx$ 35 dB.m^{-2}) to estimate accurately the DoA of an incoming vertically-polarized EM-wave using both RPC 0 and RPC 4. Considering the same emitter as before (i.e., an isotropic antenna and an emitting power of 1 W), the theoretical range $r_{\max}$ of the improved version of the Two Season VA using RPC 0 and RPC 4 for the DoA estimation has been derived and reported in Table 3.9. The ranges achieved are consistent with those displayed in Table 3.7.

Table 3.9: Simulated sensitivity and theoretical range of the improved Two Season VA prototype using RPC 0 and RPC 4 for the DoA estimation of an incident vertically-polarized EM-wave

Frequency	P_{sensi}	PNR	$r_{\max}$ † (P_e, G_e)
1.4 GHz	-115 dBW.m^{-2}	26 dB.m^{-2}	159 km † (1 W, 0 dBi)
5 GHz	-109 dBW.m^{-2}	32 dB.m^{-2}	80 km † (1 W, 0 dBi)
8.6 GHz	-106 dBW.m^{-2}	35 dB.m^{-2}	56 km † (1 W, 0 dBi)

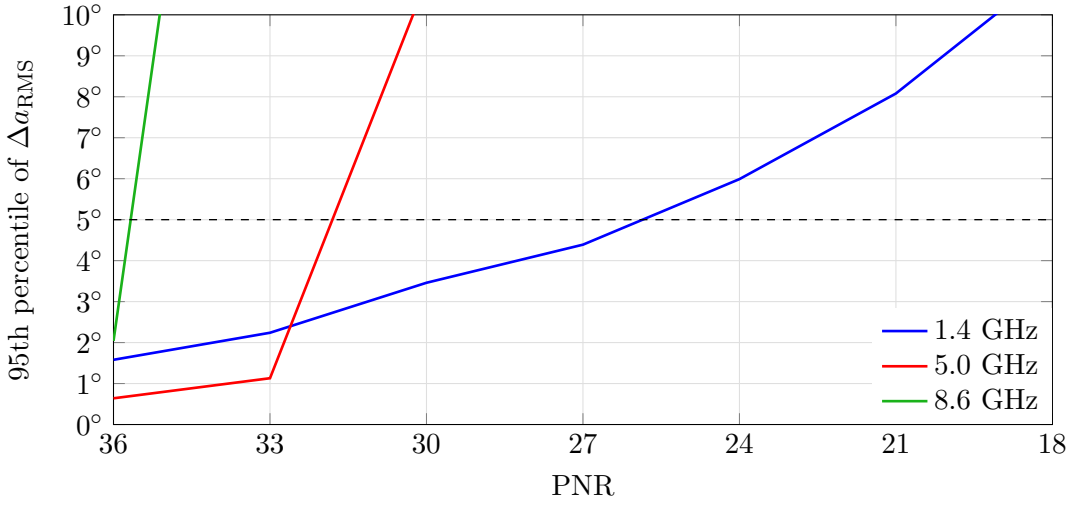

Figure 3.24: Measured 95th percentile of Δa_{RMS} at 3.4 GHz using both RPC 0 and RPC 4 for the DoA estimation of an incident vertically-polarized EM-wave

Effects of the incoming EM-wave depolarization on the DF performances

The purpose of the study that follows is to evaluate the effects of the depolarization of the incoming EM-wave on the DF performances of the improved version of the Two Season VA since this antenna is intended to estimate the DoA of vertically-polarized EM-waves. As detailed in Eq. 1.1, the polarization state of the incident EM-wave is described by the parameters γ and η. They describe the relation between the amplitudes of the two orthogonal components of the electric field and the relative phase between these components, respectively. As a reminder, a vertically-polarized EM-wave is characterized by $\gamma = 90°$ and $\eta = 0°$ while an horizontally-polarized EM-wave is characterized by $\gamma = 0°$ and $\eta = 0°$.

The evaluation of the accuracy of the DoA estimation from using both RPC 0 and RPC 4 is performed under the scenario conditions summarized in Table 3.10, which are the same of those reported in Table 2.3 except for the polarization of the incoming EM-wave. For each state of polarization of the EM-wave, the DF performances are assessed. Nevertheless, it can be noted that the incoming EM-wave is still assumed to be linearly-polarized ($\eta = 0°$). The results of this investigation are shown in Fig. 3.25 in terms of the 95th percentile of Δa_{RMS}. It can be clearly seen that the estimation errors increase with the depolarization of the incident EM-wave (relative to a vertically-polarized EM-wave). Indeed, the VA captures less power due to polarization mismatch leading to a decreased in estimation accuracy. Moreover, the estimation errors increase as well with the frequency, which yields to a reduction of the frequency coverage. Despite this, the improved version of the Two Season VA exhibits a certain robustness against small depolarization errors. Nonetheless, this study highlights one of the most significant advantages of dual-polarized DF antennas as well as complete VAs (that are, VAs that enable the measurement of all the components of the EM-wave), which is their ability to tackle the problems associated with polarization mismatch.

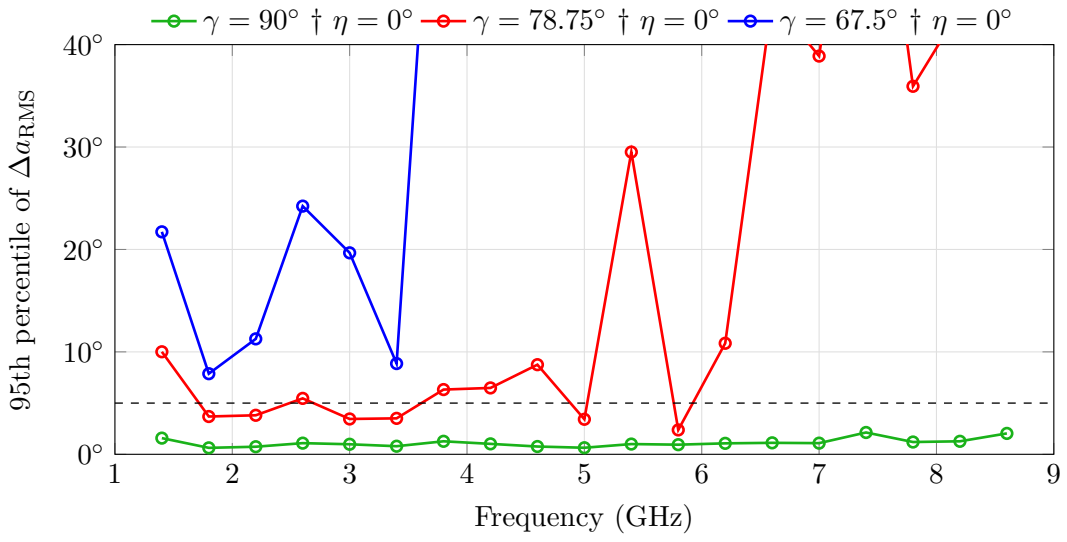

Figure 3.25: Simulated 95th percentile of Δa_{RMS} obtained with the improved version of the Two Season VA from using both RPC 0 and RPC 4, and under the scenario conditions defined in Table 3.10

Table 3.10: Parameters used for evaluating the DF performances

DoA Algorithm	MUSIC
Number of incoming EM-waves	1
Polarization of the incoming EM-wave	$\gamma \in \{90°, 78.75°, 67.5°\}$ $\eta = 0°$
Angular coverage	$\phi \in [0° \ ; \ 90°]$ $\theta \in [0° \ ; \ 90°]$
Angular resolution	$\Delta\phi = 5°$ $\Delta\theta = 2°$
Incoming EM-wave power density	-105 dBW.m^{-2}
Noise power level	-111 dBm
PNR	36 dB.m^{-2}
Snapshots per DoA estimation	100
Number of estimations per DoA	20
Frequencies of interest	1.4 GHz - 8.6 GHz with a 0.4 GHz step

3.2.4 Conclusion

As a reminder, the Two Season VA has shown good DF performances to estimate the DoA of vertically-polarized EM-waves in the upper hemisphere over an impedance bandwidth of 1.69:1 from 2.1 GHz to 3.55 GHz. The second section of this chapter was dedicated to the widening of the frequency coverage of the Two Season VA thanks to the modification of the feeding-profile of the antenna and the exploitation of the additional RP diversity technique. Hence, an improved version of the Two Season VA was designed. First, the modification of the feeding-profile of the Two Season VA has enabled the extension of the impedance bandwidth to 8.72:1 from 1.31 GHz to 11.42 GHz. However, good DF performances were only obtained until the previous upper operating frequency (approximately 3.6 GHz) without using the additional RP diversity technique. This result was expected in accordance with the earlier performances of the Two Season VA obtained from using only the measurement of the three components E_z, H_x and H_y of incoming EM-waves. Indeed, the three RPs that enable this measurement differ from those of ideal electric and magnetic dipoles as the frequency increases. Nonetheless, an accurate DoA estimate of a vertically-polarized EM-wave has been achieved up to 8.6 GHz using the additional RP diversity technique. Finally, it has been shown that the estimation errors increased if the polarization of the incoming EM-wave is no longer vertically-polarized. As a consequence, the next section focuses on adjusting the topology of the improved version of the Two Season VA in order to tackle polarization mismatch.

3.3 A dual-polarized vector antenna: the Four Season vector antenna

The aim of this section is to enhance the DF performances of the improved version of the Two Season VA by reducing the estimation errors bring by polarization mismatch. To this end, the topology of this antenna is modified, resulting in a new VA referred to as the Four Season VA. The electrical characteristics and DF performances have been evaluated through simulation and measurement.

3.3.1 Topology of the Four Season vector antenna

The improved version of the Two Season VA is able to estimate the DoA of vertically-polarized EM-waves in the upper hemisphere through the measurement of the components H_x, H_y and E_z. Since the aim of this section is to limit the estimation errors associated to polarization mismatch, it is necessary to adjust the antenna structure in order to estimate the DoA of incoming horizontally-polarized EM-waves as well. To this end, the measurement of the three components H_z, E_x and E_y is required. Besides, the modification of the antenna structure should be undertaken without affecting the quality of previous estimates of vertically-polarized EM-waves. Therefore, the two semi-circular arrays of Vivaldi antennas constituting the improved version of the Two Season VA are retained as such. The comparison of the DoA estimation accuracy of the Two Season VA mounted over an infinite or finite and octagonal ground plane in Section 2.7.4 showed that the size and shape of the metallic support do not significantly affect the DF performances. The idea is thus to replace the metallic support with a radiating element that can both acts as a ground plane for the two semi-circular arrays of the Two Season VA and enables the measurement of the three missing components H_z, E_x and E_y. As a result, the DoA of impinging EM-waves could be estimated regardless of their polarization since all six components of the incoming EM-waves would be measured.

The topology of the Four Season VA is depicted in Fig. 3.26, which consists of the two semi-circular arrays of the improved version of the Two Season VA mounted over a circular array of eight Vivaldi antennas. This latter presents also four output ports, resulting in an 8-port VA. In the same vein as for the measurement of the components E_z, H_x and H_y, the three components H_z, E_x and E_y are derived using three sets of weighting coefficients assigned to the received signals at the circular array ports. Indeed, the circular array can acts as one magnetic dipole oriented along the $\hat{z}$-axis and two electric dipoles oriented along the $\hat{x}$-axis and $\hat{y}$-axis (see the RPs depicted in Section 3.3.2.2). The weightings associated to the measurement of the six components of any incident EM-wave are summarized in Table 3.11 and are denoted by the acronym RPC 00. The port-numbering of the vertical radiating elements of the Four Season VA corresponds to the one of the Two Season VA. Therefore, the weightings used for measuring the components H_x, H_y and E_z are not changed.

Additional details on the geometry of the horizontal part of the Four Season VA are provided in Fig. 3.27 and in Table 3.12. Specifically, the horizontal circular array is designed from a scale factor of 1.5 of the vertical semi-circular array (i.e., the one used for the improved version of the Two Season VA). All dimensions are scaled except for the widths of the microstrip lines (w_4 and w_5) and the thickness of the dielectric (0.8 mm FR4 substrate) in order to keep unchanged the impedance of the input ports (50 Ω) and the characteristic impedance of each Vivaldi antenna (100 Ω). Moreover, to enable the metallic surface of the horizontal circular array to serve as

a ground plane for the vertical semi-circular arrays, a series of vias are installed to ensure the electrical connection.

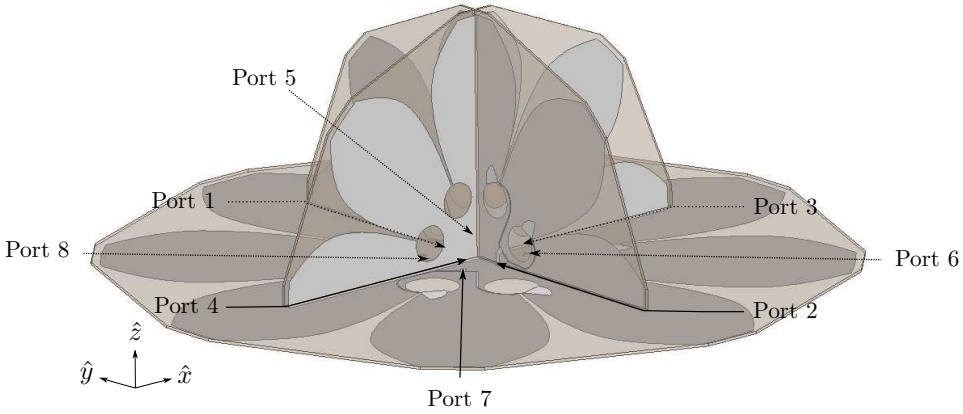

Figure 3.26: Topology of the Four Season VA and port-numbering

RPC	Measured Component	Port 1	Port 2	Port 3	Port 4	Port 5	Port 6	Port 7	Port 8
00	E_x	0	0	0	0	1	1	-1	-1
	E_y	0	0	0	0	1	-1	-1	1
	E_z	1	1	1	1	0	0	0	0
	H_x	1	-1	0	0	0	0	0	0
	H_y	0	0	1	-1	0	0	0	0
	H_z	0	0	0	0	1	-1	1	-1

Table 3.11: Set of weighting coefficients assigned to the signals received at the eight ports of the Four Season VA for measuring the six components of an incoming EM-wave

Parameter	D_h	l_{h1}	l_{h2}	l_{h3}	w_{h1}	w_{h2}
Value (in mm)	230	75.75	22.5	40.6	65.7	21.6
Parameter	w_{h3}	g_h	r_{hc}	r_{hs}	w_4	w_5
Value (in mm)	13.9	0.9	8.25	8.25	0.36	1.58

Table 3.12: Dimensions of the horizontal circular array constituting the Four Season VA

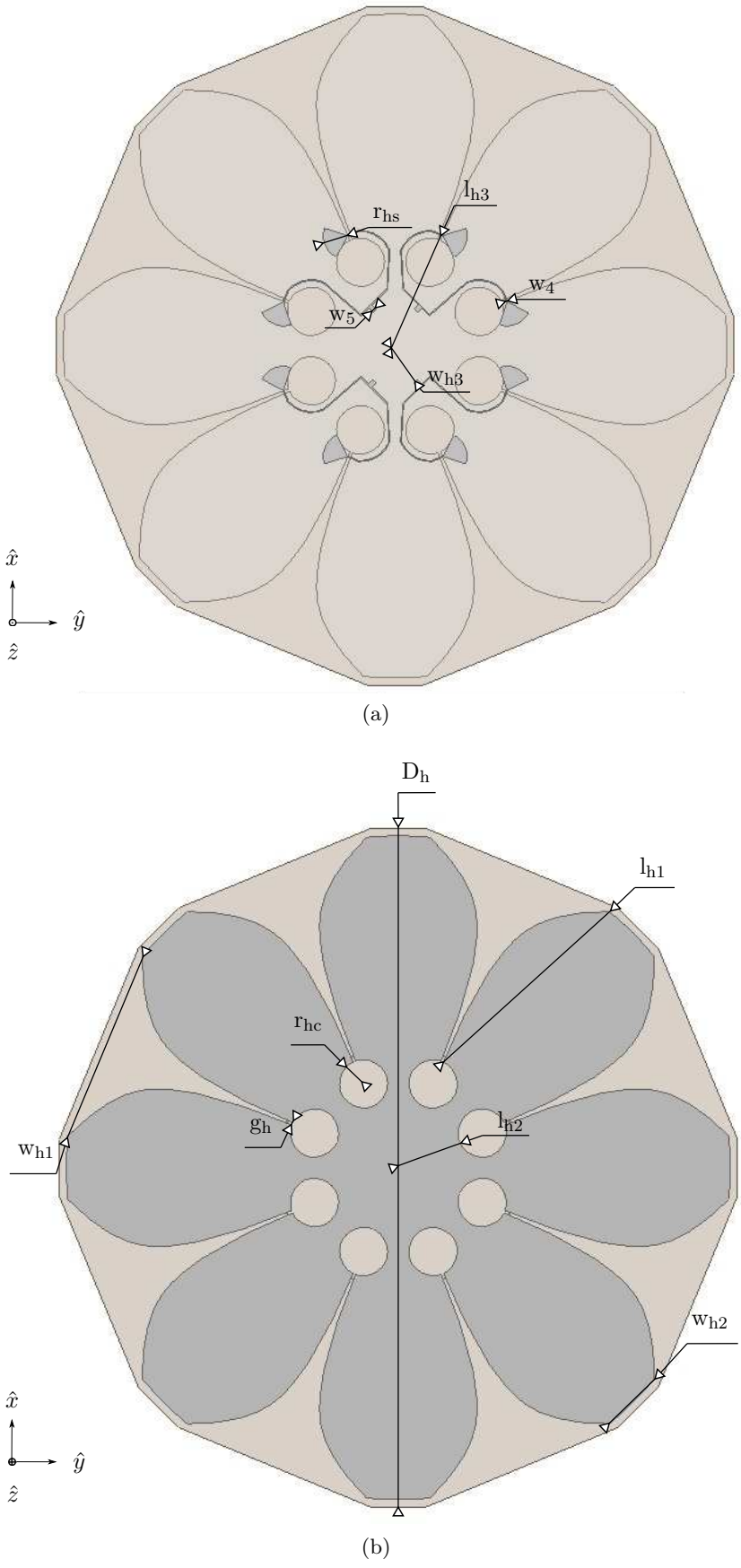

Figure 3.27: Horizontal circular array constituting the Four Season VA: (a) top view, and (b) back view

3.3.2 Electrical performances of the Four Season vector antenna

So far this section has described the topology of the reconfigurable Four Season VA, its electrical performances in terms of impedance matching and radiation properties are now assessed using full-wave EM simulations with Ansys HFSS. In addition, the proposed VA has been manufactured and measured in the LAAS-CNRS anechoic chamber. Comparisons between simulation and measurement results are carried out in order to experimentally validate the performances. A photograph of the prototype is given in Fig. 3.28.

Figure 3.28: Photograph of the Four Season VA prototype

3.3.2.1 Impedance matching and mutual coupling

The simulated and measured VSWR of the vertical and horizontal radiating elements of the Four Season VA are shown in Fig. 3.29, respectively. For symmetry reasons, only the VSWR at port 1 (vertical part) and port 5 (horizontal part) are depicted. Moreover, the VSWR that can be achieved at port 1 if there is a perfect electrical connection (i.e., instead of using vias) between the vertical part and the underside of the horizontal part is also plotted.

The measured impedance bandwidth of the vertical part of the Four Season VA is of 6.77:1 from 1.24 GHz to 8.40 GHz (for a VSWR smaller than 2.3). There is relatively a good agreement between the simulated and measured results even if the measured VSWR at port 1 is slightly degraded at high frequencies. Nonetheless, it can be noted that the VSWR can be improved through a better electrical connection. It would be interesting to investigate a different technique and manufacturing process in order to ensure a better electrical connection. The measured impedance bandwidth of the horizontal part of the Four Season VA is of 10.74:1 from 0.79 GHz to 8.49 GHz (for a VSWR smaller than 2.3). As expected, there is approximately a factor 1.5 between the lower operating frequency of the vertical and horizontal radiating elements of the Four Season VA since the horizontal part has been scaled from the vertical part with the same factor. Furthermore, the measured VSWR at port 5 is also consistent with the one simulated. Hence, the impedance bandwidth of the prototype of the Four Season VA is limited to 6.77:1 and covers the frequencies from 1.24 GHz to 8.40 GHz, since it is constrained by the bandwidth

of the vertical radiating elements. The Four Season VA is included in a half-sphere within a $0.47\lambda_{1.24\text{GHz}}$ radius. Besides, the radius of the vertical semi-circular arrays is $0.32\lambda_{1.24\text{GHz}}$ while that of the circular array is $0.30\lambda_{0.79\text{GHz}}$ (i.e., $0.47\lambda_{1.24\text{GHz}}$).

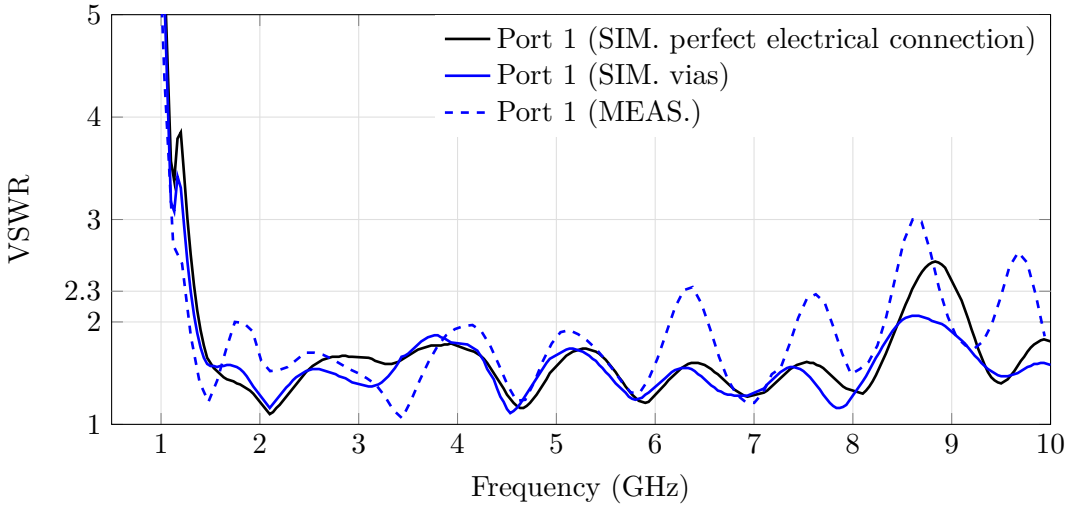

(a)

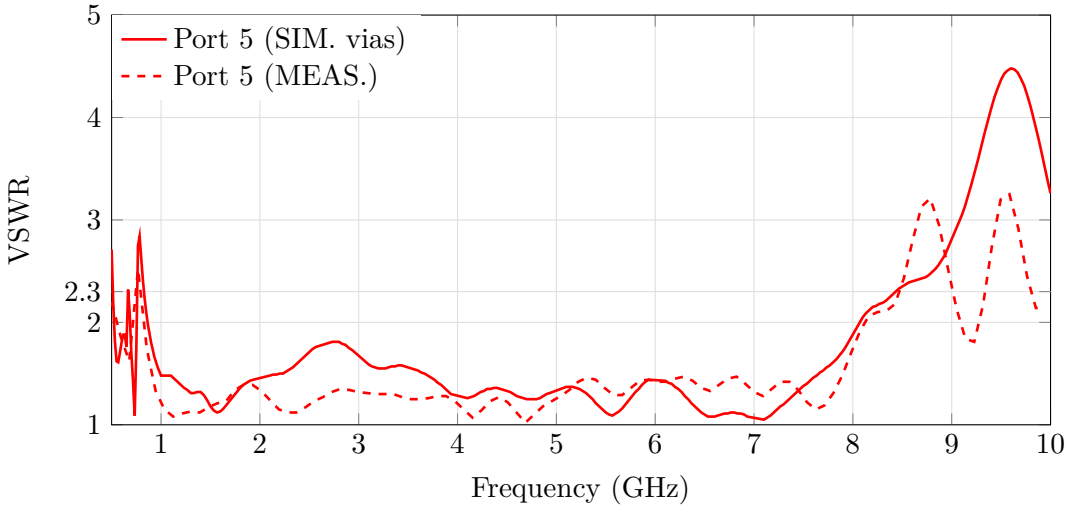

(b)

Figure 3.29: Simulated and measured VSWR of the Four Season VA: (a) port 1, and (b) port 5

The measured isolation between port 1 and the seven ports of the Four Season VA is depicted in Fig. 3.30. It can be observed that the mutual coupling between port 1 and the other vertical ports (ports $i \in [\![2, 4]\!]$) does not exceed -10 dB across the overall bandwidth and even -20 dB from 1.8 GHz. As for the mutual coupling between port 1 and the horizontal ports (ports $i \in [\![5, 8]\!]$), it is below - 20 dB over the operating bandwidth. Fig. 3.31 presents the measured isolation between port 5 and the other horizontal ports (ports $i \in [\![6, 8]\!]$). It can be seen that the mutual coupling is also less than - 20 dB in the operating frequency range. Moreover, the same level of isolation is achieved at the other ports. Besides, simulated results were not plotted for readability but are consistent with the measurement results.

Finally, it can be noted that the VSWR and the level of isolation achieved at the vertical ports of

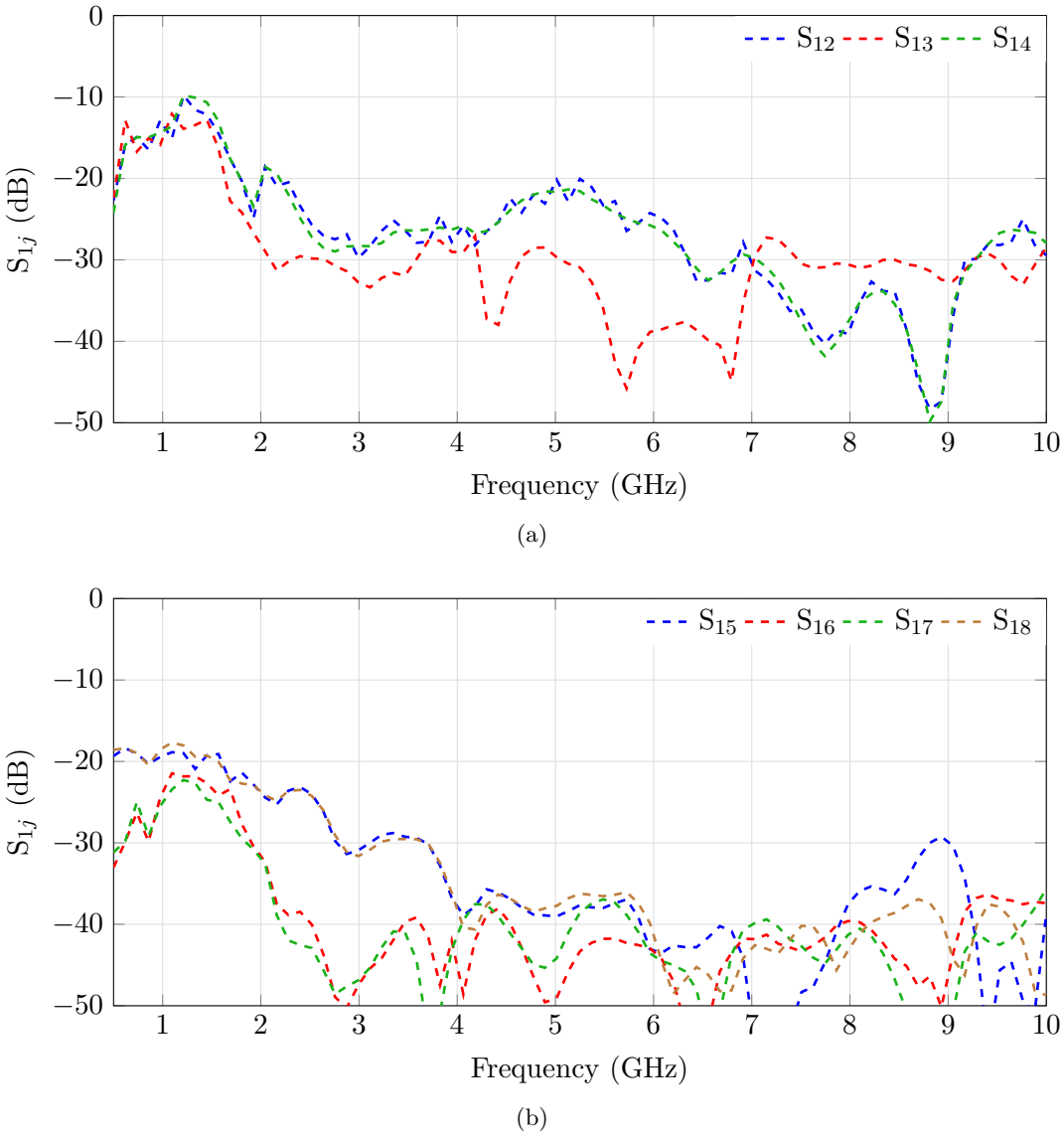

(a)

(b)

Figure 3.30: Measured mutual coupling between: (a) port 1 and the other vertical ports, and (b) port 1 and the other horizontal ports of the Four Season VA

the Four Season VA are consistent with the simulated results of the improved version of the Two Season VA reported in Section 3.2.2.1. This permits to partially and experimentally confirm the announced performances of the improved version of the Two Season VA.

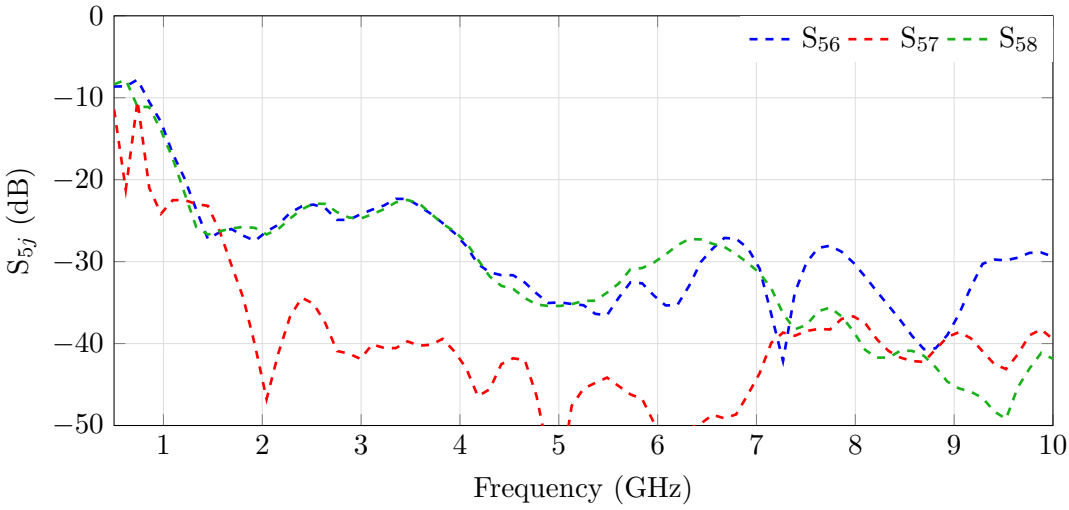

Figure 3.31: Measured mutual coupling between port 5 and the other horizontal ports of the Four Season VA

3.3.2.2 Radiation patterns

In this section, the RPs of the Four Season VA prototype associated with the measurement of the six components an incoming EM-wave are compared to simulations results. The simulated RPs associated to RPC 00 that enable the measurement of these components are displayed in Appendix H.2 at 2.8 GHz.

As a reminder, three RPs of the vertical semi-circular arrays of the Four Season VA enable the measurement of the components E_z, H_x and H_y of an incident EM-wave. Fig. 3.32(a) and Fig. 3.32(b) present the realized gain in the $\hat{y}\hat{z}$-plane at 2.8 GHz when the amplitude/phase associated to the measurement of the components E_z and H_x are impressed at the eight ports of the VA (see Table 3.11), respectively. For symmetry reasons, the RP associated with the measurement of H_y is not presented. Besides, the RPs of the Two Season VA are also plotted in order to analyze the impact of the modification of the ground plane. Looking at these figures, it can be observed that the combined RPs of the Four Season VA are similar to those in the E-plane of an electric monopole oriented along the $\hat{z}$-axis (i.e., 8-shape RP) and a magnetic dipole oriented along the $\hat{x}$-axis (i.e., omnidirectional RP), respectively. As might be expected, the use of the metallic surface of the horizontal circular array as a ground plane for the vertical semi-circular arrays (instead of the octagonal metallic surface) modify the RPs, but they remain similar to those of dipoles. The RPs at other frequencies are not presented here for the sake of brevity, but they are "similar" to those of the Two Season VA, apart from the effects of the ground plane.

As for the measurement of the components E_x, E_y and H_z of an incident EM-wave, it is performed thanks to three RPs associated to the horizontal circular array of the Four Season VA. Fig. 3.33 and Fig. 3.34 show the realized gain of the Four Season VA when the amplitude/phase for measuring the components E_x and H_z (see Table 3.11) are impressed at the eight ports of the antenna, respectively. The RPs are presented in one elevation cut (the $\hat{x}\hat{y}$-plane) and in the azimuth plane (i.e., the $\hat{x}\hat{y}$-plane) at four frequencies: 1.4 GHz, 2.8 GHz, 5 GHz, and 8 GHz within the operating band. The RPs identified in Fig. 3.33 are the ones of an electric dipole oriented along the $\hat{x}$-axis in its H-plane (i.e., omnidirectional RP) and E-plane (i.e., 8-shaped

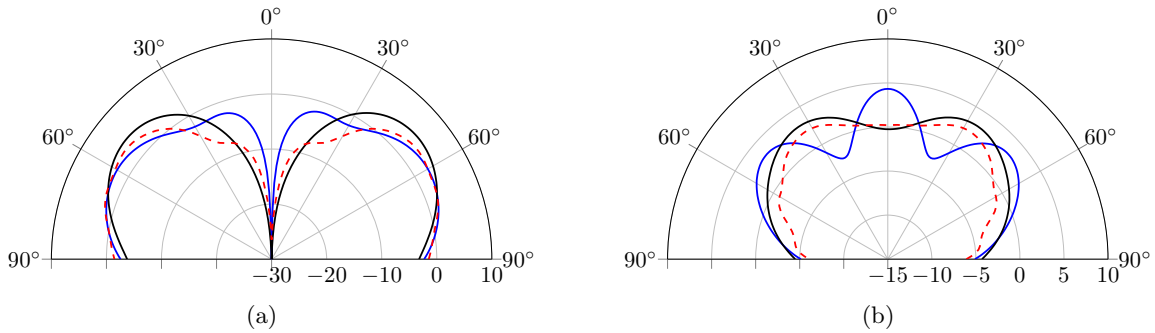

Figure 3.32: Simulated (black solid line) and measured (red dashed line) realized gain of the Four Season VA in θ-polarization and in the $\hat{y}\hat{z}$-plane associated with the amplitude/phase impressed at the eight ports of the antenna (specified in Table 3.11) for measuring at 2.8 GHz the component: (a) E_z, and (b) H_x. The blue line corresponds to the simulated RPs of the Two Season VA mounted over the octagonal ground plane.

RP) across the entire operating band. Besides, the RPs associated with the measurement of E_y are not shown for symmetry reasons. As for the RPs displayed in Fig. 3.34, they correspond to those of a magnetic dipole oriented along the $\hat{z}$-axis in its H-plane (i.e., 8-shape RP) and E-plane (i.e., omnidirectional RP) across the entire operating band. However, it can be seen that some ripples appear in the RPs of the electric and magnetic dipoles as the frequency increases, as expected by Chu's theory. Overall, there is a reasonably good agreement between the measurement and the simulation results. Nonetheless, the measured realized gain is lower. There are two plausible explanations:

- The dielectric losses were considered constant in the simulation and did not increase with the frequency as in practice, which is especially disadvantageous with a low-cost substrate such as FR-4.
- The back environment of the antenna (cables, support, absorber, and positioner) was not modeled in the simulation.

In summary, the measured RPs of the Four Season VA correspond to the ones of a complete VA (that is, a VA that enable the measurement of the six component of an incoming EM-wave) across the overall impedance bandwidth. Nevertheless, they differ from those of ideal dipoles as the frequency increases due to the emergence of fluctuations.

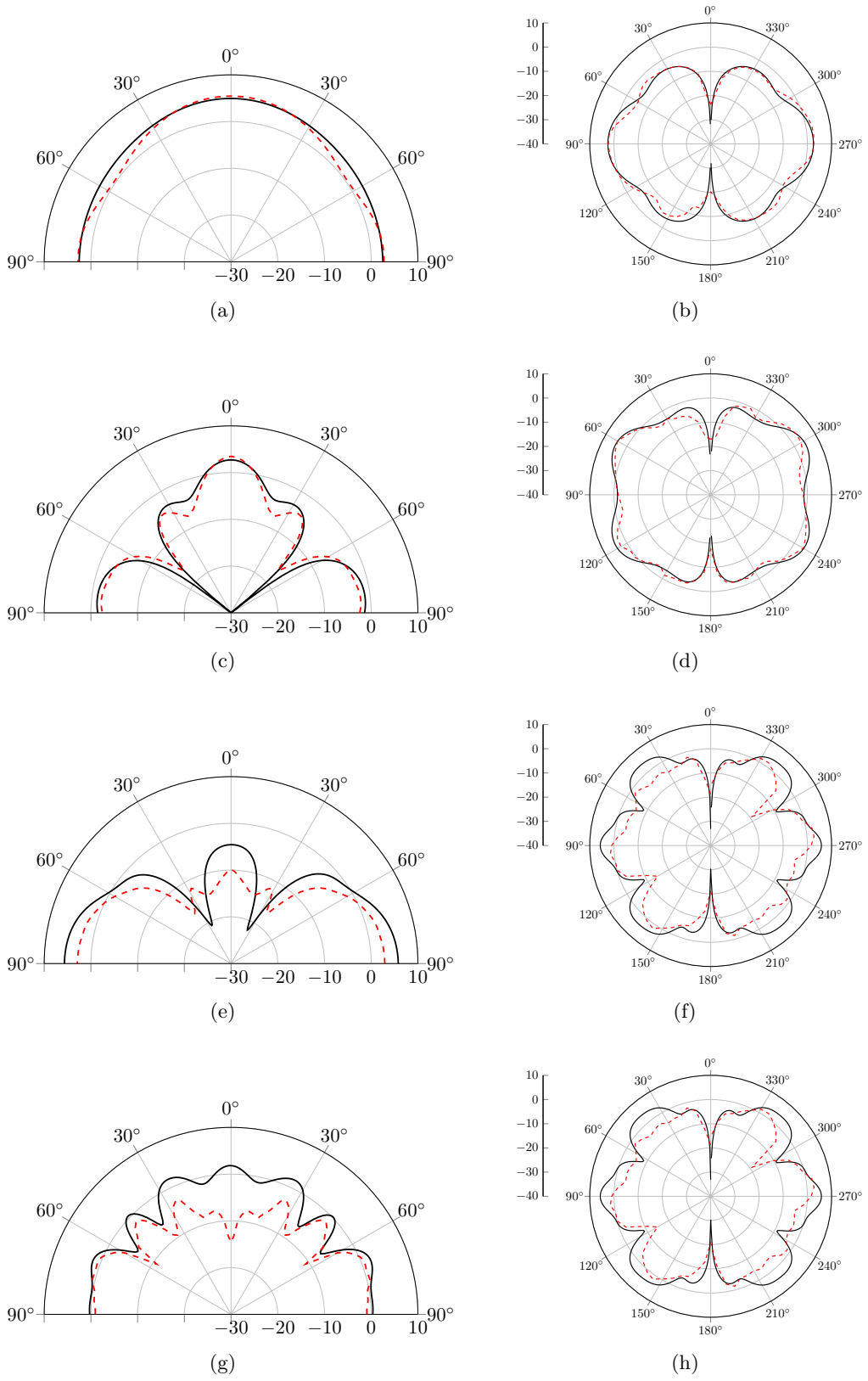

Figure 3.33: Simulated (black solid line) and measured (red dashed line) realized gain of the Four Season VA in ϕ-polarization associated with the amplitude/phase impressed at the eight ports of the antenna for measuring the component E_x (specified in Table 3.11) at: (a) 1.4 GHz, (b) 2.8 GHz, (c) 5 GHz, and (d) 8 GHz. The left and right figures correspond to the RP in the $\hat{yz}$-plane and $\hat{xy}$-plane, respectively.

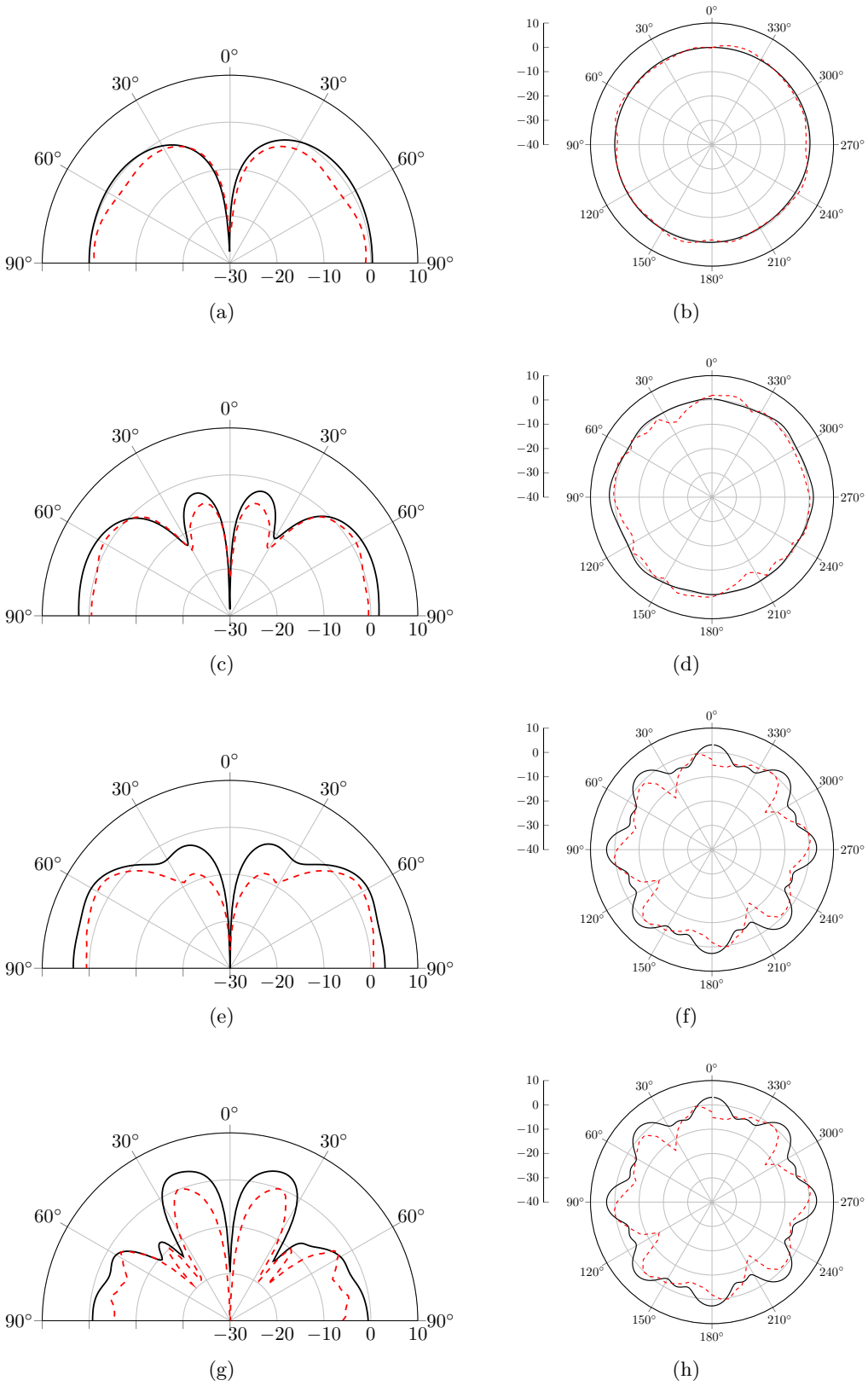

Figure 3.34: Simulated (black solid line) and measured (red dashed line) realized gain of the Four Season VA in ϕ-polarization associated with the amplitude/phase impressed at the eight ports of the antenna for measuring the component H_z (specified in Table 3.11) at: (a) 1.4 GHz, (b) 2.8 GHz, (c) 5 GHz, and (d) 8 GHz. The left and right figures correspond to the RP in the $\hat{yz}$-plane and $\hat{xy}$-plane, respectively.

3.3.2.3 Efficiency

Fig. 3.35 presents the simulated total efficiency of the Four Season VA between 1 GHz to 9 GHz to cover its impedance bandwidth, which ranges from 1.24 GHz to 8.40 GHz. The frequency step used for the efficiency evaluation is of 0.1 GHz. For symmetry reasons, only the efficiency at ports 1 and 5 is considered. It can be seen that the total efficiency decreases with the frequency. Nonetheless, the total efficiency at the vertical ports exceeds approximately 80% across the overall antenna bandwidth. For the horizontal ports, the total efficiency is above 80% up to 6.4 GHz and still higher than 60% over the rest of the bandwidth. Futhermore, it can be noted that the dielectric losses are not taken into account in this evaluation.

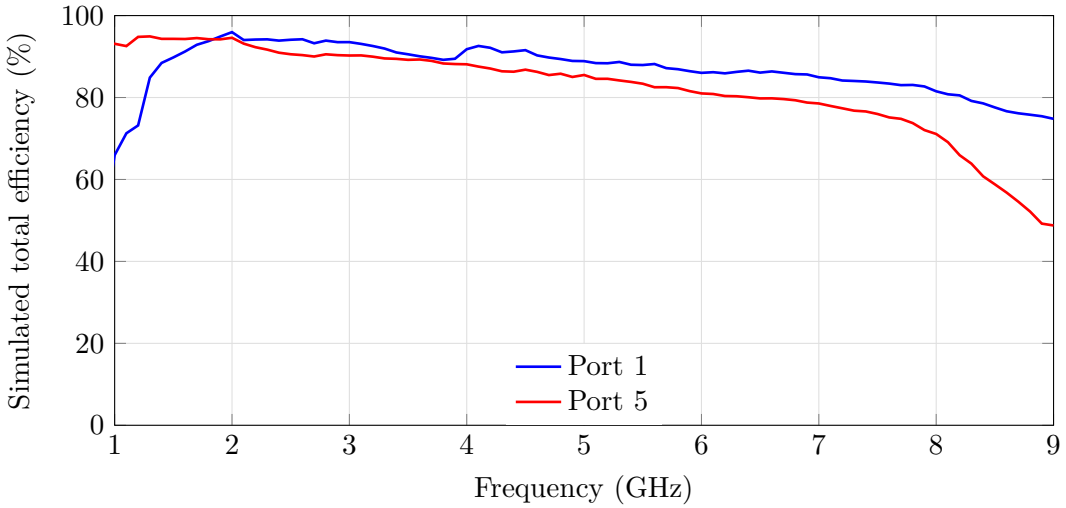

Figure 3.35: Simulated total efficiency at port 1 and port 5 of the Four Season VA

3.3.3 Direction finding performances of the Four Season vector antenna

The Four Season VA was designed to enhance the DF performances of the improved version of the Two Season VA by reducing the estimation errors bring by polarization mismatch. To this end, this VA is intended to estimate the DoA of incoming EM-waves in the upper hemisphere regardless of their polarization. In the sections that follow, the DF performances of the Four Season VA are assessed with or without using the additional RP diversity technique. In the latter case, measurement results are also provided to experimentally validate the simulation results.

3.3.3.1 Direction finding performances without additional radiation pattern diversity

The DoA estimation accuracy of the Four Season VA achievable with using the MUSIC algorithm is evaluated under the scenario conditions summarized in Table 3.13. This investigation is performed using only the measurement of the six components of the incoming linearly-polarized EM-wave (RPC 00). Besides, the polarization state of the wave is assumed to be known ($\eta = 0°$ and γ is known). Fig. 3.36 presents the maximum value and 95th percentile of the angular

distance Δa_{RMS} achieved under these conditions and for each polarization state of the incoming EM-wave. Several observations can be highlighted. First, it can be noted that the maximum error increases with the frequency regardless of the polarization of the incident EM-wave. However, the maximum estimation errors are less significant if the EM-wave is vertically- ($\gamma = 90°$) or horizontally-polarized ($\gamma = 0°$). Secondly, the 95th percentile of Δa_{RMS} does not exceed 5° up to approximately up to 7.6 GHz if the incoming EM-wave is vertically-polarized. Besides, by comparing this accuracy with the one achieved in Fig. 3.19 with the improved version of the Two Season VA using only RPC 0 (i.e., the measurement of the components E_z, H_x and H_y), it can be noted that the DoA estimation of a vertically-polarized EM-wave is improved in terms of accuracy and frequency coverage. This is due to the additional measurement of the components E_x, E_y and H_z. The same level of DoA estimation accuracy has been approximately achieved with the improved version of the Two Season VA if RPC 4 was used in addition to RPC 0 (see Fig. 3.22). Thirdly, by comparing Fig. 3.25 and Fig. 3.36, it is apparent that the Four Season VA minimizes the estimation errors that occur if the received EM-wave is no longer vertically-polarized. In particular, very good DF performances are reached if the incoming EM-wave is horizontally-polarized across the overall VA bandwidth. However, the DoA estimation is less accurate but still improved for EM-waves that are neither purely vertically- nor horizontally-polarized. The idea is now to use additional RP diversity in order to improve the DF performances, especially for the estimation of EM-waves that are not purely vertically- or horizontally-polarized.

Table 3.13: Parameters used for evaluating the DF performances

DoA Algorithm	MUSIC
Number of incoming EM-waves	1
Polarization of the incoming EM-wave	$\gamma \in \{90°, 67.5°, 45°, 22.5°, 0°\}$ $\eta = 0°$
Angular coverage	$\phi \in [0° \ ; \ 90°]$ $\theta \in [0° \ ; \ 90°]$
Angular resolution	$\Delta\phi = 5°$ $\Delta\theta = 2°$
Incoming EM-wave power density	-105 dBW.m^{-2}
Noise power level	-111 dBm
PNR	36 dB.m^{-2}
Snapshots per DoA estimation	100
Number of estimations per DoA	20
Frequencies of interest	1 GHz - 8.2 GHz with a 0.4 GHz step

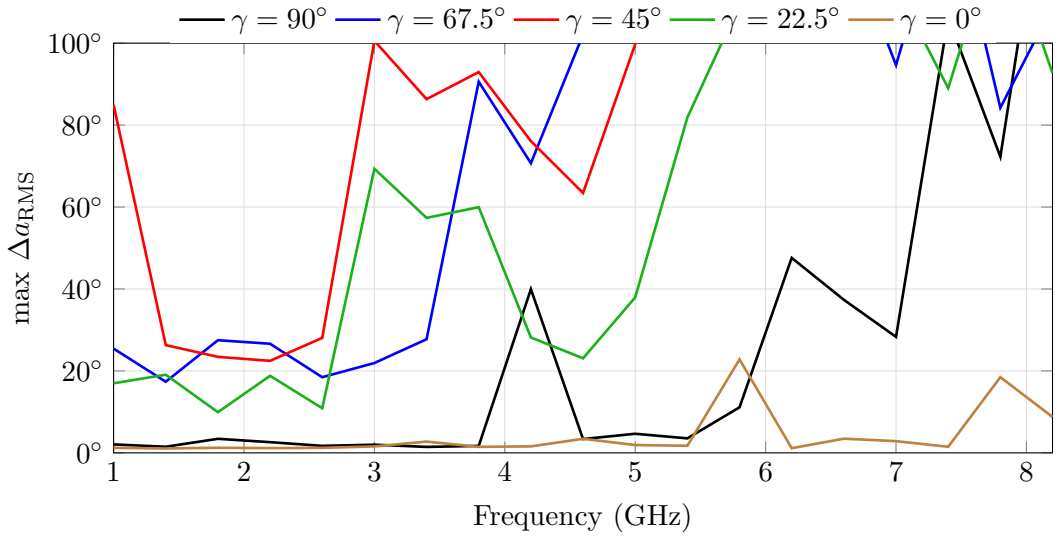

(a)

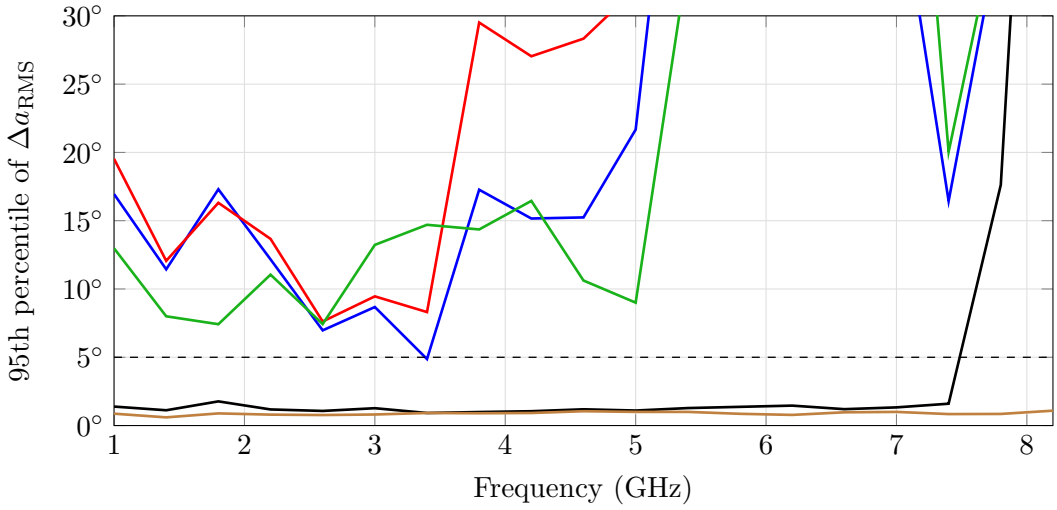

(b)

Figure 3.36: Simulated (a) max Δa_{RMS} and (b) 95th percentile of Δa_{RMS} obtained with the Four Season VA from using RPC 00, and under the scenario conditions defined in Table 3.10

3.3.3.2 Direction finding performances with additional radiation pattern diversity

Using the RP diversity technique presented in Section 3.1, the DF performances of the Four Season VA are re-evaluated in this section.

Selection of the RPCs

The first step consists in choosing the RPCs to use in addition to RPC 00 in the DoA estimation process in order to improve the DF performances regardless of the polarization of the incoming EM-wave. Let us consider again $w_i \in \{1, 0, \text{-}1\}$ ($i \in [\![1; 8]\!]$) be the possible values for the weighting

coefficients. There are normally 3^8 sets of weighting coefficients $[w_1, w_2, w_3, w_4, w_5, w_6, w_7, w_8]$ that could be assigned to the signals received by the 8-port Four Season VA. Among these 6561 sets, only the sets of the form $[w_1, w_2, w_3, w_4, 0, 0, 0, 0]$ and $[0, 0, 0, 0, w_5, w_6, w_7, w_8]$ are considered here in order to simplify the RPC selection. In this way, the vertical and horizontal parts of the Four Season VA are independently considered. As a consequence, there are only 2×3^4 sets to investigate, which yields to a total of 2×11 RPCs following the method reported in Section 3.1.1.1 (i.e., keep only one of the sets that provide the same RP and then combine the sets exhibiting to the same RPs with a rotation symmetry of 90° in the azimuth plane). The 11 RPCs associated with the vertical part of the Four Season VA are the ones of the Two Season VA indicated in Table 3.1 (with $w_i = 0$ for $i \in [\![5; 8]\!]$) since the port-numbering is unchanged. As for the 11 RPCs associated to the horizontal part, they are summarized in Table 3.14 and the corresponding RPs are given in Appendix H.2. Finally, 2 RPCs among the 22 RPCs will be selected (one for each part) to provide the highest estimation accuracy regardless of the polarization of the incoming EM-wave across the overall bandwidth.

	RPC 12				RPC 13				RPC 14			
Port 5	1	0	0	0	1	0	1	1	1	0	0	1
Port 6	0	1	0	0	1	1	0	1	1	1	0	0
Port 7	0	0	1	0	1	1	1	0	0	1	1	0
Port 8	0	0	0	1	0	1	1	1	0	0	1	1

	RPC 15				RPC 16				RPC 17			
Port 5	1	-1	1	1	1				1	0		
Port 6	1	1	-1	1	1				0	1		
Port 7	1	1	1	-1	1				1	0		
Port 8	-1	1	1	1	1				0	1		

	RPC 18				RPC 19				RPC 20			
Port 5	1	0			1	-1	0	0	1	-1	1	0
Port 6	0	1			0	1	-1	0	0	1	-1	1
Port 7	-1	0			0	0	1	-1	1	0	1	-1
Port 8	0	-1			-1	0	0	1	-1	1	0	1

	RPC 21				RPC 22			
Port 5	1	-1	0	1	1	0	-1	1
Port 6	1	1	-1	0	1	1	0	-1
Port 7	0	1	1	-1	-1	1	1	0
Port 8	-1	0	1	1	0	-1	1	1

Table 3.14: RPCs and corresponding weighting coefficients w_i ($i \in [\![5; 8]\!]$) assigned to the signals received by the 8-port Four Season VA. The weightings at ports i ($i \in [\![1; 4]\!]$) are $w_i = 0$.

The CRB on θ and ϕ is computed from the parameters displayed in Table 3.15, which involves repeating the study for each polarization state of the incoming EM-wave. The CRB_ϕ and CRB_θ corresponding to these 22 RPCs are provided in Appendix H.3. From these figures, it is clear that the DoA estimation accuracy is more or less improved in ϕ and θ as a function of the RPC as well as the frequency. For the sake of readability, only the RPCs that ensure the highest precision across the overall bandwidth are depicted in Fig. 3.37 to Fig. 3.41. The CRB obtained from using only RPC 00 are also set out for comparison purposes. For the RPCs associated with the vertical part of the Four Season VA, it can be noted that is still RPC 4 that provides the highest estimation accuracy over the entire bandwidth, and this regardless of the polarization of the incoming EM-wave. As for the RPCs associated with the horizontal part of the Four Season VA, it is RPC 15. Globally, RPC 4 is more effective than RPC 15 to enhance the DF performances, except when the polarization of the incoming EM-wave is nearly horizontal (i.e., for low γ angles) in the low-end of the frequency range (see Fig. 3.40(b) and Fig. 3.41(b)). However, it can be seen that the use of RPC 4 and RPC 15 in addition to RPC 00 slightly improves DF performances. Nonetheless, the estimation accuracy achieved through this additional RP diversity (RPC 4 and RPC 15) is clearly enhanced across the entire impedance bandwidth whatever the polarization of the incoming EM-wave.

Number of incoming EM-waves	1
Polarization of the incoming EM-wave	$\gamma \in \{90°, 67.5°, 45°, 22.5°, 0°, \}$ $\eta = 0°$
Angular coverage	$\phi \in [0° \ ; \ 360°]$ $\theta \in [0° \ ; \ 90°]$
Angular resolution	$\Delta\phi = 1°$ $\Delta\theta = 1°$
Incoming EM-wave power density	-117 dBW.m^{-2}
Noise power level	-111 dBm
PNR	24 dB.m^{-2}
Snapshots per DoA estimation	100
Frequencies of interest	1 GHz - 8 GHz with a 0.1 GHz step

Table 3.15: Parameters used for the CRB analysis

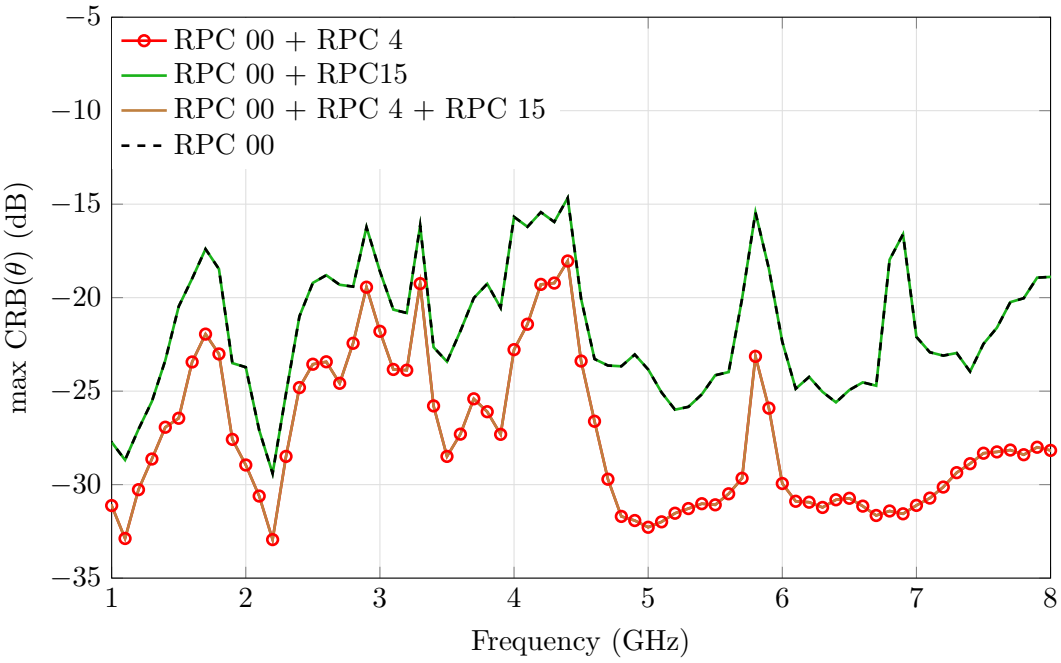

(a)

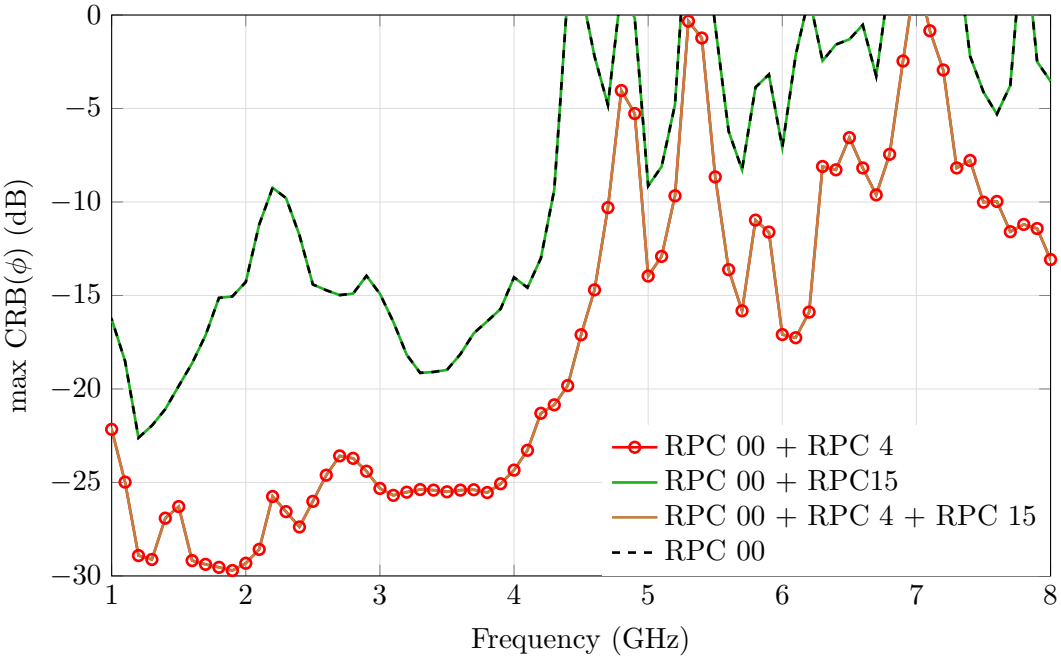

(b)

Figure 3.37: Highest simulated (a) CRLB(θ) and (b) CRLB(ϕ) of the Four Season VA using different RPCs added to the RPC 00, and under the scenario conditions defined in Table 3.15 ($\gamma = 90°$ † $\eta = 0°$, i.e. vertical polarization)

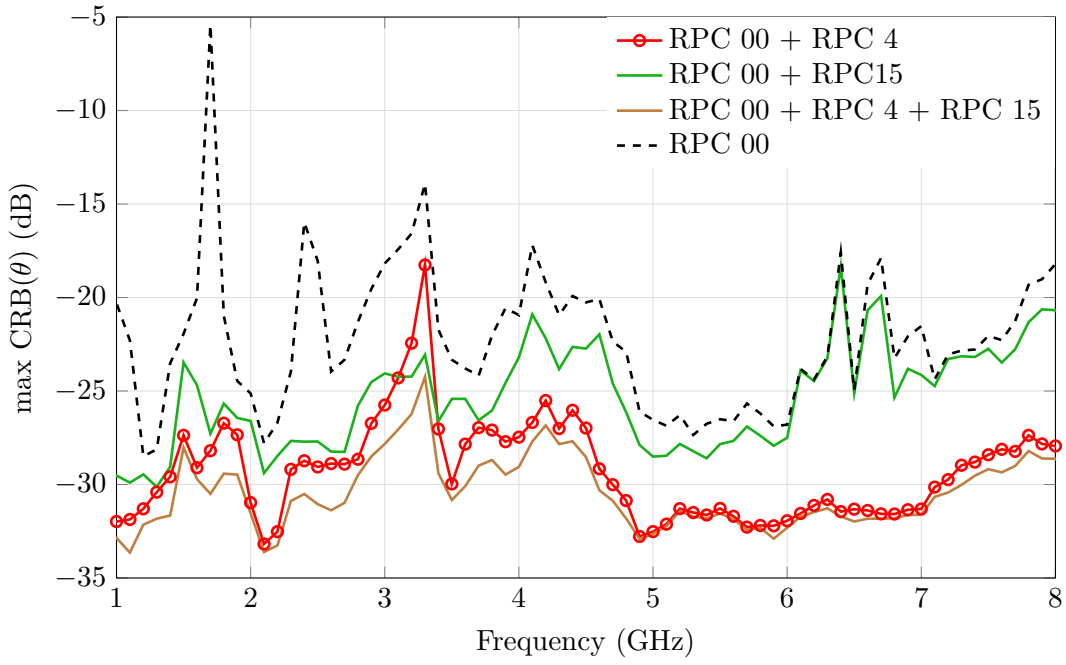

(a)

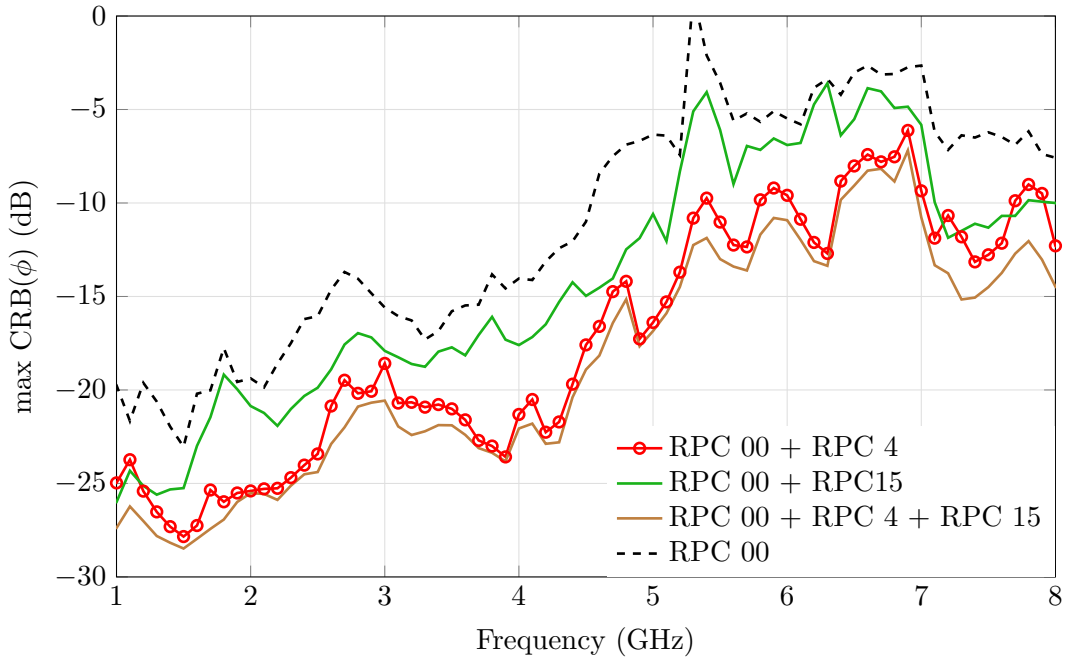

(b)

Figure 3.38: Highest simulated (a) CRLB(θ) and (b) CRLB(ϕ) of the Four Season VA using different RPCs added to the RPC 00, and under the scenario conditions defined in Table 3.15 ($\gamma = 67.5° \dagger \eta = 0°$)

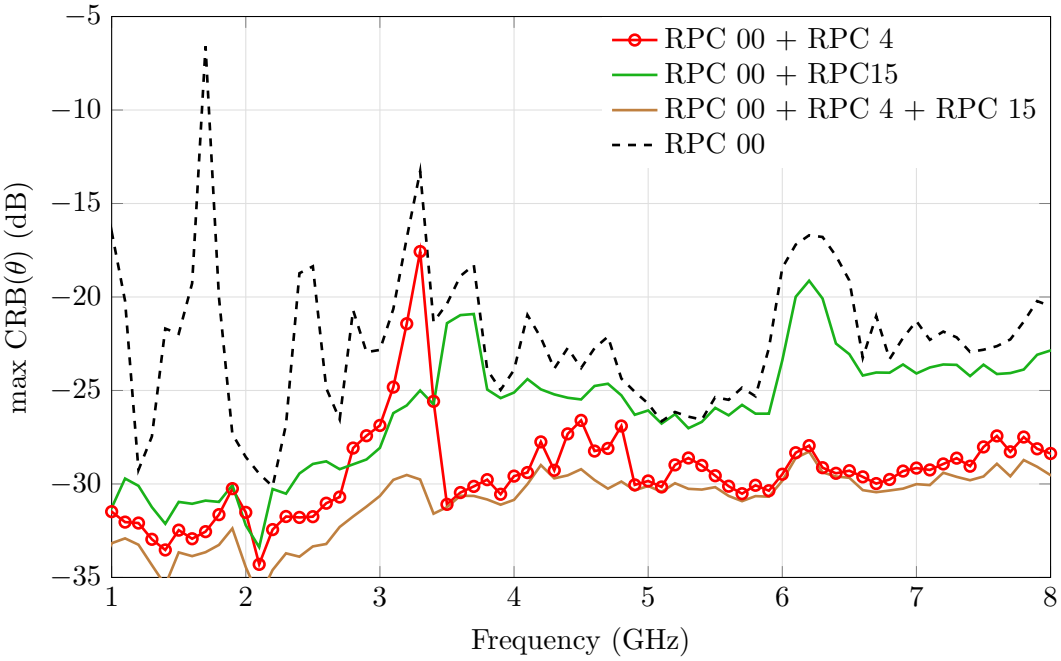

(a)

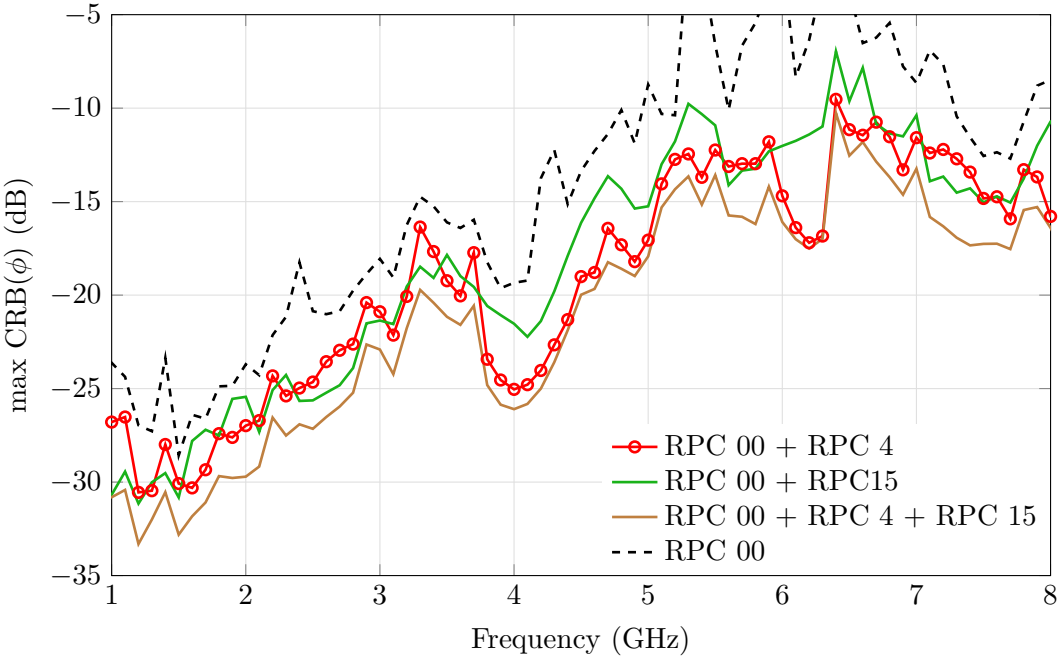

(b)

Figure 3.39: Highest simulated (a) CRLB(θ) and (b) CRLB(ϕ) of the Four Season VA using different RPCs added to the RPC 00, and under the scenario conditions defined in Table 3.15 ($\gamma = 45° \dagger \eta = 0°$)

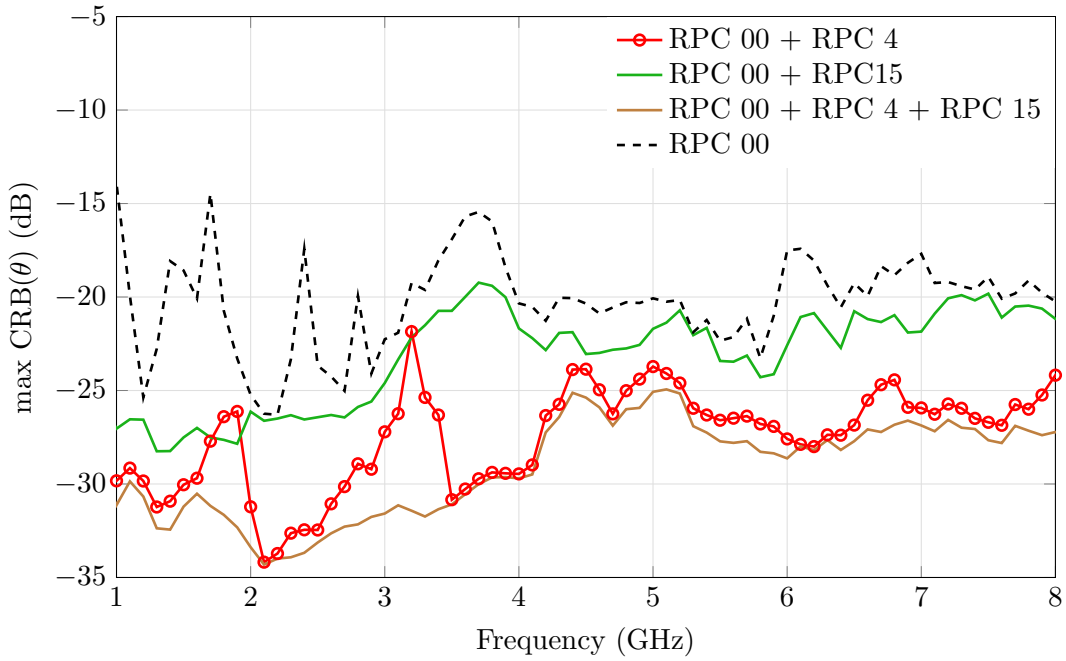

(a)

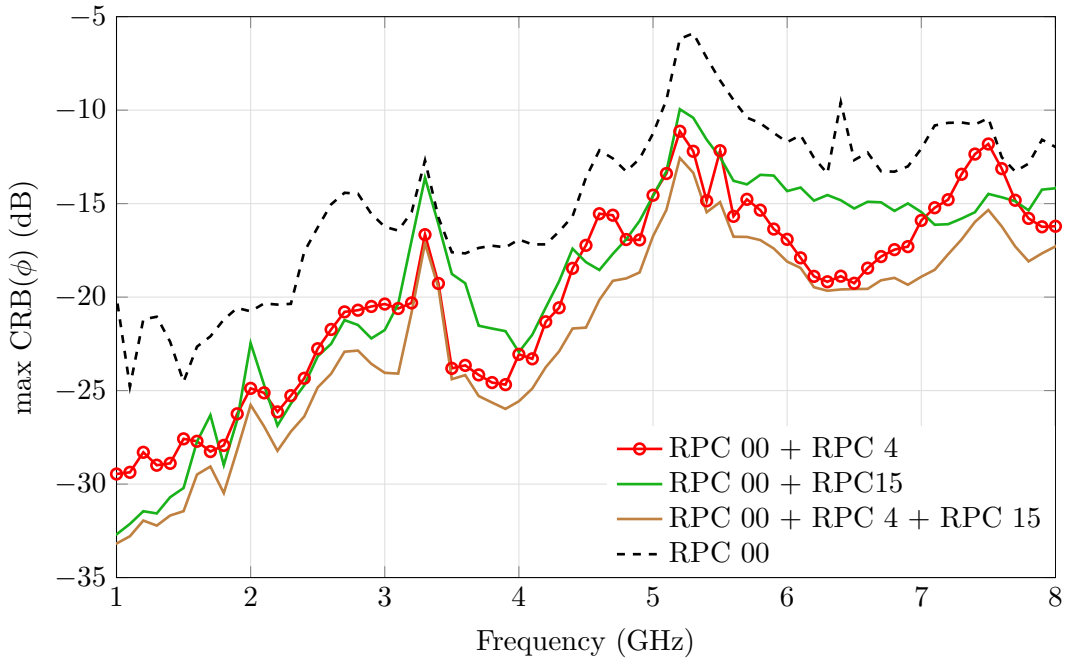

(b)

Figure 3.40: Highest simulated (a) CRLB(θ) and (b) CRLB(ϕ) of the Four Season VA using different RPCs added to the RPC 00, and under the scenario conditions defined in Table 3.15 ($\gamma = 22.5° \dagger \eta = 0°$)

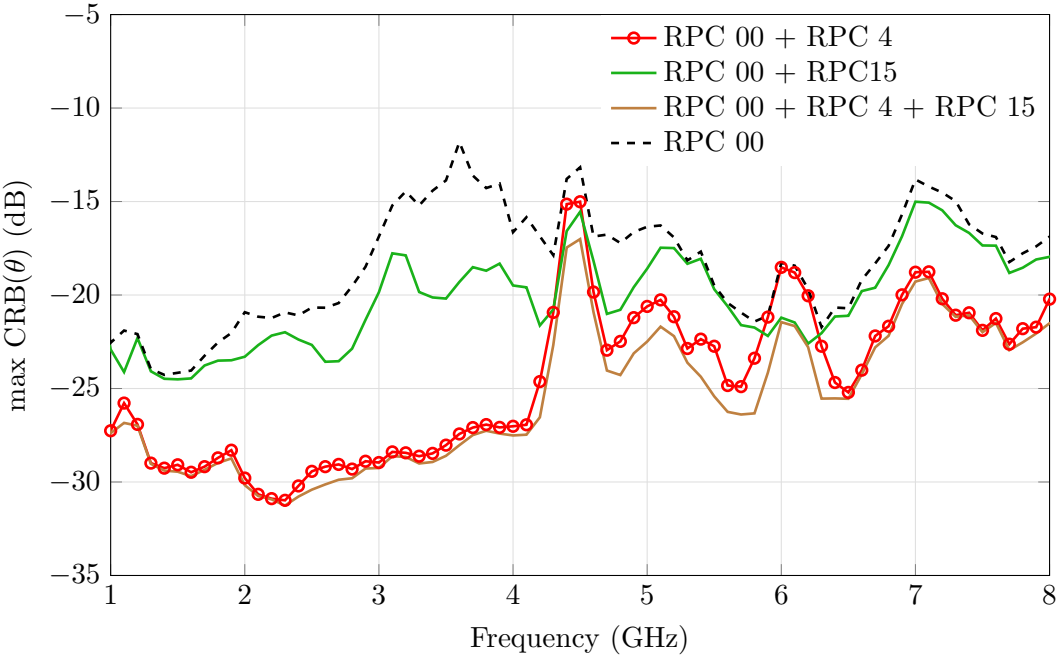

(a)

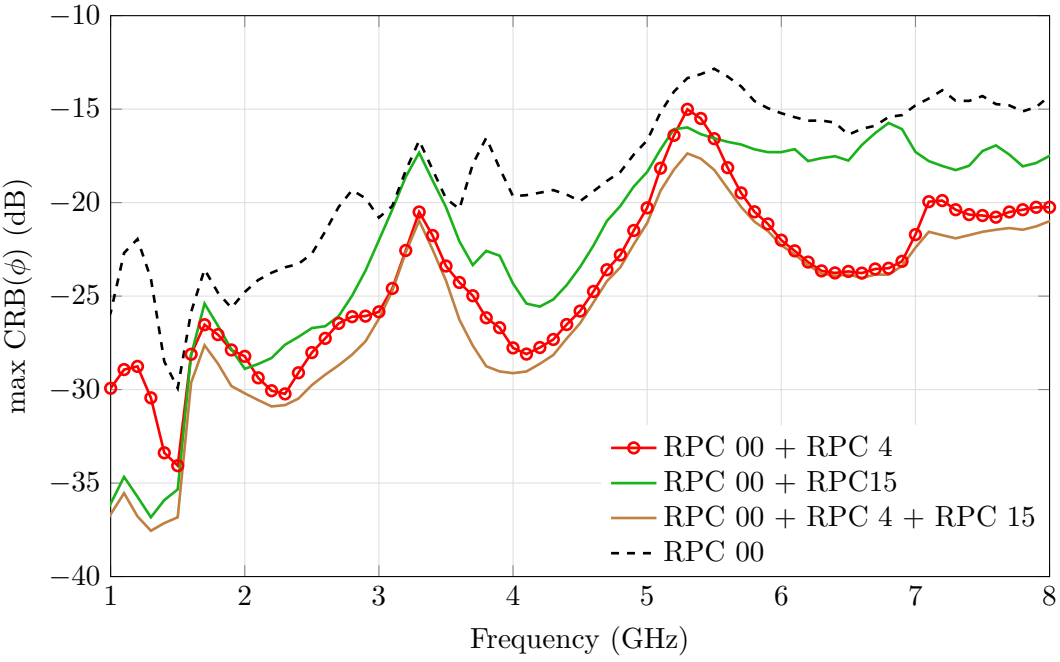

(b)

Figure 3.41: Highest simulated (a) CRLB(θ) and (b) CRLB(ϕ) of the Four Season VA using different RPCs added to the RPC 00, and under the scenario conditions defined in Table 3.15 ($\gamma = 0°$ † $\eta = 0°$, i.e. horizontal polarization)

DoA estimation accuracy

The accuracy of the DoA estimation that can be reached using the Four Season VA and the MUSIC algorithm is now evaluated. This evaluation is performed under the scenario conditions summarized in Table 3.13. The measurement of the six components of the incoming EM-wave (RPC 00) and additional RP diversity (RPC 4 and RPC 15) are employed in the DoA estimation process. Besides, the polarization state of the wave is assumed to be known ($\eta = 0°$ and γ is known). Comparisons between simulation and measurement results are also carried out to experimentally validate the DF performances.

For each polarization state of the incoming EM-wave, the simulated and measured 95th percentile of the angular distance Δa_{RMS} are displayed in Fig. 3.42 to Fig. 3.46. The simulated results obtained if only RPC 00 is used in the DoA estimation process are also recalled in these graphs for comparison purposes. Several observations can be highlighted.

First, it can be noted that the addition of RPC 4 and RPC 15 to RPC 00 clearly improves the estimation accuracy whatever the polarization of the incoming EM-wave. The aforementioned CRB study predicted this improvement.

Secondly, it can be seen that the 95th percentile of Δa_{RMS} does not exceed 5° up to approximately up to 7.6 GHz and 8 GHz if the incoming EM-wave is vertically-polarized ($\gamma = 90°$) or horizontally-polarized ($\gamma = 0°$), respectively. For the incoming linearly-polarized EM-waves that are neither purely vertically- nor horizontally-polarized, the accuracy is not so good but is still improved thanks to the use of additional RP diversity. This could have been foreseen since the additional RP diversity has been selected by restricting to sets of the form $[w_1, w_2, w_3, w_4, 0, 0, 0, 0]$ and $[0, 0, 0, 0, w_5, w_6, w_7, w_8]$, which implies considering independently the vertical and horizontal parts of the Four Season VA. These two parts permit the DoA estimation of incoming vertically- or horizontally-polarized EM-waves, respectively. Therefore, the selected RPCs mainly improve the DoA estimation for these two types of incoming EM-waves as they are inherently chosen for this purpose. All things considered, several actions can be undertaken to improve better the DoA estimation of incoming EM-waves that are neither purely vertically- nor horizontally-polarized:

- The selection of the RPCs should have taken into account the 3^8 sets of the form $[w_1, w_2, w_3, w_4, w_5, w_6, w_7, w_8]$ (if w_i is still limited to $\{1, 0, \text{-}1\}$). It would also be interesting to consider complex values for the weightings, but this would be at the cost of an increase in the number of possible sets. Therefore, an optimized process has to be implemented to keep only one of the possible sets that provide the same RP and then combine the sets exhibiting to the same RPs with rotational symmetry in order to create the possible RPCs. Since the number of RPCs would also increase, the process of selecting the RPC by computing and analyzing the CRB would be more time-consuming.
- It might be interesting to do this study for an incoming circularly-polarized EM-wave instead of separating the study for each polarization state of the incoming EM-wave to speed up the process by addressing the worst case scenario.

Finally, there is a good agreement between the simulated and measurement results, which is slightly reduced if the incoming EM-wave is neither purely vertically- nor horizontally-polarized. This can be explained by the use of the 95th percentile of Δa_{RMS} as a means of comparison, which is not sufficient to analyze the DF performances in the case of significant estimation errors across a large angular area. For illustration purposes, the angular distance Δa_{RMS} as well as

the estimation errors in θ ($E^{\theta}_{\mathrm{RMS}}$) and ϕ (E^{ϕ}_{RMS}) at 4.2 GHz are set out in Fig. 3.47 to Fig. 3.49. It can be seen that angular areas where significant estimation errors occur are quite similar in simulation and measurement but the simulated and measured 95th percentile are more or less different (e.g., for $\gamma = 67.5°$, the simulated and measured 95th percentile of Δa_{RMS} are of 4.30 and 19.59, respectively). Besides, the estimation of the DoA of an incoming EM-wave is still very accurate over a large angular area of the upper hemisphere even if the 95th percentile of Δa_{RMS} is very high (e.g., the measured 95th percentile of Δa_{RMS} for $\gamma = 67.5°$). A more in-depth study presenting the angular areas at each frequency where the estimate is correct could be interesting. These angular areas can also be predicted by the computation of the CRB, as shown in Fig. 3.50.

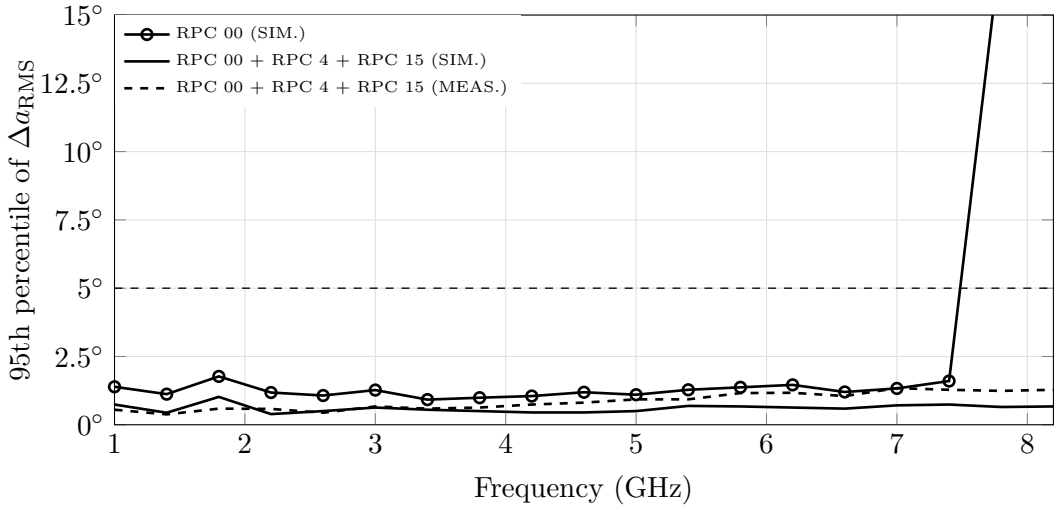

Figure 3.42: 95th percentile of Δa_{RMS} obtained with the Four Season VA from adding RPC 4 and RPC 15 to RPC 00, and under the scenario conditions defined in Table 3.10 ($\gamma = 90° \dagger \eta = 0°$, i.e. vertical polarization)

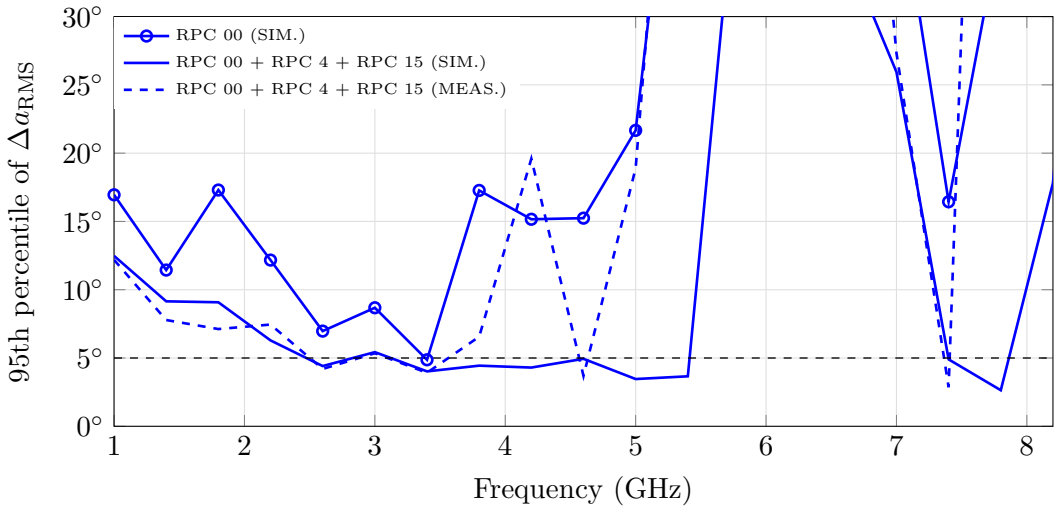

Figure 3.43: 5th percentile of Δa_{RMS} obtained with the Four Season VA from adding RPC 4 and RPC 15 to RPC 00, and under the scenario conditions defined in Table 3.10 ($\gamma = 67.5° \dagger \eta = 0°$)

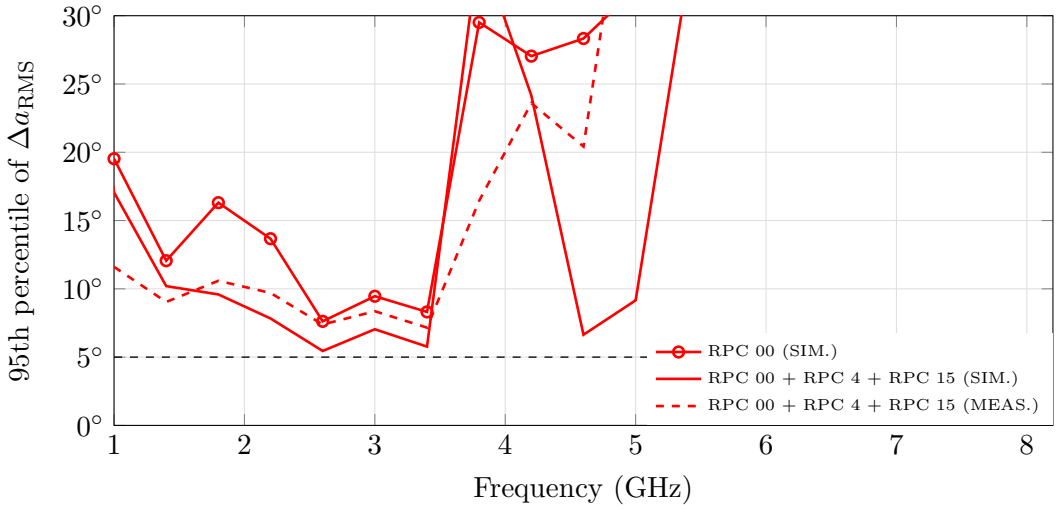

Figure 3.44: 95th percentile of Δa_{RMS} obtained with the Four Season VA from adding RPC 4 and RPC 15 to RPC 00, and under the scenario conditions defined in Table 3.10 ($\gamma = 45° \dagger \eta = 0°$)

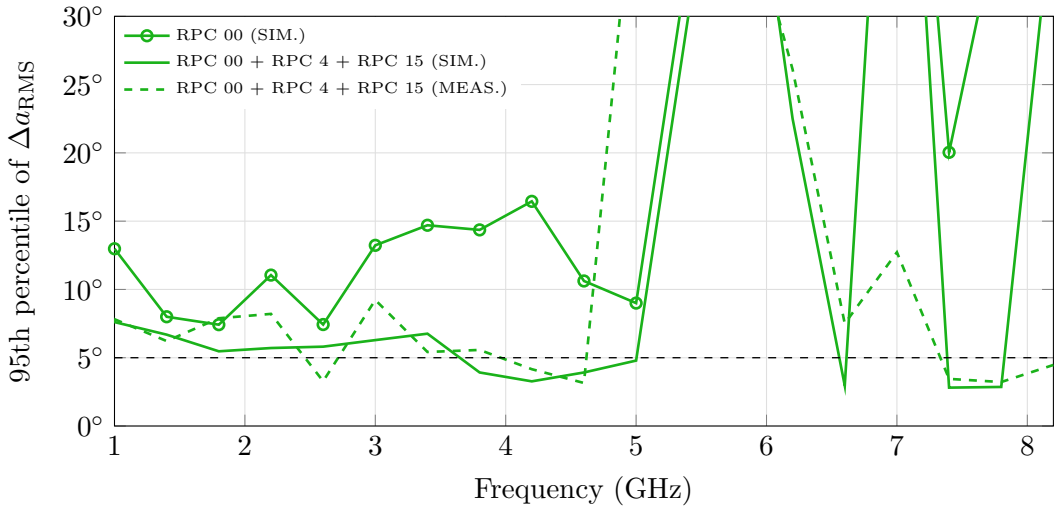

Figure 3.45: 95th percentile of Δa_{RMS} obtained with the Four Season VA from adding RPC 4 and RPC 15 to RPC 00, and under the scenario conditions defined in Table 3.10 ($\gamma = 22.5° \dagger \eta = 0°$)

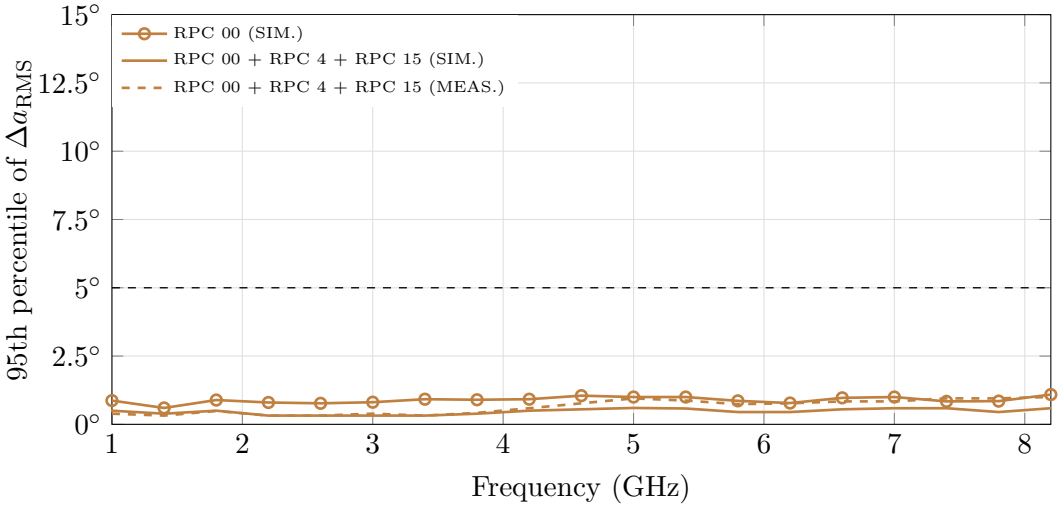

Figure 3.46: 95th percentile of Δa_{RMS} obtained with the Four Season VA from adding RPC 4 and RPC 15 to RPC 00, and under the scenario conditions defined in Table 3.10 ($\gamma = 0° \dagger \eta = 0°$, i.e. horizontal polarization)

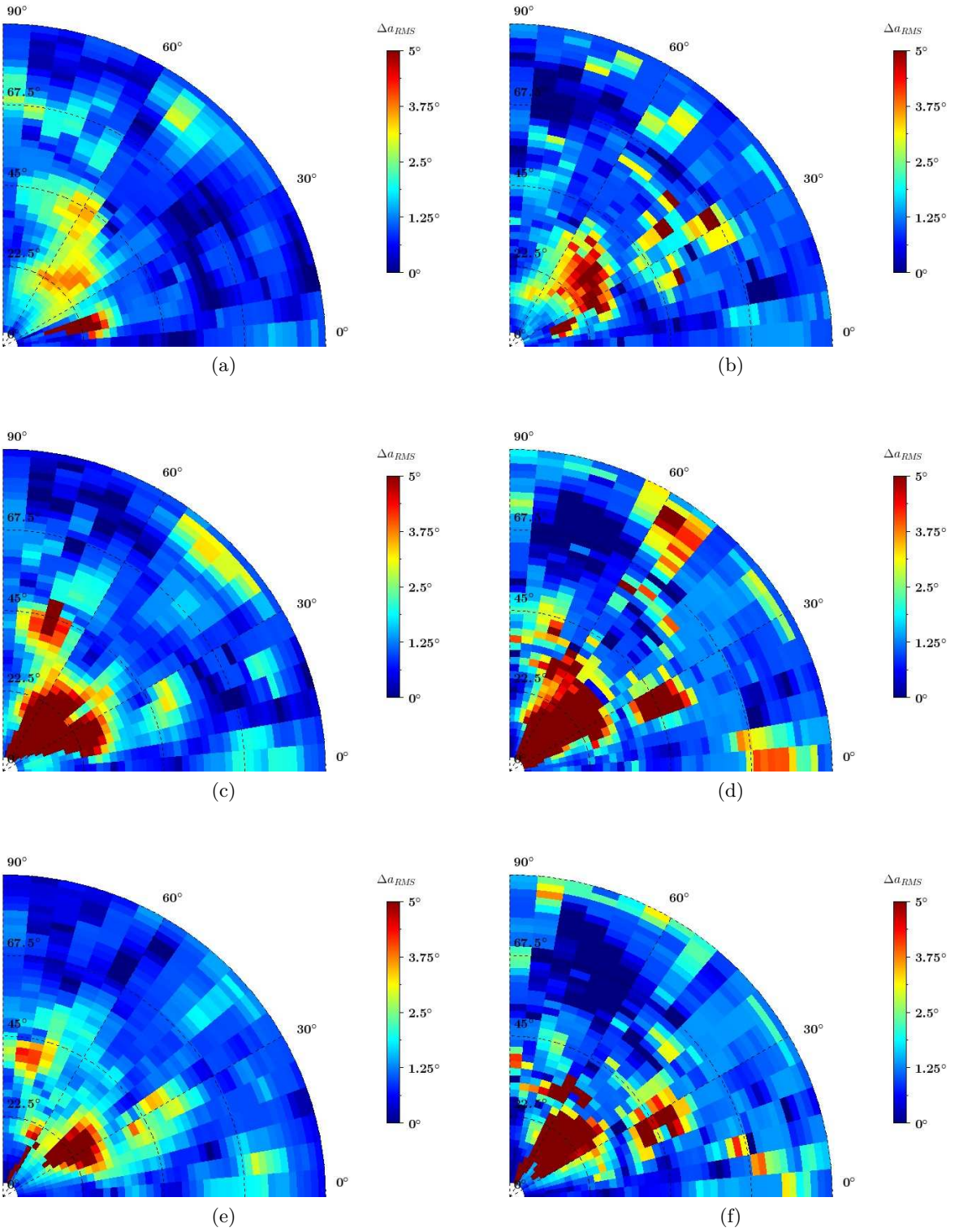

Figure 3.47: Simulated (left figures) and measured (right figures) Δa_{RMS} obtained with the Four Season VA at 4.2 GHz from adding RPC 4 and RPC 15 to RPC 00, and under the scenario conditions defined in Table 3.10: (a) & (b) $\gamma = 22.5°$, (c) & (d) $\gamma = 45°$, and (e) & (f) $\gamma = 67.5°$

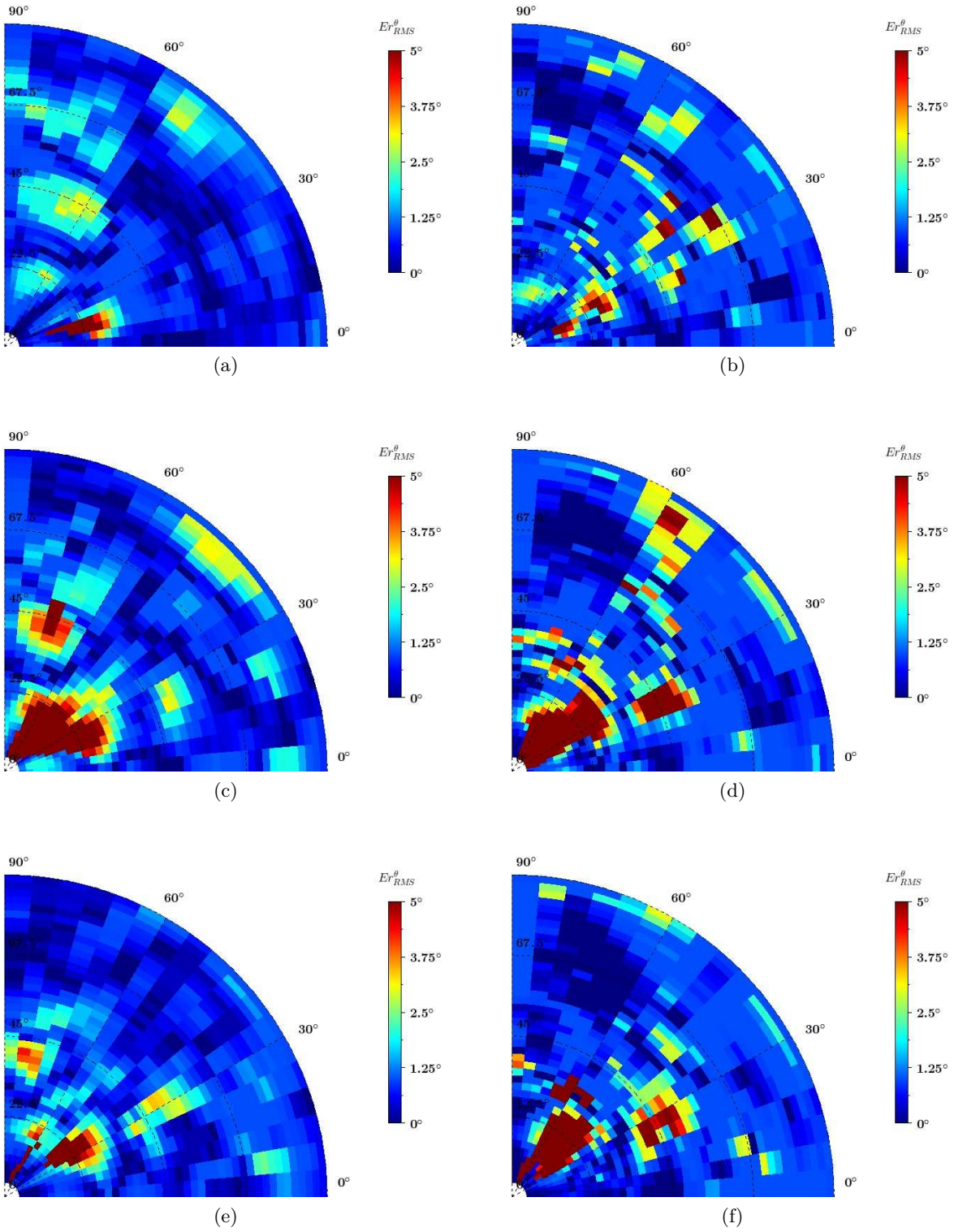

Figure 3.48: Simulated (left figures) and measured (right figures) $E^{\theta}_{\mathrm{RMS}}$ obtained with the Four Season VA at 4.2 GHz from adding RPC 4 and RPC 15 to RPC 00, and under the scenario conditions defined in Table 3.10: (a) & (b) $\gamma = 22.5°$, (c) & (d) $\gamma = 45°$, and (e) & (f) $\gamma = 67.5°$

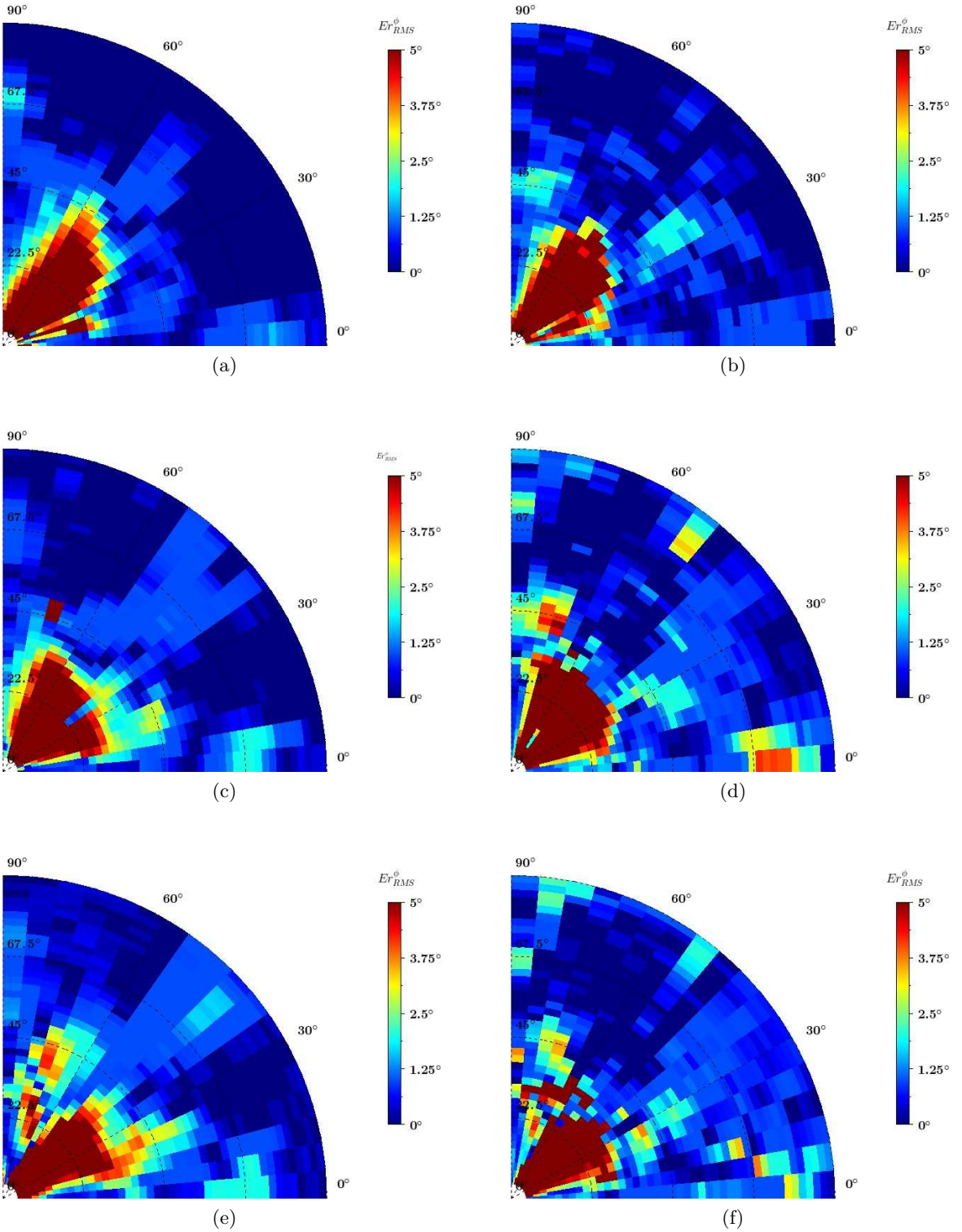

Figure 3.49: Simulated (left figures) and measured (right figures) E^{ϕ}_{RMS}obtained with the Four Season VA at 4.2 GHz from adding RPC 4 and RPC 15 to RPC 00, and under the scenario conditions defined in Table 3.10: (a) & (b) $\gamma = 22.5°$, (c) & (d) $\gamma = 45°$, and (e) & (f) $\gamma = 67.5°$

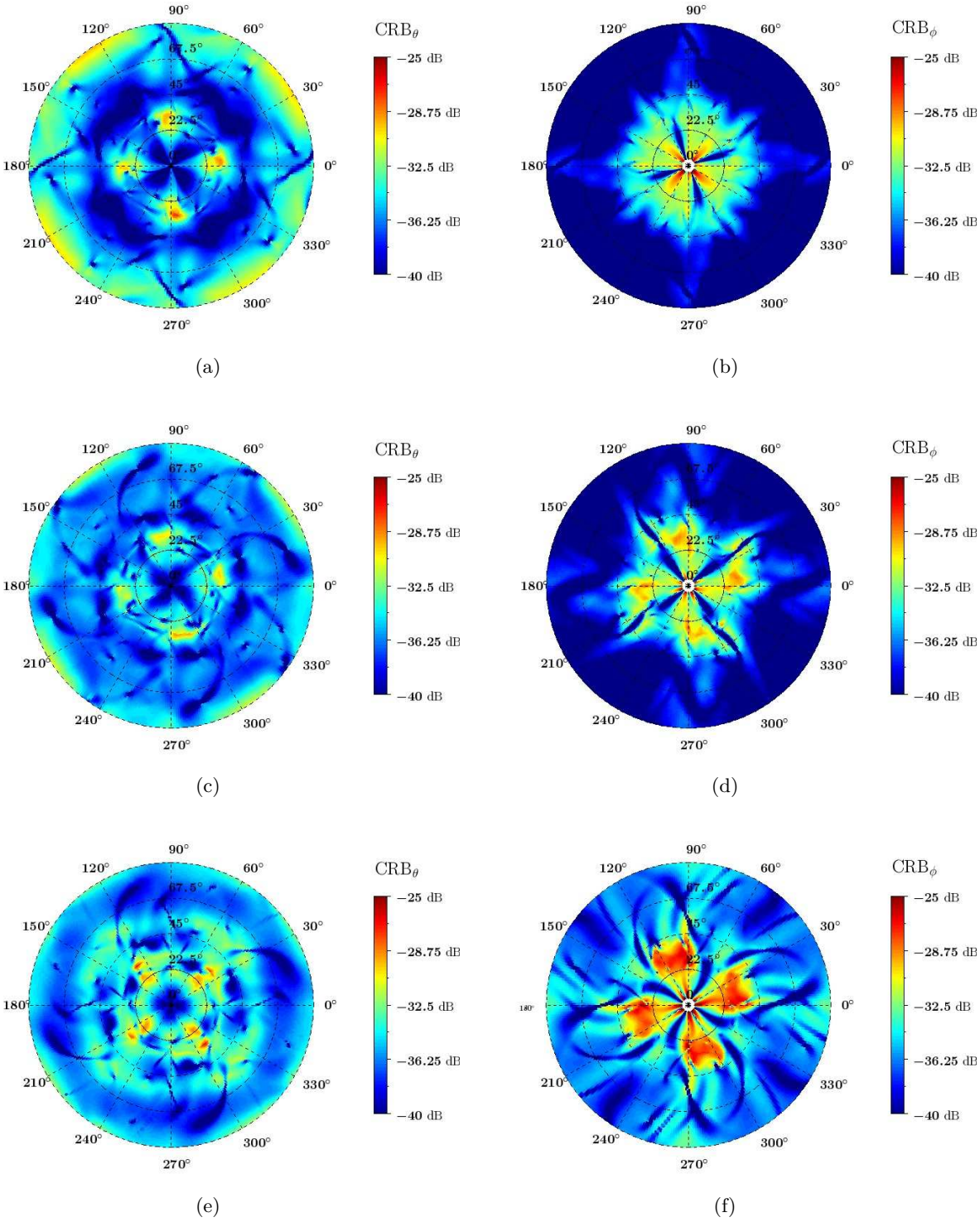

Figure 3.50: Simulated CRB on θ (left figures) and ϕ (right figures) obtained with the Four Season VA at 4.2 GHz from adding RPC 4 and RPC 15 to RPC 00, and under the scenario conditions defined in Table 3.15: (a) & (b) $\gamma = 22.5°$, (c) & (d) $\gamma = 45°$, and (e) & (f) $\gamma = 67.5°$

Sensitivity of the prototype

Let us now evaluate the sensitivity of the Four Season VA prototype at three frequencies: 1.4 GHz, 5 GHz, and 8 GHz. These frequencies are approximately the lower, central and upper operating frequencies of the VA. The sensitivity is assessed when RPC 4 and RPC 15 are used in addition to RPC 00 in the DoA estimation process. Moreover, this evaluation assumes that the incoming EM-wave is either vertically- or horizontally-polarized.

For both scenarios, the 95th percentile of Δa_{RMS} is shown in Fig. 3.51 at the three frequencies of interest and for different PNRs, ranging from 12 dB.m^{-2} to 36 dB.m^{-2} (with a step of 3 dB). The sensitivity of the Four Season VA is degraded as the frequency increases since the 95th percentile of Δa_{RMS} also rises. However, it remains approximately stable at higher frequencies for the estimation of an horizontally-polarized EM-wave. Furthermore, it can be noted that the sensitivity required to estimate the DoA of a vertically-polarized EM-wave is, for a given accuracy, higher than that of a horizontally-polarized EM-wave. This is consistent with the CRB results depicted in Fig. 3.37 and Fig. 3.41, which show that the accuracy of the azimuth angle estimate is relatively the same over the entire bandwidth for both polarizations while the elevation angle estimate is more precise at higher frequencies if the incoming EM-wave is horizontally-polarized. To estimate with a good accuracy the DoA of a vertically-polarized EM-wave, the incoming power density P_s at the VA location has to be higher than -125 dBW.m^{-2} at 1.4 GHz (PNR $\approx$ 16 dB.m^{-2}), -111 dBW.m^{-2} at 5 GHz (PNR $\approx$ 30 dB.m^{-2}) and -108 dBW.m^{-2} at 8 GHz (PNR $\approx$ 33 dB.m^{-2}). In the case of an incoming horizontally-polarized EM-wave, P_s has to exceed -128 dBW.m^{-2} at 1.4 GHz (PNR $\approx$ 16 dB.m^{-2}), -111 dBW.m^{-2} at 5 GHz (PNR $\approx$ 30 dB.m^{-2}) and -108 dBW.m^{-2} at 8 GHz (PNR $\approx$ 33 dB.m^{-2}).

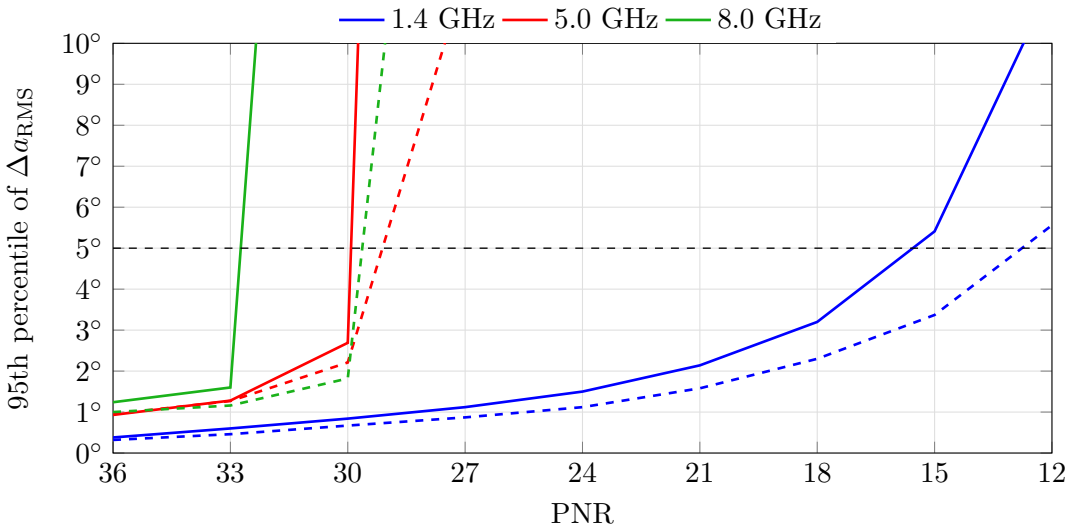

Figure 3.51: Measured 95th percentile of Δa_{RMS} achieved for different PNRs and when RPC 4 and RPC 15 are added to RPC 00 in the DoA estimation process of an incident vertically- (solid lines) or horizontally-polarized (dashed lines) EM-wave.

Considering the same emitter as before (i.e., an isotropic antenna and an emitting power of 1 W), the theoretical range $r_{\max}$ of the Four Season VA has been derived and reported in Table 3.16. It can be seen that the range decreases with the frequency, from the 502 km or 709 km at the lower operating frequency down to 71 km or 100 km at the upper frequency for the estimation of

an impinging vertically- or horizontally-polarized EM-wave, respectively. For a given accuracy, the range reached for the estimation of a horizontally-polarized EM-wave is greater than that of a vertically-polarized EM-wave.

Table 3.16: Measured sensitivity and theoretical range of the Four Season VA prototype using RPC 00, RPC 4, and RPC 15 for the DoA estimation of an incident vertically-polarized EM-wave.

Frequency	P_{sensi}	PNR	$r_{\max}$ † (P_e, G_e)
$\gamma = 90°$ † $\eta = 0°$ (vertical polarization)			
1.4 GHz	-125 dBW.m^{-2}	16 dB.m^{-2}	502 km † (1 W, 0 dBi)
5 GHz	-111 dBW.m^{-2}	30 dB.m^{-2}	100 km † (1 W, 0 dBi)
8 GHz	-108 dBW.m^{-2}	33 dB.m^{-2}	71 km † (1 W, 0 dBi)
$\gamma = 0°$ † $\eta = 0°$ (horizontal polarization)			
1.4 GHz	-128 dBW.m^{-2}	13 dB.m^{-2}	709 km † (1 W, 0 dBi)
5 GHz	-112 dBW.m^{-2}	29 dB.m^{-2}	112 km † (1 W, 0 dBi)
8 GHz	-111 dBW.m^{-2}	30 dB.m^{-2}	100 km † (1 W, 0 dBi)

3.3.4 Conclusion

As a reminder, the improved version of the Two Season VA has shown good simulated DF performances to estimate the DoA of an incident vertically-polarized EM-wave in the upper hemisphere and over a bandwidth of 6.56:1 from 1.31 GHz to 8.6 GHz using the additional RP diversity technique. Nevertheless, the estimation errors increased in case of depolarization (i.e., if the incoming EM-wave was no longer vertically-polarized). Therefore, the third section of this chapter has been dedicated to the modification of the topology of the VA in order to tackle polarization mismatch, which led to the development of the Four Season VA. This VA consists of two semi-circular arrays of Vivaldi antennas (which correspond to those of the improved version of the Two Season VA) mounted over a circular array of Vivaldi antennas. The RP reconfigurability of the Four Season VA enables notably the measurement of the six component of an incoming EM-wave (RPC 00). A prototype of this antenna has been manufactured and experimentally characterized. The measured impedance bandwidth is of 6.11:1 from 1.24 GHz to 8.40 GHz, which means that the Four Season VA is included in a half-sphere within a $0.47\lambda_{1.24\text{GHz}}$ radius. Globally, a fairly good agreement between the experimental and simulations results has been obtained for both electrical characteristics and DF performances. Across the upper hemisphere, an accurate estimation of the DoA of an incoming EM-wave either vertically- or horizontally-polarized is achieved up to 8 GHz from using only RPC 00. If the incident EM-wave is not vertically-polarized, the DoA estimation is more accurate with the Four Season than with the improved version of the Two Season VA. Nonetheless, the accuracy is not as good (but nevertheless better in comparison to the previous Two Season VA) if the incoming EM-wave is not purely vertically- or horizontally-polarized. The additional RP diversity technique was then used in order to enhance the DF performances in this case. This results in an overall

enhancement of the DoA estimation accuracy over the VA bandwidth, but there is still a need to improve it further. To this end, future research should be devoted to the development of an optimized selection process and an expanded choice of RPCs.

3.4 Conclusion

In the previous chapter, the Two Season VA has been proposed. This VA has shown good DF performances to estimate the DoA of an incident vertically-polarized EM-wave in the upper hemisphere through the measurement of the three components E_z, H_x and H_y (RPC 0) and over an impedance bandwidth of 1.69:1 from 2.1 GHz to 3.55 GHz. Three actions have been carried out in this chapter to improve the DF performances of this antenna.

First, the DoA estimation accuracy was enhanced by making further use of the RP reconfigurability of the VA. In other words, new RPs were employed in the DoA estimation process in addition to the synthesized RPs of the two magnetic dipoles and one electric monopole. Specifically, a method based on the realistic CRB (i.e., derived from the actual RPs of the antenna) has been proposed to select efficiently and rapidly the additional RP diversity to be used. An improvement of the simulated and measured DF performances of the Two Season VA has been demonstrated using this additional RP diversity technique.

Secondly, the frequency coverage of the Two Season was widened through a modification of the antenna feeding and the use of the additional RP diversity technique. Hence, an improved version of the Two Season VA has been designed. This VA has exhibited a simulated impedance bandwidth of 8.72:1 from 1.31 GHz to 11.42 GHz thanks to the modification of the antenna feeding. The additional RP diversity technique subsequently has enabled the extension of the frequencies range in which good DF performances can be achieved up to 8.6 GHz. Without it, the upper operating frequency was limited to approximately 3.6 GHz since the three RPs that measured the components E_z, H_x and H_y differ from those of ideal electric and magnetic dipoles as the frequency increases.

Thirdly, the topology of the improved version of the Two Season VA has been adjusted in order to improve the DF performances in case of polarization mismatch, which has led to the development of the Four Season VA. The experimental results in terms of electrical characteristics and DF performances were relatively consistent with the simulation results. The prototype of this VA has enabled the measurement of the six components of an incoming EM-wave over an impedance bandwidth of 6.11:1 from 1.24 GHz to 8.40 GHz. An accurate estimation of the DoA of an incoming vertically- or horizontally-polarized EM-wave has been achieved across the 3-D upper half-space and up to 8.0 GHz using only the measurement of these components. The DoA estimate which was less accurate if the incoming EM-wave was neither purely vertically- nor horizontally-polarized has then been improved using the additional RP diversity technique. However, the accuracy was still not as good as for vertically- or horizontally-polarized EM-waves. Future research should focus on developing an optimized selection process and the possibility of offering a wider choice of RPCs.

Conclusion

The main objective of this Ph.D. thesis was the study and design of a passive and wideband VA for DF over the 3-D space with compactness and minimal complexity constraints. More precisely, the objective was to design a passive and compact VA that is able to estimate with the highest accuracy and over the widest possible frequency range of operation the DoA of incident EM-waves over the 3-D space, regardless of their polarization. Several significant milestones towards this objective have been achieved:

I. A passive and wideband VA intended to estimate the DoA of vertically-polarized EM-waves in the upper hemisphere has been designed. The antenna was mounted over a metallic support in view of embedded applications.

II. A new DoA estimation process for VAs has been proposed in order to enhance their DF performances in terms of estimation accuracy, frequency coverage, robustness to angular ambiguity and polarization mismatch.

III. A passive and wideband VA intended to estimate the DoA of vertically- and horizontally-polarized EM-waves in the upper hemisphere has been designed to overcome the errors due to polarization mismatch.

These research axes have been established according to the state of the art realized in **Chapter 1** concerning the different techniques used to estimate the DoA of incoming EM-waves and the most recent DF antennas. This state of the art has identified the challenges facing current DF antennas. Specifically, it seemed very challenging to design a compact and wideband DF antenna for DF over the 3-D space and regardless of the polarization of the incoming EM-waves. Recent studies have shown the potential of VAs to provide this 3-D coverage and compactness. However, the attention was mainly focused on the implementation of active and wideband VA structures. No wideband and passive VA has been reported up to now. Prior to this Ph.D. work, passive structures were limited to multi-band coverage. Besides, the DoA estimation was also restricted to vertically-polarized EM-waves.

Chapter 2 was dedicated to the design of the first passive and wideband VA. This VA was intended to estimate the DoA of vertically-polarized EM-waves in the upper hemisphere through the measurement of the three components E_z, H_x and H_y. The VA was mounted over a ground plane in view of embedded applications. A state of the art regarding the techniques used in antenna design to achieve wideband impedance matching has been provided. A feasibility study of a compact antenna based on one of these techniques (that is, the overlapping bandwidths technique) and the theory of electrically small antennas has then been carried out. This has been shown not to be suitable for designing a compact and wideband antenna. Hence, a state of art of wideband electric and magnetic dipoles has been provided in order to identify the radiating

elements that would be worthwhile to consider for designing the VA. Although the literature contained many electric dipoles, this was not the case for magnetic dipoles. Hence, the first step of designing the passive and wideband VA was to conceive the magnetic dipoles. Each magnetic dipole has been designed from a semi-circular array of Vivaldi antennas mounted over a ground plane. This design was based on Chu's theory regarding the use of a circular array of directive antennas to obtain an omnidirectional RP. Then, the VA which was referred to as the Two Season VA has been proposed. This VA consisted of only two orthogonal and colocated dual-port semi-circular arrays of Vivaldi antennas and enabled through its RP reconfigurability the measurement of the three components E_z, H_x and H_y of an incoming EM-wave. A prototype of the Two Season VA was manufactured and experimentally characterized. The prototype exhibited an impedance bandwidth of 1.69:1 from 2.1 GHz to 3.55 GHz. It was included in a half-sphere within a $0.52\lambda_{2.1\text{ GHz}}$ radius and mounted on a finite metallic and octagonal support of radius $1.14\lambda_{2.1\text{ GHz}}$. The theoretical and estimated DF performances of the Two Season VA have been assessed using the realistic CRB (derived from the actual RPs of the antenna) and the popular DOA estimation algorithm called MUSIC, respectively. An accurate DoA estimation of an incoming vertically-polarized EM-wave has been measured across the overall bandwidth and the 3-D upper hemisphere using only the measurement of these three components. As the frequency increased, the presence of ripples in the RPs degraded the DF performances. Overall, a good agreement between the experimental results and the simulation results has been obtained for both electrical characteristics and DF performances.

Chapter 3 was devoted to the improvement of the DF performances of the Two Season VA. Three methods have been proposed to achieve the desired result. First, the DoA estimation process of the Two Season VA has been improved by exploiting new RP diversity in addition to that employed to measure the electric and magnetic components of the incident vertically-polarized EM-waves. A method based on the CRB has been proposed for selecting efficiently and rapidly the new RPs to be added in the DoA estimation process that maximizes the accuracy of the estimate across the overall bandwidth. The main advantage of this method is its independence to the estimation technique used for estimating the DoA of the impinging EM-waves. The simulated and measured DF performances of the Two Season VA in terms of DoA estimation accuracy, robustness to angular ambiguities and sensitivity have been improved from taking leverage of the RP reconfigurability of the antenna. Secondly, the frequency coverage of the Two Season VA has been extended through a modification of the antenna feeding and the use of the additional RPs diversity technique. This has led to the development of an improved version of the Two Season VA, which exhibited a simulated impedance bandwidth of 8.72:1 from 1.31 GHz to 11.42 GHz. However, good DF performances have been only obtained until 3.6 GHz without using the additional RPs diversity technique since the initial RPs differ from those of ideal electric and magnetic dipoles due to the emergence of ripples. Nevertheless, the use of additional RPs diversity has extended the operating band up to 8.6 GHz, in which an accurate estimation of a vertically-polarized EM-wave has been achieved. However, it has been shown that the estimation errors increased if the polarization of the incoming EM-wave was no longer vertically-polarized. Thirdly, the topology of the Two Season VA has been modified in order to estimate the DoA of incoming EM-waves in the upper hemisphere, regardless of their polarization. This led to the development of a new VA which was referred to as the Four Season VA, for which a prototype has been manufactured and experimentally characterized. The Four Season VA consisted of two semi-circular arrays of Vivaldi antennas (which correspond to those of the improved version of the Two Season VA) mounted over another circular array of Vivaldi antennas, which acted as a ground plane. The vertical and horizontal arrays enabled the measurement of the six compo-

nents (E_x,E_y,E_z,H_x,H_y, and H_z) of an incoming EM-wave thanks to its RP reconfigurability. The prototype exhibited an impedance bandwidth of 6.11:1 from 1.24 GHz to 8.40 GHz, which means that the Four Season VA was included in a half-sphere within a $0.47\lambda_{1.24\text{GHz}}$ radius. The experimental and simulations results for both electrical characteristics and DF performances have shown a reasonably good agreement. The measurement of the six components of an incoming EM-wave has enabled the accurate estimation of the DoA across the upper 3-D half space and up to 8 GHz if the EM-wave was either vertically- or horizontally-polarized. Moreover, the estimation accuracy achieved with the Four Season was higher than the one reached with the improved version of the Two Season VA. However, the accuracy obtained with the Four Season VA was at a lower level (but nevertheless better in comparison to that reached with the Two Season VA) if the incoming EM-wave was not purely vertically- or horizontally-polarized. The use of the additional RPs technique has then enabled the enhancement of the DoA estimation accuracy regardless of the polarization of the incoming EM-wave. Nonetheless, the estimation was still not as accurate than for purely vertically- or horizontally-polarized EM-waves.

To sum up, the findings from this Ph.D. make several contributions to the current literature:

I. The wideband frequency coverage of VAs, which up to now has not yet been addressed from passive structures. Furthermore, an original antenna arrangement has been proposed to synthesize the radiation patterns of magnetic and electric dipoles.

II. The improvement of the DF performances of VAs (in terms of DoA estimation accuracy, sensitivity, robustness to angular ambiguity and polarization mismatch) by adding new RP diversity to the one commonly used by standard VAs (i.e., the RP diversity that allows the measurement of the six components of the incident EM-wave) in the DoA estimation process. Moreover, a method based on the CRB to select efficiently and rapidly the additional RP diversity has also been reported.

III. Two prototypes have been manufactured to experimentally validate the simulated results regarding the electrical characteristics and DF performances.

Perspectives for future work

At the end this Ph.D. thesis, the Four Season VA has been proposed to estimate over a wide frequency range the DoA of impinging EM-waves from the 3-D upper half-space, regardless of their polarization. Both simulations and measurements have shown that the DoA estimation of vertically- or horizontally-polarized is very accurate. In addition, it has been shown that the use of additional RPs diversity enables the improvement of the estimation accuracy if the polarization of the incoming EM-waves is neither purely vertical nor horizontal. Starting from the research made in this Ph.D., several studies can be conducted related to three different domains: VA design, DF performances, and other uses of this antenna.

VA design

The future investigations regarding the Four Season VA design can best be treated under three headings:

- The Four Season VA manufacturing process (i.e., the use of vias to electrically connect the vertical and horizontal parts of the antenna) needs to be reconsidered in order to improve the impedance matching of the vertical part of the VA.
- It could be interesting to design a receiver circuit for future practical use.
- The widespread applications that require DF coupled with the current trend of miniaturization have led toward the necessity of designing very compact, wideband and efficient DF antennas. Several techniques have been tested during this Ph.D. (resonant ring, antenna loading, corrugated Vivaldi antennas, sinusoidal modulation of the exponential tapered profile of the Vivaldi antennas, modification of the conductivity profile) to miniaturize the semi-circular arrays of Vivaldi antennas constituting the improved version of the Two Season VA but were not reported here for brevity reason. Apart from the method based on the modification of the conductivity profile, these different techniques did not lead to the miniaturization of the antenna. Nonetheless, this miniaturization occurred at the drastic expense of efficiency. It might be worth exploring new miniaturization techniques. It could be also of great interest to design active antennas and study their incorporation into the Four Season VA in order to cover lower frequencies and thus reduce the size of the antenna.
- The electrical characteristics of the Four Season VA when mounted on a carrier could be assessed. Besides, the height between the VA and the metallic ground plane could be significantly reduced using an artificial magnetic conductor (AMC) surface. To this end, it would be useful to develop a wideband AMC surface.

DF performances

The key future investigations on DF performances can be listed as follows:

- The additional RPs diversity selection process should be optimized to further improve the DoA estimation accuracy of incoming EM-waves that differ from purely vertically- or horizontally-polarized EM-waves. This can notably be done by offering a wider choice of RPCs (i.e., using RPs associated to weighting coefficients of the form $[w_1, w_2, w_3, w_4, w_5, w_6, w_7, w_8]$ where w_i is a complex value instead of restricting the choice to $[w_1, w_2, w_3, w_4, 0, 0, 0, 0]$ and $[0, 0, 0, 0, w_5, w_6, w_7, w_8]$ with $w_i \in \{1, 0, \text{-}1\}$). As a consequence, an optimized process has to be implemented to keep only one of the possible sets that provide the same RP and then combine the sets exhibiting to the same RPs with rotational symmetry to create the possible RPCs. Since the number of RPCs would increase, the process of selecting the RPC by computing and analyzing the CRB would be more time-consuming. It might be useful to select the efficient RPC for an incoming circularly-polarized EM-wave instead of separating the selection process for each polarization state of the impinging EM-wave to speed up the process by addressing the worst case scenario.
- A more in-depth investigation of the DF performances of the Four Season VA could also be conducted. For instance, the DoA estimation accuracy needs to be evaluated more closely in

various environments (e.g., multi-source with different polarization, multi-path). In addition, it will be important to explore the DF performances when the VA is mounted on a carrier. Besides, a study of the trajectories of moving sources would be very interesting for various applications.

- The polarization state of the incoming EM-wave is assumed to be known in this Ph.D. work, although this is rarely the case in practice. The MUSIC algorithm enables the estimation of the DoA as well as the polarization, for which a four-dimensional peak search is required. Therefore, the computation time would increase. Besides, knowing the polarization state of an incident EM-wave can be useful in various applications, in particular in electronic warfare. Hence, it would be worthwhile to reduce the computation time thanks to new estimation algorithms (e.g., DR-MUSIC[6], Q-MUSIC[7]).
- The study of a Four Season VA array and its impact on the DF performances may be worth investigating. For example, the Four Season VA could be mounted on each wing of an aircraft and on each side of the vertical stabilizer.

Other uses of this antenna

Although this Ph.D. was focused on DF, the proposed Four Season VA may well be useful for MIMO (multiple input multiple output) applications as well as for RP reconfigurable antenna applications. For instance, this antenna could undoubtedly be used to provide an omnidirectional RP and circular polarization over a wide operating bandwidth.

[6]Dimensionality Reduction
[7]Quaternion

Publications

International journals

[J1] J. Duplouy, C. Morlaas, H. Aubert, P. Potier, P. Pouliguen, and C. Djoma. Wideband and reconfigurable vector antenna using radiation pattern diversity for 3-D direction-of-arrival estimation. *IEEE Transactions on Antennas and Propagation*, In press.

[J2] J. Duplouy, C. Morlaas, H. Aubert, P. Potier, P. Pouliguen, and C. Djoma. Reconfigurable grounded vector antenna for 3-D electromagnetic direction-finding applications. *IEEE Antennas and Wireless Propagation Letters*, 17(2):197–200, Feb 2018.

Communications in international conferences with technical programme committee

[I1] J. Duplouy, C. Morlaas, H. Aubert, P. Potier, P. Pouliguen, and C. Djoma. 3D direction-of-arrival estimation using a wideband vector antenna. In *IEEE International Symposium on Antennas and Propagation (APSURSI)*, Boston, July 2018.

[I2] J. Duplouy, C. Morlaas, H. Aubert, P. Potier, P. Pouliguen, and C. Djoma. Grounded colocated antennas for wideband vector sensor applications. In *IEEE International Symposium on Antennas and Propagation (APSURSI)*, San Diego, July 2017.

Communications in national (French) conferences

[N1] J. Duplouy, C. Morlaas, H. Aubert, P. Potier, P. Pouliguen, and C. Djoma. Antenne vectorielle large-bande pour la radiogoniométrie 3D. In *Assemblée générale GDR ONDES*, page 2p., Sophia Antipolis, France, October 2017.

[N2] J. Duplouy, C. Morlaas, and H. Aubert. Dipôle magnétique large-bande pour la radiogoniométrie 3D à l'aide d'une antenne vectorielle. In *Journées Nationales Micro-Ondes (JNM)*, page 4p., Saint-Malo, France, May 2017.

Appendix A

The MUSIC algorithm

The aim of this appendix is first to describe in more details the well-known MUSIC (MUltiple SIgnal Classification) algorithm (Section A.1), and then present the expression of the MUSIC spatial spectrum associated with VAs (Section A.2).

A.1 The MUSIC algorithm, a subspace-based method

Within the class of the subspace-based DoA algorithms described in Section 1.2.4.2, the MUSIC algorithm developed by R. Schmidt in 1986 [31] is among the most popular due in large part to its generality. Indeed, it can be used with arrays of arbitrary but known configuration and response. Moreover, it enables the estimation of multiple parameters per source (such as the azimuth and elevation angles of an incoming EM-wave as well as its polarization state). Nonetheless, the MUSIC algorithm generality comes at a cost. The array response has to be known for all possible combinations of source parameters either through a calibration process (method adopted in this Ph.D. work, see Section 2.7.1) or thanks to an analytical characterization [1].

Basically, the MUSIC algorithm is based on the concept of signal and noises subspaces.

Let us consider an array of P sensors and V ($V < P$) incoming EM-waves traveling in an isotropic, homogeneous and lossless medium and incident upon the array. In presence of V incoming EM-waves, the output voltage $\boldsymbol{x} \in \mathbb{C}^{P,1}$ received at time t can be written as follows

$$\boldsymbol{x}(t) = \boldsymbol{D}(\boldsymbol{\Omega}).\boldsymbol{s}(t) + \boldsymbol{n}(t), \tag{A.1}$$

where $\boldsymbol{D}(\boldsymbol{\Omega}) = [\boldsymbol{d}(\boldsymbol{\Omega}_1) \dots \boldsymbol{d}(\boldsymbol{\Omega}_v) \dots \boldsymbol{d}(\boldsymbol{\Omega}_V)] \in \mathbb{C}^{P,V}$ is the array spatial response to the V incident EM-waves characterized by the parameters $\boldsymbol{\Omega}_v$. In Eq. A.1, $\boldsymbol{s} \in \mathbb{C}^{V,1}$ and $\boldsymbol{n} \in \mathbb{C}^{P,1}$ are the signal vector associated with these incoming EM-waves (i.e., the amplitude and phase of each signal) and the additive white Gaussian noise, respectively. The noise is assumed spatially invariant with zero-mean and covariance matrix $\mathbf{R}_{\boldsymbol{n}} = \sigma_n^2 \boldsymbol{I} \in \mathbb{C}^{P,P}$.

First, the signal and noise subspaces are first identified using eigendecomposition of the covariance matrix $\mathbf{R}_{\boldsymbol{X}}$ of the received signal $\boldsymbol{x}$. This matrix can be expressed as follows

$$\begin{aligned} \mathbf{R}_{\boldsymbol{X}} &= E\left[\boldsymbol{x}\boldsymbol{x}^{\mathrm{H}}\right], \\ &= \sum_{p=1}^{P} \lambda_{\boldsymbol{x},p} \boldsymbol{v}_{\boldsymbol{x},p} \boldsymbol{v}_{\boldsymbol{x},p}^{\mathrm{H}}, \end{aligned} \tag{A.2}$$

where $\lambda_{\boldsymbol{x},p}$ and $\boldsymbol{v}_{\boldsymbol{x},p}$ denote the eigenvalues and corresponding orthonormal eigenvectors of $\mathbf{R}_{\boldsymbol{X}}$. The eigenvalues are then arranged in the descending order, that is

$$\lambda_{\boldsymbol{x},1} \geqslant \lambda_{\boldsymbol{x},2} \geqslant \cdots \geqslant \lambda_{\boldsymbol{x},V} \geqslant \lambda_{\boldsymbol{x},V+1} = \lambda_{\boldsymbol{x},V+2} = \cdots = \lambda_{\boldsymbol{x},P} = \sigma_n^2. \tag{A.3}$$

The eigenvectors $\boldsymbol{V}_{\boldsymbol{x},S} = [\boldsymbol{v}_{\boldsymbol{x},1}, \ldots, \boldsymbol{v}_{\boldsymbol{x},V}]$ corresponding to the V largest eigenvalues span the signal subspace while the remaining $P - V$ eigenvectors $\boldsymbol{V}_{\boldsymbol{x},N} = [\boldsymbol{v}_{\boldsymbol{x},V+1}, \ldots, \boldsymbol{v}_{\boldsymbol{x},P}]$ span the orthogonal space, where there is only noise. This space is commonly referred to as the noise subspace. In practice, the covariance matrix $\mathbf{R}_{\boldsymbol{X}}$ is unknown and an estimate of the spatial covariance matrix of $\boldsymbol{x}$ over N snapshots is used. This latter is defined as follows

$$\hat{\mathbf{R}_{\boldsymbol{X}}} = \frac{1}{N} \sum_{n=1}^{N} \boldsymbol{x}[t_n] \boldsymbol{x}^{\mathrm{H}}[t_n]. \tag{A.4}$$

Since there are imperfections in deriving $\hat{\mathbf{R}_{\boldsymbol{X}}}$, the noise subspace eigenvalues will not be exactly equal to σ_n^2. However, they form a group around this value and thus can be distinguished from the signal subspace eigenvalues. The separation becomes easier and more pronounced if the number of snapshots used for the estimation increases, and ideally reaches infinity.

Secondly, the MUSIC algorithm implies that the steering vectors of the incoming EM-waves are orthogonal to the noise subspace eigenvectors, namely

$$\boldsymbol{V}_{\boldsymbol{x},N}^{\mathrm{H}} \boldsymbol{D}(\boldsymbol{\Omega}_l) = \mathbf{0}, \; l \in [\![1; L]\!]. \tag{A.5}$$

The MUSIC spatial spectrum P_{MUSIC} is defined as follows

$$P_{\mathrm{MUSIC}}(\boldsymbol{\Omega}) = \frac{1}{\boldsymbol{D}^{\mathrm{H}}(\boldsymbol{\Omega}) \boldsymbol{V}_{\boldsymbol{x},N} \boldsymbol{V}_{\boldsymbol{x},N}^{\mathrm{H}} \boldsymbol{D}(\boldsymbol{\Omega})}, \tag{A.6}$$

from which the parameters of the incoming EM-waves are estimated. When $\boldsymbol{D}(\boldsymbol{\Omega})$ is orthogonal with each column of $\boldsymbol{V}_{\boldsymbol{x},N}$, the value of the denominator is zero, but due to the existence of the noise, it is actually a minimum which corresponds to a peak of P_{MUSIC}.

A.2 MUSIC spatial spectrum and vector antennas

Both DoA and polarization state of an incoming EM-wave can be estimated thanks to a VA. According to Eq. A.6, the MUSIC spatial spectrum is defined as follows

$$P_{\mathrm{MUSIC}}(\phi, \theta, \gamma, \eta) = \frac{1}{\boldsymbol{D}^{\mathrm{H}}(\phi, \theta, \gamma, \eta) \boldsymbol{V}_{\boldsymbol{x},N} \boldsymbol{V}_{\boldsymbol{x},N}^{\mathrm{H}} \boldsymbol{D}(\phi, \theta, \gamma, \eta)}. \tag{A.7}$$

Hence, the parameters $\boldsymbol{\Omega}_v = [\theta_v \; \phi_v \; \eta_v \; \gamma_v]^{\mathrm{T}}$ of each EM-waves are given by

$$(\phi, \theta, \gamma, \eta) = arg \left\{ \max_{\phi,\theta,\gamma,\eta} P_{\mathrm{MUSIC}}(\phi, \theta, \gamma, \eta) \right\}. \tag{A.8}$$

Estimating these parameters requires a lot of computer resources since P_{MUSIC} is a fourth order function. Nevertheless, recent studies propose solutions to optimize computation times. For example, an observation model based on quaternion formalism results in a reduction by half of the memory resource demand and calculation costs [127]. Another example is the dimensionality

reduction MUSIC (DR-MUSIC) algorithm, which enables the reduction of the dimensionality of search from a four-dimensional search to two two-dimensional searches using the Rayleigh-Ritz theorem [128].

Throughout this Ph.D. work, only one incoming EM-wave is considered ($V = 1$) and its polarization state is assumed to be known. As a consequence, $\boldsymbol{D} = \boldsymbol{d}$ and the MUSIC spatial spectrum is expressed as follows

$$P_{\mathrm{MUSIC}}(\phi, \theta) = \frac{1}{\boldsymbol{d}^{\mathrm{H}}(\phi, \theta)\boldsymbol{V}_{\boldsymbol{x},N}\boldsymbol{V}_{\boldsymbol{x},N}^{\mathrm{H}}\boldsymbol{d}(\phi, \theta)}. \tag{A.9}$$

The parameters $\boldsymbol{\Omega}_v = [\theta_v \ \phi_v]^{\mathrm{T}}$ of the EM-wave are given by

$$(\phi, \theta) = arg\left\{\max_{\phi,\theta} P_{\mathrm{MUSIC}}(\phi, \theta)\right\}, \tag{A.10}$$

where P_{MUSIC} is a second order function.

Appendix B

Vector antennas fundamental parameters

Contents

The aim of this appendix is to present various figures-of-merit that need to be analyzed to describe the performances of a VA such as the frequency bandwidth (Section B.1), the RP (Section B.2), the directivity (Section B.3), and the polarization (Section B.4). It can be noted that some parameters are intercorrelated. Besides, since the vector antenna is a multi-elements antenna, each element must satisfy the parameters described hereafter.

B.1 Frequency bandwidth

The frequency bandwidth of an antenna corresponds to the range of frequencies over which the antenna performances are optimal with respect to specific standards. These specifications are set out accordingly to a particular application. For DF, the performances of a VA are notably evaluated through its impedance and pattern bandwidths. Therefore, the resulting frequency bandwidth may be limited by either one or both of these bandwidths.

The impedance bandwidth is based on a criterion related to the antenna input impedance. It corresponds to the range of frequencies over which the antenna is matched with its transmission line. The Voltage Standing Wave Ratio (VSWR) describes how well the antenna is impedance matched to its transmission line and is expressed as follows

$$\mathrm{VSWR} = \frac{1 + |\Gamma|}{1 - |\Gamma|}, \tag{B.1}$$

where Γ is the reflection coefficient. It characterizes the relative fraction of the incident RF power that is reflected back due to the impedance mismatch and is expressed as

$$\Gamma = \frac{Z_{\mathrm{in}} - Z_0}{Z_{\mathrm{in}} + Z_0}, \tag{B.2}$$

where Z_{in} and Z_0 denote the antenna input impedance and characteristic impedance of the transmission line, respectively. In general, the antenna match is considered very good if $\mathrm{VSWR} \leqslant 2$ (or $|\Gamma| \leqslant \frac{1}{3}$), which corresponds to a reflection of about 11% of input power. Indeed, the

reflected power is given in percent by

$$\text{Reflected Power } (\%) = 100|\Gamma|^2. \tag{B.3}$$

The pattern bandwidth is based on criteria related to gain, directivity and polarization. Since these parameters can be frequency dependent, it corresponds to the range of frequencies over which they remain relatively stable with respect to acceptable variations. These parameters are described hereafter.

On another note, the frequency bandwidth of a wideband antenna is usually expressed as the ratio of the upper to lower frequencies of acceptable performance.

B.2 Radiation pattern

A RP describes the spatial distribution of the EM-field radiated or received by an antenna. In other words, it corresponds to the field of view of an antenna. Therefore, the RP is a key aspect of a DF antenna since it defines the angular coverage over which it is possible to estimate the DoA of an incoming EM-wave.

Most often, the RP is determined in the far-field region (also called Fraunhofer region), which is defined for a distance r from the source greater than $2D^2/\lambda$ (with λ the wavelength and D the largest dimension of the antenna). In this region, the angular field distribution is practically independent of the distance from the antenna. Thus, the far-field RP of an antenna is a function of the spatial coordinates which are specified by the azimuth angle ϕ and the elevation angle θ.

There are several ways to represent the spatial distribution of the EM-field. It can be simply described by a plot of the magnitude of the electric field (or magnetic field) expressed in V.m^{-1} (or A.m^{-1}) as a function of the spatial coordinates. However, it is convenient to plot the normalized far-field pattern given by

$$f(\phi, \theta) = \frac{\|E(\phi, \theta)\|}{\|E\|_{\max}}. \tag{B.4}$$

Hence, the maximum value is unity. Besides, since the EM-field of the propagating wave decreases by $1/r$, it is more convenient to represent the spatial distribution of the EM-field using the radiation intensity. This corresponds to the power radiated or received in a given direction per unit solid angle and is expressed as follows

$$U(\theta, \phi) = \frac{1}{2}\mathfrak{Re}\left\{\boldsymbol{E} \times \boldsymbol{H}^*\right\}.r^2\boldsymbol{r} = S(\theta, \phi)r^2, \tag{B.5}$$

where S denotes the time average Poynting vector (average power density). The use of the radiation intensity presents the advantage to provide a physical value that is independent of r.

In practice, the RP of a linearly polarized antenna is described in terms of its E-plane and H-plane patterns. These planes correspond respectively to the planes containing the electric or magnetic field vector and the direction of maximum radiation. Besides, these planes are orthogonal.

On another note, an isotropic antenna presents the most extensive field of view for an antenna because it radiates or receives an EM-field uniformly in all directions. However, an isotropic antenna is purely theoretical and does not exist in practice since EM-waves are transverse.

However, there is a way to achieve isotropic coverage using the six-elements VA. Indeed, the EM-field may be separately measured by each element and digitally recombined to create an isotropic antenna.

B.3 Directivity, gain and efficiency

The directivity D of an antenna is equal to the ratio of its radiation intensity in a given direction to the radiation intensity averaged over all directions. It corresponds to the radiation intensity U_{iso} that an isotropic antenna would radiate over all directions with the same total power density P_{rad}, that gives

$$D(\theta, \phi) = \frac{U(\theta, \phi)}{U_{\text{iso}}} = \frac{4\pi U(\theta, \phi)}{P_{\text{rad}}}. \tag{B.6}$$

As its name suggests, the directivity of an antenna gives an indication of the directive properties of an antenna by comparing the radiation intensity at a given direction to that of an isotropic antenna. In practice, directivity is expressed in decibels (dBi) using

$$D_{\text{dBi}}(\theta, \phi) = 10 \log D(\theta, \phi) \tag{B.7}$$

instead of a dimensionless quantity. The letter i is used in reference to an isotropic antenna.

Although the directivity of an antenna is a useful parameter for describing the performances of an antenna, it depends only on the RP. On the other hand, the gain of an antenna which is closely related to the directivity takes into account the fact that some of the input power is actually lost on the antenna itself (dielectric, conduction, and ohmic losses) as well as its directive properties. In other words, it describes how efficiently the antenna transforms the available power at its input port into a radiated power in a specific direction. Therefore, the gain G is defined as the ratio of the radiation intensity in a given direction to that of an isotropic antenna given the same accepted power input P_{in}, or

$$G(\theta, \phi) = \frac{4\pi U(\theta, \phi)}{P_{\text{in}}}. \tag{B.8}$$

Similar to the directivity, the gain is usually expressed in decibels (dBi) using

$$G_{\text{dBi}}(\theta, \phi) = 10 \log G(\theta, \phi). \tag{B.9}$$

It follows from Eq. B.6 and Eq. B.8 that the radiation efficiency of an antenna can be calculated as

$$\eta_r(\theta, \phi) = \frac{G(\theta, \phi)}{D(\phi, \theta)} = \frac{P_{\text{rad}}}{P_{\text{in}}}, \tag{B.10}$$

which takes into account the dielectric, conduction, and ohmic losses within its structure. Radiation efficiency is commonly quoted in percentage and should be as close as possible to 100%. Other losses can reduce the efficiency of an antenna. They correspond to the losses introduced by the impedance mismatch between the antenna and its transmission line, which are characterized by the mismatch efficiency

$$\eta_m = (1 - |\Gamma|^2). \tag{B.11}$$

Thus, the total efficiency of the antenna is given by

$$\eta(\theta, \phi) = \eta_r(\theta, \phi)\eta_m. \tag{B.12}$$

In practice, the effect of the impedance mismatch is also considered to describe the gain of an antenna by defining the realized gain as

$$\mathrm{RG}(\theta, \phi) = \eta_m G(\theta, \phi). \tag{B.13}$$

B.4 Polarization

The polarization of an EM-wave describes the time-varying direction and magnitude of the electric field vector. In other words, it corresponds to the figure that the electric field traces out with time while propagating at a fixed observation point. Thus, the polarization state of an EM-wave is defined from the observation of the electric field along the direction.

The polarization of an antenna corresponds to the polarization of the EM-wave radiated in a given direction by the antenna. If the direction is not specified, the polarization is conveniently determined by the one in the maximum gain direction. In practice, the polarization state of the EM-wave radiated by an antenna is specified at a point in the far-field region. In this region, a local plane wave can be used to describe this EM-wave. Therefore, the polarization of the EM-wave radiated by the antenna corresponds to the polarization of the plane wave at that point.

The polarization can be classified as linear, circular or elliptical. The elliptical polarization corresponds to the general case. Moreover, the polarization state of an EM-wave is described by Eq. 1.1.

Appendix C

The three-element vector antenna

Contents

The aim of this appendix is first to establish the observation model of an ideal VA that enables the measurement of the components E_z, H_x and H_y of incoming EM-waves (Section C.1), then make some comments thereon (Section C.2).

C.1 Observation model of the three-element vector antenna

Some particular VAs are not able to measure the six components of the incoming EM-wave but only three. A typical example is the grounded VA that enables only the measurement of the components E_z , H_x and H_y (see, e.g, the third and fourth VAs shown in Table 1.6 [14, 66]). In the section that follows, the observation model of a VA that enables only the measurement of these three components is described. As a reminder, since each element of the VA is a short electric or magnetic dipole, the output voltage $\{e_z\}$ or $\{h_i\}_{i=x,y}$ from each dipole is proportional to the electric field or magnetic field component along the dipole. According to Eq. 2.5, the steering vector of the three-element VA is expressed as follows

$$\boldsymbol{d}(\phi,\theta,\gamma,\eta) = \begin{bmatrix} e_z \\ h_x \\ h_y \end{bmatrix} = \begin{bmatrix} -\sin(\theta) & 0 \\ -\sin(\phi) & -\cos(\phi)\cos(\theta) \\ \cos(\phi) & -\sin(\phi)\cos(\theta) \end{bmatrix} \begin{bmatrix} \sin\gamma e^{j\eta} \\ \cos(\gamma) \end{bmatrix}. \tag{C.1}$$

Considering the same scenario as the one drawn in Section 2.1.4.1, the output voltage $\boldsymbol{x} \in \mathbb{C}^{3,1}$ received at time t through the three-element VA can be written as follows

$$\boldsymbol{x}(t) = \boldsymbol{D}(\boldsymbol{\Omega}).\boldsymbol{s}(t) + \boldsymbol{n}(t), \tag{C.2}$$

where $\boldsymbol{D}(\boldsymbol{\Omega}) = [\boldsymbol{d}(\boldsymbol{\Omega}_1)\dots\boldsymbol{d}(\boldsymbol{\Omega}_v)\dots\boldsymbol{d}(\boldsymbol{\Omega}_V)] \in \mathbb{C}^{3,V}$ is the VA response to the V incident EM-waves characterized by $\boldsymbol{\Omega}_v = [\theta_v\ \phi_v\ \eta_v\ \gamma_v]^{\mathrm{T}}$. In Eq. C.2, $\boldsymbol{s} \in \mathbb{C}^{V,1}$ and $\boldsymbol{n} \in \mathbb{C}^{3,1}$ are the signal vector associated with these incoming EM-waves (i.e., the amplitude and phase of each signal) and the additive white Gaussian noise, respectively. The noise is assumed spatially invariant with zero-mean and covariance matrix $\mathbf{R}_{\boldsymbol{n}} = \sigma_n^2\boldsymbol{I} \in \mathbb{C}^{3,3}$.

C.2 Remarks

Depending on the polarization of the incident EM-wave, the expression of the steering vector associated to the three-element VA can be simplified and some interesting comments can be formulated. Let us consider that the incoming EM-wave is vertically-polarized ($\gamma = 90°$, $\eta = 0°$). Therefore Eq. C.1 is simplified as follows

$$\boldsymbol{d}(\phi, \theta, 90°, 0°) = \begin{bmatrix} -\sin(\theta) \\ -\sin(\phi) \\ \cos(\phi) \end{bmatrix}. \tag{C.3}$$

According to Eq. C.3, the variations of the components of $\boldsymbol{d}$ are separable in θ and ϕ. Indeed, while the z-component of the electric field depends only on the elevation angle θ, the x-component and y-component of the magnetic field are function of of the azimuth angle ϕ. Hence, the DoA of the incoming EM-wave can be derived easily as follows [74]

$$\begin{aligned} &\phi = \tan^{-1}\left(\frac{H_y}{H_x}\right) \text{ if } H_x \text{ and } E_z \text{ are in phase,} \\ &\phi = \tan^{-1}\left(\frac{H_y}{H_x}\right) + \frac{\pi}{2} \text{ if } H_x \text{ and } E_z \text{ are in phase opposition,} \\ &\theta = \sin^{-1}\left(\frac{|E_z|}{\sqrt{(H_x^2 + H_y^2)\zeta}}\right). \end{aligned} \tag{C.4}$$

From Eq. C.4, the estimation of the azimuth angle ϕ depends only on the RPs of the magnetic dipoles whereas the estimation of the elevation angle θ depends mostly on the RP of the electric dipole.

Let us consider that the incoming EM-wave is horizontally-polarized ($\gamma = 0°$, $\eta = 0°$). Therefore, Eq. C.1 is simplified as follows

$$\boldsymbol{d}(\phi, \theta, 0°, 0°) = \begin{bmatrix} 0 \\ -\cos(\phi)\cos(\theta) \\ -\sin(\phi)\cos(\theta) \end{bmatrix}. \tag{C.5}$$

According to Eq. C.5, only the two components of the magnetic field vary in function of θ and ϕ since the component of the electric field zero regardless of the DoA of the incoming EM-wave. In addition, they exhibit the same variation in θ. As a consequence, the elevation angle θ cannot be estimated. The angular coverage is thus limited.

Appendix D

Study of one of the constitutive semi-circular arrays of the Two Season vector antenna

Contents

The aim of this appendix is first to analyze the impact of some parameters of the semi-circular arrays that constitute the Two Season VA upon the bandwidth (Section D.1), and then to provide an overview of its electrical performances (Section D.2) when used as a magnetic dipole. In this appendix, only one of the semi-circular arrays constituting the Two Season VA is taken into account, and this one is mounted on an infinite ground plane.

D.1 Parametric studies

Parametric studies on the opening rate R (defined in Eq. 2.21), w_1, l_2 and r_c are carried out through full-wave EM simulations. Main interests are to simultaneously maximize the bandwidth, minimize the lower frequency of operation f_L, and limit the mid-band amplitude of the VSWR. Although interesting to observe, the higher operating frequency is mainly determined by the undesirable emergence of grating lobes leading to omnidirectionality defects and is therefore not considered as a selection criterion. Only one parameter is varied at a time while the other parameters (summarized in Table 2.1) are fixed.

The simulated VSWR at port 1 of the semi-circular array of Vivaldi antennas (depicted in Fig. 2.21) is shown in Fig. D.1 for different opening rate R values, varying from 100 mm^{-1} to 120 mm^{-1} with a 10 mm^{-1} step. Furthermore, only the VSWR at port 1 is plotted for symmetry reasons. It can be seen that f_L decreases as R increases. However, the mid-band amplitude of the VSWR also increases with R. Hence, an opening rate R of 110 mm^{-1} is chosen for the following studies in order to provide a good trade-off between f_L and the amplitude of the VSWR at the central frequency.

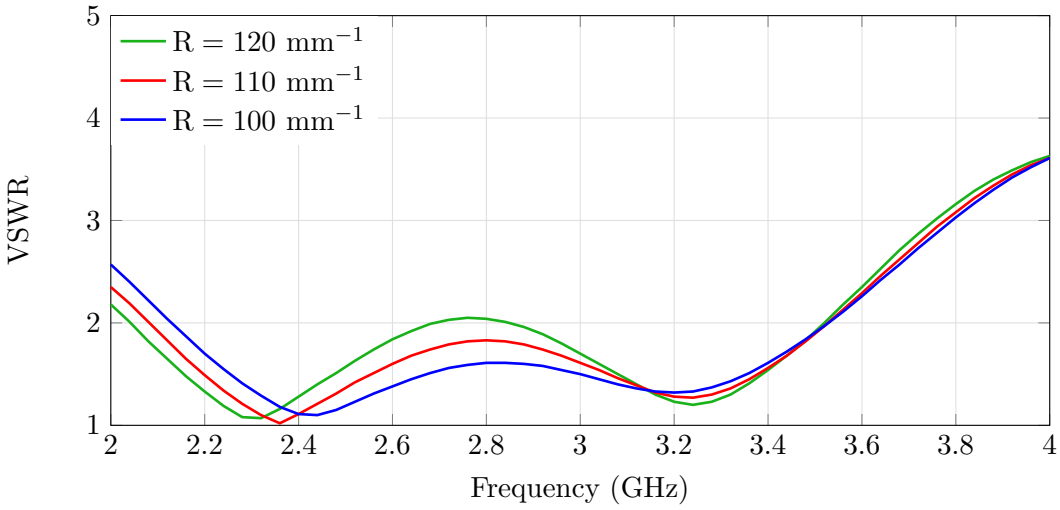

Figure D.1: Simulated VSWR of the semi-circular array used for designing the Two Season VA with different opening rate R

In the same vein, Fig. D.2 presents the simulated VSWR of the antenna when the aperture width w_1 of the Vivaldi antennas constituting the array is swept from 41.3 mm to 46.3 mm with a 2.5 mm step. On one hand, it can be observed that f_L decreases with w_1. On the other hand, the wider the aperture, the smaller the mid-band amplitude of the VSWR. As a consequence, the aperture width is kept to 43.8 mm.

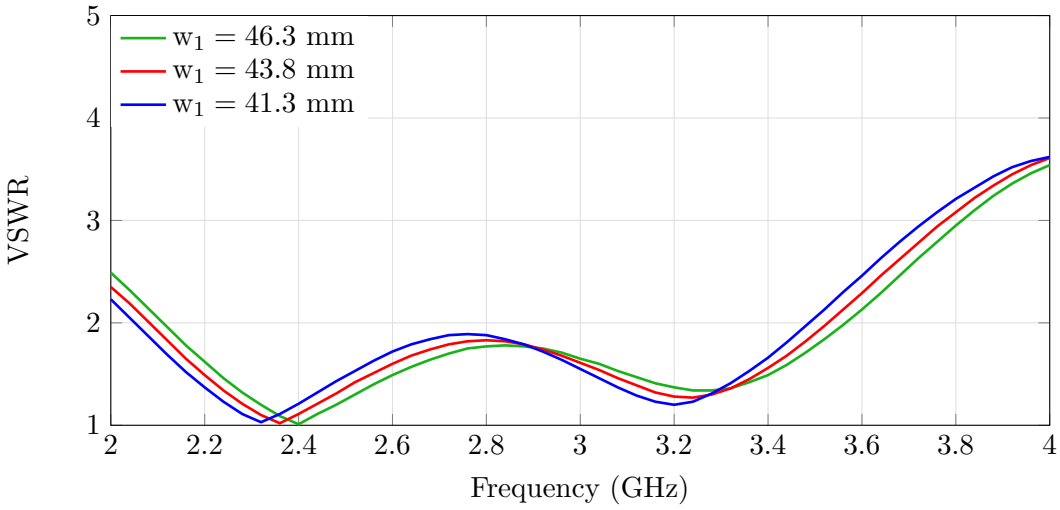

Figure D.2: Simulated VSWR of the semi-circular array used for designing the Two Season VA with different aperture width w_1

Turning now to the study of the parameter l_2 (or equivalently, to the study of the "length" l_1 of the taper profile of the Vivaldi antennas since the radius of the cavities is fixed). Fig. D.3 shows the simulated VSWR of the antenna for a range of l_2 values between 15 mm to 19 mm with a 2 mm step. As l_2 decreases, the length l_1 of the taper profile of the Vivaldi antennas increases, thus lowering f_L. Moreover, the variation of l_2 does not alter the amplitude of the VSWR in the mid-band. Hence, the parameter l_2 is set as small as possible, that is 15 mm, which allows

a little space for the feeding section.

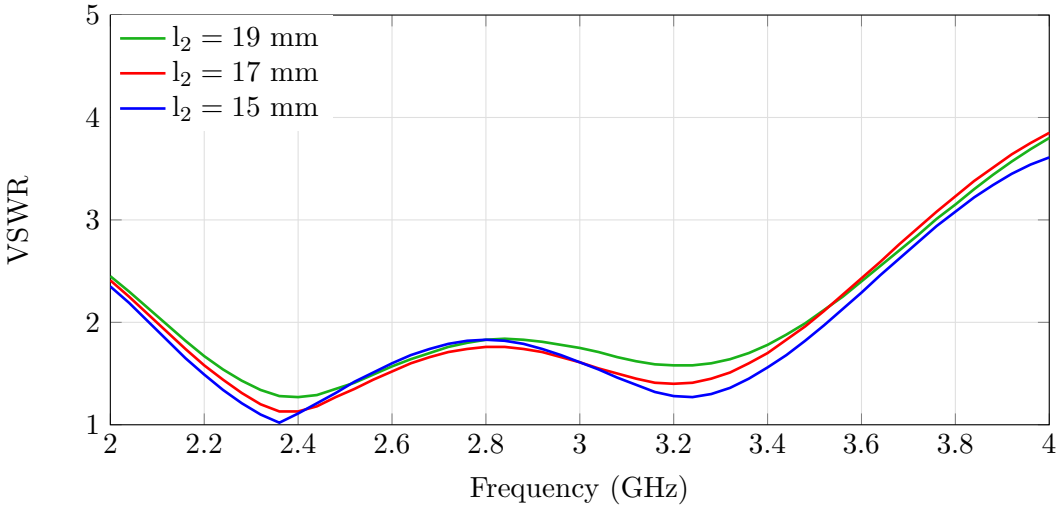

Figure D.3: Simulated VSWR of the semi-circular array used for designing the Two Season VA with different l_2

Finally, the last parameters studied are the radius of the cavity r_c and the radial stub r_s. Using $r_c = r_s$, the simulated VSWR is plotted in Fig. D.4 for different values of r_c, varying from 5 mm to 6 mm with a 0.5 mm step. It can be observed that the variation of r_c does not alter the amplitude of the VSWR in the mid-band. However, f_L decreases as r_c increases. Furthermore, r_c cannot exceed 5.5 mm due to the structural size limitations. Hence, the radius r_c is kept at 5.5 mm to facilitate the orthogonal crossing of two semi-circular arrays.

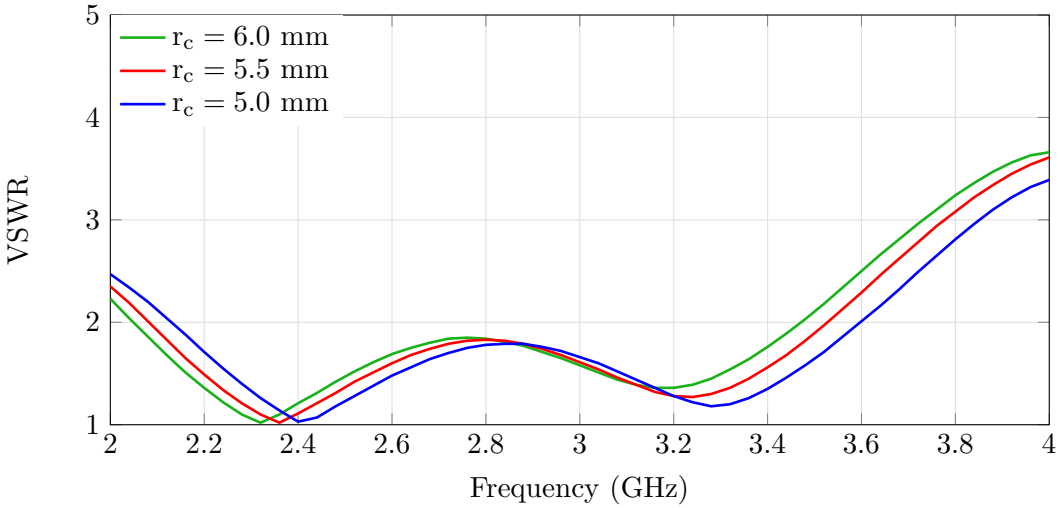

Figure D.4: Simulated VSWR of the semi-circular array used for designing the Two Season VA with different cavity radius r_c

D.2 Electrical performances

So far this appendix has focused on the impact of several parameters of the semi-circular array (which is used for designing the Two Season VA) upon its bandwidth. The final parameters of this array are given in Table 2.1. The following section will assess the electrical performances in terms of impedance matching and radiation properties when this semi-circular array is used as a magnetic dipole.

D.2.1 Impedance matching and mutual coupling

The simulated VSWR at port 1 of the semi-circular and the mutual coupling between port 1 and port 2 are shown in Fig. D.5 and Fig. D.6, respectively. It can be noted that an impedance bandwidth ratio of 1.70:1 from 2.08 GHz to 3.53 GHz is achieved (for a VSWR smaller than 2). Moreover, an excellent level of isolation is also obtained since the mutual coupling between the two ports does not exceed -20 dB over the operating bandwidth.

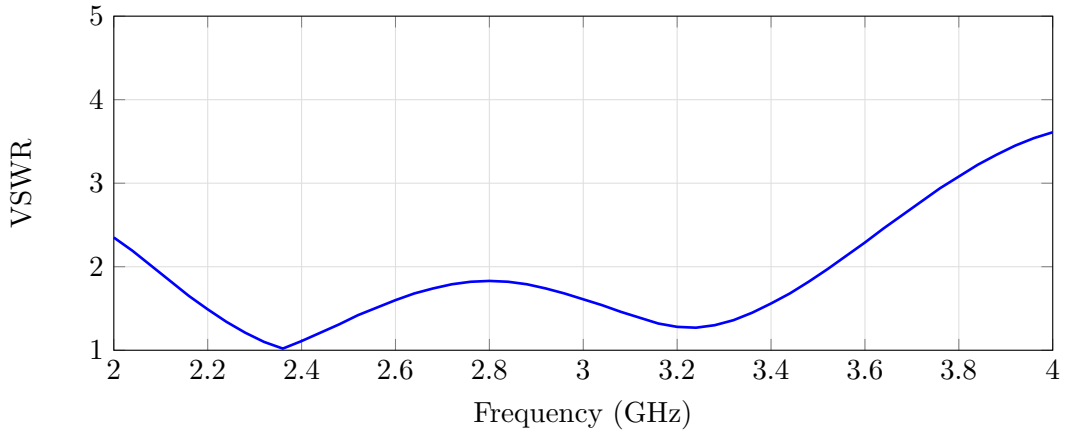

Figure D.5: Simulated VSWR of the semi-circular array used for designing the Two Season VA

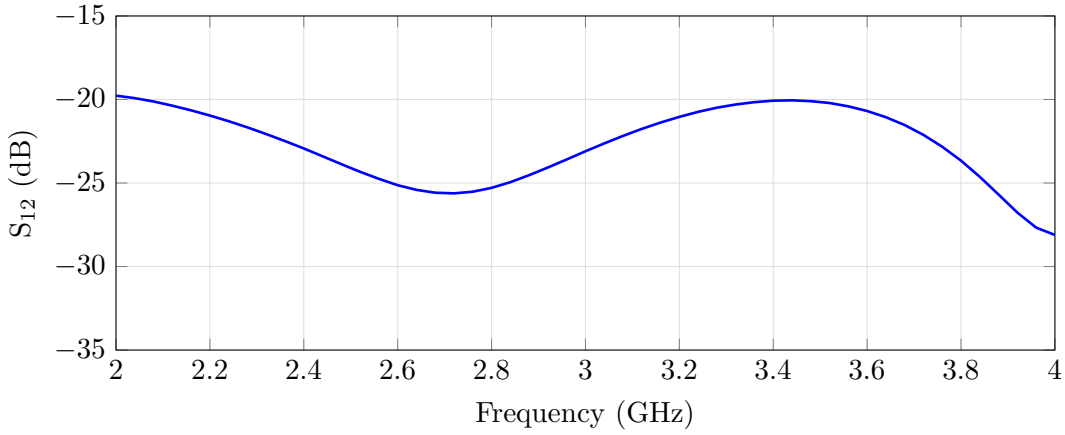

Figure D.6: Isolation at the ports of the semi-circular array used for designing the Two Season VA

D.2.2 Radiation patterns

Let us consider that the semi-circular is positioned at the center of the Cartesian coordinate system along the $\hat{x}$-axis, and a 180° phase differential is applied to its two feeding ports. Fig. D.8 presents the realized gain in the θ-polarization at 2.2 GHz, 2.8 GHz and 3.4 GHz, which approximatively are the lower, center and upper frequencies of the operating bandwidth. The RPs in Fig. D.8(a) and Fig. D.8(b) coincide to the ones of a wideband magnetic dipole oriented along the $\hat{y}$-axis in its E-plane (i.e., omnidirectional RP) and H-plane (i.e., 8-shape RP), respectively. As it can be observed in Fig. D.8(a), the RP is omnidirectional with horizontal polarization. However, in accordance with Chu's theory (see Section 2.5.1.1), there are some ripples arising as the frequency increases. The good omnidirectionality performance is confirmed through Fig. D.7 where the gain variation in the $\hat{yz}$-plane is plotted. As expected during the design process, the fluctuations are lower than 2 dB over the entire bandwidth. Finally, RPs at other operating frequencies across the bandwidth (not shown here for brevity) are similar to the ones plotted here.

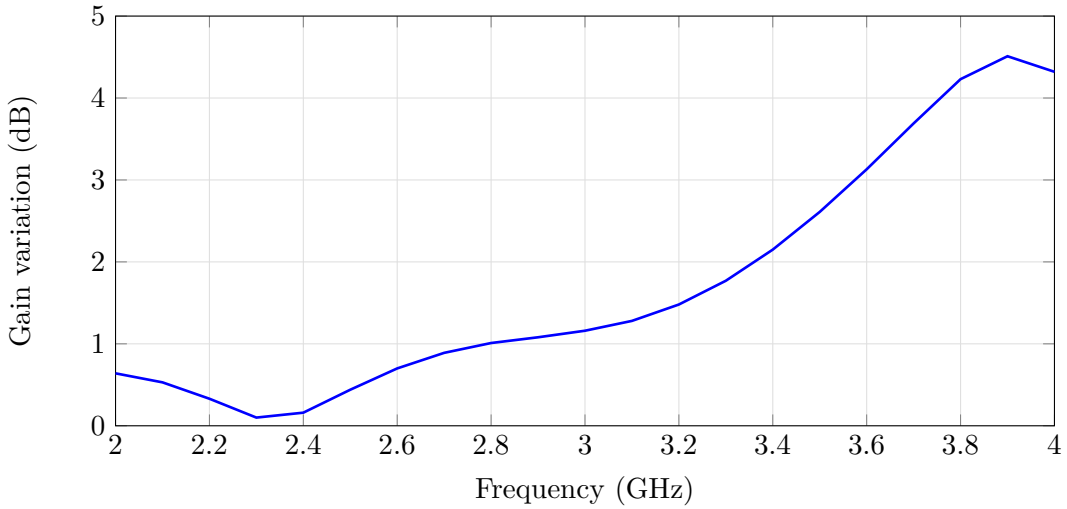

Figure D.7: Simulated gain variation in the $\hat{yz}$-plane of the semi-circular array when used as a magnetic dipole and mounted on an infinite ground plane

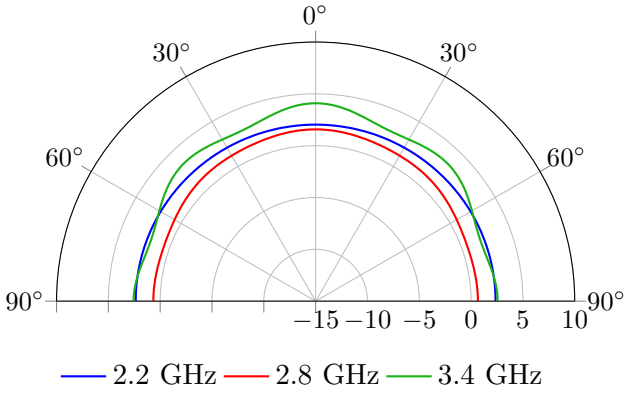

(a)

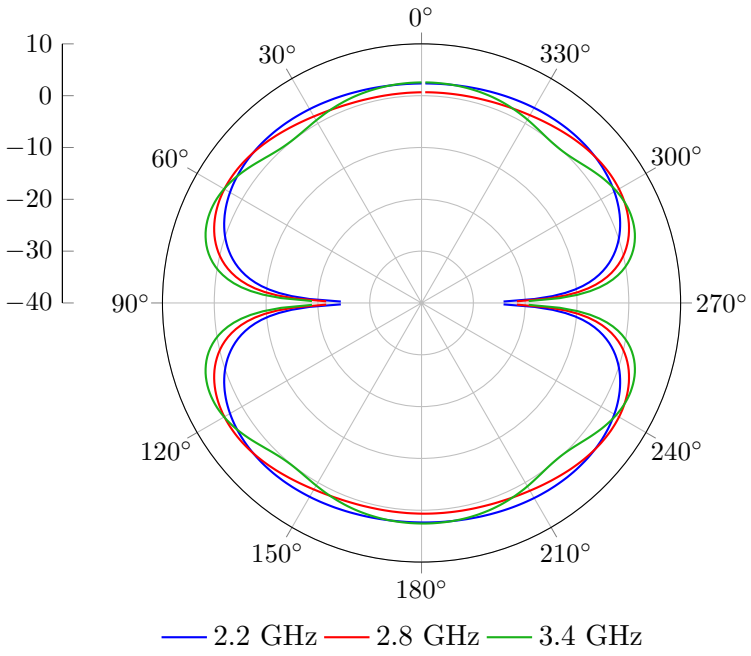

(b)

Figure D.8: Simulated realized gain in the θ-polarization of the semi-circular array when used as a magnetic dipole and mounted on an infinite ground plane at three frequencies across the bandwidth in the (a) $\hat{x}z$-plane, and (b) $\hat{x}y$-plane

Appendix E

LAAS-CNRS anechoic chamber

Contents

The aim of this appendix is first to present the anechoic chamber of the LAAS-CNRS used for the measurements performed during this Ph.D. work (Section E.1), and then provide some photographs of the prototypes (Section E.2).

E.1 Presentation

All the measurements performed during this Ph.D. work were carried out in the anechoic chamber of the LAAS-CNRS shown in Fig. E.1. Specifically, an anechoic chamber is an experimental room whose interior surfaces are covered with radiation absorbent materials that attenuate the reflections of EM-waves. Hence, an anechoic chamber reproduces the free-space radiation conditions, free-space meaning that there are no EM interferences. The LAAS-CNRS anechoic chamber is specified to operate in the frequency band from 1 GHz to 40 GHz.

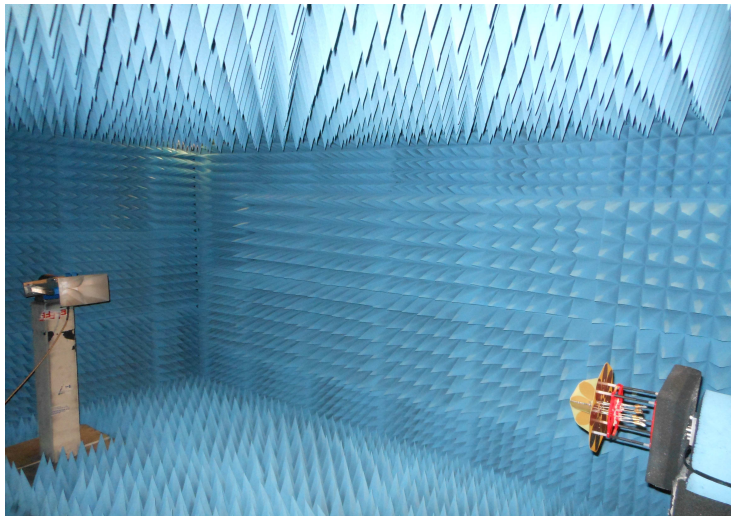

Figure E.1: Photograph of the LAAS-CNRS anechoic chamber

As depicted in Figure 1, there are two positioners located at the ends of the anechoic chamber and 3 meters apart. The first is used to fix the reference antenna and rotates 360° along the horizontal axis to specify the polarization of the measurement (see Fig. E.2(b)). The second is used to fixed the antenna under test (AUT) and rotates 360° along the horizontal axis and 180° along the vertical axis (see Fig. E.2(b)). Hence, the azimuth and elevation angles of the AUT can be varied as desired.

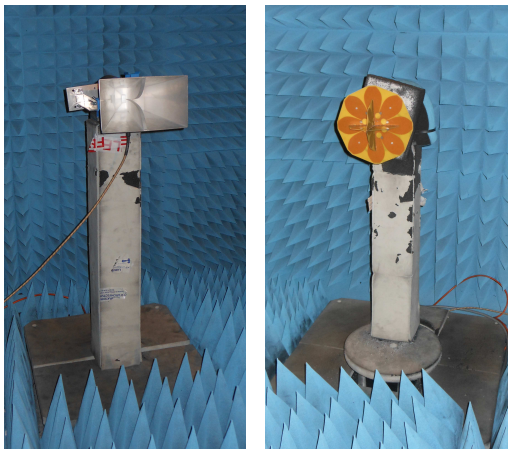

(a) (b)

Figure E.2: Photographs of (a) the reference antenna positioner, and (b) the AUT positioner

The gain of the AUT is measured using a gain comparison method, which consists of measuring the gain of this antenna relative to the power levels detected by the known reference antenna. The reference antenna used here is the Dorado horn antenna (see Fig. E.2(a)). This antenna operates from 1 GHz to 12 GHz. First, two Dorado antennas are mounted on the positioners and are aligned to present the same polarization. A thorough calibration is performed at bore-sight direction. Then, the AUT is mounted over the second positioner with extreme care to ensure the exact alignment. The relative power level is obtained from the Anristsu 37397D vector network

analyzer, and this enables the computation of the gain relative to the reference antenna. The gain of the standard reference is finally added to the relative gain to obtain the gain of the AUT. Basically, this method is based on the Friis transmission formula given in Eq. 1.14.

E.2 Photographs of the prototypes

Photographs of the Two Season VA and the Four Season VA taken at the time of their measurement are shown in Fig. E.3.

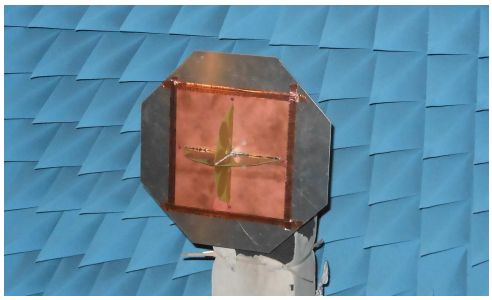

(a)

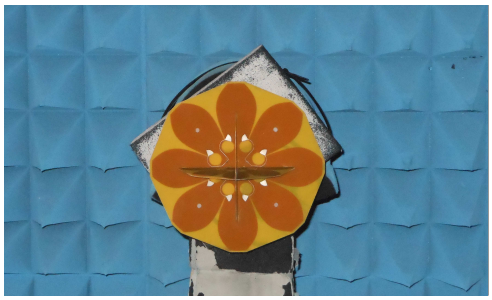

(b)

Figure E.3: Photographs of (a) the Two Season VA, and (b) the Four Season VA

Appendix F

The Two Season vector antenna: additional results

Contents

The aim of this appendix is to present additional results concerning the Two Season VA. First, the simulated RPs of RPC 0 that enable the measurement of the three components H_x, H_y and E_z of an incoming EM-wave are provided (Section F.1). Secondly, the measured RPs at each port while the other ports are impedance matched are shown (Section F.2). Thirdly, the simulated RPs associated to the 11 RPCs are set out (Section F.3). Finally, some DF performances results are given when RPC 4 is added to RPC 0 in the DoA estimation process (Section F.4).

F.1 Simulated radiation patterns used for the measurement of H_x, H_y and E_z

The simulated RPs of RPC 0 are displayed at three frequencies (2.2 GHz, 2.8 GHz, and 3.4 GHz, thus covering the entire VA bandwidth) in Fig. F.1 to Fig. F.3 and Fig. F.4 to Fig. F.6 when the Two Season VA is mounted either on the infinite ground plane or the finite octagonal ground plane, respectively. Therefore, the impact of the finite size ground plane on the RPs can be analyzed. As a reminder, RPC 0 corresponds to the RPs that enable the measurement of the three components H_x, H_y and E_z of an incoming EM-wave.

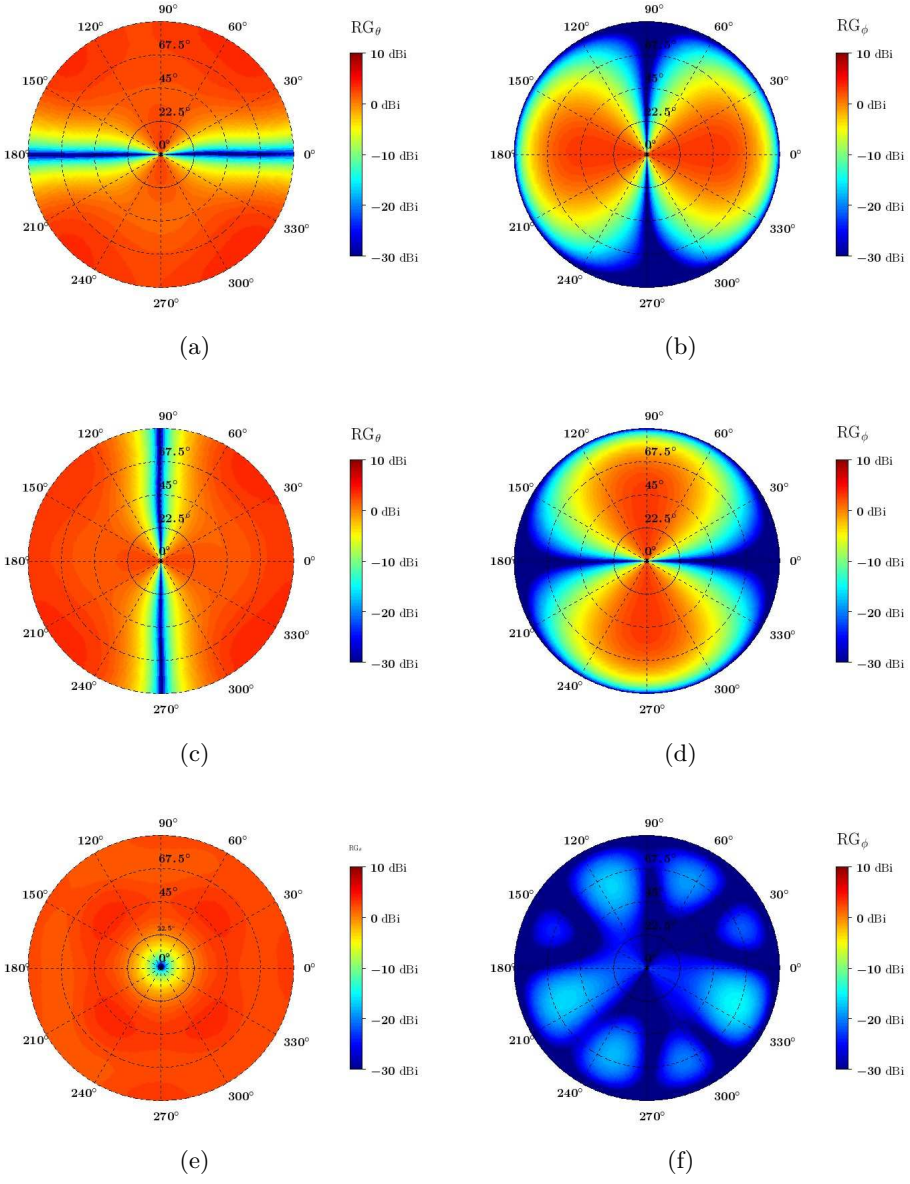

Figure F.1: Simulated realized gain in the θ-polarization (left figures) and ϕ-polarization (right figures) of the Two Season VA (mounted on an infinite ground plane) used for measuring the three components (RPC 0): (a) H_x, (b) H_y, and (c) E_z of the incoming EM-wave at 2.2 GHz.

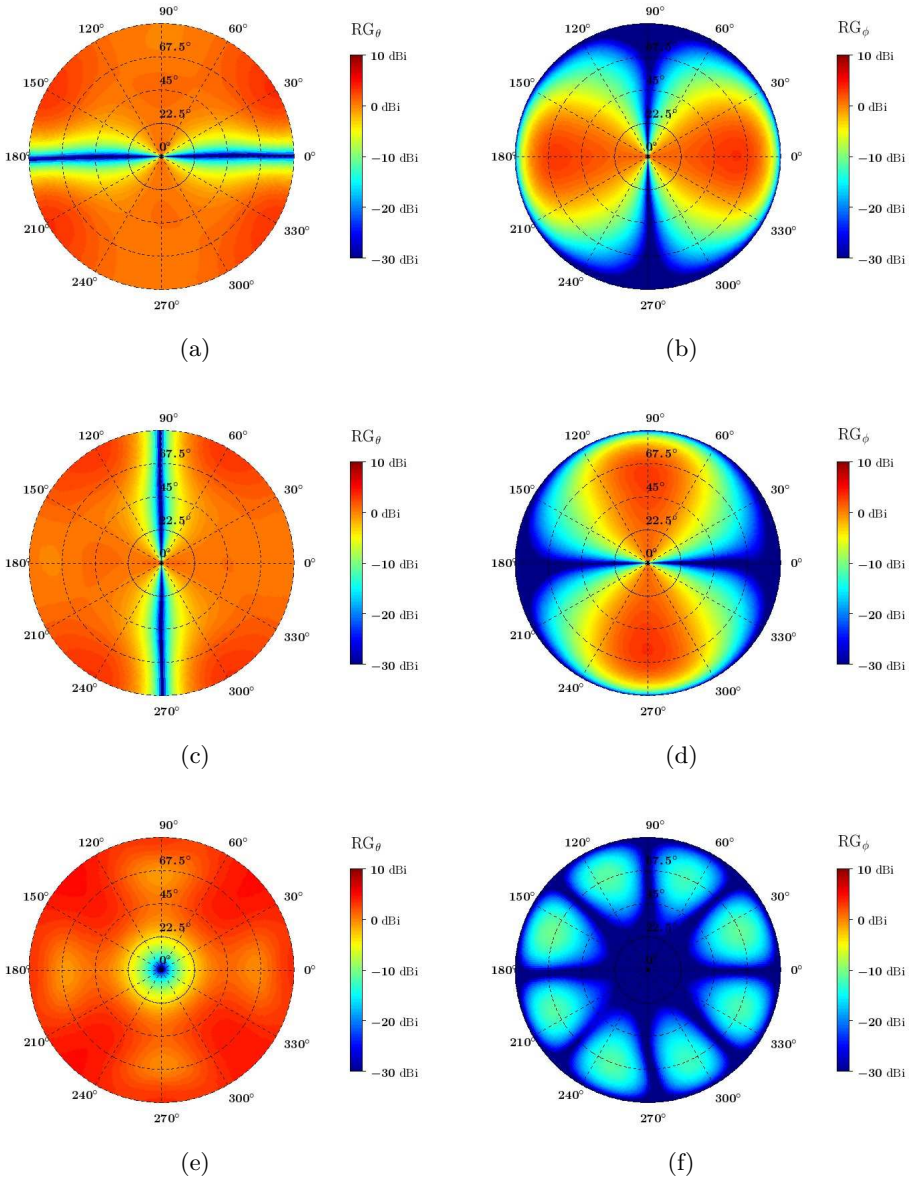

Figure F.2: Simulated realized gain in the θ-polarization (left figures) and ϕ-polarization (right figures) of the Two Season VA (mounted on an infinite ground plane) used for measuring the three components (RPC 0): (a) H_x, (b) H_y, and (c) E_z of the incoming EM-wave at 2.8 GHz.

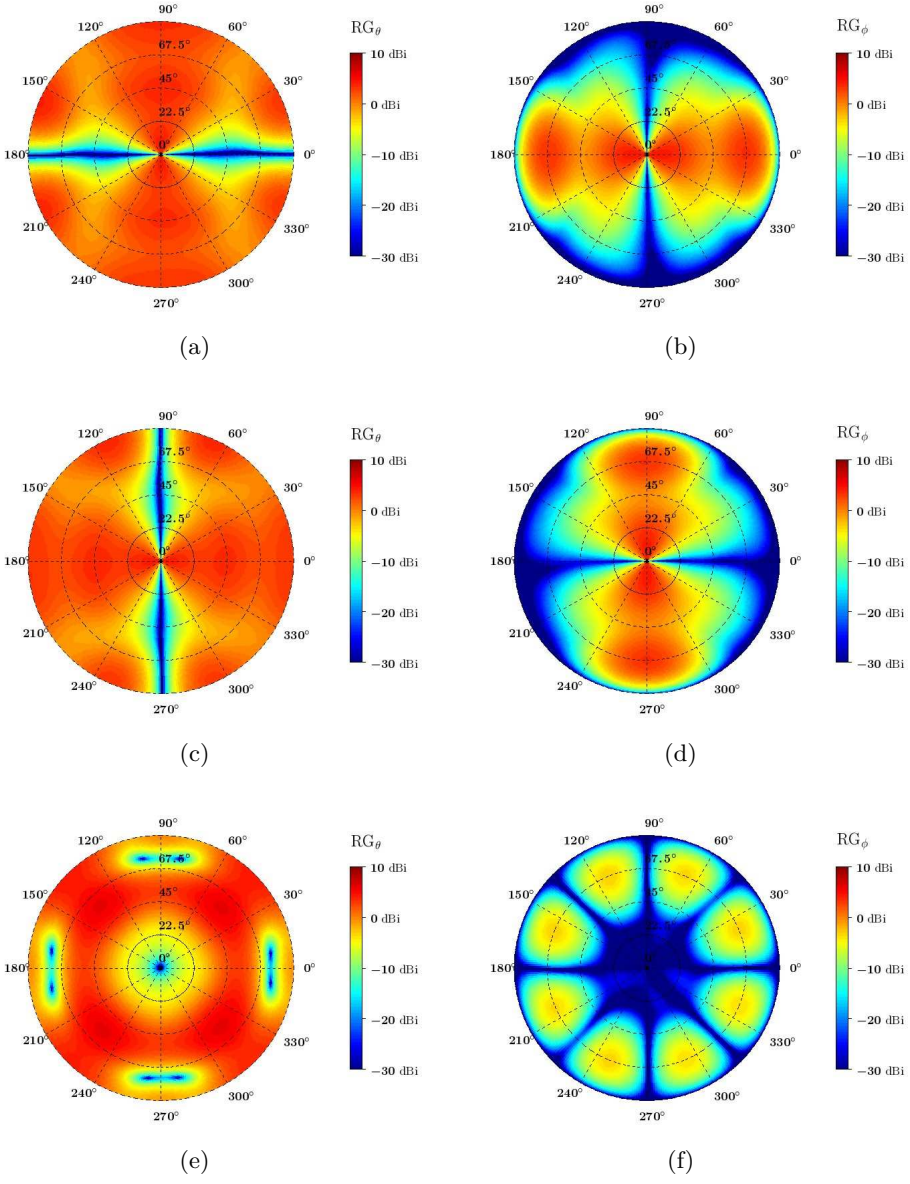

Figure F.3: Simulated realized gain in the θ-polarization (left figures) and ϕ-polarization (right figures) of the Two Season VA (mounted on an infinite ground plane) used for measuring the three components (RPC 0): (a) H_x, (b) H_y, and (c) E_z of the incoming EM-wave at 3.4 GHz.

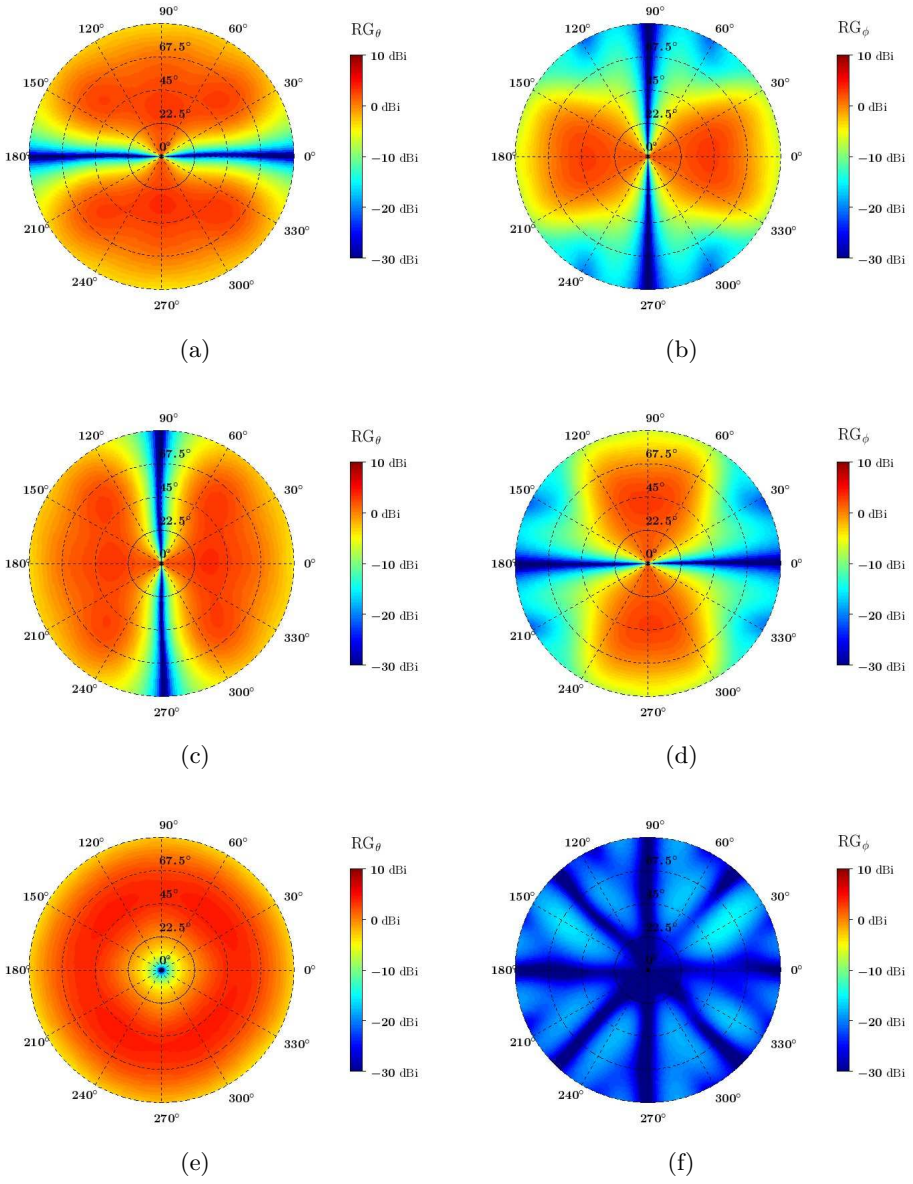

Figure F.4: Simulated realized gain in the θ-polarization (left figures) and ϕ-polarization (right figures) of the Two Season VA (mounted on the octagonal metallic support) used for measuring the three components (RPC 0): (a) H_x, (b) H_y, and (c) E_z of the incoming EM-wave at 2.2 GHz.

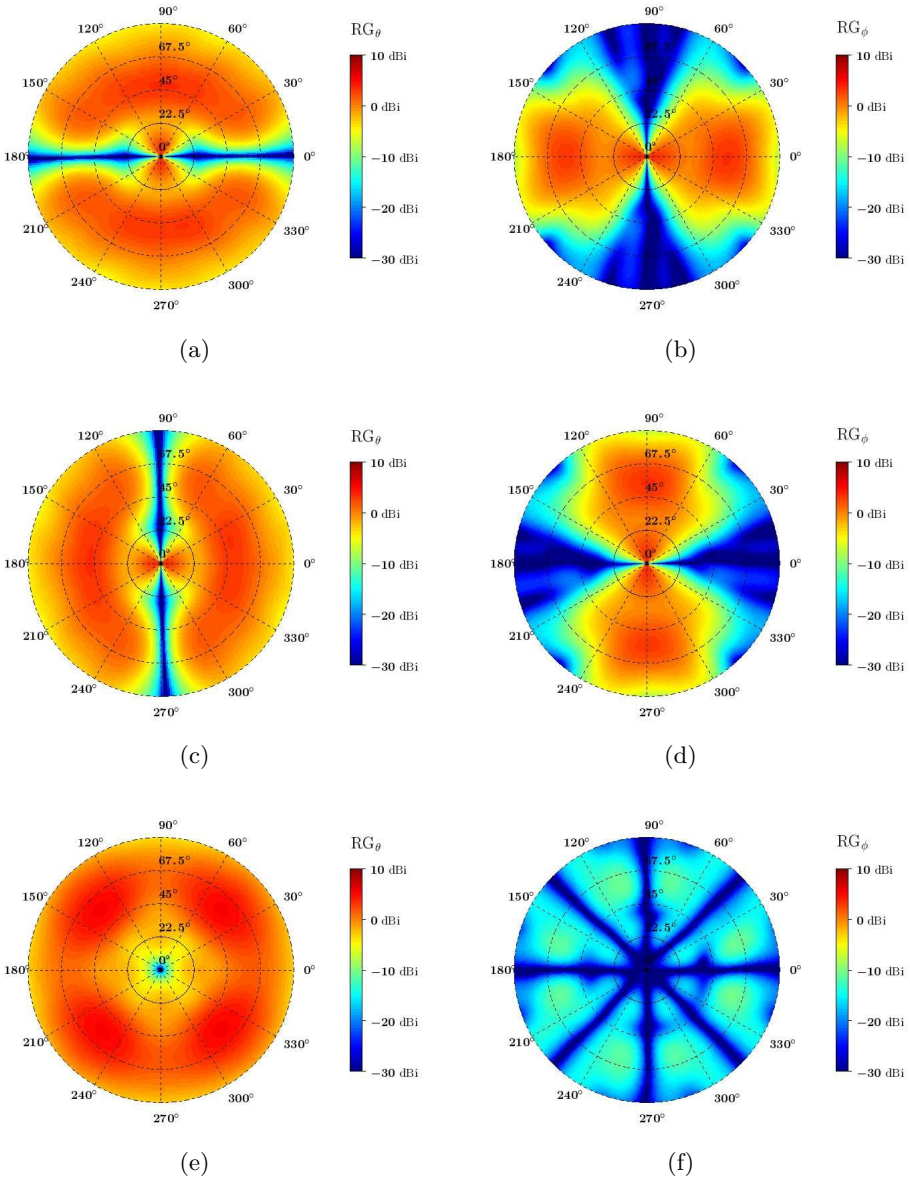

Figure F.5: Simulated realized gain in the θ-polarization (left figures) and ϕ-polarization (right figures) of the Two Season VA (mounted on the octagonal metallic support) used for measuring the three components (RPC 0): (a) H_x, (b) H_y, and (c) E_z of the incoming EM-wave at 2.8 GHz.

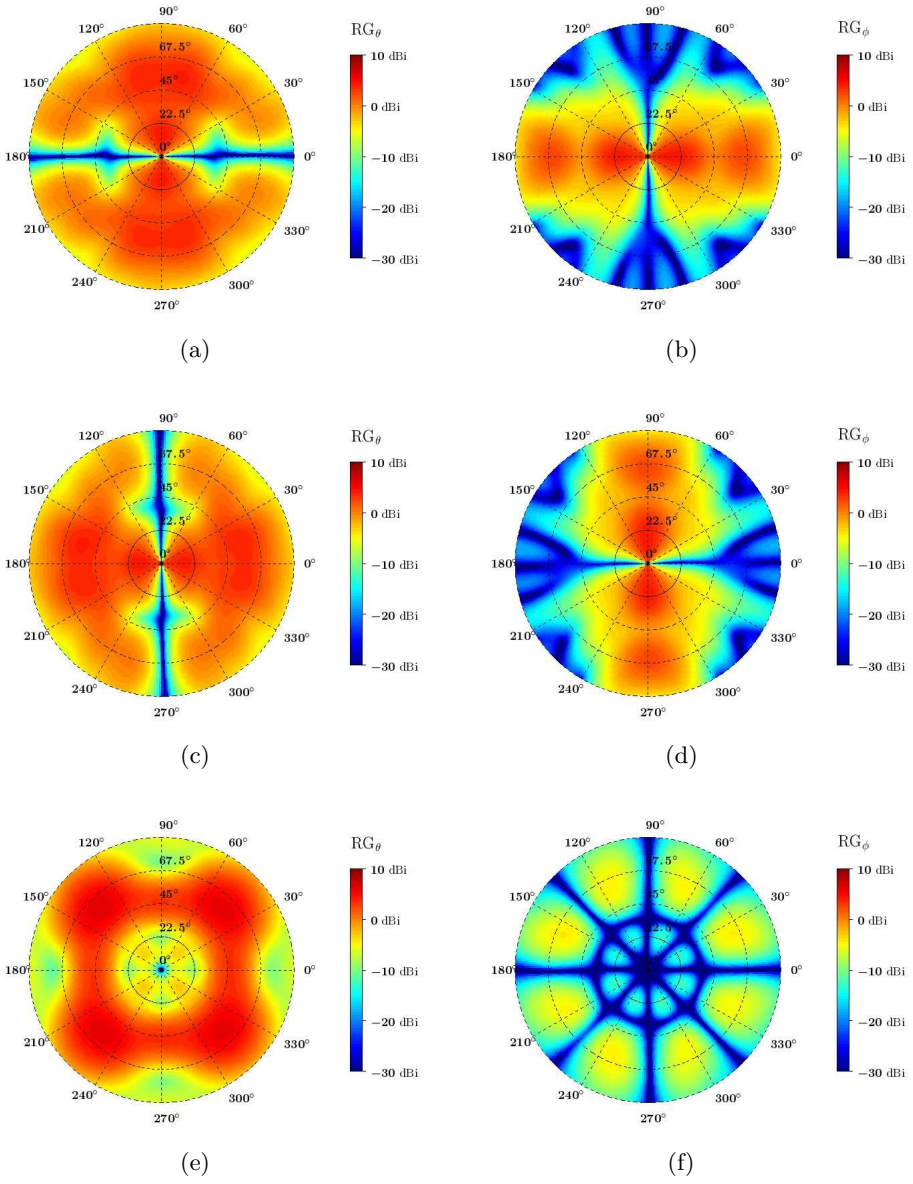

Figure F.6: Simulated realized gain in the θ-polarization (left figures) and ϕ-polarization (right figures) of the Two Season VA (mounted on the octagonal metallic support) used for measuring the three components (RPC 0): (a) H_x, (b) H_y, and (c) E_z of the incoming EM-wave at 3.4 GHz.

F.2 Measured radiation patterns

The RPs of each port of the Two Season VA were successively fed while the other ports were impedance matched, and four RPs (one pattern per port) were measured over the entire VA frequency band. For symmetry reasons, only the RPs in the θ-polarization and ϕ-polarization of port 1 are depiced in Fig. F.7 and Fig. F.8, respectively. Simulations results are also displayed for comparison purpose.

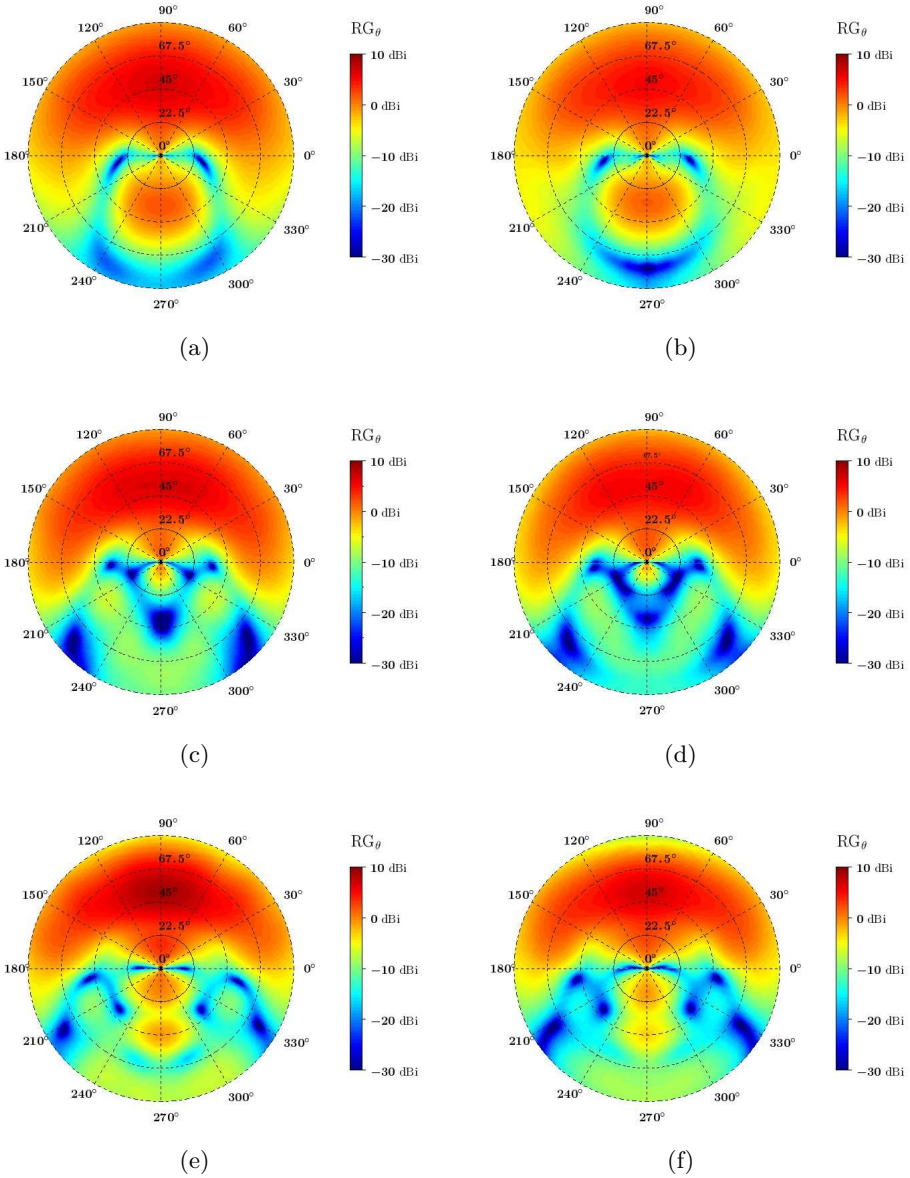

Figure F.7: Simulated (left figures) and measured (right figures) realized gain in the θ-polarization of port 1 of the Two Season VA (mounted on the octagonal metallic support) at the three following frequencies: (a) & (b) 2.2 GHz, (c) & (d) 2.8 GHz, and (e) & (f) 3.4 GHz.

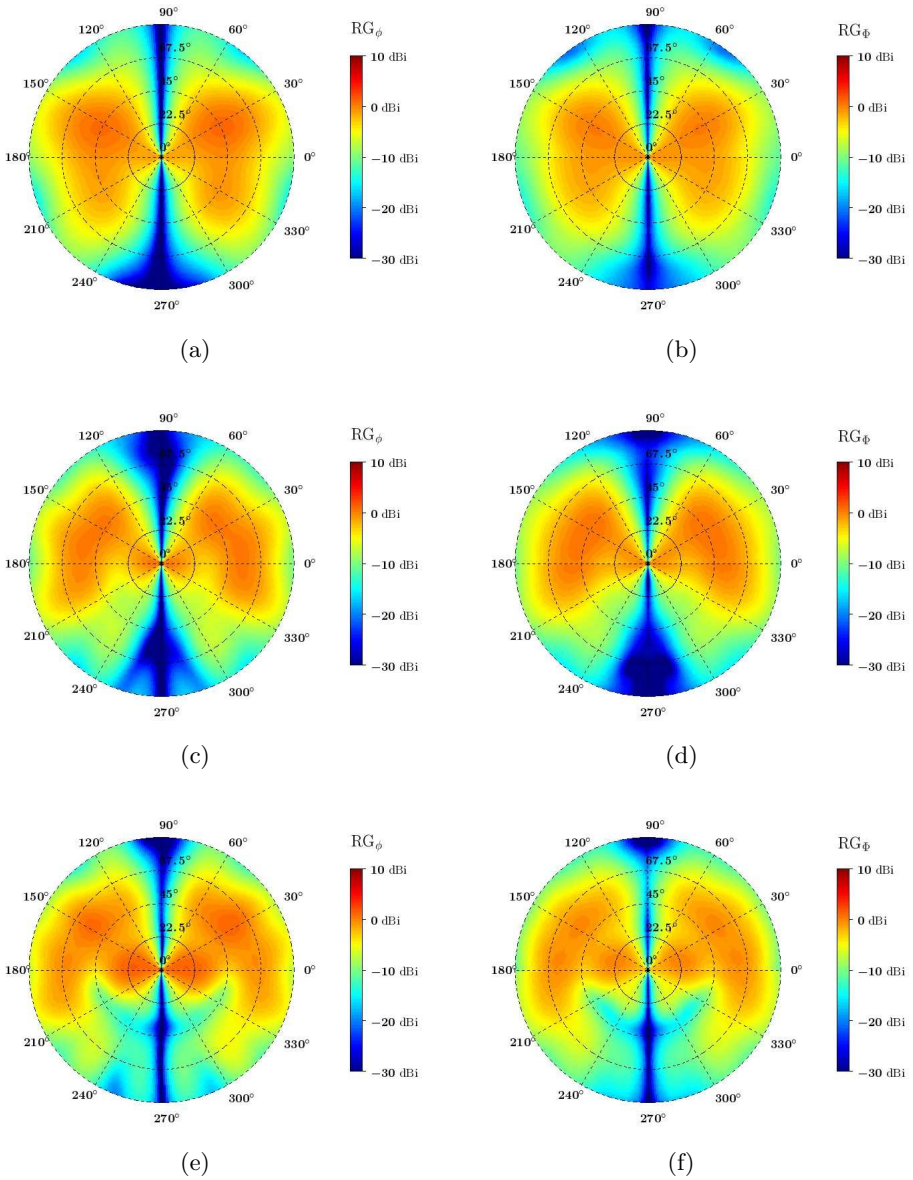

Figure F.8: Simulated (left figures) and measured (right figures) realized gain in the ϕ-polarization of port 1 of the Two Season VA (mounted on the octagonal metallic support) at the three following frequencies: (a) & (b) 2.2 GHz, (c) & (d) 2.8 GHz, and (e) & (f) 3.4 GHz.

F.3 Radiation patterns combinations

Fig. F.9 and Fig. F.10 presents the simulated RPs of the Two Season VA (mounted over the finite and octagonal metallic support) associated with the 11 RPCs at 3.4 GHz and in the θ-polarization and ϕ-direction, respectively. Only one RP by RPC is displayed since the RPs within a RPC exhibit a rotation symmetry of 90° in the azimuth plane. The RPs at 2.2 GHz and 2.8 GHz are similar to the ones displayed here, but are not provided for brevity.

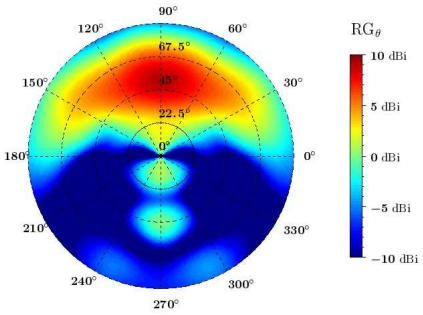
90°
120°
60°
67.5°
150°
45°
30°
22.5°
180°
0°
210°
330°
240°
300°
270°
RG$_\theta$
10 dBi
5 dBi
0 dBi
−5 dBi
−10 dBi

(a)

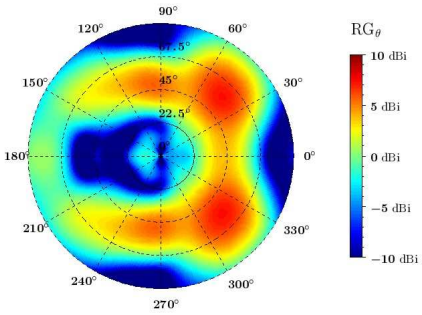
90°
120°
60°
67.5°
150°
45°
30°
22.5°
180°
0°
210°
330°
240°
300°
270°
RG$_\theta$
10 dBi
5 dBi
0 dBi
−5 dBi
−10 dBi

(b)

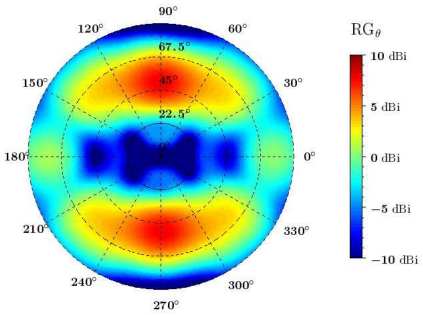
90°
120°
60°
67.5°
150°
45°
30°
22.5°
180°
0°
210°
330°
240°
300°
270°
RG$_\theta$
10 dBi
5 dBi
0 dBi
−5 dBi
−10 dBi

(c)

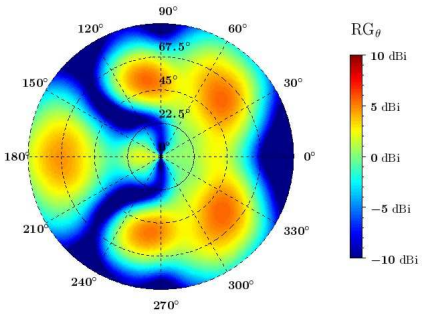
90°
120°
60°
67.5°
150°
45°
30°
22.5°
180°
0°
210°
330°
240°
300°
270°
RG$_\theta$
10 dBi
5 dBi
0 dBi
−5 dBi
−10 dBi

(d)

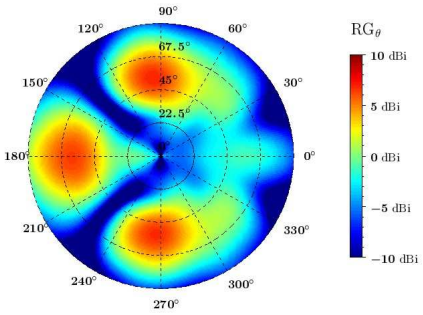
90°
120°
60°
67.5°
150°
45°
30°
22.5°
180°
0°
210°
330°
240°
300°
270°
RG$_\theta$
10 dBi
5 dBi
0 dBi
−5 dBi
−10 dBi

(e)

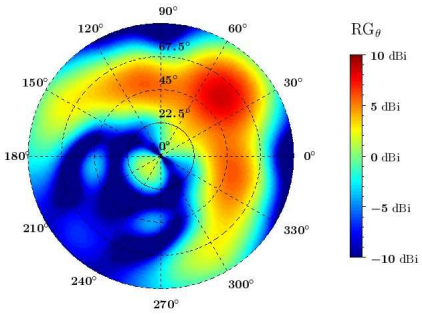
90°
120°
60°
67.5°
150°
45°
30°
22.5°
180°
0°
210°
330°
240°
300°
270°
RG$_\theta$
10 dBi
5 dBi
0 dBi
−5 dBi
−10 dBi

(f)

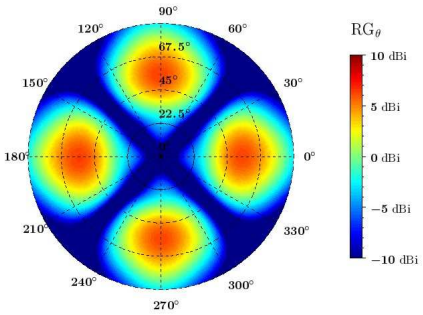
90°
120°
60°
67.5°
150°
45°
30°
22.5°
180°
0°
210°
330°
240°
300°
270°
RG$_\theta$
10 dBi
5 dBi
0 dBi
−5 dBi
−10 dBi

(g)

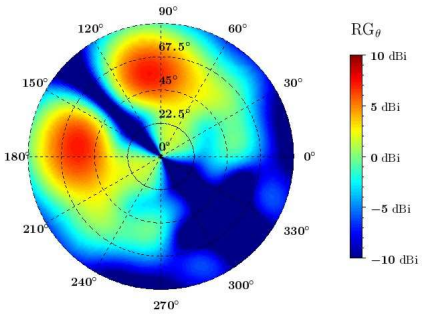
90°
120°
60°
67.5°
150°
45°
30°
22.5°
180°
0°
210°
330°
240°
300°
270°
RG$_\theta$
10 dBi
5 dBi
0 dBi
−5 dBi
−10 dBi

(h)

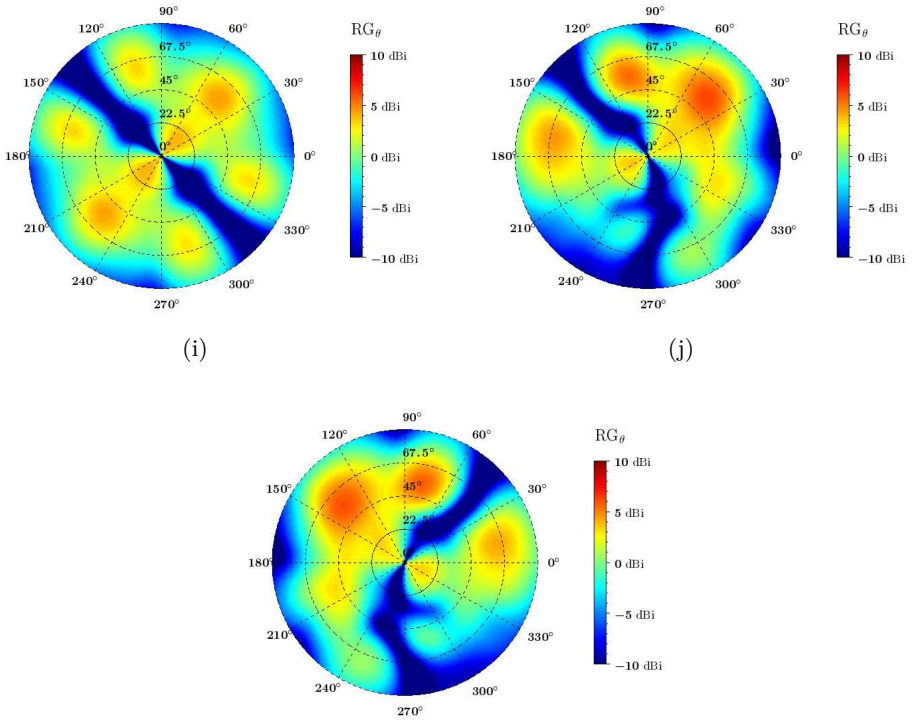

(i) (j)

(k)

Figure F.9: Simulated realized gain in the θ-polarization of the Two Season VA (mounted over the finite and octagonal metallic support) at 3.4 GHz associated with the first set of weighting coefficients of: (a) to (k) RPC 1 to RPC 11. Elevation angles θ are given on the radial axis and azimuth angles ϕ are given on the angular axis.

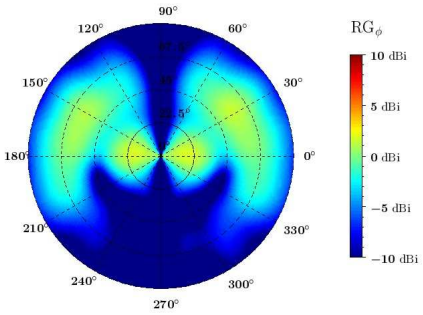
90°
120°
60°
150°
30°
180°
0°
210°
330°
240°
300°
270°
67.5°
45°
22.5°
0°
RG$_\phi$
10 dBi
5 dBi
0 dBi
−5 dBi
−10 dBi

(a)

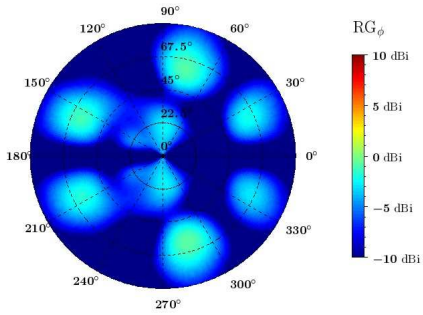
90°
120°
60°
150°
30°
180°
0°
210°
330°
240°
300°
270°
67.5°
45°
22.5°
0°
RG$_\phi$
10 dBi
5 dBi
0 dBi
−5 dBi
−10 dBi

(b)

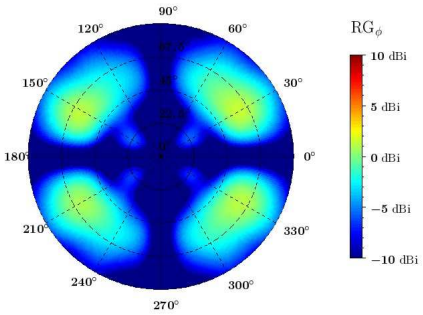
90°
120°
60°
150°
30°
180°
0°
210°
330°
240°
300°
270°
67.5°
45°
22.5°
0°
RG$_\phi$
10 dBi
5 dBi
0 dBi
−5 dBi
−10 dBi

(c)

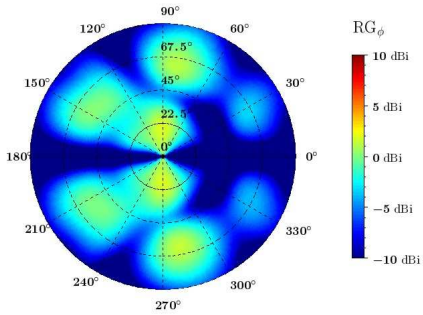
90°
120°
60°
150°
30°
180°
0°
210°
330°
240°
300°
270°
67.5°
45°
22.5°
0°
RG$_\phi$
10 dBi
5 dBi
0 dBi
−5 dBi
−10 dBi

(d)

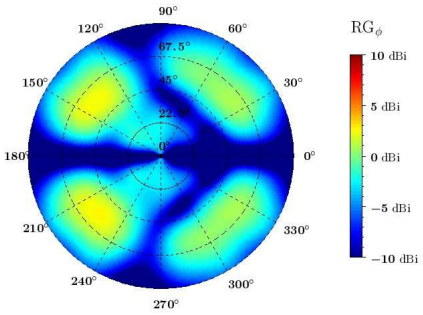
90°
120°
60°
150°
30°
180°
0°
210°
330°
240°
300°
270°
67.5°
45°
22.5°
0°
RG$_\phi$
10 dBi
5 dBi
0 dBi
−5 dBi
−10 dBi

(e)

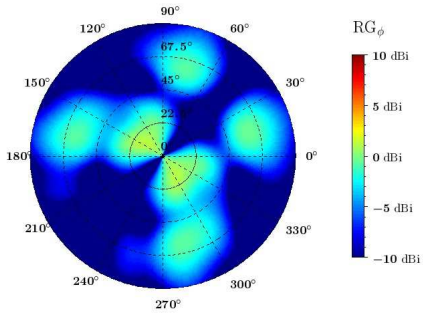
90°
120°
60°
150°
30°
180°
0°
210°
330°
240°
300°
270°
67.5°
45°
22.5°
0°
RG$_\phi$
10 dBi
5 dBi
0 dBi
−5 dBi
−10 dBi

(f)

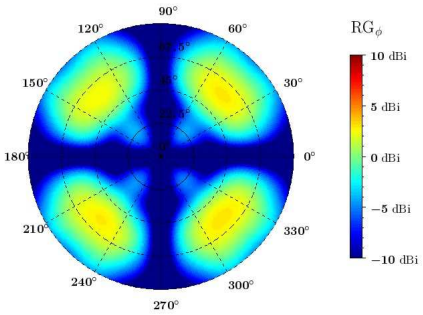
90°
120°
60°
150°
30°
180°
0°
210°
330°
240°
300°
270°
67.5°
45°
22.5°
0°
RG$_\phi$
10 dBi
5 dBi
0 dBi
−5 dBi
−10 dBi

(g)

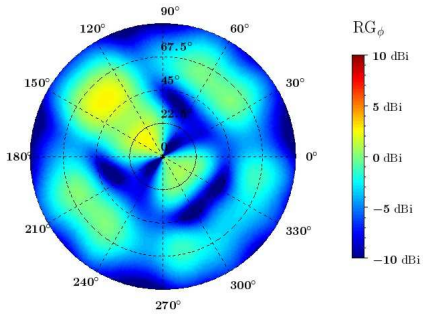
90°
120°
60°
150°
30°
180°
0°
210°
330°
240°
300°
270°
67.5°
45°
22.5°
0°
RG$_\phi$
10 dBi
5 dBi
0 dBi
−5 dBi
−10 dBi

(h)

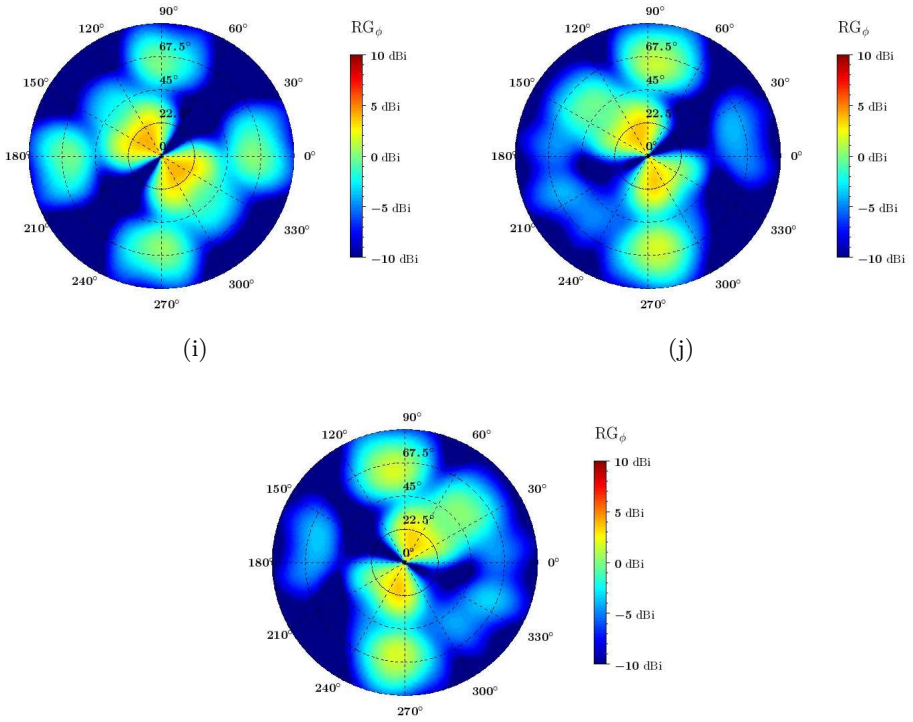

Figure F.10: Simulated realized gain in the ϕ-polarization of the Two Season VA (mounted over the finite and octagonal metallic support) at 3.4 GHz associated with the first set of weighting coefficients of: (a) to (k) RPC 1 to RPC 11. Elevation angles θ are given on the radial axis and azimuth angles ϕ are given on the angular axis.

F.4 Simulated and measured direction finding performances

Under the scenario conditions defined in Table 2.3, the simulated and measured estimation errors E^{θ}_{RMS} and E^{ϕ}_{RMS} obtained with the Two Season VA using both RPC 0 and RPC 4 are set out Fig. F.11 and Fig. F.12, respectively. These results are complementary to those concerning the angular distance Δa_{RMS} provided in Section 3.1.2.1. Moreover, the maximum RMS error as well as the 95th percentile of the E^{θ}_{RMS} and E^{ϕ}_{RMS} are also shown in Table F.1 and Table F.2, respectively.

Table F.1: Simulated and measured E^{θ}_{RMS} obtained with the Two Season VA using both RPC 0 and RPC 4, and under the scenario conditions defined in Table 2.3

Frequency	Simulated		Measured	
	max E^{θ}_{RMS}	95th percentile of E^{θ}_{RMS}	max E^{θ}_{RMS}	95th percentile of E^{θ}_{RMS}
2.2 GHz	1.2°	0.7°	2.4°	0.6°
2.8 GHz	1.3°	1.0°	1.4°	1.0°
3.4 GHz	1.3°	0.8°	1.9°	0.9°

Table F.2: Simulated and measured E^{ϕ}_{RMS} obtained with the Two Season VA using both RPC 0 and RPC 4, and under the scenario conditions defined in Table 2.3

Frequency	Simulated		Measured	
	max E^{ϕ}_{RMS}	95th percentile of E^{ϕ}_{RMS}	max E^{ϕ}_{RMS}	95th percentile of E^{ϕ}_{RMS}
2.2 GHz	0.7°	0.5°	0.8°	0.5°
2.8 GHz	0.9°	0.7°	1.0°	0.7°
3.4 GHz	1.0°	0.6°	1.1°	0.7°

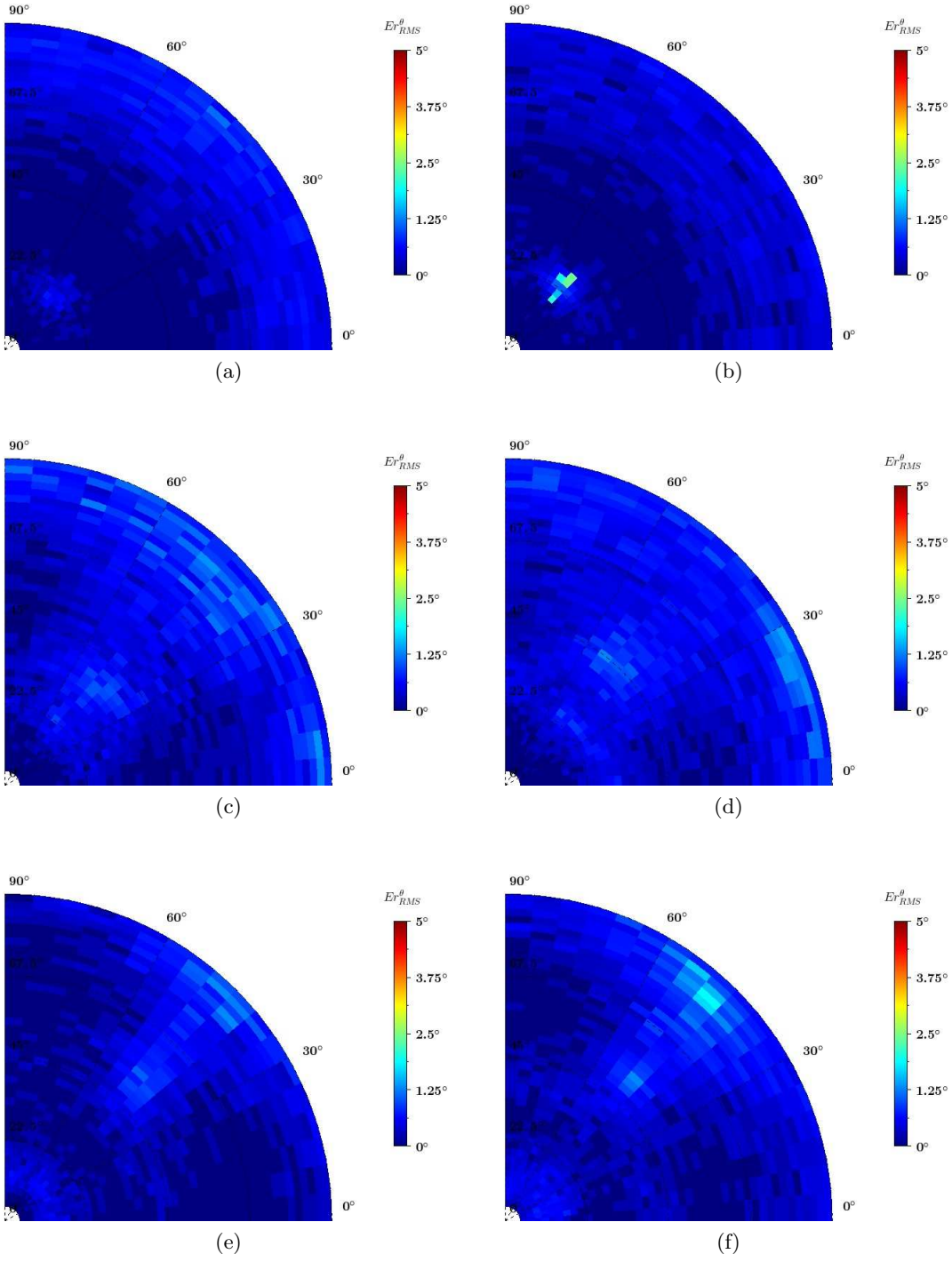

Figure F.11: Simulated (left figures) and measured (right figures) $E^{\theta}_{\mathrm{RMS}}$ obtained with the Two Season VA using both RPC 0 and RPC 4, and under the scenario conditions defined in Table 2.3 at the following frequencies: (a) & (b) 2.2 GHz, (c) & (d) 2.8 GHz, and (e) & (f) 3.4 GHz. Elevation angles θ are given on the radial axis and azimuth angles ϕ are given on the angular axis.

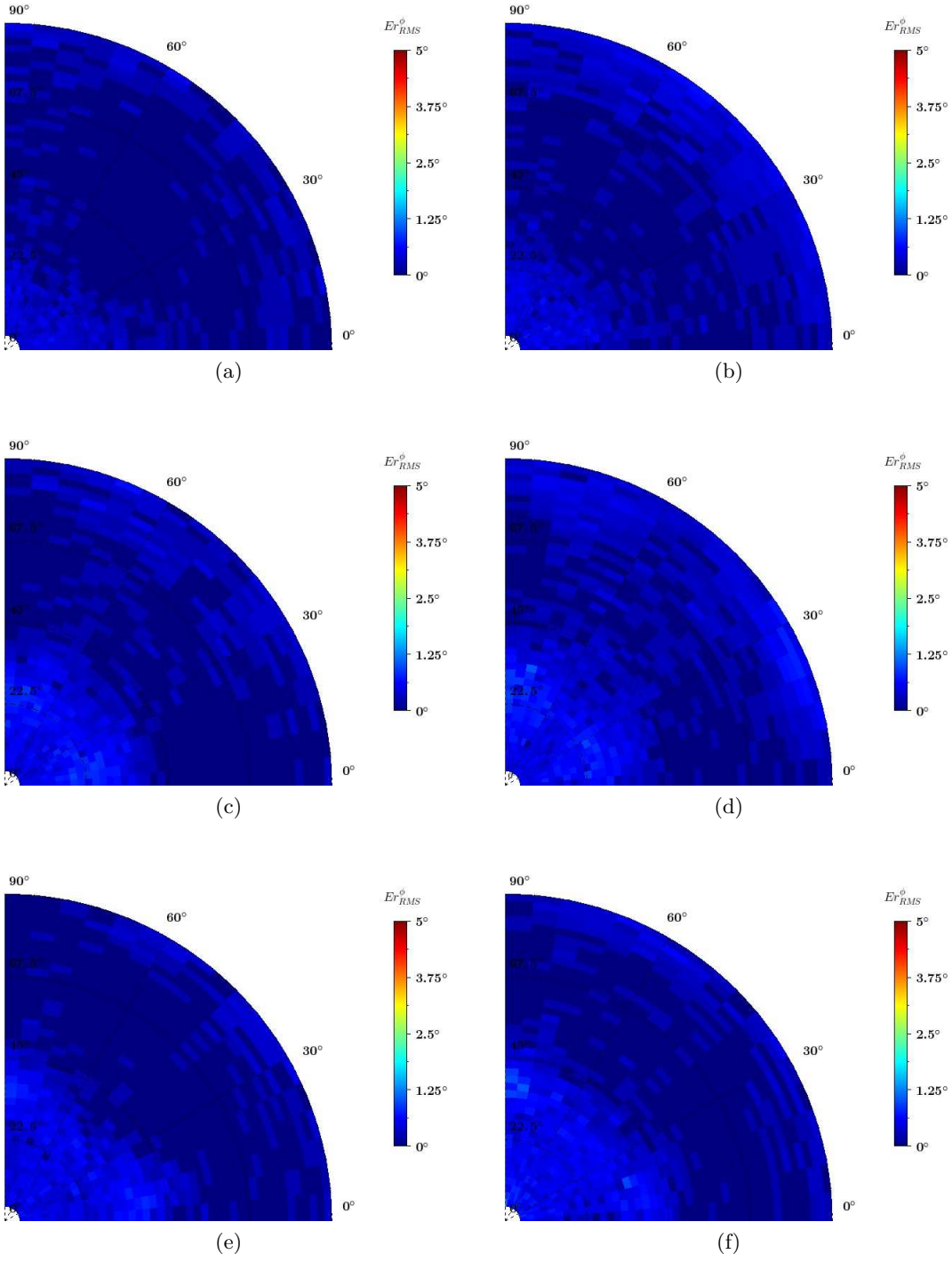

Figure F.12: Simulated (left figures) and measured (right figures) E^{ϕ}_{RMS} obtained with the Two Season VA using both RPC 0 and RPC 4, and under the scenario conditions defined in Table 2.3 at the following frequencies: (a) & (b) 2.2 GHz, (c) & (d) 2.8 GHz, and (e) & (f) 3.4 GHz. Elevation angles θ are given on the radial axis and azimuth angles ϕ are given on the angular axis.

Appendix G

Definition of the power density to noise ratio

Contents

The aim of this appendix is first to explain why the use of SNR is not suited for the evaluation of the DF performances with a VA and introduce another quantity to describe the operational situation (Section G.1). This quantity is the power density to noise ratio whose acronym is PNR. Then, some numerical values used for the DF performances evaluation throughout this Ph.D. work are also provided (Section G.2).

G.1 Signal to noise ratio versus power density to noise ratio

As stated in [74] and in accordance to the VA topology, it is difficult to assign the same value of SNR (defined in Eq. 1.13) to the noise floor power $P_n = \sigma_n^2$ of the receiver. Indeed, the SNR varies as a function of the DoA of the incoming EM-wave and is different at the output of each VA element according to their diversity of polarization and RP.

For the sake of clarity, let us use the illustrative example described in [74], where two antenna elements measure the same incoming power density P_s through two identical receiver channels as shown in Fig. G.1. Two different settings are possible:

- The two antenna elements have the same gain (particular case) in the direction of the wave vector $\boldsymbol{k}(\phi, \theta)$ (i.e., $G_1(\phi, \theta) = G_2(\phi, \theta)$), so the measured signal power is also equal (i.e., $P_{a1}(\phi, \theta) = P_{a2}(\phi, \theta)$). As a consequence, an identical SNR is reached at the output of both channels.
- The two antenna elements have a non-identical gain (general case) in the direction of the wave vector $\boldsymbol{k}(\phi, \theta)$ (i.e., $G_1(\phi, \theta) \neq G_2(\phi, \theta)$), therefore the measured signal power is also different (i.e., $P_{a1}(\phi, \theta) \neq P_{a2}(\phi, \theta)$). As a consequence, a different SNR is reached at the output of both channels. Accordingly, the same value of SNR cannot be associated with all channels of a VA.

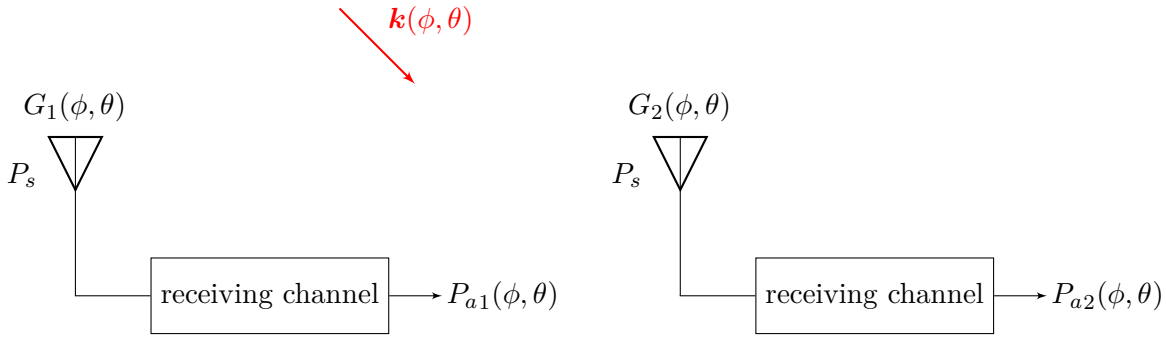

Figure G.1: Measurement of an incident EM-wave using two antenna elements

The EM-wave power density to noise ratio (PNR) was introduced in order to analyze the DF performances of a VA with respect to a quantity describing the given operational situation in terms of received power level relative to the background noise level, which does not depend on the DoA of the incident EM-wave. The PNR is defined as follows

$$\text{PNR} = \frac{P_s}{P_n}. \tag{G.1}$$

It can be noted that in addition to being spatially invariant, the PNR is identical regardless of the VA element used.

G.2 Numerical values

Throughout this thesis, the noise floor power of the receiver is set to -111 dBm using Eq. 1.12 and standard figures of a modern GSM receiver, that is a noise factor of 10 dB and an equivalent noise bandwidth of 200 kHz (see, e.g., [14]). Since P_n is fixed, the PNR is only controlled through the power density of the incoming EM-wave.

Appendix H

The Four Season vector antenna: additional results

Contents

The aim of this appendix is to present additional results concerning the Four Season VA. First, the simulated RPs of RPC 00 that enable the measurement of the six components E_z, E_y, E_z, H_x, H_y, and H_z of an incoming EM-wave are displayed (Section H.1). Secondly, the simulated RPCs associated with the horizontal part of the Four Season VA are set out (Section H.2). Thirdly, results from the CRB study performed in Section 3.3.3.2 consisting of adding one of the 22 available RPCs to RPC 00 in the DoA estimation process are provided (Section H.3).

H.1 Simulated radiation patterns used for DoA estimation of an incoming EM-wave

The simulated RPs of RPC 00 that enable the measurement of the six components E_z, E_y, E_z, H_x, H_y, and H_z are displayed at 2.8 GHz in Fig. H.1.

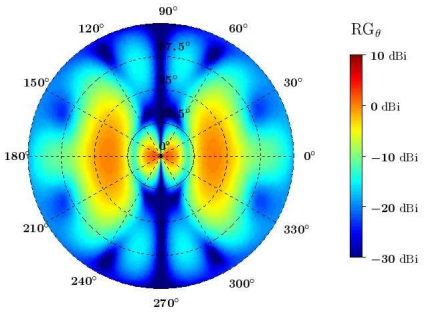
90°
120°
60°
67.5°
150°
45°
30°
22.5°
180°
0°
0°
210°
330°
240°
300°
270°
RG$_\theta$
10 dBi
0 dBi
−10 dBi
−20 dBi
−30 dBi

(a)

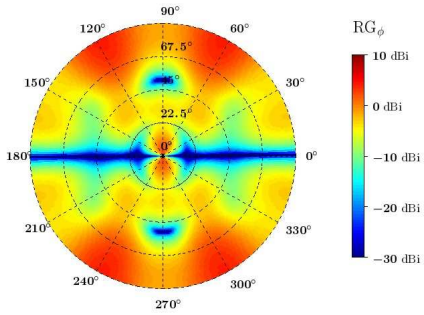
90°
120°
60°
67.5°
150°
45°
30°
22.5°
180°
0°
0°
210°
330°
240°
300°
270°
RG$_\phi$
10 dBi
0 dBi
−10 dBi
−20 dBi
−30 dBi

(b)

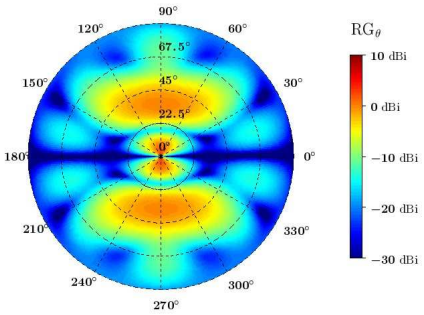
90°
120°
60°
67.5°
150°
45°
30°
22.5°
180°
0°
0°
210°
330°
240°
300°
270°
RG$_\theta$
10 dBi
0 dBi
−10 dBi
−20 dBi
−30 dBi

(c)

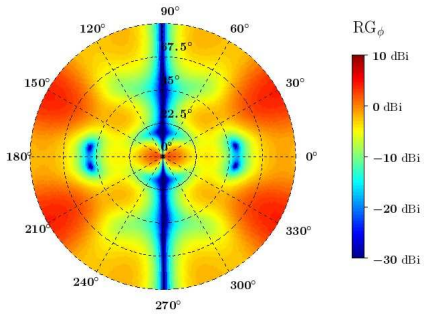
90°
120°
60°
67.5°
150°
45°
30°
22.5°
180°
0°
0°
210°
330°
240°
300°
270°
RG$_\phi$
10 dBi
0 dBi
−10 dBi
−20 dBi
−30 dBi

(d)

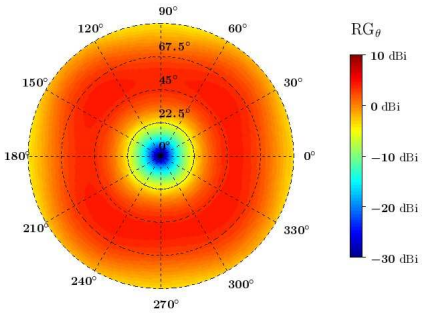
90°
120°
60°
67.5°
150°
45°
30°
22.5°
180°
0°
0°
210°
330°
240°
300°
270°
RG$_\theta$
10 dBi
0 dBi
−10 dBi
−20 dBi
−30 dBi

(e)

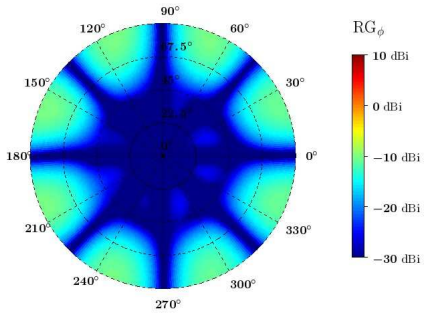
90°
120°
60°
67.5°
150°
45°
30°
22.5°
180°
0°
0°
210°
330°
240°
300°
270°
RG$_\phi$
10 dBi
0 dBi
−10 dBi
−20 dBi
−30 dBi

(f)

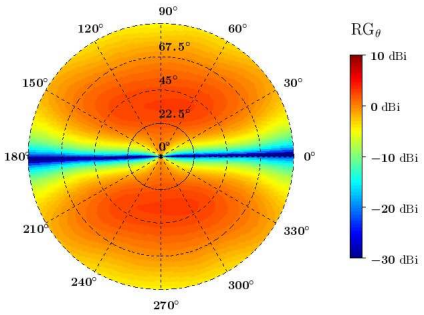
90°
120°
60°
67.5°
150°
45°
30°
22.5°
180°
0°
0°
210°
330°
240°
300°
270°
RG$_\theta$
10 dBi
0 dBi
−10 dBi
−20 dBi
−30 dBi

(g)

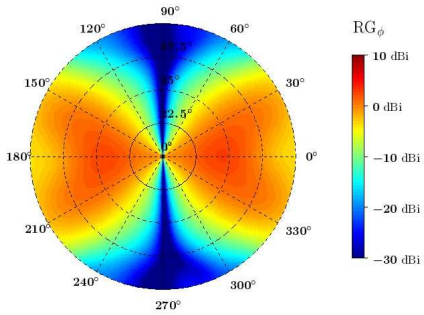
90°
120°
60°
67.5°
150°
45°
30°
22.5°
180°
0°
0°
210°
330°
240°
300°
270°
RG$_\phi$
10 dBi
0 dBi
−10 dBi
−20 dBi
−30 dBi

(h)

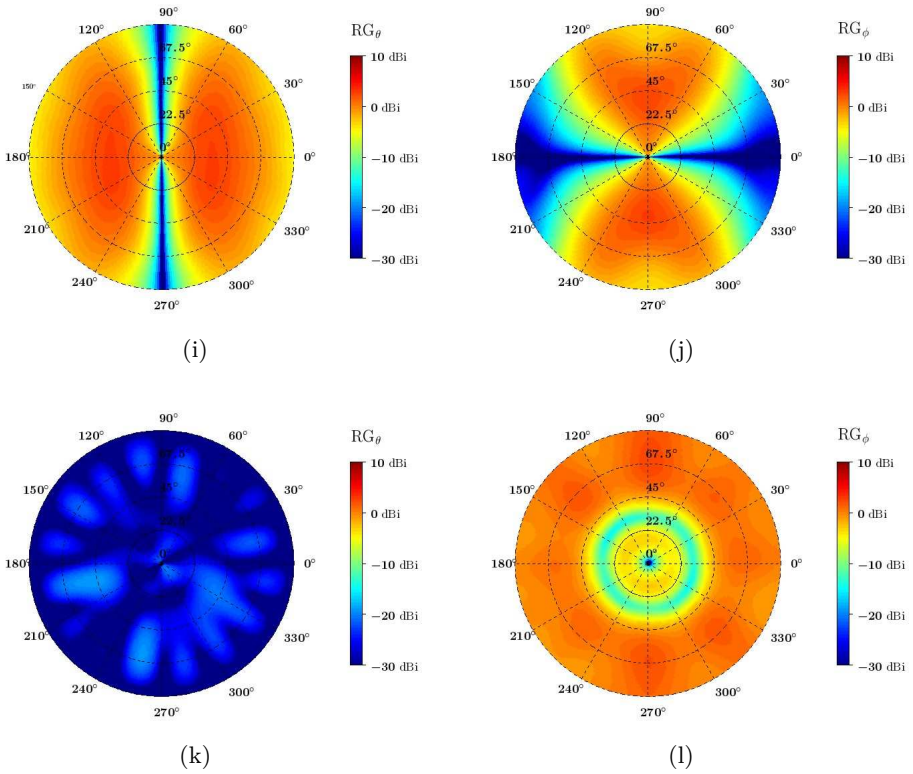

Figure H.1: Simulated realized gain in the θ-polarization (left figures) and in ϕ-polarization (right figures) of the Four Season VA used for measuring the six components (RPC 00): (a) & (b) E_x, (c) & (d) E_y, (e) & (f) E_z, (g) & (h) H_x, (i) & (j) H_y, and (k) & (l) H_z of an incoming EM-wave at 2.8 GHz. Elevation angles θ are given on the radial axis and azimuth angles ϕ are given on the angular axis.

H.2 Radiation patterns combinations

Fig. H.2 and Fig. H.3 present the simulated RPCs of the Four Season VA associated with the horizontal part of the antenna. They are displayed at 3.4 GHz and in the θ-polarization and ϕ-direction, respectively. Only one RP by RPC is shown since the RPs within a RPC exhibit the same RP with a rotation symmetry of 90° in the azimuth plane.

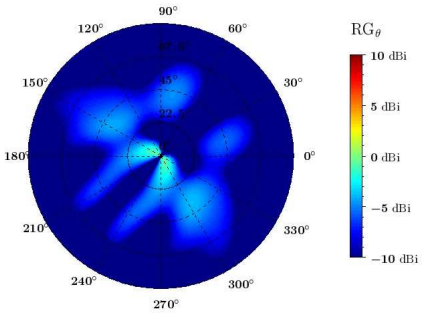
90°
120°
60°
150°
30°
180°
0°
210°
330°
240°
300°
270°
RG$_\theta$
10 dBi
5 dBi
0 dBi
−5 dBi
−10 dBi

(a)

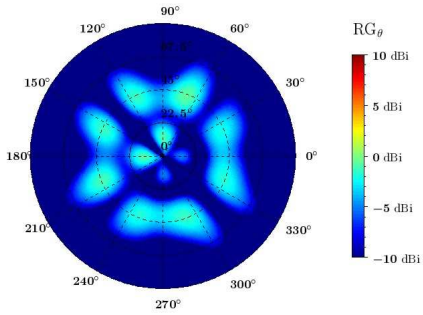
90°
120°
60°
150°
30°
180°
0°
210°
330°
240°
300°
270°
RG$_\theta$
10 dBi
5 dBi
0 dBi
−5 dBi
−10 dBi

(b)

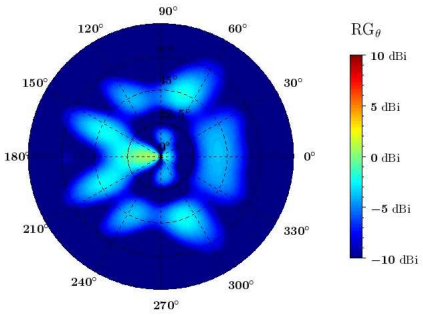
90°
120°
60°
150°
30°
180°
0°
210°
330°
240°
300°
270°
RG$_\theta$
10 dBi
5 dBi
0 dBi
−5 dBi
−10 dBi

(c)

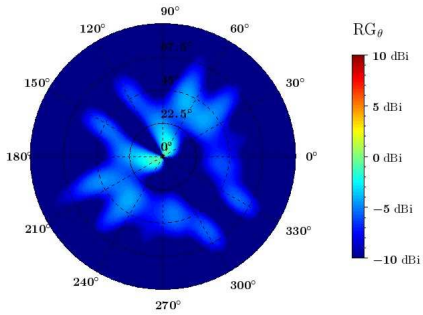
90°
120°
60°
150°
30°
180°
0°
210°
330°
240°
300°
270°
RG$_\theta$
10 dBi
5 dBi
0 dBi
−5 dBi
−10 dBi

(d)

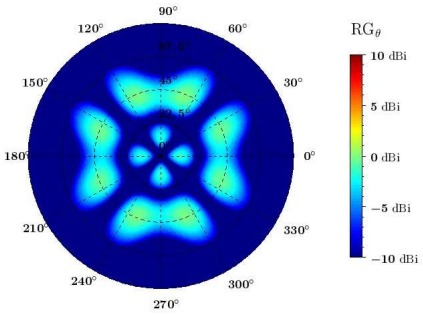
90°
120°
60°
150°
30°
180°
0°
210°
330°
240°
300°
270°
RG$_\theta$
10 dBi
5 dBi
0 dBi
−5 dBi
−10 dBi

(e)

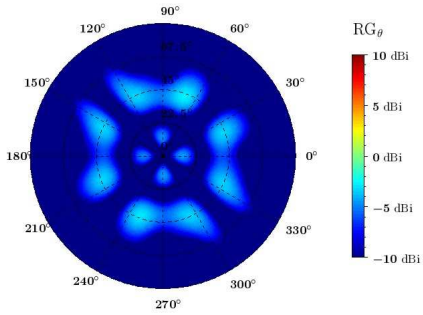
90°
120°
60°
150°
30°
180°
0°
210°
330°
240°
300°
270°
RG$_\theta$
10 dBi
5 dBi
0 dBi
−5 dBi
−10 dBi

(f)

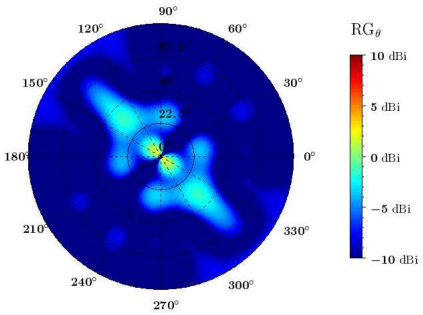
90°
120°
60°
150°
30°
180°
0°
210°
330°
240°
300°
270°
RG$_\theta$
10 dBi
5 dBi
0 dBi
−5 dBi
−10 dBi

(g)

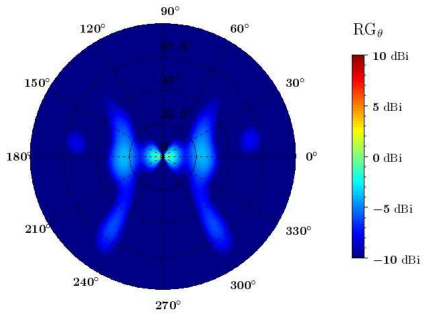
90°
120°
60°
150°
30°
180°
0°
210°
330°
240°
300°
270°
RG$_\theta$
10 dBi
5 dBi
0 dBi
−5 dBi
−10 dBi

(h)

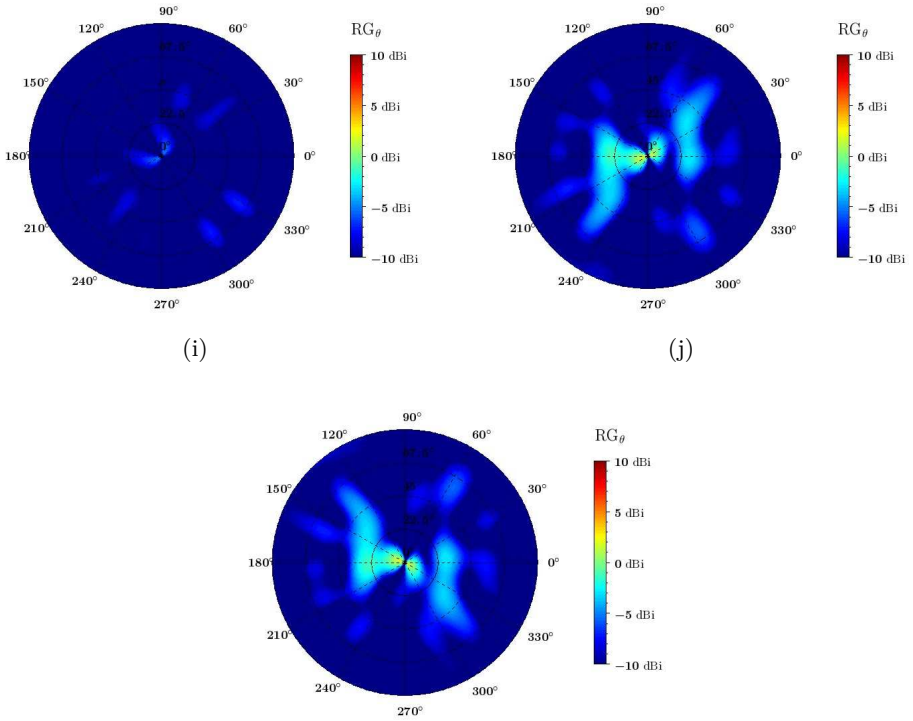

(i) (j)

(k)

Figure H.2: Simulated realized gain in the θ-polarization of the Four Season VA at 3.4 GHz associated with the first set of weighting coefficients of: (a) to (k) RPC 12 to RPC 22. Elevation angles θ are given on the radial axis and azimuth angles ϕ are given on the angular axis.

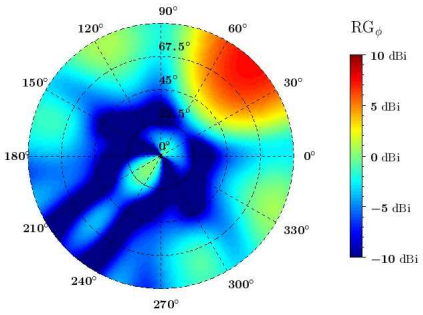
90°
120°
60°
67.5°
45°
30°
150°
180°
0°
210°
330°
240°
300°
270°
RG$_\phi$
10 dBi
5 dBi
0 dBi
−5 dBi
−10 dBi

(a)

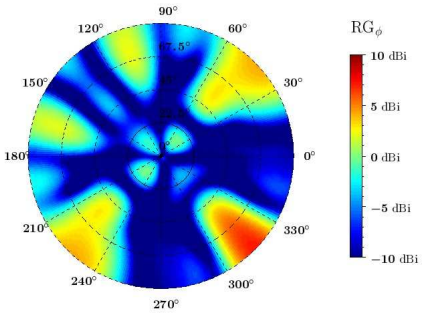
90°
120°
60°
67.5°
45°
30°
150°
180°
0°
210°
330°
240°
300°
270°
RG$_\phi$
10 dBi
5 dBi
0 dBi
−5 dBi
−10 dBi

(b)

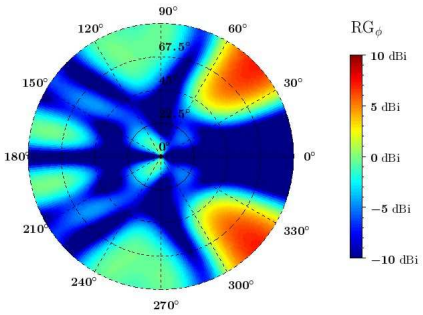
90°
120°
60°
67.5°
45°
30°
150°
180°
0°
210°
330°
240°
300°
270°
RG$_\phi$
10 dBi
5 dBi
0 dBi
−5 dBi
−10 dBi

(c)

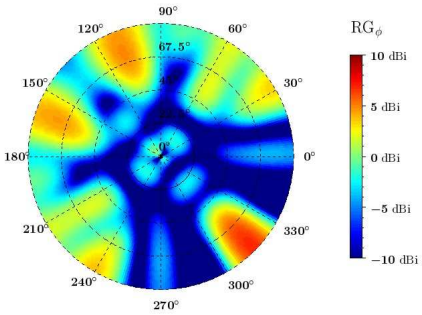
90°
120°
60°
67.5°
45°
30°
150°
180°
0°
210°
330°
240°
300°
270°
RG$_\phi$
10 dBi
5 dBi
0 dBi
−5 dBi
−10 dBi

(d)

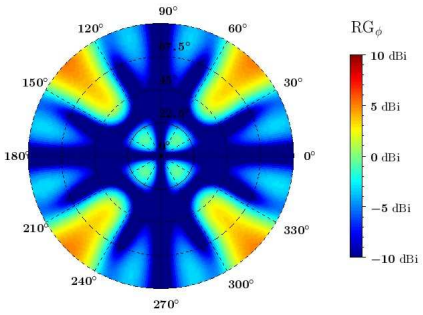
90°
120°
60°
67.5°
45°
30°
150°
180°
0°
210°
330°
240°
300°
270°
RG$_\phi$
10 dBi
5 dBi
0 dBi
−5 dBi
−10 dBi

(e)

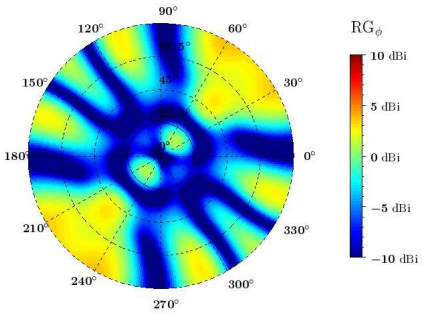
90°
120°
60°
67.5°
45°
30°
150°
180°
0°
210°
330°
240°
300°
270°
RG$_\phi$
10 dBi
5 dBi
0 dBi
−5 dBi
−10 dBi

(f)

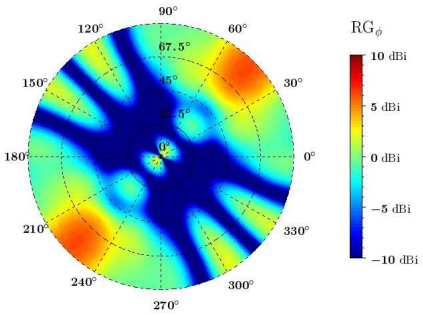
90°
120°
60°
67.5°
45°
30°
150°
180°
0°
210°
330°
240°
300°
270°
RG$_\phi$
10 dBi
5 dBi
0 dBi
−5 dBi
−10 dBi

(g)

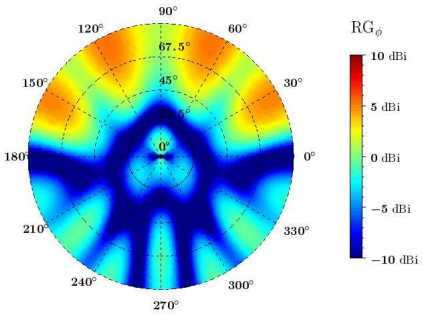
90°
120°
60°
67.5°
45°
30°
150°
180°
0°
210°
330°
240°
300°
270°
RG$_\phi$
10 dBi
5 dBi
0 dBi
−5 dBi
−10 dBi

(h)

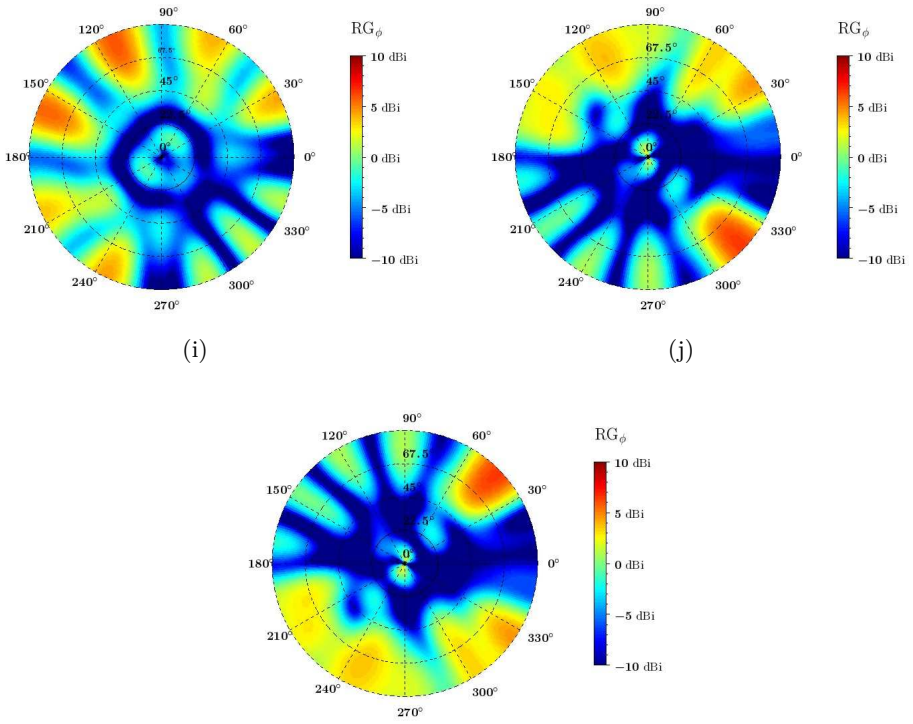

Figure H.3: Simulated realized gain in the ϕ-polarization of the Four Season VA at 3.4 GHz associated with the first set of weighting coefficients of: (a) to (k) RPC 12 to RPC 22. Elevation angles θ are given on the radial axis and azimuth angles ϕ are given on the angular axis.

H.3 Selection of the radiation patterns combinations

In Section 3.3.3.2, a CRB study is performed under the scenario summarized in Table 3.15 in order to select two RPCs among the 22 available RPCs (one for each part of the Four Season VA). The CRB on θ and ϕ are displayed in Fig. H.4 to Fig. H.23. The goal of this study is to select the RPCs that provide the highest estimation accuracy regardless of the polarization of the incoming EM-wave across the overall bandwidth of the Four Season VA.

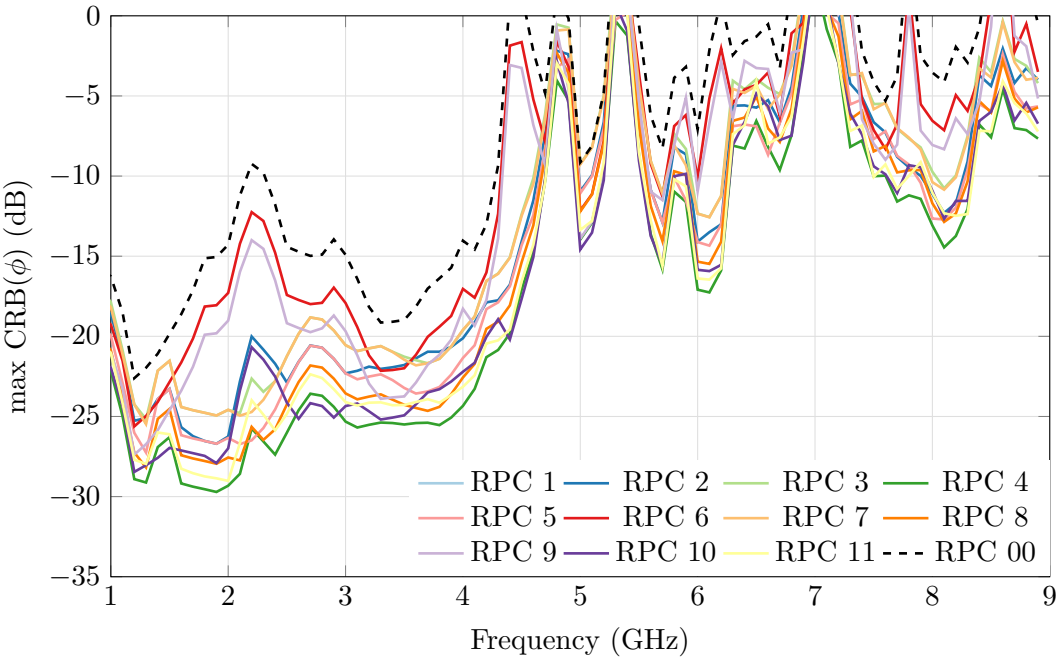

Figure H.4: Highest simulated CRLB(ϕ) of the Four Season VA using different RPCs [1 to 11] added to the RPC 00, and under the scenario conditions defined in Table 3.15 ($\gamma = 90°$ † $\eta = 0°$, i.e. vertical polarization)

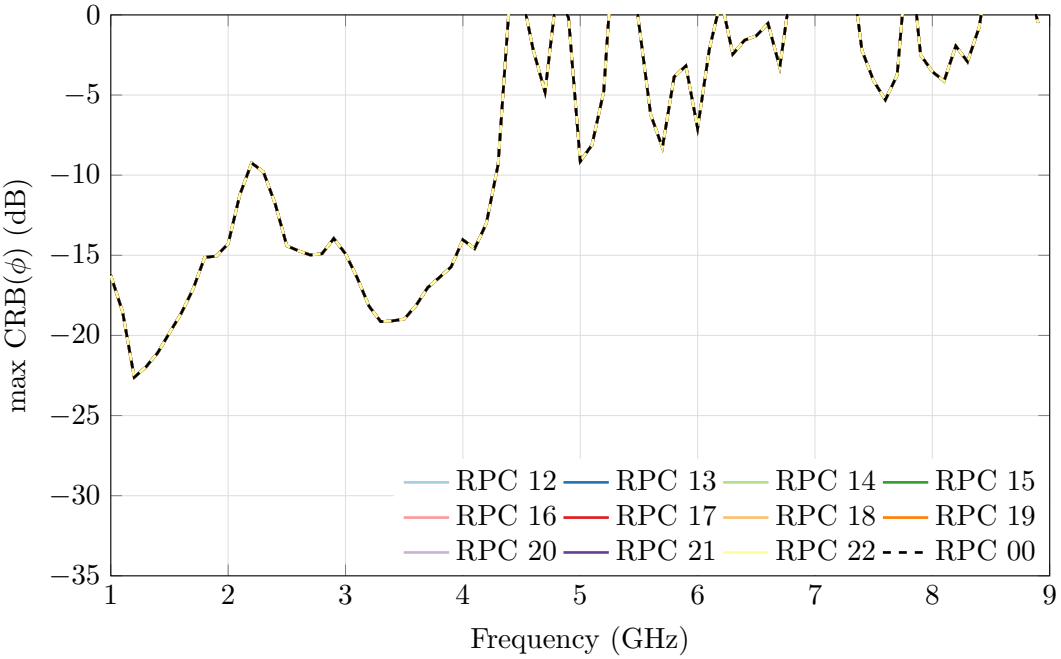

Figure H.5: Highest simulated CRLB(ϕ) of the Four Season VA using different RPCs [12 to 22] added to the RPC 00, and under the scenario conditions defined in Table 3.15 ($\gamma = 90°$ † $\eta = 0°$, i.e. vertical polarization)

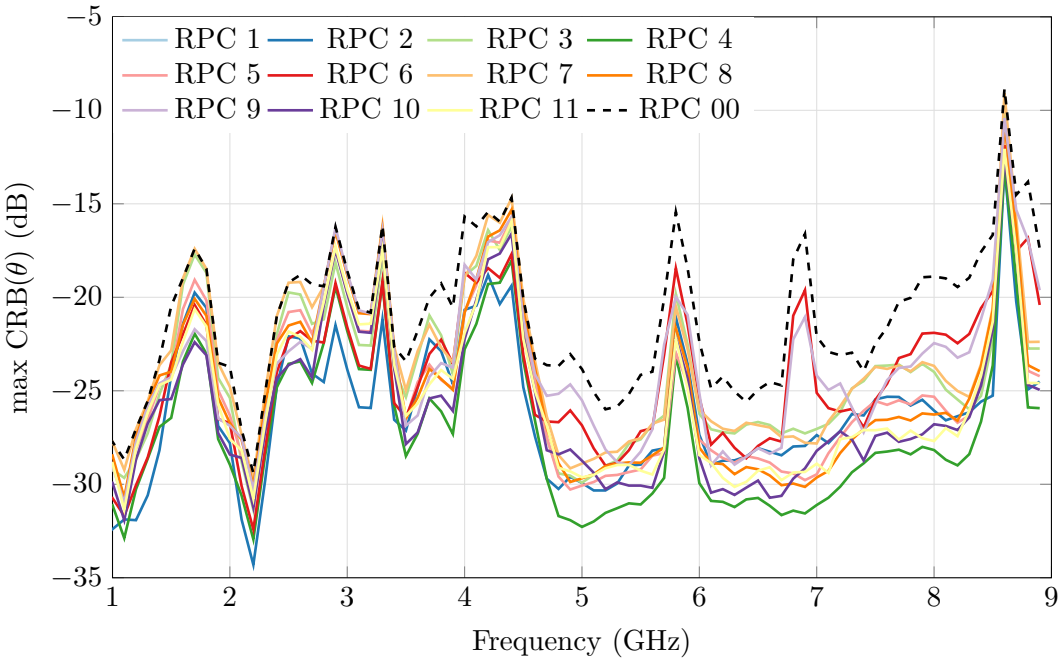

Figure H.6: Highest simulated CRLB(θ) of the Four Season VA using different RPCs [1 to 11] added to the RPC 0, and under the scenario conditions defined in Table 3.15 ($\gamma = 90°$ † $\eta = 0°$, i.e. vertical polarization)

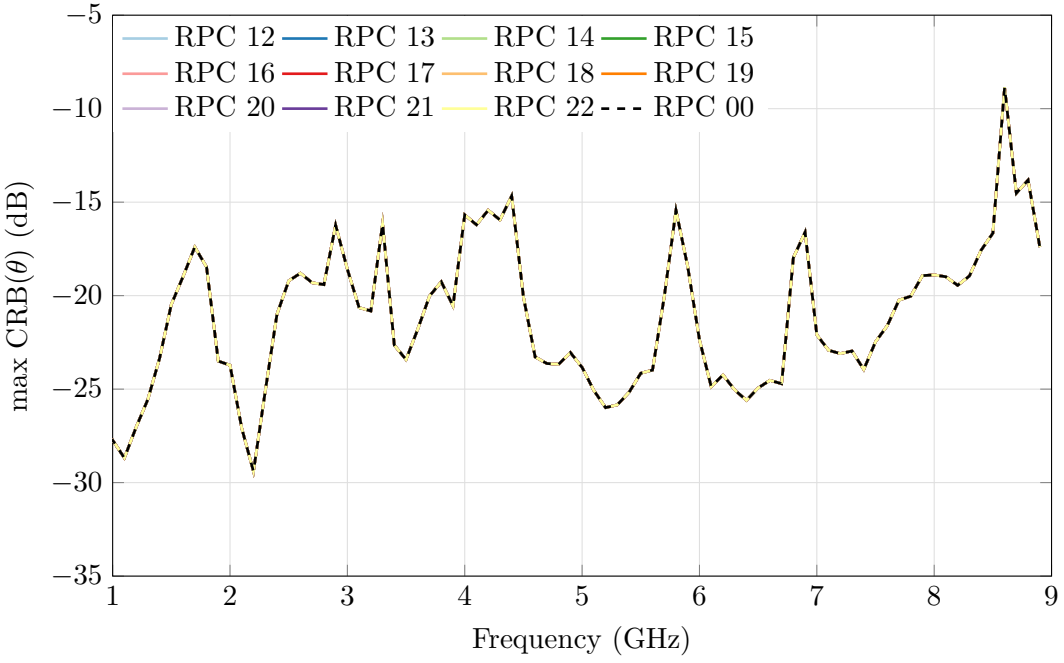

Figure H.7: Highest simulated CRLB(θ) of the Four Season VA using different RPCs [12 to 22] added to the RPC 00, and under the scenario conditions defined in Table 3.15 ($\gamma = 90°$ † $\eta = 0°$, i.e. vertical polarization)

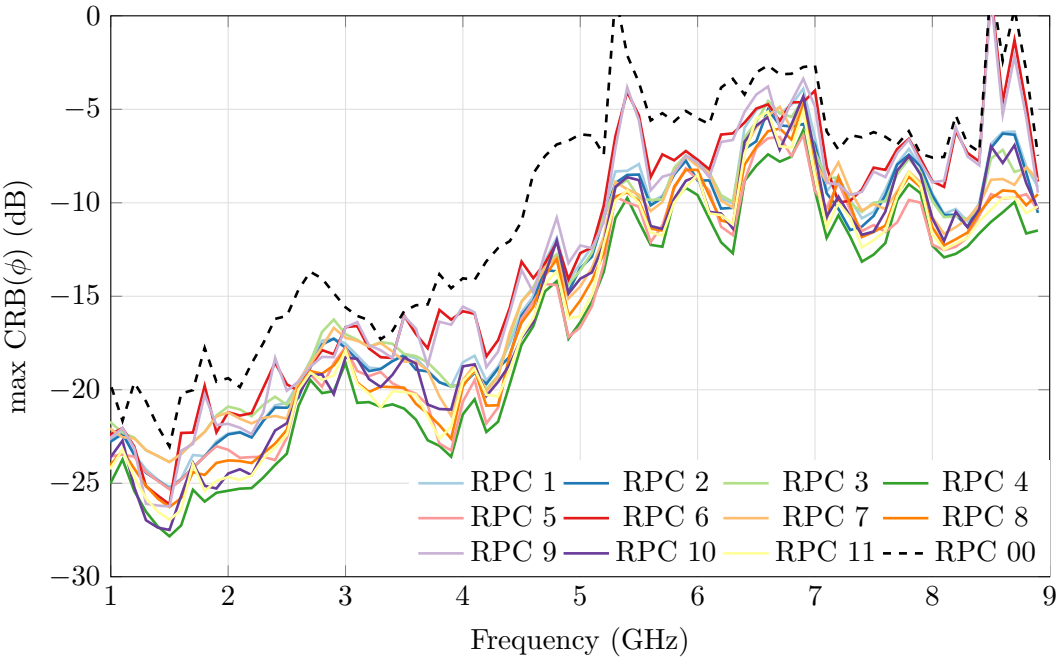

Figure H.8: Highest simulated CRLB(ϕ) of the Four Season VA using different RPCs [1 to 11] added to the RPC 00, and under the scenario conditions defined in Table 3.15 ($\gamma = 67.5°$ † $\eta = 0°$)

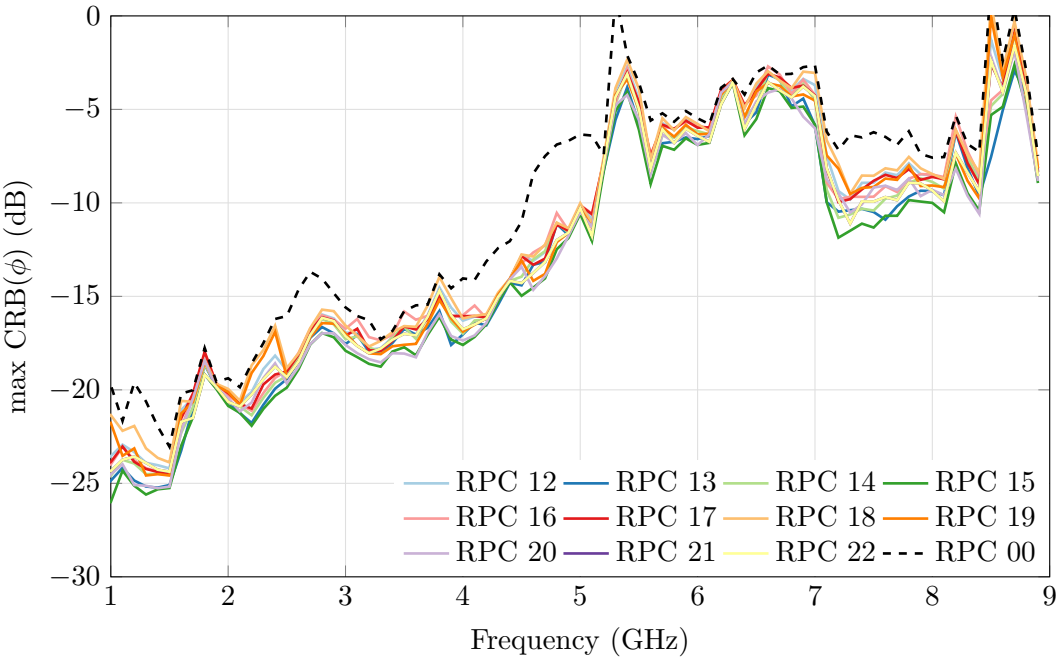

Figure H.9: Highest simulated CRLB(ϕ) of the Four Season VA using different RPCs [12 to 22] added to the RPC 00, aand under the scenario conditions defined in Table 3.15 ($\gamma = 67.5°$ † $\eta = 0°$)

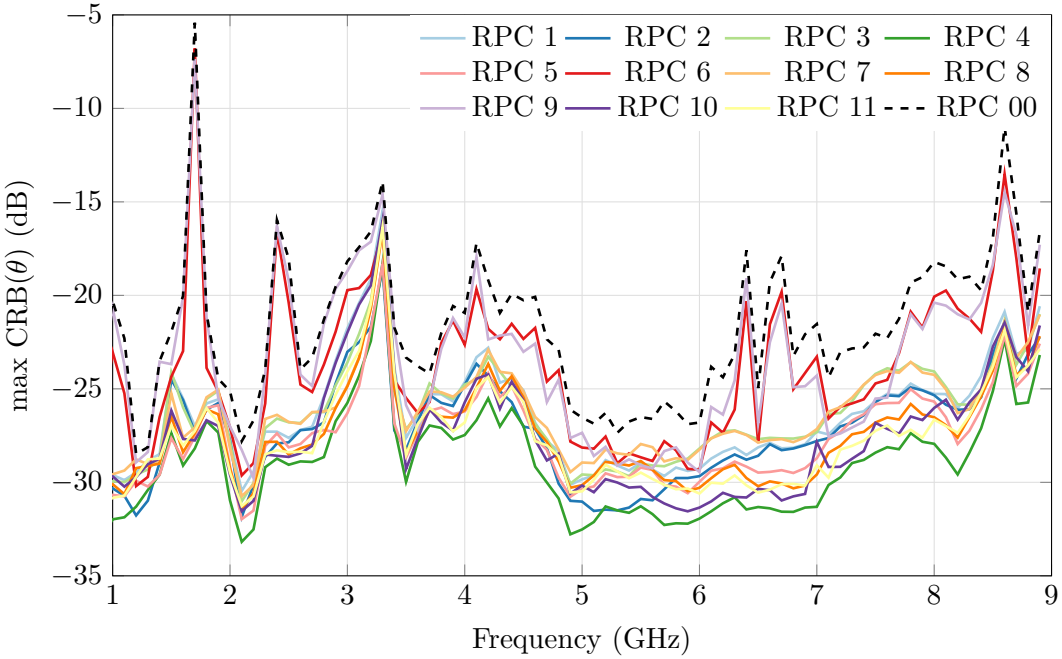

Figure H.10: Highest simulated CRLB(θ) of the Four Season VA using different RPCs [1 to 11] added to the RPC 0, and under the scenario conditions defined in Table 3.15 ($\gamma = 67.5° \dagger \eta = 0°$)

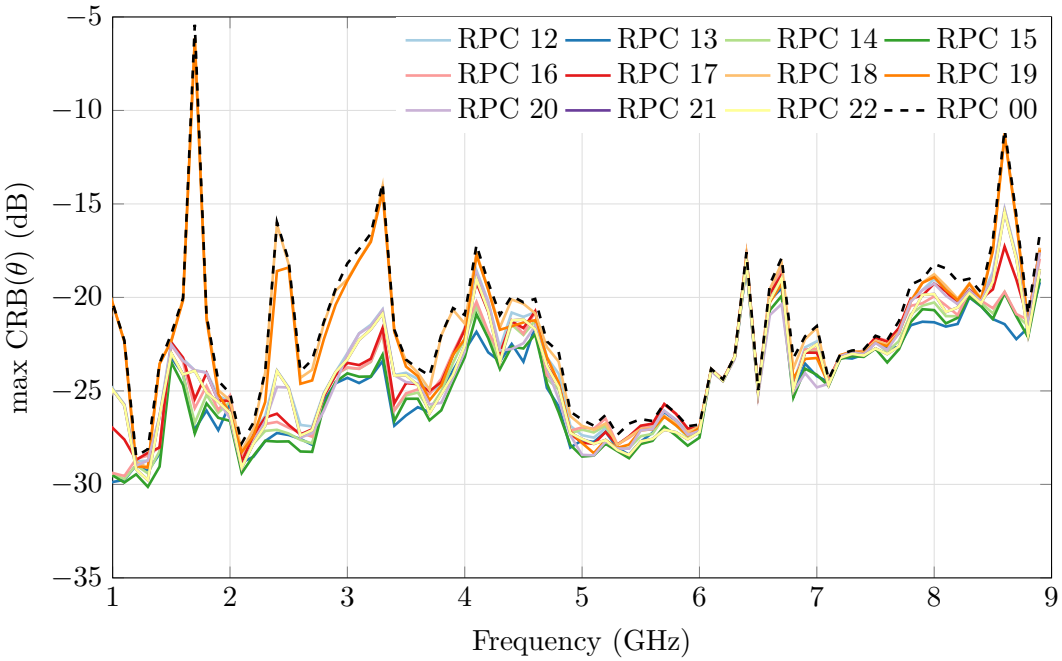

Figure H.11: Highest simulated CRLB(θ) of the Four Season VA using different RPCs [12 to 22] added to the RPC 00, and under the scenario conditions defined in Table 3.15 ($\gamma = 67.5° \dagger \eta = 0°$)

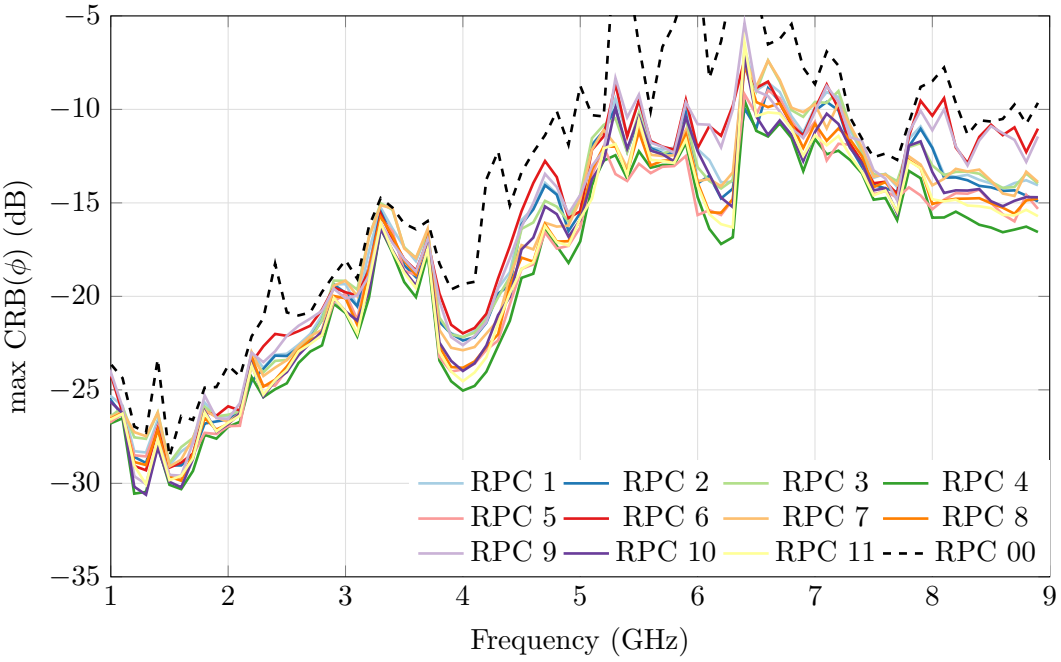

Figure H.12: Highest simulated CRLB(ϕ) of the Four Season VA using different RPCs [1 to 11] added to the RPC 00, and under the scenario conditions defined in Table 3.15 ($\gamma = 45° \dagger \eta = 0°$)

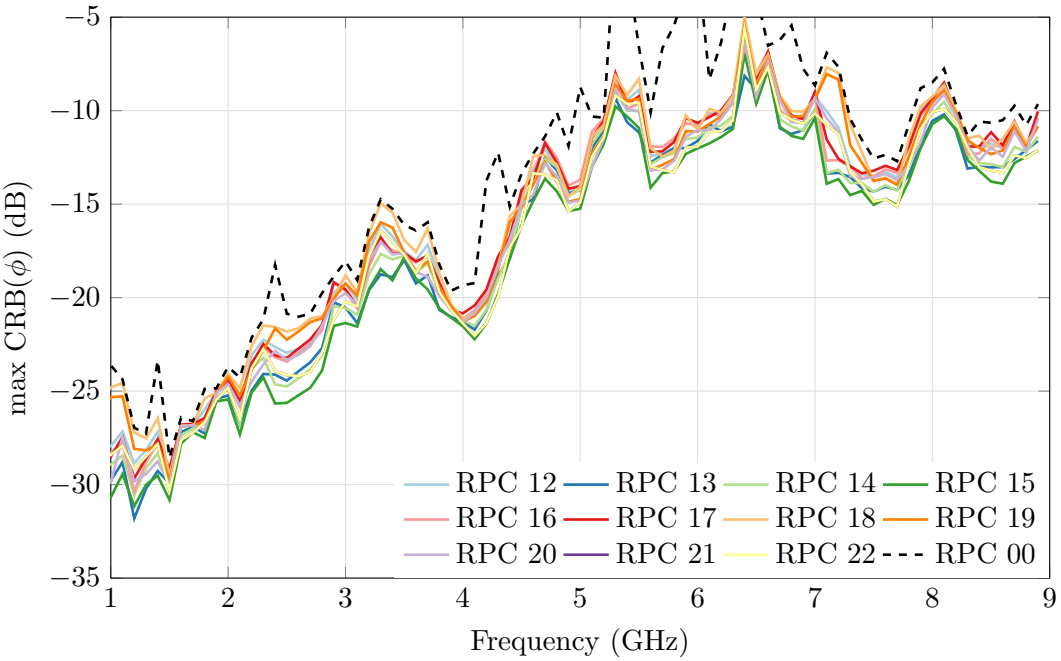

Figure H.13: Highest simulated CRLB(ϕ) of the Four Season VA using different RPCs [12 to 22] added to the RPC 00, and under the scenario conditions defined in Table 3.15 ($\gamma = 45° \dagger \eta = 0°$)

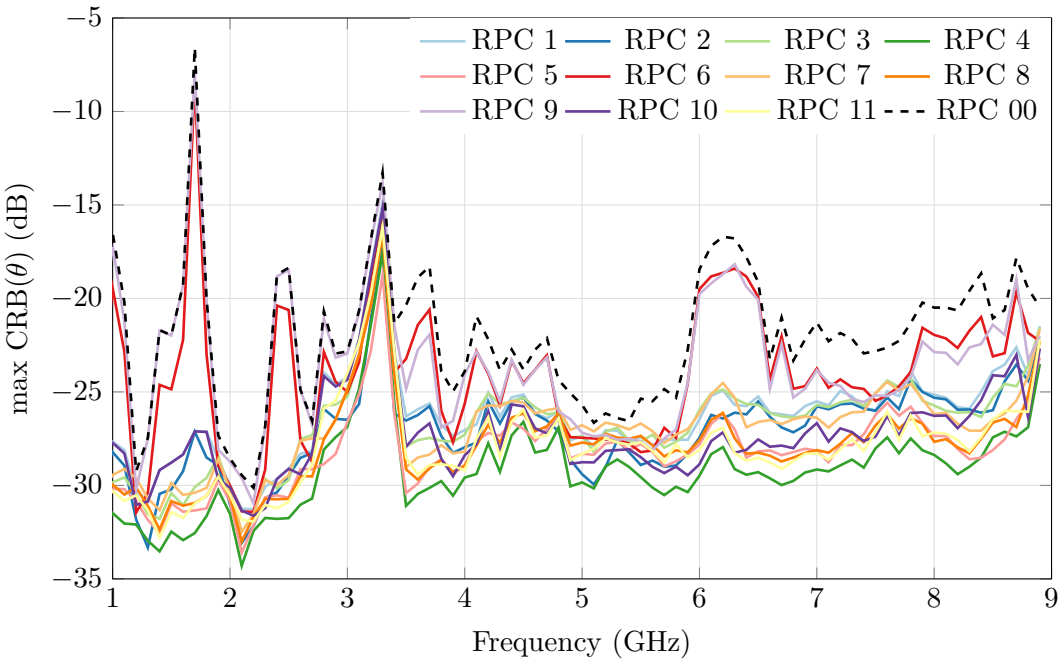

Figure H.14: Highest simulated CRLB(θ) of the Four Season VA using different RPCs [1 to 11] added to the RPC 0, and under the scenario conditions defined in Table 3.15 ($\gamma = 45°$ † $\eta = 0°$)

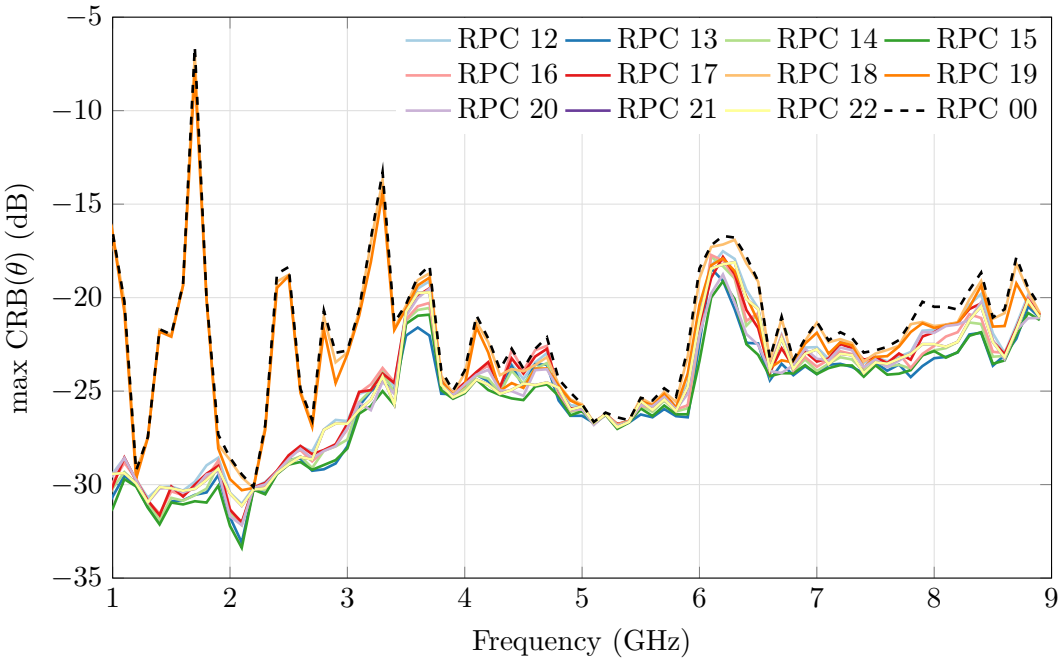

Figure H.15: Highest simulated CRLB(θ) of the Four Season VA using different RPCs [12 to 22] added to the RPC 00, and under the scenario conditions defined in Table 3.15 ($\gamma = 45°$ † $\eta = 0°$)

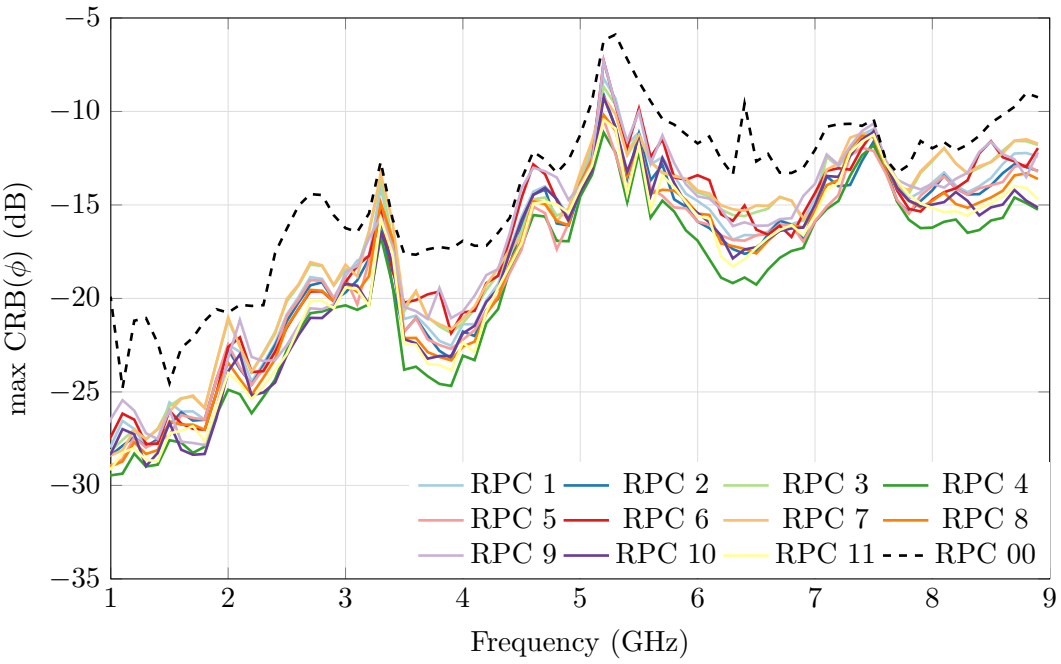

Figure H.16: Highest simulated CRLB(ϕ) of the Four Season VA using different RPCs [1 to 11] added to the RPC 00, and under the scenario conditions defined in Table 3.15 ($\gamma = 22.5°$ † $\eta = 0°$)

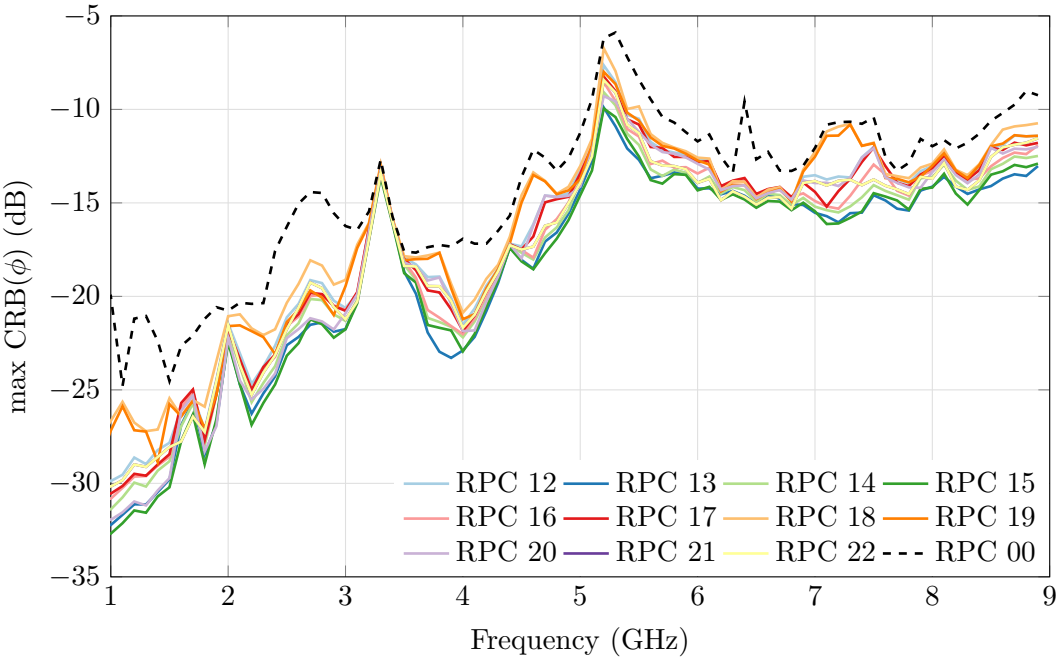

Figure H.17: Highest simulated CRLB(ϕ) of the Four Season VA using different RPCs [12 to 22] added to the RPC 00, and under the scenario conditions defined in Table 3.15 ($\gamma = 22.5°$ † $\eta = 0°$)

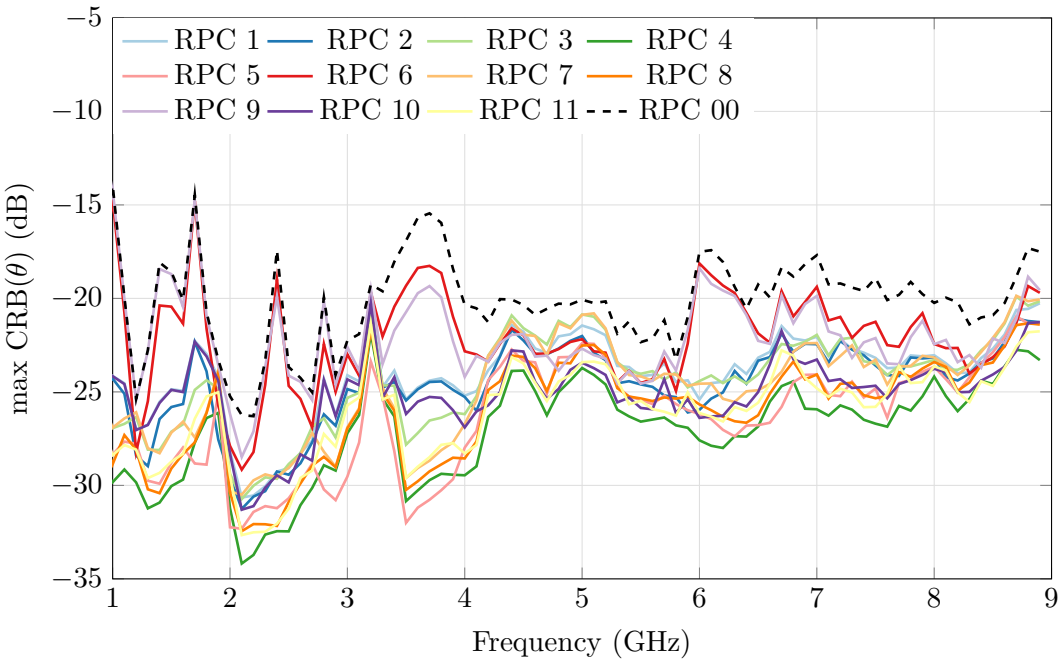

Figure H.18: Highest simulated CRLB(θ) of the Four Season VA using different RPCs [1 to 11] added to the RPC 0, and under the scenario conditions defined in Table 3.15 ($\gamma = 22.5° \dagger \eta = 0°$)

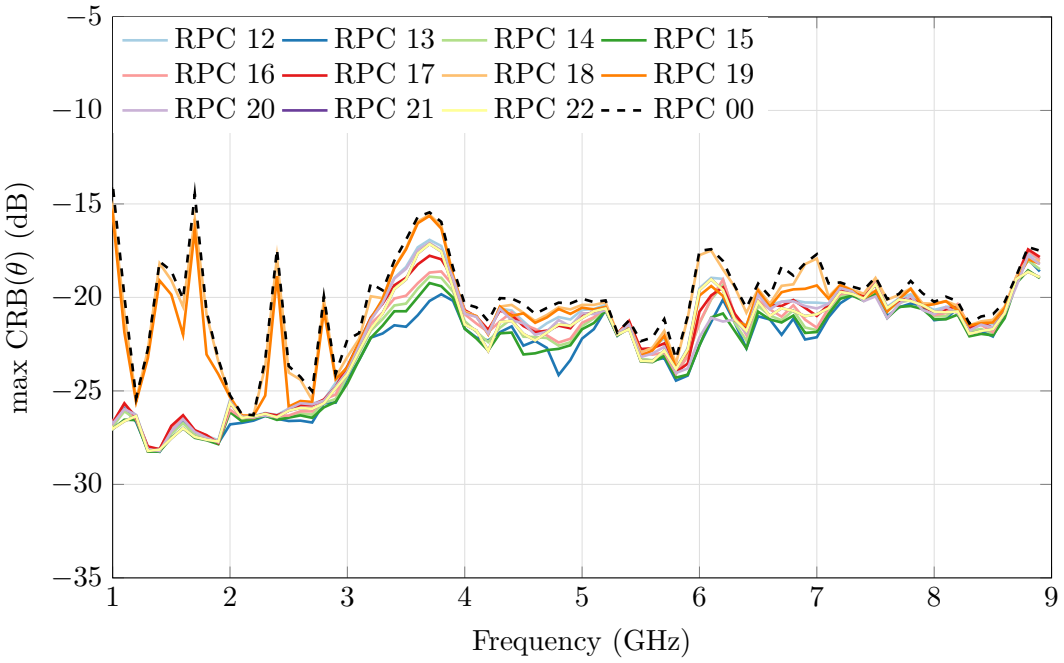

Figure H.19: Highest simulated CRLB(θ) of the Four Season VA using different RPCs [12 to 22] added to the RPC 00, and under the scenario conditions defined in Table 3.15 ($\gamma = 22.5° \dagger \eta = 0°$)

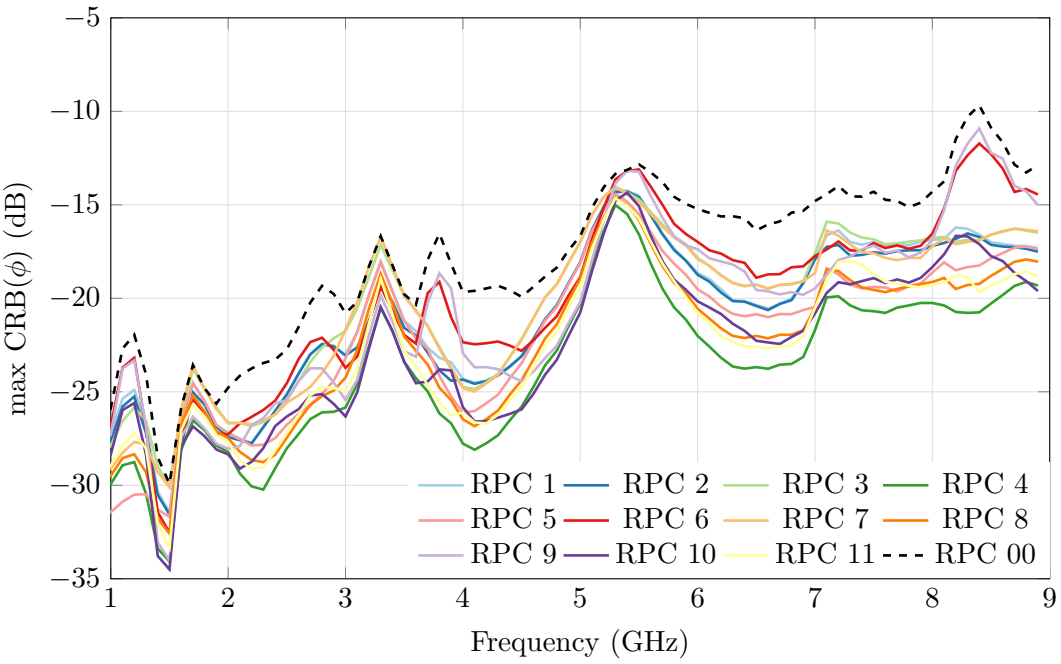

Figure H.20: Highest simulated CRLB(ϕ) of the Four Season VA using different RPCs [1 to 11] added to the RPC 00, and under the scenario conditions defined in Table 3.15 ($\gamma = 0°$ † $\eta = 0°$, i.e. horizontal polarization)

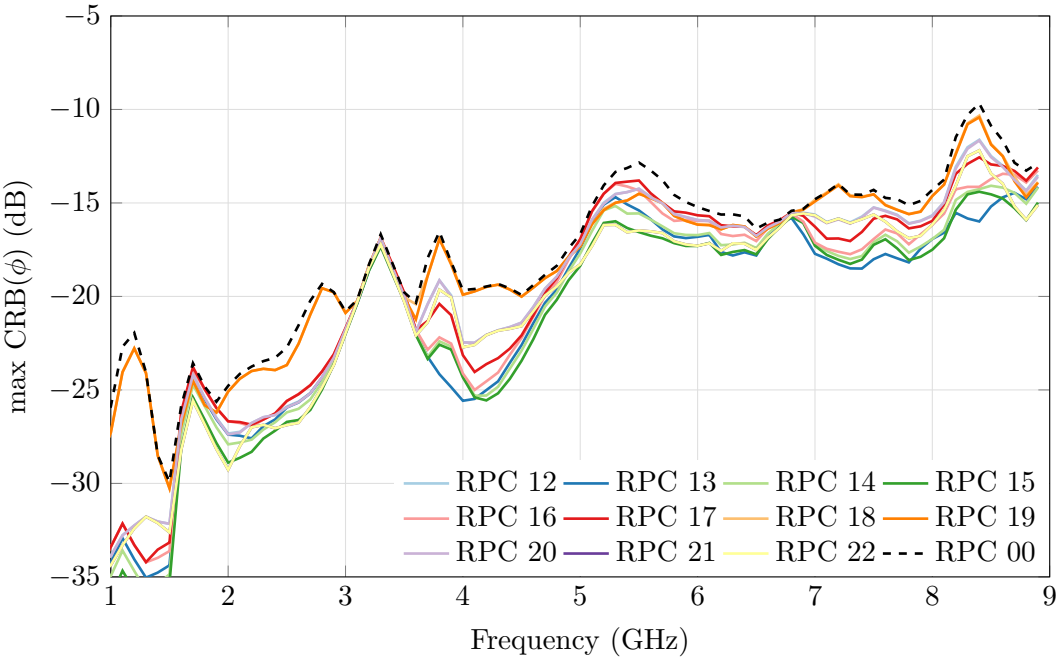

Figure H.21: Highest simulated CRLB(ϕ) of the Four Season VA using different RPCs [12 to 22] added to the RPC 00, and under the scenario conditions defined in Table 3.15 ($\gamma = 0°$ † $\eta = 0°$, i.e. horizontal polarization)

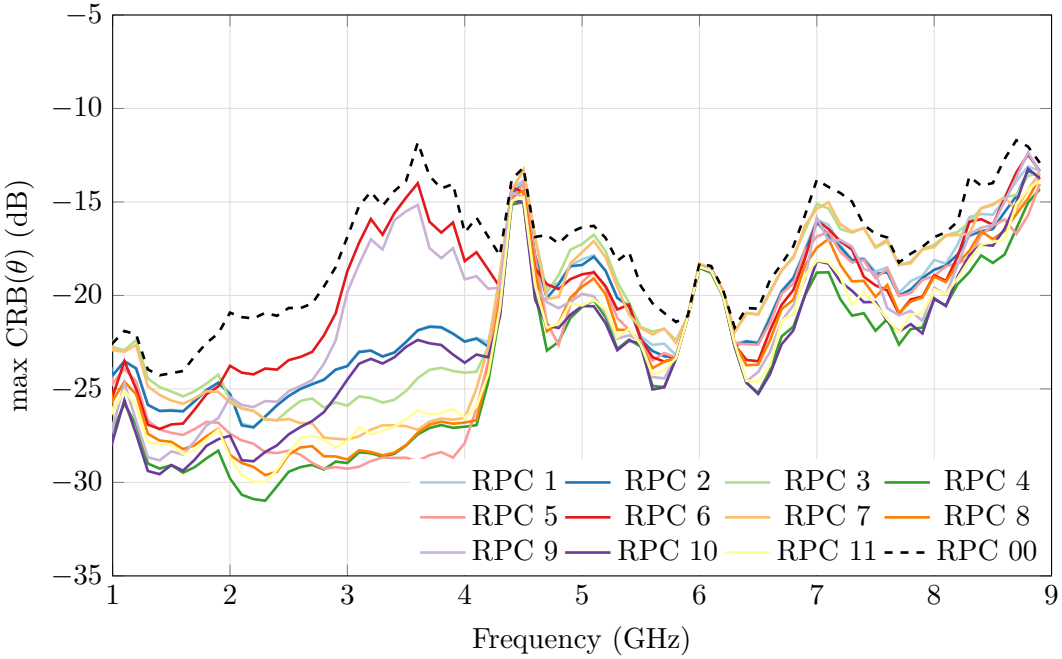

Figure H.22: Highest simulated CRLB(θ) of the Four Season VA using different RPCs [1 to 11] added to the RPC 00, and under the scenario conditions defined in Table 3.15 ($\gamma = 0° \dagger \eta = 0°$, i.e. horizontal polarization)

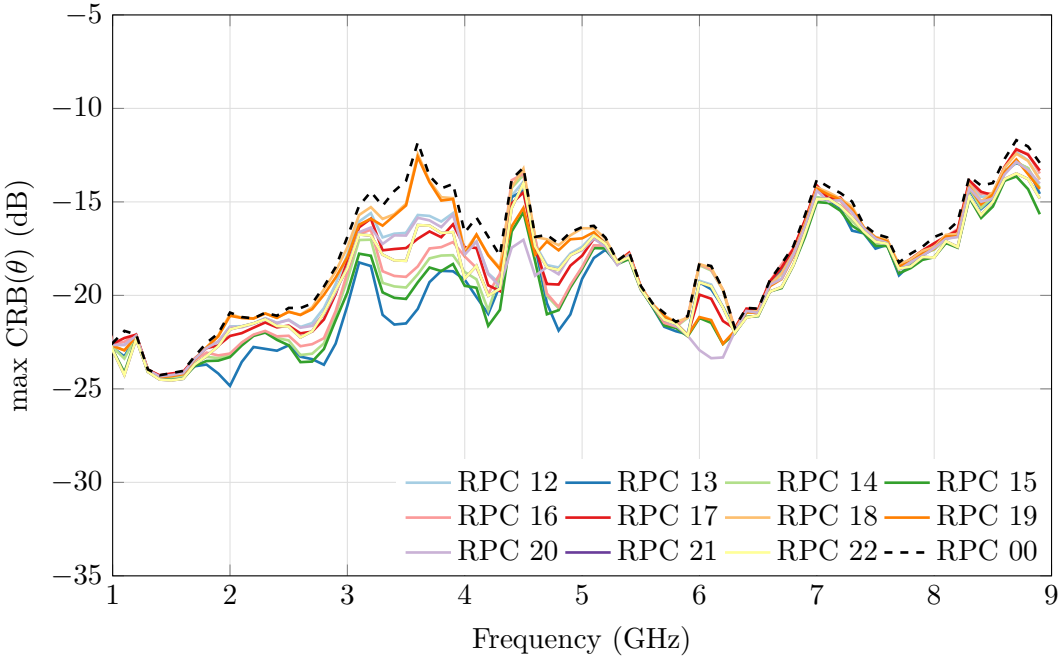

Figure H.23: Highest simulated CRLB(θ) of the Four Season VA using different RPCs [12 to 22] added to the RPC 00, and under the scenario conditions defined in Table 3.15 ($\gamma = 0° \dagger \eta = 0°$, i.e. horizontal polarization)

Bibliography

[1] T. E. Tuncer and B. Friedlander, *Classical and Modern Direction-of-Arrival Estimation*. Academic Press, 2009.

[2] S. Chandran, *Advances in Direction-of-Arrival Estimation*. Artech House, 2005.

[3] Rohde & Schwarz, "Antenne ADD253," http://www.rohde-schwarz.com/en/product/add253, visited on Jun. 21, 2018.

[4] CRFS, "DF antenna RFeye Array 300," https://www.crfs.com/all-products/hardware/direction-finders/array-300/, visited on Jun. 21, 2018.

[5] TCI, "DF antenna Model 643," https://www.tcibr.com/product/tci-model-643-dual-polarized-vhfuhf-df-and-spectrum-monitoring-antenna/, visited on Jun. 21, 2018.

[6] A. Bellion and C. Le Meins, "Directional multiple-polarization wide band antenna network," Patent, Dec. 21, 2007, US20110133986A1.

[7] L. Scorrano and L. Dinoi, "Experimental characterization of a dual-polarized direction finding array for VHF-UHF frequency bands," in *European Conference on Antennas and Propagation (EUCAP)*, March 2017, pp. 1295–1298.

[8] Y. Lo and S. Lee, *Antenna Handbook: Volume III Applications*. Springer US, 1993.

[9] M. Pralon, "Compact antenna arrays for efficient direction of arrival estimation," Ph.D. dissertation, Ilmenau University of Technology, 2017.

[10] P. Gething, *Radio Direction Finding and Superresolution*, ser. Electromagnetics and Radar. P. Peregrinus Ltd., 1991.

[11] A. Nehorai and E. Paldi, "Vector-sensor array processing for electromagnetic source localization," *IEEE Transactions on Signal Processing*, vol. 42, no. 2, pp. 376–398, Feb. 1994.

[12] B. Almog, "Compact 3D direction finder," Patent EP20 120 184 835, 2013.

[13] A. Musicant, B. Almog, N. Oxenfeld, and R. Shavit, "Vector sensor antenna design for VHF band," *IEEE Antennas and Wireless Propagation Letters*, vol. 14, pp. 1404–1407, 2015.

[14] J. Lominé, C. Morlaas, C. Imbert, and H. Aubert, "Dual-band vector sensor for direction of arrival estimation of incoming electromagnetic waves," *IEEE Transactions on Antennas and Propagation*, vol. 63, no. 8, pp. 3662–3671, Aug. 2015.

[15] B. de Fontenelle, *Histoire de l'Académie royale des sciences avec les mémoires de mathématique et de physique*. Imprimerie royale, 1734.

[16] F. Delaveau and Y. Livran, "Radiosurveillance du spectre - goniométrie et localisation," *Techniques de l'ingénieur*, 2012.

[17] "Introduction into theory of direction finding," ser. Radio Monitoring and Radio Location. Rohde & Schwarz, 2000.

[18] E. Bellini and A. Tosi, "System of directed wireless telegraphy," Patent US943 960A, 1907.

[19] A. Rembovsky, A. Ashikhmin, V. Kozmin, and S. Smolskiy, "Radio monitoring: problems, methods and equipment," ser. Lecture Notes in Electrical Engineering. Springer US, 2009, vol. 43.

[20] R. E. Ellis and F. Adcock, "Improvements in means for determining the direction of a distant source of electro-magnetic radiation," Patent GB130 490A, 1919.

[21] P. Dessapt, "Bellini-tosi direction finder," https://ece.illinois.edu/about/history/antenna/photos.asp, visited on Jun. 26, 2018.

[22] R. A. W. Watt and J. F. Herd, "An instantaneous direct-reading radiogoniometer," *Journal of the Institution of Electrical Engineers*, vol. 64, no. 353, pp. 611–617, May 1926.

[23] US Air Force public affairs, "Wullenweber antenna at elmendorf afb, alaska," https://commons.wikimedia.org/wiki/File:CDAA_Elmendorf_AFB.PNG, visited on Jun. 26, 2018.

[24] "Signaux précis pour le test des récepteurs de radionavigation," ser. Actualités. Rohde & Schwarz, 2007, no. 192.

[25] "The European table of frequency allocations and applications in the frequency range 8.3 kHz to 3000 GHz." Electronic Communications Committee (ECC) within the European Conference of Postal and Telecommunications Administrations (CEPT), 2017.

[26] H. Cramer, *Mathematical Methods of Statistics*. Princeton University Press, 1946.

[27] C. Rao, "Information and the accuracy attainable in the estimation of statistical parameters," *Bulletin of the Calcutta Mathematical Society*, vol. 37, no. 3, pp. 81–91, 1945.

[28] P. Stoica and A. Nehorai, "MUSIC, maximum likelihood, and Cramer-Rao bound," *IEEE Transactions on Acoustics, Speech, and Signal Processing*, vol. 37, no. 5, pp. 720–741, May 1989.

[29] R. Fisher, "The logic of inductive inference," *Journal of the Royal Statistical Society*, no. 1, pp. 39–82, 1935.

[30] G. Maral and M. Bousquet, *Satellite Communications Systems: Systems, Techniques, and Technology*, 5th ed., ser. Communication and Distributed Systems. Wiley, 2009.

[31] R. Schmidt, "Multiple emitter location and signal parameter estimation," *IEEE Transactions on Antennas and Propagation*, vol. 34, no. 3, pp. 276–280, Mar. 1986.

[32] M. Eric, A. Zejak, and M. Obradovic, "Ambiguity characterization of arbitrary antenna array: type I ambiguity," in *IEEE International Symposium on Spread Spectrum Techniques and Applications*, vol. 2, Sep 1998, pp. 399–403.

[33] D. Spielman, A. Paulraj, and T. Kailath, "Performance analysis of the MUSIC algorithm," in *IEEE International Conference on Acoustics, Speech, and Signal Processing*, vol. 11, Apr 1986, pp. 1909–1912.

[34] K. Wei, Z. Xin, J. Xianjun, and C. Canfeng, "3-D ambiguity analysis method of arbitrary antenna array for direction finding," in *IEEE International Wireless Symposium*, March 2014, pp. 1–4.

[35] M. Eric, A. Zejak, and M. Obradovic, "Ambiguity characterization of arbitrary antenna array: type II ambiguity," in *IEEE International Symposium on Spread Spectrum Techniques and Applications*, vol. 3, Sep 1998, pp. 955–958.

[36] S. U. Pillai and B. H. Kwon, "Forward/backward spatial smoothing techniques for coherent signal identification," *IEEE Transactions on Acoustics, Speech, and Signal Processing*, vol. 37, pp. 8–15, 1989.

[37] J. E. Evans, "High resolution angular spectrum estimation technique for terrain scattering analysis and angle of arrival estimation," in *IEEE Acoustics, Speech and Signal Processing Workshop on Spectral Estimation*, Hamilton, 1981, pp. 134–139.

[38] T. J. Shan and T. Kailath, "Adaptive beamforming for coherent signals and interference," *IEEE Transactions on Acoustics, Speech, and Signal Processing*, vol. 33, no. 3, pp. 527–536, Jun 1985.

[39] T. J. Shan, M. Wax, and T. Kailath, "On spatial smoothing for direction-of-arrival estimation of coherent signals," *IEEE Transactions on Acoustics, Speech, and Signal Processing*, vol. 33, no. 4, pp. 806–811, Aug 1985.

[40] J. M. Beukers and H. M. Jaffe, "Doppler direction finder," Patent US3 329 955A, 1966.

[41] G. Multedo, "Radiosurveillance du spectre," *Techniques de l'ingénieur*, 1994.

[42] J. Li, "Direction and polarization estimation using arrays with small loops and short dipoles," *IEEE Transactions on Antennas and Propagation*, vol. 41, no. 3, pp. 379–387, March 1993.

[43] J. Capon, "High-resolution frequency-wavenumber spectrum analysis," *Proceedings of the IEEE*, vol. 57, no. 8, pp. 1408–1418, Aug 1969.

[44] A. Paulraj, R. Roy, and T. Kailath, "A subspace rotation approach to signal parameter estimation," *Proceedings of the IEEE*, vol. 74, no. 7, pp. 1044–1046, July 1986.

[45] A. Barabell, "Improving the resolution performance of eigenstructure-based direction-finding algorithms," in *IEEE International Conference on Acoustics, Speech, and Signal Processing*, vol. 8, Apr 1983, pp. 336–339.

[46] B. D. Rao and K. V. S. Hari, "Performance analysis of root-music," *IEEE Transactions on Acoustics, Speech, and Signal Processing*, vol. 37, no. 12, pp. 1939–1949, Dec 1989.

[47] M. Wax and T. Kailath, "Optimum localization of multiple sources by passive arrays," *IEEE Transactions on Acoustics, Speech, and Signal Processing*, vol. 31, no. 5, pp. 1210–1217, Oct 1983.

[48] I. Ziskind and M. Wax, "Maximum likelihood localization of multiple sources by alternating projection," *IEEE Transactions on Acoustics, Speech, and Signal Processing*, vol. 36, no. 10, pp. 1553–1560, Oct 1988.

[49] A. Bellion, C. Le Meins, A. Julien-Vergonjanne, and T. Monediere, "A new compact dually polarized direction finding antenna on the UHF band," in *IEEE International Symposium on Antennas and Propagation (APSURSI)*, July 2008, pp. 1–4.

[50] Alaris, "Antenna DF-A0031," http://www.alarisantennas.com/products/wideband-portable-direction-finding-antenna-array/, visited on Jun. 21, 2018.

[51] Alaris, "Antenna DF-A0049," http://www.alarisantennas.com/products/quick-deployment-hf-nvis-df-element/, visited on Jun. 21, 2018.

[52] Rohde & Schwarz, "Antenne ADD170," http://www.rohde-schwarz.com/en/product/add170, visited on Jun. 21, 2018.

[53] N. Lorho, "Étude de la conception d'une antenne compacte ultra large-bande à diversité de polarisation. application à la radiogoniométrie." Ph.D. dissertation, Université de Nantes, Mar. 2017.

[54] G. Villemaud, C. Dall'omo, T. Monediere, and B. Jecko, "Multiband antennas for an emergency rescue system based on cellular phones localisation," in *International Conference on Applied Electromagnetics and Communications*, Oct 2003, pp. 320–323.

[55] R. Sarkis, C. Craeye, A. Ferreol, and P. Morgand, "Design of triple band antenna array for GSM/DCS/UMTS handset localization," in *European Conference on Antennas and Propagation (EuCAP)*, March 2009, pp. 3051–3054.

[56] R. N. Pack, G. Lasser, and D. S. Filipovic, "Performance characterization of four-arm MAW spiral antennas for digital direction-of-arrival sensing," *IEEE Transactions on Antennas and Propagation*, vol. 66, no. 6, pp. 2761–2769, June 2018.

[57] D. Sengupta, J. Ferris, R. Larson, G. Hok, and T. Smith, "Azimut and elevation direction finder study," University of Michigan, Radiation Laboratory, Department of Electrical Engineering, Tech. Rep., 1966.

[58] J. Ferris, P. Wilcox, and W. Zimmerman, "Azimuth and elevation direction finder techniques," University of Michigan, Radiation Laboratory, Department of Electrical Engineering, Tech. Rep., 1968.

[59] "3D 360° tracking antenna array IsoLOG 3D (20 MHz to 20 GHz) ultra wideband, real-time spectrum monitoring and direction finding," AARONIA, Tech. Rep., 2016.

[60] D. Farina, "Superresolution compact array radiolocation technology (SuperCART) project," Flam & Russell Tech. Rep, Tech. Rep., 1990.

[61] J. Bull, "Field probe for measuring vector component of an electromagnetic field," Patent US5 300 885A, 1994.

[62] L. L. Monte, B. Elnour, and D. Erricolo, "Distributed 6D vector antennas design for direction of arrival applications," in *International Conference on Electromagnetics in Advanced Applications*, Sept 2007, pp. 431–434.

[63] L. L. Monte, B. Elnour, D. Erricolo, and A. Nehorai, "Design and realization of a distributed vector sensor for polarization diversity applications," in *International Waveform Diversity and Design Conference*, June 2007, pp. 358–361.

[64] M. J. Slater, C. D. Schmitz, M. D. Anderson, D. L. Jones, and J. T. Bernhard, "Demonstration of an electrically small antenna array for UHF direction-of-arrival estimation," *IEEE Transactions on Antennas and Propagation*, vol. 61, no. 3, pp. 1371–1377, March 2013.

[65] ELTA, "ELK-7065 - airborne HF COMINT/DF system," http://www.iai.co.il/2013/34484-45408-en/Groups_ELTA_EltaNumbers_Products.aspx.

[66] J. Lominé, C. Morlaas, and H. Aubert, "Novel vector sensors design with three co-located or distributed elements for the 3D DOA estimation," *Progress In Electromagnetics Research B*, vol. 57, pp. 207–220, 2014.

[67] "Active receiving antennas webcast." Rohde & Schwarz, https://www.rohde-schwarz.com/de/applikationen/active-receiving-antennas-webcast-application-video_56281-483385.html.

[68] G. H. Tan and C. H. Rohner, "Low-frequency array active-antenna system," in *Radio Telescopes*, vol. 4015. International Society for Optics and Photonics, 2000, pp. 446–458.

[69] S. Hebib, "Nouvelle topologie d'antennes multi-bandes pour applications spatiales," Ph.D. dissertation, Université de Toulouse, 2008.

[70] E. Ferrara and T. Parks, "Direction finding with an array of antennas having diverse polarizations," *IEEE Transactions on Antennas and Propagation*, vol. 31, no. 2, pp. 231–236, Mar 1983.

[71] I. Ziskind and M. Wax, "Maximum likelihood localization of diversely polarized sources by simulated annealing," *IEEE Transactions on Antennas and Propagation*, vol. 38, no. 7, pp. 1111–1114, Jul 1990.

[72] W. Stutzman and G. Thiele, *Antenna Theory and Design*, 3rd ed. Wiley, 2012.

[73] A. Chabory, C. Morlaas, and B. Souny, "Efficiency characterization of vector-sensor antennas with distributed elements for 3d direction finding," in *IEEE APS Topical Conference on Antennas and Propagation in Wireless Communications*, Sept 2011, pp. 819–822.

[74] J. Lominé, "Étude d'une antenne vectorielle UHF multibande appliquée à la goniométrie 3D," Ph.D. dissertation, Université de Toulouse, 2014.

[75] X. Yuan, K. T. Wong, Z. Xu, and K. Agrawal, "Various compositions to form a triad of collocated dipoles/loops, for direction finding and polarization estimation," *IEEE Sensors Journal*, vol. 12, no. 6, pp. 1763–1771, June 2012.

[76] K. T. Wong and X. Yuan, "Vector cross-product direction-finding with an electromagnetic vector-sensor of six orthogonally oriented but spatially noncollocating dipoles/loops," *IEEE Transactions on Signal Processing*, vol. 59, no. 1, pp. 160–171, Jan 2011.

[77] L. C. Godara, *Handbook of Antennas in Wireless Communications*. CRC Press, Inc., 2001.

[78] K. T. Wong, "Direction finding/polarization estimation-dipole and/or loop triad(s)," *IEEE Transactions on Aerospace and Electronic Systems*, vol. 37, no. 2, pp. 679–684, Apr 2001.

[79] C. M. S. See and A. Nehorai, "Source localization with distributed electromagnetic component sensor array processing," in *Seventh International Symposium on Signal Processing and Its Applications, 2003. Proceedings.*, vol. 1, July 2003, pp. 177–180 vol.1.

[80] M. Hurtado and A. Nehorai, "Performance analysis of passive low-grazing-angle source localization in maritime environments using vector sensors," *IEEE Transactions on Aerospace and Electronic Systems*, vol. 43, no. 2, pp. 780–789, April 2007.

[81] C. A. Balanis, *Antenna Theory: Analysis and Design.* Wiley-Interscience, 2005.

[82] J. L. Volakis, *Antenna Engineering Handbook*, 4th ed. McGraw-Hill Companies, 2007.

[83] Y. Mushiake, "Self-complementary antennas," *IEEE Antennas and Propagation Magazine*, vol. 34, no. 6, pp. 23–29, Dec 1992.

[84] H. G. Booker, "Slot aerials and their relation to complementary wire aerials (Babinet's principle)," *Journal of the Institution of Electrical Engineers*, vol. 93, no. 4, pp. 620–626, 1946.

[85] J. Dyson, "The equiangular spiral antenna," *IRE Transactions on Antennas and Propagation*, vol. 7, no. 2, pp. 181–187, April 1959.

[86] P. Mayes, "Conical log-spiral antenna," https://ece.illinois.edu/about/history/antenna/photos.asp, visited on Jun. 26, 2018.

[87] R. H. DuHamel and D. E. Isbell, "Broadband logarithmically periodic antenna structures," in *IRE International Convention Record*, vol. 5, March 1957, pp. 119–128.

[88] D. Isbell, "Log periodic dipole arrays," *IRE Transactions on Antennas and Propagation*, vol. 8, no. 3, pp. 260–267, May 1960.

[89] D. E. Isbell, "Frequency independent unidirectional antennas," Patent US3 210 767A, 1960.

[90] D. H. Werner and S. Ganguly, "An overview of fractal antenna engineering research," *IEEE Antennas and Propagation Magazine*, vol. 45, no. 1, pp. 38–57, Feb 2003.

[91] M. Sindou, G. Ablart, and C. Sourdois, "Multiband and wideband properties of printed fractal branched antennas," *Electronics Letters*, vol. 35, no. 3, pp. 181–182, Feb 1999.

[92] H. Schantz, *The Art and Science of Ultrawideband Antennas*, ser. Artech House antennas and propagation library. Artech House, 2005.

[93] H. Wheeler, "Fundamental limitations of small antennas," *Proceedings of the IRE*, vol. 35, no. 12, pp. 1479–1484, Dec 1947.

[94] R. Hansen, "Fundamental limitations in antennas," *Proceedings of the IEEE*, vol. 69, no. 2, pp. 170–182, Feb 1981.

[95] H. Wheeler, "The radiansphere around a small antenna," *Proceedings of the IRE*, vol. 47, no. 8, pp. 1325–1331, Aug 1959.

[96] J. McLean, "A re-examination of the fundamental limits on the radiation Q of electrically small antennas," *Antennas and Propagation, IEEE Transactions on*, vol. 44, no. 5, pp. 672–, May 1996.

[97] K. R. Carver and J. Mink, "Microstrip antenna technology," *Antennas and Propagation, IEEE Transactions on*, vol. 29, no. 1, pp. 2–24, Jan 1981.

[98] O. Lodge, "Electric telegraphy," Patent US0 609 154, 1898.

[99] G. Dubost and S. Zisler, *Antennes à large bande: théorie et applications*, ser. Monographies d'électronique, 1976.

[100] N. P. Agrawall, G. Kumar, and K. P. Ray, "Wide-band planar monopole antennas," *IEEE Transactions on Antennas and Propagation*, vol. 46, no. 2, pp. 294–295, Feb 1998.

[101] X. L. Liang, *Ultra-Wideband Antenna and Design*. InTech, 2012. [Online]. Available: http://www.intechopen.com/books/ultra-wideband-current-status-and-future-trends/ultra-wideband-antenna-and-design

[102] S.-Y. Suh, W. L. Stutzman, and W. A. Davis, "A new ultrawideband printed monopole antenna: the planar inverted cone antenna (pica)," *IEEE Transactions on Antennas and Propagation*, vol. 52, no. 5, pp. 1361–1364, May 2004.

[103] G. Goubau, "Antenna structures having reactance at free end," Patent US3 967 276A, 1976.

[104] C. Friedman, "Wide-band matching of a small disk-loaded monopole," *IEEE Transactions on Antennas and Propagation*, vol. 33, no. 10, pp. 1142–1148, October 1985.

[105] N. Behdad, M. Li, and Y. Yusuf, "A very low-profile, omnidirectional, ultrawideband antenna," *IEEE Antennas and Wireless Propagation Letters*, vol. 12, pp. 280–283, 2013.

[106] M. Li and N. Behdad, "A compact, capacitively fed UWB antenna with monopole-like radiation characteristics," *IEEE Transactions on Antennas and Propagation*, vol. 65, no. 3, pp. 1026–1037, March 2017.

[107] K. Wei, Z. Zhang, and Z. Feng, "Design of a wideband horizontally polarized omnidirectional printed loop antenna," *IEEE Antennas and Wireless Propagation Letters*, vol. 11, pp. 49–52, 2012.

[108] A. Alford and A. G. Kandoian, "Ultrahigh-frequency loop antennas," *Electrical Engineering*, vol. 59, no. 12, pp. 843–848, Dec 1940.

[109] C. Lin, L. Kuo, and H. Chuang, "A horizontally polarized omnidirectional printed antenna for wlan applications," *IEEE Transactions on Antennas and Propagation*, vol. 54, no. 11, pp. 3551–3556, Nov 2006.

[110] A. Adams, "Flush mounted rectangular cavity slot antennas–theory and design," *IEEE Transactions on Antennas and Propagation*, vol. 15, no. 3, pp. 342–351, May 1967.

[111] J. Hirokawa, "Cavity-backed wide slot antenna."

[112] B. Ghosh, S. K. M. Haque, and N. R. Yenduri, "Miniaturization of slot antennas using wire loading," *IEEE Antennas and Wireless Propagation Letters*, vol. 12, pp. 488–491, 2013.

[113] Y. Yu, F. Jolani, and Z. Chen, "A wideband omnidirectional horizontally polarized antenna for 4G LTE applications," *IEEE Antennas and Wireless Propagation Letters*, vol. 12, pp. 686–689, 2013.

[114] Z. D. Wang, Y. Z. Yin, X. Yang, and J. J. Wu, "Design of a wideband horizontally polarized omnidirectional antenna with mutual coupling method," *IEEE Transactions on Antennas and Propagation*, vol. 63, no. 7, pp. 3311–3316, July 2015.

[115] H. Y. Zhang, F. S. Zhang, F. Zhang, T. Li, and C. Li, "Bandwidth enhancement of a horizontally polarized omnidirectional antenna by adding parasitic strips," *IEEE Antennas and Wireless Propagation Letters*, vol. 16, pp. 880–883, 2017.

[116] T. S. Chu, "On the use of uniform circular arrays to obtain omnidirectional patterns," *IRE Transactions on Antennas and Propagation*, vol. 7, no. 4, pp. 436–438, October 1959.

[117] L. Lewis, M. Fassett, and J. Hunt, "A broadband stripline array element," in *Antennas and Propagation Society International Symposium, 1974*, vol. 12, Jun 1974, pp. 335–337.

[118] P. J. Gibson, "The Vivaldi aerial," in *9th European Microwave Conference*, Sept 1979, pp. 101–105.

[119] K. S. Yngvesson, T. L. Korzeniowski, Y. S. Kim, E. L. Kollberg, and J. F. Johansson, "The tapered slot antenna-a new integrated element for millimeter-wave applications," *IEEE Transactions on Microwave Theory and Techniques*, vol. 37, no. 2, pp. 365–374, Feb 1989.

[120] T. S. P. See, X. Qing, and Z. N. Chen, "A wideband horizontally polarized omnidirectional antenna," in *IEEE 4th Asia-Pacific Conference on Antennas and Propagation*, June 2015, pp. 294–295.

[121] H. Liu, Y. Liu, W. Zhang, and S. Gao, "An ultra-wideband horizontally polarized omnidirectional circular connected vivaldi antenna array," *IEEE Transactions on Antennas and Propagation*, vol. 65, no. 8, pp. 4351–4356, Aug 2017.

[122] J. Shin and D. H. Schaubert, "A parameter study of stripline-fed vivaldi notch-antenna arrays," *IEEE Transactions on Antennas and Propagation*, vol. 47, no. 5, pp. 879–886, May 1999.

[123] S. Appadwedula and C. M. Keller, "Direction-finding results for a vector sensor antenna on a small UAV," in *Fourth IEEE Workshop on Sensor Array and Multichannel Processing*, July 2006, pp. 74–78.

[124] H. V. Trees, *Optimum Array Processing: Part IV of Detection, Estimation, and Modulation Theory*, ser. Detection, Estimation, and Modulation Theory. Wiley, 2004.

[125] R. Pöhlmann, S. Alkubti Almasri, S. Zhang, T. Jost, A. Dammann, and P. A. Hoeher, "On the Potential of Multi-Mode Antennas for Direction-of-Arrival Estimation," *ArXiv e-prints*, Submitted in June 2018.

[126] R. Pohlmann, S. Zhang, T. Jost, and A. Dammann, "Power-based direction-of-arrival estimation using a single multi-mode antenna," in *Workshop on Positioning, Navigation and Communications (WPNC)*, Oct 2017, pp. 1–6.

[127] S. Miron, N. Le Bihan, and J. Mars, "Quaternion - MUSIC for vector sensor array processing," *IEEE Transactions on Signal Processing*, vol. 54, pp. 1218–1229, 2006.

[128] L. Wang, L. Yang, G. Wang, Z. Chen, and M. Zou, "Uni-vector-sensor dimensionality reduction MUSIC algorithm for DoA and polarization estimation," *Mathematical Problems in Engineering*, 2014.

Abstract — Direction finding plays a crucial role in various civilian and military applications, related to either radionavigation or radiolocation. Most of the direction finding antennas operate over a wide frequency band, but only a minority of them enable the direction of arrival estimation of an incoming electromagnetic field over a 3-D angular coverage (i.e., estimation of both azimuth and elevation angles). An original approach to obtain a 3-D angular coverage consists in measuring the six components of the incident electromagnetic field through a so-called vector antenna. The aim of this Ph.D. is to design a passive, compact and wideband vector antenna in order to cover a maximum of applications. Two vector antennas have been designed, manufactured and experimentally characterized. Unlike conventional topology, they enable the measurement of the components of an incoming electromagnetic field thanks to the radiation pattern reconfigurability of an original arrangement of Vivaldi antennas. The first prototype is mounted over a finite metallic support and enables the direction of arrival estimation of vertically-polarized electromagnetic fields over a 1.69:1 bandwidth while the second one can be used regardless of the polarization of the incoming electromagnetic fields over a 8:1 bandwidth. Moreover, the direction finding performances of these vector antennas have been improved in terms of estimation accuracy, sensitivity, robustness to angular ambiguity and polarization mismatch by synthesizing new radiation patterns in the estimation process. A method based on the Cramer-Rao lower bound has been proposed to select efficiently and rapidly the additional radiation patterns.

Keywords: 3-D direction finding antenna, vector antenna, wideband electric and magnetic dipoles, radiation pattern reconfigurable antenna, radiation pattern diversity.

Résumé — La radiogoniométrie joue un rôle crucial dans diverses applications, aussi bien civiles que militaires, liées soit à la radionavigation ou à la radiolocalisation. La plupart des antennes de goniométrie opèrent sur une large bande de fréquences, mais seule une minorité d'entre elles permettent l'estimation de la direction d'arrivée d'un champ électromagnétique incident sur une couverture angulaire 3-D (c.-à-d., l'estimation à la fois des angles d'azimut et d'élévation). Une approche originale permettant d'obtenir une couverture angulaire 3-D consiste à mesurer les six composantes d'un champ électromagnétique incident à l'aide d'une antenne dite vectorielle. L'objectif de cette thèse est de concevoir une antenne vectorielle passive, compacte et large-bande afin de couvrir un maximum d'applications. Deux antennes vectorielles ont été conçues, fabriquées et caractérisées expérimentalement. À la différence d'une topologie conventionnelle, elles permettent de mesurer les composantes d'un champ électromagnétique incident grâce à la reconfigurabilité en diagramme de rayonnement d'un arrangement original d'antennes Vivaldi. Le premier prototype est monté sur un support métallique fini et permet l'estimation de la direction d'arrivée de champs électromagnétiques polarisés verticalement sur une bande passante de 1.69:1 tandis que le second peut être utilisé quelle que soit la polarisation des champs électromagnétiques incidents sur une bande passante de 8:1. De plus, les performances de goniométrie de ces antennes vectorielles ont été améliorées du point de vue de la précision, de la sensibilité, de la robustesse face aux ambiguïtés angulaires et aux erreurs de dépolarisation en synthétisant de nouveaux diagrammes de rayonnement dans le processus d'estimation. Une méthode basée sur la borne de Cramer-Rao a été élaborée afin de sélectionner efficacement et rapidement les diagrammes de rayonnement supplémentaires.

Mots-clés : antenne de goniométrie 3-D, antenne vectorielle, dipoles électrique et magnétique large-bande, antenne reconfigurable en diagramme, diversité de diagramme de rayonnement.